Dissertation submitted to the Boards of the Faculty of Life Sciences, in fulfilment of the degree of Doctor of Philosophy

Natural and bioinspired silk spinning

Gwilym Davies
Oxford Silk Group
Department of Zoology

Pembroke College

The University of Oxford

Supervisors

Prof. Fritz Vollrath
Dr. David Porter

Trinity 2013

Natural and bioinspired silk spinning

Thesis abstract

Gwilym Davies

Pembroke College
Trinity 2013

Oxford Silk Group
The Department of Zoology

Dissertation submitted to the Boards of the Faculty of Life Sciences, in fulfilment of the degree of Doctor of Philosophy in Zoology

This thesis describes an investigation into silk spinning, with the objective of producing high performance silk fibres in the laboratory using a novel spinning device based upon observations on natural spinning glands and processes. After an in-depth literature review the work is reported in two sections: natural and artificial spinning. The literature provides fragmented data on different aspects of natural silk production, and artificial spinning has not yet reproduced fibres with the properties of native silk fibres, despite unfounded claims of biomimetic spinning.

The first half of the thesis looks at natural silk spinning. The work started with a general study of the morphology of spider and silkworm spinning ducts: First, how the silk fibre develops as the dope flows through the gland; and second the relationship between silk fibre properties and both gland morphology and spinning speed. More detailed studies using histochemical and spectroscopic investigations showed that the silk ducts of the spider *Nephila edulis* and the silkworm *Bombyx mori* both contain β-chitin, despite an evolutionarily distant common ancestor. Finally, observations showed that the duct of *N. edulis* consists of alternating nanoporous discs, and FEA modelling indicated that the duct is optimised for mechanical integrity and permeability.

The second half of the thesis describes the development of a spinning device that uses natural silk dope mainly taken from *B. mori* as feedstock. It begins with a description of the gradual development of the engineering aspects of the spinning device, to meet challenges raised during the spinning investigation. The development of a centrifugal capillary rheometer, for practical quantitative insights into rheological processes is then presented. Finally the spinning investigation is reported: first, the screening of spinning in glass capillaries based upon natural gland dimensions and flow rates, which have been shown to induce fibrillation in silk dope in a rheometer, and also included initiation of instability through heat applied along the capillary; second, the final spinning evaluation, using lessons learned from all the screening trials throughout the project, but also including a key development of a hydrophobic coating on the capillary tip to inhibit droplet formation and massively increase the process stability and ease of fibre production.

The main conclusions from this work are that good silk fibre cannot be spun by flow shear stress alone; and, that heat instability induces indiscriminate gelation of the silk, whose disordered molecular structure gives poor silk fibre properties. The body of work behind these conclusions provides fundamental background information and new insights that will contribute to the next stages of development of artificial silk spinning, from obtaining a better understanding of the biology of natural spinning glands to the engineering difficulties of implementing the bioinspired principles.

Acknowledgements

Publications

Several chapters of this thesis were revised or partly revised from the following publications, with the collaborators noted.

Chapter 3 General investigation into silk spinning gland morphology

2013 Davies, G.J.G., Knight, D.P. & Vollrath, F. - Structure and function of the major ampullate spinning duct of the golden orb weaver, *Nephila edulis*. *Tissue and Cell,* 45 (5): 306-311

Chapter 4 Extracellular morphology of the silk duct

2013 Davies, G.J.G., Knight, D.P. & Vollrath, F. - Chitin in the Silk Gland Ducts of the Spider *Nephila edulis* and the Silkworm *Bombyx mori*. *PLOS ONE,* 8 (8): e73225

Chapter 5 Internal Microstructure and function of the silk duct

2013 Davies, G.J.G., Vollrath, F. & Knight, D.P. - Ultrastructure and Properties of the Major Ampullate Spinning Duct of the Golden Orb Weaver, *Nephila edulis*, submitted.

Contents

Acknowledgements i

Publications ii

Contents iii

List of Abbreviations, Symbols and Units xi

Chapter 1. Introduction 1

1.1 Overview 1

1.2 Natural silk spinning 5

1.3 Artificial silk spinning attempts 12

1.4 Thesis and introduction to chapters 16

Chapter 2. Methods 23

2.1. Biological preparation 23

2.1.1. Spider 23

2.1.2. Silkworm 25

2.2. Duct and capillary measurement 26

2.3. Fibre testing 27

2.3.1. Fibre collection 27

2.3.2. Fibre mounting onto frames 27

2.3.3. Tensile testing 27

2.3.4. Fibre cross section measurement 28

2.3.5. Fibre solubility 28

2.3.6. Fibre polarization 28

Chapter 3. General investigation into silk spinning gland morphology 29

3.1. Introduction 29

3.2. Methods development 35

3.2.1. Preliminary study 35

3.2.2. Spider morphology study 36

3.2.3. Sectioned silkworm duct study 40

3.2.4. Silk properties 43

3.3. Results and discussion 44

3.3.1. Preliminary study 44

3.3.2. Spider morphology study 48

3.3.3. Sectioned silkworm duct study 57

3.3.4. Silk properties 63

3.4. Summary and conclusions 68

Chapter 4. Extracellular morphology of the silk duct 71

4.1. Introduction 71

4.2. Methods 73

4.2.1. Specimen preparation 73

4.2.2. Histochemical detection of extent of chitin along the duct 73

4.2.3. Spectroscopic detection of chitin 74

4.3. Results 75

4.3.1. Presence of chitin 75

4.3.2. Longitudinal distribution of chitin 77

4.3.3. FTIR spectroscopy of ducts 78

4.4. Discussion 82
4.4.1. Correlation between chitin histochemistry and FTIR spectroscopy 82
4.4.2. Chitin presence in silk duct walls 83
4.4.3. Relevance of chitin in silk spinning 83
4.4.4. Relevance of chitin to origins of silk ducts 84
4.5. Conclusion 85
Chapter 5. Internal Microstructure and function of the silk duct 87
5.1. Introduction 87
5.1.1. Context 87
5.1.2. Structural rigidity 87
5.1.3. Diffusion across the duct 88
5.1.4. Literature relevant to the duct in relation to structure and diffusion 88
5.1.5. Specific aims of this chapter 89
5.2. Biological imaging: Methods section 90
5.2.1. Ultrastructure of the cuticle lining of the duct 90
5.2.2. Light microscopy of the cuticle lining of the duct 91
5.3. Biological imaging: Results 92
5.3.1. Ultrastructure of the cuticle lining of the duct 92
5.3.2. Light microscopy of the cuticle lining of the duct after chitin test 96
5.4. FEA: Methods section 98
5.4.1. Introduction to FEA use 98
5.4.2. Shape and parameters assumed by FEA 98
5.4.3. Materials assumed for FEA 102

5.4.4. Test constraints 102
5.5. FEA: Results 103
5.6. Discussion 105
5.6.1. Ultrastructure and material of the cuticle lining of the duct 105
5.6.2. Finite element analysis 107
5.7. Conclusions 109
Chapter 6. Bioinspired silk spinning: Strategy and device development 111
6.1. Movement generation apparatus: syringe pump 113
6.2. Spinning nozzles 113
6.2.1. Laser engraved 113
6.2.2. Glass capillaries: hand pulled 114
6.2.3. Glass capillary puller 114
6.2.4. Epoxy chip mount for capillary 115
6.2.5. Epoxy chip hybrid 117
6.2.6. One Luer, one seal 118
6.2.7. Two Luer nozzle 118
6.2.8. Shortened Luer nozzle 119
6.3. Gelation initiator: capillary heating 120
6.3.1. Temperature measurement 120
6.3.2. Humidifier annulus 120
6.3.3. Hot coil 121
6.3.4. Peltier 122
6.4. Fibre collection from nozzle 123

6.4.1. Fibre pulling 123
6.4.2. Collecting rod rotation 124
6.4.3. Fibre collection rods 124
6.4.4. Horizontal movement driver 125
6.5. Computer interface 125
6.6. Fibre mounting 126
6.7. Final setup 127
Chapter 7. Capillary rheology with centripetal force 129
7.1. Introduction 129
7.2. Methods 131
7.2.1. Experimental apparatus 131
7.2.2. Materials 132
7.2.3. Preliminary calculations 132
7.2.4. Experimental testing of analytical equation 133
7.2.5. Fibre Spinning 134
7.3. Results and discussion 135
7.3.1. Comparing model to experimental results 135
7.3.2. Dope rheology 139
7.3.3. Fibre characterization 140
7.4. Summary and conclusion 143
Chapter 8. Bioinspired silk spinning: synthetic screening trials 145
8.1. Introduction 145
8.2. Methods 149

8.3. Results 151
8.3.1. Initial screening trials to scope problem. 151
8.3.2. Temperature augmented spinning 157
8.3.3. Fibre analysis 163
8.4. Summary and discussion 169
Chapter 9. Controlled shear spinning 173
9.1. Introduction 173
9.2. Materials and methods 175
9.2.1. Fibre spinning 176
9.2.2. Annealing 176
9.2.3. Fibre characterization 177
9.3. Results 177
9.3.1. Hydrophobicity 177
9.3.2. Fibre spinning: silkworm dope 179
9.3.3. Fibre spinning: spider dope 189
9.4. Summary and discussion 191
9.5. Conclusions 196
Chapter 10. Conclusions 197
10.1. Thesis summary 197
10.2. Technical achievements 199
10.3. Scientific findings and their implications 201
10.4. Suggestions for future developments 202
10.5. Final summary 203

Appendix A. 3D section preparation 205

A.a. Overview 205

A.b. Collection & Identification 205

A.c. Immobilization of specimen 206

A.d. Fixing 206

A.e. Dehydration & clearing 206

A.f. Infiltration & Embedding 207

A.g. Sectioning 207

A.h. Mounting 209

A.i. Staining 210

A.j. Image acquisition 211

A.k. Image processing 211

A.l. 3D reconstruction 211

A.m. Wax embedding protocol 211

A.m.i. Fixation 212

A.m.ii. Dehydration 212

A.m.iii. Infiltration 212

A.m.iv. Embedding 212

A.n. H&E Staining 213

A.o. Image acquisition 214

A.p. Image processing 214

A.q. 3D reconstruction packages 215

A.r. Amira protocol 216

Appendix B. Centrifuge model development 219

B.a. Derivation and analysis of equations 219

B.a.i. Centripetal force into capillary flow 219

B.a.ii. Dimensional analysis 220

B.b. Development of model equation data 222

Appendix C. Spinning device development 229

C.a. 'One Luer one seal' Nozzle spinning 229

C.b. 'Two Luer' spinning instructions 229

C.c. 'Shortened Luer' spinning instructions 230

C.d. Hot coil heating device 231

C.e. Peltier modifications 232

C.f. Collecting rod rotation 233

C.f.i. Generation 2 233

C.g. Collecting rods 234

C.h. Horizontal movement 235

C.h.i. Lego with motor 235

C.h.ii. Floppy disc drive frame with motor 236

C.i. Software details and code 236

C.i.i. Background 236

C.i.ii. Code 236

Appendix D. References 243

List of Abbreviations, Symbols and Units

Abbreviation	Meaning
3D	Three-dimensional
ca	Circa
CAD	Computer aided design
cm	Centimetres
CO_2	Carbon dioxide
CryoSEM	Cryogenic scanning electron microscopy
DPX	Di-n-Butyl phthalate in xylene
EDAX	Energy dispersive x-ray
EM	Electron microscopy
EtOH	Ethanol
FEA	Finite element analysis
FTIR	Fourier transform infrared spectroscopy
g	Gram
GPa	Gigapascal
Gsm	Gram per square metre
HFA	Hydrofluoroalkane
HFIP	Hexafluoro-2-propanol
kDA	Kilo dalton, mass on atomic scale
KOH	Potassium hydroxide
m	Metre
ml	Millilitre
mm	Millimetre
mN	Micro Newton
MPa	Megapascal
N	Newton
NIH	(United States) National Institutes of Health

Nm	Nanometre
Pa	Pascal
PEEK	Poly(aryl ether ether ketone)
pH	Decimal cologarithm of hydrogen (measure of acidity)
pI	Isoelectric point
PWM	Pulse wave modulation
Px	Pixel
Rheo-FTIR	Rheo-optical Fourier transform infrared spectroscopy
RPM	Revolutions per minute
RSF	Reconstituted silk fibroin
SEM	Scanning electron microscopy
SF	Silk fibroin
Sp1, Sp2	Spider protein 1, 2
TEM	Transmission electron microscopy
USB	Universal serial bus
w/v	Weight per volume
w/w	Weight per weight
Wt. %	Weight percent
μm	Micrometre
μN	Milli Newton

Chapter 1. Introduction

1.1 Overview

Silks are a class of proteins spun by arthropods for a variety of biological functions. Constructed of long protein chains, silk is able to resist large tensile forces without breaking, is biocompatible and environmentally friendly. Silk's remarkable properties have been known for over 400 years, with a very appropriate comment for this thesis being included by Robert Hooke in his seminal work, Micrographia (London 1665):

"There might be a way found out, to make a...composition if not full as good, nay better, then that ... substance it be out of which, the Silk-worm wire-draws his clew. If such a composition were found, it were certainly an easie matter to find very quick ways of drawing it out into small wires for use. I need not mention the use of such an Invention, nor the benefit that is likely to accrue to the finder, they being sufficiently obvious."

Despite Hooke's confidence in the ease with which artificial silk fibres would be made, not until the last twenty years have attempts with scientific basis been made towards the aim of finding a method of spinning fibres with properties comparable to spider or insect silks. This introduction gives a brief outline of silk properties and then reviews previous work: first, the observations on the natural spinning process for silk in spiders and silkworms and, second, previous attempts to spin artificial silk fibres. This reflects the overall strategy of this work, which was to use detailed observations of natural silk spinning glands and processes to guide the production of 'synthetic' silk fibres in the laboratory, using natural silk material as the feedstock. Finally, a brief summary of the content of this thesis is given to guide the reader through the work.

Many species can produce several different types of silk. For example, spiders may produce up to seven different types of silk from their specialised set of glands, for up to nine distinct functions (Foelix, 1996). Of all silks produced in the biological realm, 'dragline' or 'lifeline' silks of spiders and the cocoon silks of silkworms generate the most interest because of their excellent tensile properties (a combination of high strength and toughness (Porter et al., 2012) and being available in large enough quantities for study. The tensile properties of dragline silk produced from the major ampullate gland of the golden orb weaving spiders are compared with important man-made fibres, including the aramid fibre Kevlar (Vollrath and Knight, 2001), as summarised in Table 1.1 and illustrated in Fig. 1.1.

Although the specific ultimate tensile strength or modulus properties of silks are not as high as some of the materials in the table, the form of the stress strain curve gives a toughness that surpasses all man-made fibres. While some doubt has been cast recently upon the bulk mechanical properties of silk in any form other than thin fibres (Porter et al., 2013), silks do have major advantages for the future through their excellent biocompatibility and biodegradability (Altman et al., 2003).

While its properties may be attractive, natural silk does have practical disadvantages for modern industrial production of products such as textiles. Complex are steps required to extract the silk fibres from cocoons to produce yarns, or a very large number of spiders are needed to provide spider silk in any quantity, with their cannibalistic nature that precludes rearing in high densities. Therefore, there is a need to produce artificial silk that removes these disadvantages, or at least makes silk fibre production more compatible with other synthetic fibres, and reduces some of the product variability of properties generally associated with natural materials.

Although considerable effort has been expended in attempts to spin artificial silk fibres, a convincing analogue has yet to emerge. This failure may be due to an incomplete understanding of the complex biological interactions that together make up the silk production line.

There is a continued need for studies of the silk production process from both a biological and engineering perspective (Vollrath et al., 2011) until equivalent fibres can be produced artificially. To give a grounding in natural methods, the first half of this chapter concerns an in-depth literature review into natural silk spinning. Spiders produce silks with a better and wider range of mechanical properties than the silks produced by silkworms, so this part of the thesis is mainly concerned with how spider silk dope is processed into fibres. However, it will be shown that these processes are clearly similar in silkworms.

The aim of this thesis was to develop a bioinspired artificial spinning system that can spin fibres with properties similar to natural fibres. This has been attempted many times before, so the second half of this chapter concerns an in-depth literature review into artificial spinning attempts and processes upon which this study could be built. Although there are many examples of artificial silk fibre spinning, artificial fibres with mechanical properties that approach those of natural fibres have not been produced. Contrary to what has been stated, very few aspects of the natural spinning system have been incorporated into artificial silk spinning. It therefore seemed a reasonable hypothesis that incorporating further biological inspiration into artificial spinning might facilitate the production of better quality artificial silk.

Although spider silks can have better properties than silkworm silks, the dope feedstock of the spider often contains multiple spidroin proteins that result in complex structural changes during processing (Guan et al., 2011) and are produced by the animal in quantities too small to be useful as a study feedstock. Although silkworms evolved independently from spiders, their dopes have many features in common (Holland et al., 2006a). Dope of the domesticated Chinese *Bombyx mori* is the simplest to study and use, and the dope is available in relatively large quantities. Therefore the artificial spinning sections shall be concerned mainly on the *Bombyx mori* feedstock. By using natural feedstock, we can concentrate on device development and avoid complications that arise with regenerated silk fibroin, for example.

Table 1.1 Summary of fibre properties of various fibres in comparison with major ampullate gland silk reproduced from (Cunniff et al., 1994), PEEK from (Albérola et al., 1997)

Fibre	Modulus (GPa)	Strength (GPa)	Elongation at break (toughness) (%)
Nephila clavipes major ampullate gland silk	22	1.1	9
High tenacity nylon	5	0.9	18
PEEK	4	1.5	150
Industrial polyester	15	0.9	13
Kevlar 29	62	2.8	3.5
Kevlar 49	124	2.8	2.5
Spectra 1000	171	3.0	2.7
High modulus graphite	393	2.6	0.6

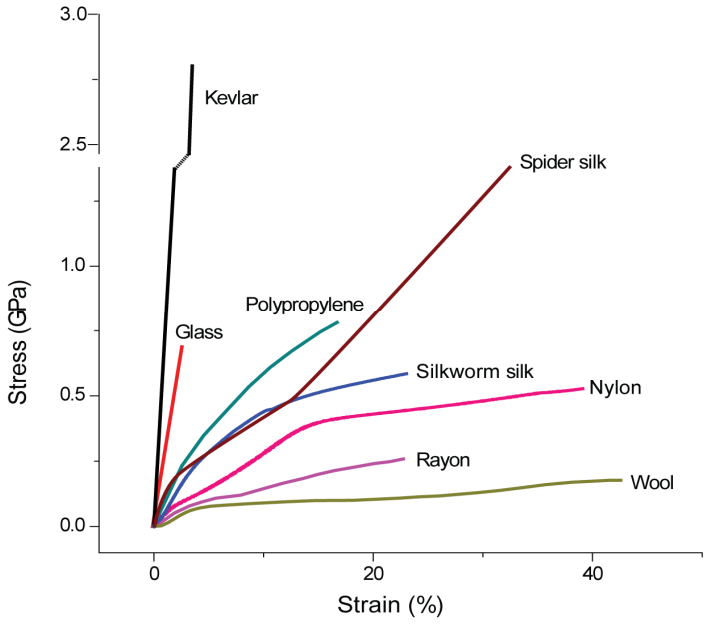


Fig. 1.1 Stress-strain curves of various (labelled) fibres in comparison with major ampullate gland silk. Data from (Wynne, 1997), Guan, J. and Holland, C. (personal communications)

1.2 Natural silk spinning

The synthesis, storage and fibre formation of these remarkable polymers have been extensively studied. Understanding all of the stages of silk formation may be crucial for effective production of artificial silk.

The silk production process in silkworms and spiders is largely similar, and the spinning glands are compared in Fig. 1.2. Spiders have existed for four hundred million years (Shear et al., 1989, Selden et al., 1991), evolving into forty thousand species (Vollrath, 1992), of which over ten thousand are spinners of orb-like webs intended to catch flying prey (Elices et al., 2009). Regarding the origins of silk and silk-producing glands, a number of theories have been put forward, but none has emerged as consensus. Given that some insects possess malpighian tubules which are normally part of the excretory system but are sometimes converted to produce silk-like fibres (Maziarski and Lozinski, 1911, Thomsen, 1921), an early idea was that spider silk ducts may have arisen via the same pathway as they also possess this tubule system (Knight and Vollrath, 2001). Other evolutionary origins postulated for the silk duct include juvenile limb buds (that also produce chelicerae, pedipalps and walking legs) (Dawydoff, 1949), coxal glands (Bristowe, 1958, Kaston, 1964, Gertsch, 1979) or the ectoderm (Foelix, 1982). Additionally, glands producing the sperm web may have arisen from epigastric glands (Shultz, 1987), as males of some species of spider can spin from their epigastric glands (Peters and Kovoor, 1991). Given the complexity of the silk duct, a combination of these theories may be true.

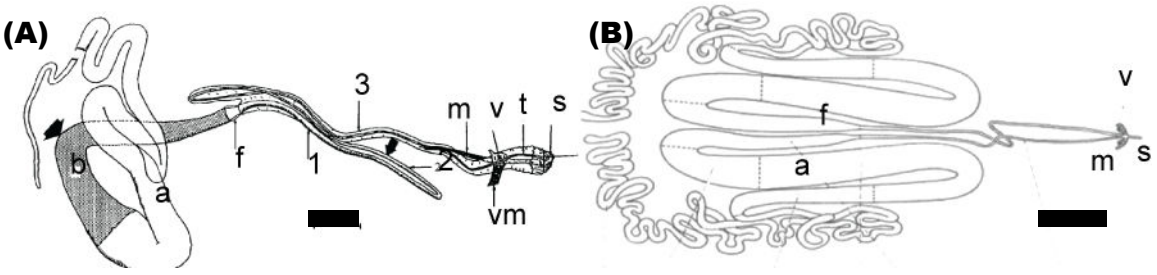


Fig. 1.2 Schematic diagram of spinning glands, showing their remarkable similarity despite unrelated evolutionary development (though their topology differs). (A) the major ampullate gland from a *Nephila edulis* spider, reproduced from (Knight and Vollrath, 1999). Letters and numbers on the image correspond to: a- A zone, b- B zone, f- funnel, 1, 2, 3- first, second and third limbs of duct, m- duct levator muscle, v- valve, vm- valve muscle, s- spigot t- terminal tubule. Scale bar 1mm. (B) a pair of spinning glands from a *Bombyx mori* silkworm, reproduced from (Akai, 1983). Letters correspond to equivalents in spider. Scale bar 10 mm.

Detailed investigations of the spider silk gland are typically carried out by first anesthetizing the spider with carbon dioxide gas before dissection (Work, 1977). Unspun silk proteins are produced in the long tail of the gland (left hand side of Fig. 1.2), the wall of which is composed of cells markedly different in appearance to the remainder of the gland. The first set of cells in this portion of the gland form the A zone, which secrete an alkaline or neutral secretion (Kovoor, 1977, Kovoor, 1987, Kovoor, 1990, Peakall, 1969). Cells lining the second zone (the B zone) secrete a protein and polysaccharide (Kovoor, 1987) as a homogenous coat onto the core secreted by the A zone (Vollrath and Knight, 1999). This substance is then transported to the sac-like ampulla to be stored until needed in an aqueous silk dope solution (Prudhomme and Couble, 1979, Sponner et al., 2005).

This unspun silk feedstock known as 'dope' consists of a repetitive co-polymer structure (Ayoub et al., 2007), of two proteins, Sp1 (lacking proline residues) and Sp2 (rich in proline residues) (Hayashi et al., 1999, Hinman et al., 2000). The relative proportions of these may be altered by external factors: if the spider is starved the fraction of Sp2 becomes reduced and stiffer silk fibres are produced (Guehrs et al., 2008). Silks are a type of protein. Proteins consist of a string of amino acids with amine, carboxyl, and hydrogen groups common to every amine group. A fourth group R- varies between amino acids, of which there are 20 different types but only 3 types (glycine, alanine, serine) are commonly found in silks (Fig. 1.3).

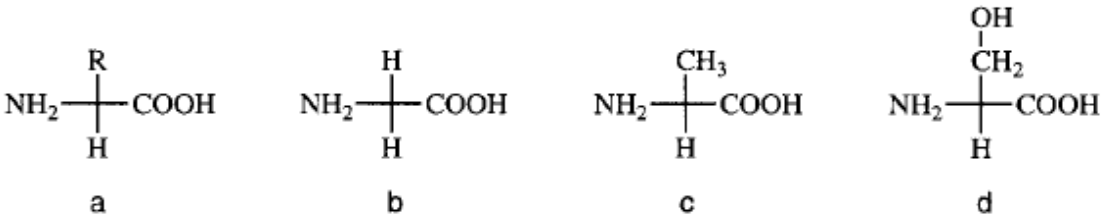


Fig. 1.3 All amino acids take the form of a), with an amine, carboxyl, hydrogen and variable (R) group. In silks these are mainly b) glycine, c) alanine, d) serine. Reproduced from (Craig, 1997)

These protein backbone can be of different lengths, with spider major ampullate silks of a size 250-320 kDa (Xia et al., 2010a) and *Bombyx mori* silk proteins 350 kDA (Oyama et al., 1984).

Due to variations in the amino acids and sequence of the protein, plus rotation between the different amino acids of the chain, the protein can form a wide variety of different shapes. Shapes that silks form include α-helix, cross and parallel β-sheets (Fig. 1.4) (Craig, 1997). α-helices are rarely the only type of structural silks, which usually include parallel β-sheets as well, which form when hydrogen bonds form between chains (Craig, 1997). If the correct structure of the amino acid chain is not formed during spinning, the properties of the material are unlikely to be silk-like.

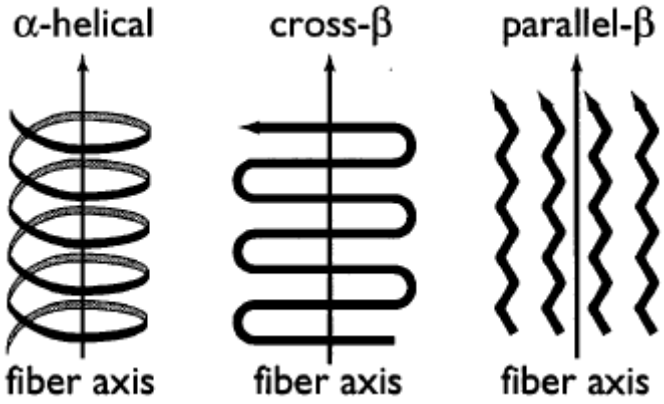


Fig. 1.4 Schematic of protein folding possibilities, reproduced from (Craig, 1997)

The golden coloured dope inside the duct is at a pH of 6.9 ± 0.1 (Knight and Vollrath, 2001). The colouring is possibly due to benzoquinone, naphthoquinone, and xanthurenic acid, and it becomes colourless if in an acidic environment (Holl and Henze, 1988). The dope consist of proteins in random coil structure (Kenney et al., 2002, Hijirida et al., 1996) with β-sheets absent (Liivak et al., 1997). It may be induced by pH change to pH 4.8 to transition from a sol to a gel, and is reversible if left for a few minutes (Terry et al., 2004).

When required for spinning, abdominal pressure may be responsible for transferring silk dope into the duct (Wilson, 1962a), connected to the ampulla by the funnel (Knight and Vollrath, 1999) which acts as mechanical reinforcement and prevents shear induced coagulation of the dope (Vollrath and Knight, 2001). It appears that flow through the duct is under active control of the spider (Vollrath and Knight, 2001), possibly by abdominal pressure which may assist in pumping

(Wilson, 1962a, Foelix, 1996) or by other means. Some ducts appear innervated, for example the duct of the piriform gland of *A. Diadematus* (Kovoor and Zylberberg, 1980).

The gland differs between species, and sometimes between sexes. For example, male *Linyphia triangularis* spider glands are proportionally very large in comparison with equivalent glands of their females (though other glands do not differ in size), yet the histochemical results of the duct structure are the same as in female (Peters and Kovoor, 1991). The duct grows in length and diameter during spider development, so may allow production of larger fibres (Townley et al., 1991a) and permit successful spinning despite wide variation in draw rates (Vollrath and Knight, 2001). As the spider develops it must moult to increase in size, but continued spinning of silk is essential for its survival. Therefore orb weaving spiders have a system of accessory ampullate glands (Townley et al., 1991a) - one primary major ampullate gland and two secondary glands. The secondary glands are activated alternately each moult (Townley et al., 1993a), allowing the unused gland to lapse into a quiescent state found to be small yellowish structures (Townley et al., 1991a) adhered to the conjunctive sheath that surrounds the duct of the ampullate gland (Kovoor and Zylberberg, 1972).

Conventional histological investigations of the long hollow tube of the duct suggested it had a flattened lumen, but 3D tomographic representation of silkworm ducts proved them to be of circular cross section (Moriya et al., 2008b). The duct describes a convergent geometry, finalised with a hyperbolic tapering die (Knight and Vollrath, 1999), as noted for *Nephila edulis* (Knight and Vollrath, 1999) and *Nephila clavipes* (Kojic et al., 2004). It is thought that the extremely gradual taper of the duct induces slow elongational flow, delaying formation of a solid filament until in the vicinity of the draw down taper and the high flow rates within (Knight and Vollrath, 1999).

The duct is folded into an s-shape of three limbs, clearly longer than would be needed to connect the ampulla to the spigot (Bell and Peakall, 1969), so this may be assumed to have further function in the production of silk fibre. Interestingly, although the ducts of *Loxosceles laeta* and

Latrodectus hesperus are very short in comparison with the ducts of similar sized *Nephila* (Knight and Vollrath, 2002b, Casem et al., 2002), the latter produces fibres with tensile properties similar to those attained by fibres of the orb web spiders. However, feedstock residence time within the duct of *Nephila* spiders is eight times longer than in *Bombyx mori* silkworms (Breslauer et al., 2009), and the silk produced from these spiders has better properties than of the silkworms, which suggests that there may be other factors than length of duct that contribute to the properties of the silk fibre.

The silk protein uses water as its spinning solvent (Kojic et al., 2004), with a water content of 70% at the start of the duct and 20% at the end (Hijirida et al., 1996), suggesting that water is removed from the silk dope in the duct (Bell and Peakall, 1969, Kovoor and Zylberberg, 1982, Tillinghast et al., 1984). The walls of the duct are birefringent (Work, 1977), and are adorned with a polysaccharide component which may serve for this resorption of water (Kovoor and Zylberberg, 1982). Any water still remaining at the end of the duct may be reabsorbed via long columnar cells at the distal end of the duct (Tillinghast et al., 1984, Vollrath et al., 1998). The microstructure of the duct wall resembles the structure of a hollow fibre dialysis membrane which may indicate another mechanism by which the contents are modified as they travel through the duct (Vollrath and Knight, 1999).

Ion concentration also changes along the length of the duct. Proton pumps have been found in the epithelium of the distal part of the duct (Vollrath et al., 1998), thought to be involved in the Na^+ and Cl^- concentration decrease and K^+ rise through the duct (Knight and Vollrath, 2001).

Proton pumps are also thought to acidify the silk proteins in the duct (Kovoor, 1987, Vollrath and Knight, 2001, Dicko et al., 2004b, Vollrath et al., 1998). The pH and calcium ion concentration are directly linked (Foo et al., 2006). The pH has been measured as 6.9 ± 0.1 in ampulla and 6.3 ± 0.1 in lumen just before spigot (Knight and Vollrath, 2001), or more recently the apparent pH values 7.268 ± 0.353 to 6.306 ± 0.424 from tail to spigot, with an isoelectric point (pI) of 4.22 (Dicko et al., 2004b). pH contributes to the final silk structure (Dabora and Marqusee, 1994) by

increasing viscosity of the silk dope and therefore increasing beta sheet content (Dicko et al., 2004b). Combined with the salt ions, this influences strain-dependence during the shear in the duct (Chen et al., 2002b) and the acidity also helps to draw down the fibre (Vollrath et al., 1998).

The beta sheets may help to lock the silk molecules into a solid fibre (Vollrath and Knight, 2001), occurring not only adjacent to the valve (Knight et al., 2000) but also further up the duct. Different factors can combine to induce beta sheets (Chen et al., 2006), and they can also be formed by elongational flow (Knight et al., 2000). Spontaneous beta sheet formation due to elongational flow poses somewhat of a problem for the spider, as rapid extensional flow occurs in the internal draw down taper (Knight and Vollrath, 1999), but before that premature crystallisation must be prevented by slow elongational flow rate (Kerkam et al., 1991, 1994, Willcox et al., 1996), brought about by the shape of the duct, which may also coax the dope proteins into optimum orientation for spinning (Rising et al., 2005).

As the contents approach the distal end of the duct, the further acidification and dehydration (Tillinghast et al., 1984) represent the final step before conversion of the random coil protein into an elastomeric solid (Tatham and Shewry, 2000, Vollrath and Knight, 2001), (Knight and Vollrath, 2002a, Kenney et al., 2002, Chen et al., 2003). Flask-shaped cells, present underneath the duct cuticle just before the valve (Vollrath et al., 1998), are thought to apply pheromones to the silk threads (Knight and Vollrath, 2002b). At a certain point along the duct, instead of flowing in contact with the duct's inner lining, the silk dope pulls away from the wall of the duct into a filament in a draw down taper (Knight et al., 2000, Gosline et al., 1986). This has been observed 2.45 mm before the valve (Vollrath and Knight, 1999) and at 4 mm from the distal end of the duct (Knight and Vollrath, 1999), with a fibre diameter of 20 ± 2 μm in the lumen to 8 μm at the spigot (Knight and Vollrath, 1999). The position of this drawdown can shift backwards in the gland in as little as a few hundredths of a second (Work, 1977) with increasing reeling speed, with the precise position thought to be the location at which extensional strain has accumulated (Breslauer et al., 2009). Within this drawdown the protein molecules orient and align, expelling water that is subsequently removed by specialised epithelial cells covering the apical lining of the duct wall.

This removal of water initiates the formation of cross-linked beta sheet crystallites interspersed with disordered regions at the molecular level, giving silk its distinguishing properties (Knight et al., 2000). The combination of ion pH change, removal of water and drawdown all contribute to the process of silk dope gelation, in which as the silk proteins become unstable, hydrogen bonds form promoting formation of crystals, making a conversion into a stable, solid-like material with infinite relaxation time. Though seemingly essential for the formation of silk structures in *Nephila*, draw down may not be always necessary to produce silk. For example, although the spider *Loxosceles laeta* is able to produce flat ribbons of silk from a short s-shaped duct, a draw down does not form part of the silk production (Knight and Vollrath, 2002b).

At the distal end of the duct, the structure termed the 'valve' (Wilson, 1962b), thought to clamp around the drawn-down silk (which is strong enough at this point of the duct), to enable controlled descending along the dragline silks (Wilson, 1962a, Wilson, 1962b, Vollrath and Knight, 1999). Initially thought to also act as a restriction die (Wilson, 1962b, Wilson, 1962a), the morphology of the valve was later shown to be incapable of this function (Vollrath and Knight, 1999) and instead may act as a friction brake (Ortlepp and Gosline, 2004), and to restart fibre spinning in the event of fibre breakage, either by clamping the fibre or pumping liquid dope to restart the drawdown (Vollrath and Knight, 1999). Silkworms have a similar structure known as the silk press, which evidence suggests may also act as a pump to restart broken filaments (Moriya et al., 2008b).

Following the valve (and a further short section of duct) lies the spigot which links the silk duct with the outside world. In conventional orb weavers the spigot has tight cuticular lips thought to strip any remaining water from the circular in cross section fibre (Riekel et al., 1999). However, again the spider *Loxosceles laeta* demonstrates that cuticular lips are not necessary for spinning silk: the lumen of their spigots is flattened, forming extremely thin ribbons that are then spun into flat sheets, thought to adhere to neighbouring fibres by van de Walls forces (Knight and Vollrath, 2002b).

The silk fibre outside the body is not produced by pressurized extrusion (Knight and Vollrath, 1999), but is rather pulled (Wilson, 1969) by the legs or directly by the weight of the spider upon the silk, and it undergoes some further draw down in diameter after exiting the spigot (Vollrath and Knight, 1999). Overall, the dragline thickness increases with moult size and spider weight (Garrido et al., 2002b) and accordingly there is a strong correlation between the maximum force a fibre can withstand and the weight of the spider that produces it (Osaki, 1996).

The properties of silk laid down during normal spider walking do not depend on speed of locomotion, though will not be sufficient to arrest the spider if a fall were to occur. When climbing vertically, however, the silk produced is thicker but with the same material properties, so is able to resist the falling forces (Garrido et al., 2002a). During a fall, spinning speed has been measured from 0.05-1.3 m/s (Ortlepp and Gosline, 2004), possibly limited by the speed of diffusion of material into the silk in the duct (Foo et al., 2006).

To collect silk for testing, the method of forced silking by immobilising a spider and collecting its silk around a rotating mandrel is used (Work and Emerson, 1982). Carbon dioxide gas is often used for immobilising, though if fibres are reeled whilst the spider is still anaesthetized the silk properties are not necessarily related to the silk diameter (Perez-Rigueiro et al., 2006) so it is preferable to wait for complete recovery of the spider before silking (Ortlepp and Gosline, 2004). The properties of fibres produced from forced silking are often poorly reproducible (Cunniff, 1994, Madsen et al., 1999), (Vollrath et al., 2001), unless at slow speeds (Guinea et al., 2005) likely because the spider actively resists the silking with its valve. Nevertheless, the silk is birefringent though the duct contents are not (Work, 1977), and increased reeling speed results in increased orientation of the spidroin molecules (Liu et al., 2005) and creates beta sheet stacks more regularly along the long axis resulting in a stiffer, stronger fibre (Chen et al., 2006).

1.3 Artificial silk spinning attempts

To artificially spin a fibre requires production of feedstock, a method of controlling extrusion through a nozzle or spinneret, and a method for collecting the resultant fibre (Fig. 1.5). In the

absence of large amounts of the unspun silk ‘dope’ to which Hooke referred, current spinning research concentrates on reconstituted silk fibroin (RSF) as the feedstock, a material obtained by washing insect silk cocoons and using a chaotropic agent such as lithium bromide to solubilise the silk fibres into a liquid form (Tashiro and Otsuki, 1970). The success of RSF may be limited by its dissimilarity to natural dope, indicated by the differing rheological properties of Newtonian RSF and non-Newtonian dope (Iizuka, 1966). Recently it was conclusively established that the rheological properties of the two feedstocks differ not in degree but in kind (Holland et al., 2007). Due to this major structural difference, silk spinning (mainly of RSF) requires a specialised spinning system with similarities closer to inefficient synthetic polymer fibre melt or solvent extrusion production line than to a biological spinning process, as will be shown below.

What follows is a survey of methods used for spinning silk in a ‘natural’ way, described and compared here and summarised with references in Table 1.2 at the end of this chapter.

The most common method of spinning silk is by wet spinning, whereby a feedstock is injected directly into a coagulation bath. The solution must first be mixed with a solvent, usually hexafluoroisopropanol, to obtain the correct rheology for spinning. Other solvents (in descending order of popularity), formic acid, polyethylene glycol, hexafluoroacetone-trihydrate and N-Methylmorpholine-N-oxide are also used with little obvious to differentiate the methods.

The spinning solution is injected by a syringe pump or gas pressure through a spinneret, into the bath of coagulating agent of methanol, isopropanol, ethanol, formic acid or ammonium sulphate which serves to dehydrate the fibre and remove other solvents. Fibres are left in the coagulation bath for a period of time, ranging from 30 seconds to 24 hours. Next, the fibres are removed for testing, or further processed to improve fibre properties. The most common post-processing step is to post-draw the fibre, lengthening it by factors of up to six times (but most commonly three). This extra step also serves to reduce the diameter of the fibre, stretching the molecules to make the fibre stiffer. This post-drawing is performed in either distilled water, in the coagulant previously used, in air, or in steam. Choice of drawing medium can affect not only the molecules

inside the fibre, but also the surface morphology. For example, steam has been shown to smooth an originally rough fibre surface (Yan et al., 2010).

Fig. 1.5 A typical wet spinning line featuring an extrusion unit, baths and rollers, reproduced from (Plaza et al., 2012)

RSF is not the only source of feedstock available; attempts have also used reconstituted spider silk fibroin, recombinant silkworm, spider or honeybee protein molecules, and non-reconstituted silkworm or spider silk.

Spinning methods other than conventional wet spinning have been tried, which include: microfluidic channels (in which the feedstock is flow-focussed into a shape resembling a spinning duct), feedstock pulled apart by tweezers, spontaneous assembly of fibres in long tubes, and dry spinning without the use of a coagulating bath. A promising approach is to use a porous membrane cast to a desired shape, subject of a patent (Knight and Vollrath, 2005) but not a publication. A body of research concerns the process of electrospinning, in which feedstock is pumped through a needle and electrostatic forces used to propel tendrils onto a collecting receptacle (Luo et al., 2012). This has been used to produce fibres of silk dope, but the very unnatural fibres produced allows us to not consider them in this study of bioinspired silk spinning.

The published tensile results of each of these methods are compared in Fig. 1.6. In this figure the results are classified by the feedstock (represented by different line patterns) and the post draw bath type (line colour), and compared with natural fibres from the major ampullate duct of the golden orb spider *Nephila edulis* and degummed cocoon fibres of the Chinese silkworm *Bombyx mori*, both from published sources (Guan et al., 2012).

In general, Fig. 1.6 shows that, without post-draw treatment, artificial fibres do not have particularly interesting qualities; the highest breaking stress is less than 100 MPa and the greatest strain less than 15%. This is most probably due to the large diameter of the fibres, and the amorphous state of the long chain protein molecules within. Only after extensive stretching in air, water or methanol do the fibres develop notable properties. Some of the best fibres in the literature are methanol-drawn RSF fibres (Zhou et al., 2009), which have some tensile properties very similar to the native silkworm. However, despite an ammonium sulphate coagulation bath enabling 5x post-draw in methanol, the authors note a level of crystallinity still lower than natural fibres. The air-drawn recombinant fibre (Xia et al., 2010b) shows a modulus stiffer than spider fibres, and a breaking stress of around 600 MPa. Although the measurements are impressive, this fibre in fact behaves very little like natural silk fibres, with negligible post-yield modulus. Notably, the results have not been replicated for either of these two fibres in the years since their publication, which may indicate the difficulty in reproducing these fibres.

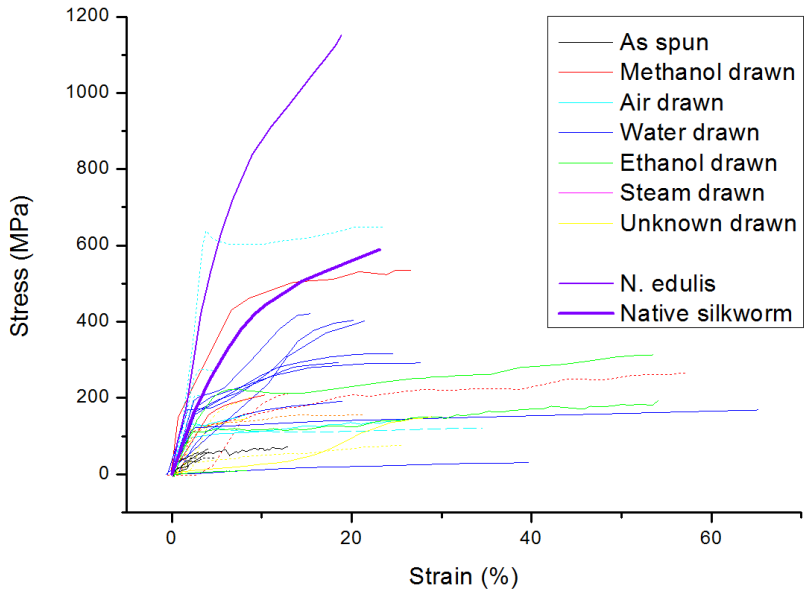


Fig. 1.6 Tensile data for published artificial compared to natural fibres. Apart from the two solid purple lines indicating natural silks, solid lines (–) indicate RSF, dashes (- - -) indicate SF, dots (. . .) indicate engineered protein source

Fig. 1.6 demonstrates that although artificial fibres have been spun with many different tensile properties, the tensile properties do not look like natural silks, but instead resemble the fibres of

conventional polymer fibres despite the assertion from many of these papers that they are bioinspired (Elices et al., 2011). Why these properties are produced is unknown. The exception to the conventional polymer-like fibres is the red line denoting a 6x post drawn methanol dehydrated fibre with a diameter of 10 μm (Zhou et al., 2009), but this appears to be a single fibre that could not be replicated.

The results of these experiments indicate that if one is to reliably spin fibres with silk-like properties, both the feedstock and the spinning apparatus need improvement. Studying natural silk production may yield important new insights.

1.4 Thesis and introduction to chapters

The first half of this thesis is devoted to learning more about the natural spinning system of spiders and silkworms. The topics covered will be those not presented in detail in the literature: a detailed study of the duct internal shape, wall thickness, spigot size and silk thickness related to spider size. The material of the duct wall of both spiders and silkworms were investigated, and the structure and mechanical properties of the spider duct wall were studied. Within this section, the chapters are arranged chronologically, with each chapter building upon the work in the previous chapter.

Using some of the details learnt in the first half of the thesis, in combination with established knowledge from the literature, the second half of the thesis details attempts to spin artificial silk based upon flow fields and conditions expected within the natural spinning duct. When natural-like flow fields alone were found insufficient to produce natural fibres, methods were used in an attempt to initiate controlled gelation of the silk dope to promote molecular extension and alignment. This second section is arranged into a device development chapter, in which the engineering developments that enable spinning are described chronologically, followed by two chapters that detail the scientific developments and analysis performed on spinning processes.

The contents of each chapter are outlined below:

Chapter 2 details the main experimental methods used in this thesis, so that repitition throughout the remainder of the thesis is kept to a minimum.

Chapter 3 describes a study at the morphology of spider and silkworm spinning ducts, how the silk fibre develops as the dope flows through the gland, and the relation between silk fibre properties and both gland morphology and spinning speed.

Chapter 4 is a study which used histochemical and spectroscopic investigations of the silk ducts of both the spider *Nephila edulis* and the silkworm *Bombyx mori,* which indicated that they both contain β-chitin, despite an evolutionarily distant common ancestor.

Chapter 5 uses electron microscopy to study the ultrastructure of the spinning duct wall, and computer modelling and the results of the previous chapter are used to test hypotheses of why the duct may have this size and structure.

Chapter 6 describes the engineering developments that were required to spin fibres from native silk dope. This chapter was made separate from the subsequent spinning chapters to avoid confusion or repetition in the scientific spinning chapters.

Chapter 7 tests the hypothesis that silk dope can be forced through a glass capillary, by using a novel centrifuge device to create a pressure force upon the feedstock. First a mathematical model of the device was derived from standard equations, then validated experimentally and improved using rheological calibration oil. Calculations were performed using the model to predict the flow of silk dope through the capillary, but the theoretical results were far from experimental outcomes. Fibres that happened to be formed were characterized, and information from these studies was incorporated into the next generation of spinning device.

Chapter 8 details the result of spinning fibres from native dope through a stationary capillary, with pressure generated by a syringe pump. This chapter tests the hypothesis that fibres with silk like properties could be spun using shear stress alone, and that fibres with silk like properties could be spun with a combination of shear stress and heat as an initiator of dope gelation. Both tests were

hampered by the inability to spin fibres without a droplet, though the fibres spun were tensile tested.

Chapter 9 details an attempt to spin fibres from native silk dope using controlled shear stresses, adding an instability instigator, and characterizing the fibres produced.

Chapter 10 concludes the work detailed in this thesis. The work created more questions than it answered, some of which will be addressed. The work will be placed within the wider context of artificial silk spinning and studies of silk dope.

Table 1.2 Summary of published silk fibre spinning

Date	Method	Feedstock	Solvent	Spinneret	Powered by	Coagulant	Post draw	Ref
1993	Patent	Dissolved SF	HFIP	-	-	Yes, including methanol	Lock, RL US patent 5252285	
1996	Wet	Dried SF	LiBr * H_20 = 40 wt. %, and EtOH : H_20 = 100 : 0 v/v	0.3-0.5mm ID x 0.6-4mm L	N/A	Ethanol, methanol, Isopropanol, lithium bromide	1-3.2x in water @ 61 ° C	(Matsumoto et al., 1996)
1998	Wet	2.5% w/w RSF	HFIP	Nanofabricated silicon hole	Syringe pump	Overnight in 100% methanol	Omitted, in omitted, annealed.	(Liivak et al., 1998)
	Wet	*Nephila clavipes*	HFIP	Nanofabricated silicon hole	Syringe pump	Water, methanol, 2-propanol, acetone. Only acetone successful	-	(Seidel et al., 1998)
	Wet	15 wt. % protein	HFIP	26 gauge needle, air	Syringe pump	2cm air gap, overnight methanol	1-3x wet with methanol	(Trabbic and Yager, 1998)
2000	Wet	*Nephila clavipes* 2.5% w/w	HFIP	150-250 µm ID, 1/4" L	Syringe pump	Acetone	1-3.5x in air, 1-9 in air after 2x water annealing	(Seidel et al., 2000)
2002	Wet	25% w/v protein Constructs	Urea	HPLC tubing 0.125mm ID	Syringe pump	Methanol + water	-	(Arcidiacono et al., 2002)
	Wet	Mammalian cell rc-spider silk 10-28% w/b		?	?	Methanol	<5x in methanol	(Lazaris et al., 2002)
	Wet	RSF	HFA	0.2 mm ID x 1.2mm L	High pressure N_2	2 cm air gap, methanol overnight	3x in methanol	(Yao et al., 2002)
2003	Wet	SF+	Calcium nitrate-methanol solution	0.254, 0.381, 0.508mm ID nozzle, l/d=2	Nitrogen gas at 0.34 MPa	100% methanol	-	(Ha et al., 2003)
	MAS, RSF dry	*Nephila edulis* MAs +guanidine-HCl	-	Pull away with needle	Hand	-	-	(Shao et al., 2003)
	Wet	RSF 10% w/w	HFIP	0.2mm ID spinneret	High pressure nitrogen gas	Methanol overnight	3x in distilled water, steam annealed @ 125 ° C. Air dried	(Zhao et al., 2003)
2005	Patent	any	Any	'Bio mimicking', permeable	Pressure regulating valve or pump		Knight & Vollrath Patent 10/148,101	
	Wet	SF	NMMO	100, 200, 300 µm diameter	N/A	5mm air gap, ethanol	0-3x in air, vacuum dried	(Marsano et al., 2005)
	Wet	SF	Formic acid, TFA <13% w/v	Needle 0.71 ID	Mechanical pump	Methanol 4h	~3x in wet state	(Ha et al., 2005)
	Wet	SF+	Ionic liquid (EMIC)	Needle 0.26mm ID x l 23 mm	'Air removed'.	50mm air gap, Methanol, Acetonitrile, water, ethyl acetate, acetone, hexanes	2x	(Phillips et al., 2005)
2007	Wet	RSF	?	?	?	Methanol, ethanol	?	(Baoqi et al.,

Date	Method	Feedstock	Solvent	Spinneret	Powered by	Coagulant	Post draw	Ref
								2007)
	Wet	SF	Formic acid, phosphoric acid	22 gauge needle	Syringe pump	Methanol overnight	5x in distilled water @ 60 ° C	(Ki et al., 2007)
	E coli spontaneo-usly assembled	Gene expression	-	Fibres similar to RSF	-	Formic acid	-	(Stark et al., 2007)
	Bacteria proteins	Gene expression	HFIP+ 15% H_2O	PEEK tubing 0.127 mm ID	Piston extruder	90% isopropyl alcohol	-	(Teule et al., 2007)
	Wet spun							
2008	Wet	Protein expression	HFIP	0.005 in PEEK tubing	-	Isopropanol	-	(Brooks et al., 2008)
	Microfluidic	Recombinant eADF3	-	PDMS converging microfluidic plate	Syringe pump	Potassium phosphate	-	(Rammensee et al., 2008)
	Wet	RSF+ recombinant	HFIP	0.8 mm ID	Syringe pump	20mm air, methanol 3h	3x in water @ 40 -50° C	(Zhenghua et al., 2008)
	Wet	RSF	HFIP	0.45 mm ID	Syringe pump	Methanol 3h	2-3x in distilled water @ 40 ° C	(Zhu et al., 2008)
	Wet	SF	NMMO 50% w/w	?	?	10mm air, ethanol, post draw, then ethanol 48h	3.8x in omitted	(Plaza et al., 2008)
2009	Wet	RSF	PEG	Extruded to gas powered	Nitrogen gas	Aqueous 30% w/v ammonium sulphate 60 ° C	1-6x in steam	(Zhou et al., 2009)
	Wet	RSF 17% w/w	NMMO	100 µm	?	10mm air, ethanol.	3x in air, washed, vacuum dried	(Perez-Rigueiro et al., 2009)
	Wet	RSF	Osmotically stressed LiBr=PEG	0.25 mm ID, 1.5 mm L	High pressure nitrogen	10mm air at 25° C, methanol and water 1:1 25° C	None	(Sohn and Gido, 2009)
	Wet	RSF pH10.4		0.45 ID	Syringe pump	Methanol acetic acid 7:3 v/v 3-4h 20m/min	3x in coagulant	(Zhenghua et al., 2009)
2010	Wet	Recombinant piriform protein	HFIP	?	?	90% Isopropanol		(Geurts et al., 2010)
	Wet	RSF+ nylon 6	Formic acid	22 G needle	Syringe pump	Methanol overnight 20ml/h, dried under tension	None	(Ko et al., 2010)
	Wet	Recombinant protein	HFIP	26 G needle	Syringe pump	90 v/v% methanol	5x, air, air dried	(Xia et al., 2010b)
	Tweezer separation	Recombinant honeybee	20 wt.% PEG	Droplet between tweezers	Tweezer spring	90% methanol	2x in 90 % methanol, air dried	(Weisman et al., 2010)
	Wet	RSF pH 6.5-7 protein conc. 10-30%	PEG	Tantalum die, 6x 0.2 mm ID 4.7-11 m/min	Nitrogen 0-0.3 MPa	Ammonium sulphate 30/40 % w/v then overnight	4x Under steam makes smoother	(Yan et al., 2010)
	Wet	RSF	HFIP, HFA 15% w/v	0.45 mm ID 20 m/min	Syringe pump	Methanol bath room temp 3h	1.5-3x Distilled water 40 ° C	(Zhu et al., 2010)
	Wet	RSF+5% w/w silk like protein	HFA	20 m/min	Syringe pump	Methanol bath room temp 3h	3x Distilled water 40 ° C	
2011	Wet	Recombinant MASp1	HFIP	0.005 in PEEK tubing 0.7 mm/min	Syringe pump	100% Isopropanol	3x in 75% isopropanol/ water	(An et al., 2011)
	Microfluidic	RSF	PEO	Hydrodynamic focussing, methanol bath	Syringe pump	30 s in methanol bath	Not noted	(Kinahan et al., 2011)

Date	Method	Feedstock	Solvent	Spinneret	Powered by	Coagulant	Post draw	Ref
	Wet	Recombinant rcSp1, 2	HFIP	'Extruder'	Syringe pump	2-propanol	5x steam	(Elices et al., 2011)
	Dry	RSF	MES-tris	Air spun then dried and	Syringe pump	No, but 24 h in silica gel	1-3x ethanol	(Wei et al., 2011a)
	Dry	RSF pH 5.2-6.9, Ca^{2+} conc. 0.3M	MES-tris	250-500 µm ID 20 mm L Capillary 10 µl/min	Syringe pump	No, but 24 h in silica gel	-	(Wei et al., 2011b)
2012	Wet	SF	90% formic acid	22 G needle 0.337 mm ID 20 ml/h	-	Methanol overnight	5.5x at 25 ° C in air	(Cho et al., 2012)
	Wet	RSF at 90 ° C	-	100 µm ID, 4 m/min	-	50mm air, methanol	1-4.4 in water	(Plaza et al., 2012)

Chapter 2. Methods

This chapter describes the methods were common to many of the chapters, which are detailed here to avoid repetition.

2.1. Biological preparation

2.1.1. Spider

2.1.1.1. Spider rearing

Nephila edulis specimens were reared at 20 ° C ± 5 ° C, fed *Drosophila melanogaster* and *Calliphora vomitaria* flies *ad libitum* and their webs sprayed with a fine mist of water from an automated system twice daily.

2.1.1.2. Spider preparation

Experimental specimens were confined in a 100 ml pot with foam lid and the pot flushed with a flow of CO_2 at 0.5 bar for five minutes. This procedure caused the spider to become anaesthetised and immobile for around ten minutes. In this time available spiders were weighed using an analytical balance (Sartorius BP121S).

2.1.1.3. Spider cephalothorax measurement

Whilst still anaesthetized, the specimen was imaged using a digital camera (Canon A640) mounted upon an stereo microscope (Olympus SZ4045TR) then instantaneously killed by crushing the cephalothorax between a blunt instrument and hard surface. The width of the cephalothorax at its widest point (the standard metric for spider development (Hagstrum, 1971)) was measured from the digital image with scientific imaging software (NIH ImageJ) at its widest point, perpendicular to a line drawn along the central axis of the spider (Fig. 2.1).

Length of cephalothorax was also measured along the line of this axis, from the front to the edge of a circle drawn to the same curvature of the rear diverging protrusions. This construction circle was drawn as it is often difficult to distinguish the rear of the cephalothorax due to detritus from

the severing of the junction with opisthosoma, and impossible to image in live specimens in which the opisthosoma obscures.



Fig. 2.1 Diagram of *Nephila* cephalothorax, with width and length measurements taken marked in red

2.1.1.4. Spider duct dissection

Both major ampullate glands and their associated ducts were dissected in Spider Ringer solution (Groome et al., 1991) in the following systematic manner: the outer cuticle of the entire segment save that immediately around the spinnerets was gently peeled away with sharp forceps. Book lungs and outer fatty reserves were removed, and the remainder split along the central axis to give two mirrored sections. Each were floated in Spider Ringer solution (Groome et al., 1991) in a petri dish, and all internal structures were gently excised save the major ampullate glands.

Spiders with evidence of accessory ampullate glands as in Fig. 2.2 (A) were discarded as that indicates recent or incipient ecdysis (Tillinghast et al., 1991) and therefore incomplete duct formation. The majority of outer cuticle surrounding each spigot was carefully removed along with the gland ampulla at the junction with the funnel, leaving the spigot attached to the spinning duct via a minimum of cuticle. Ducts were then gently unfolded to their full length.

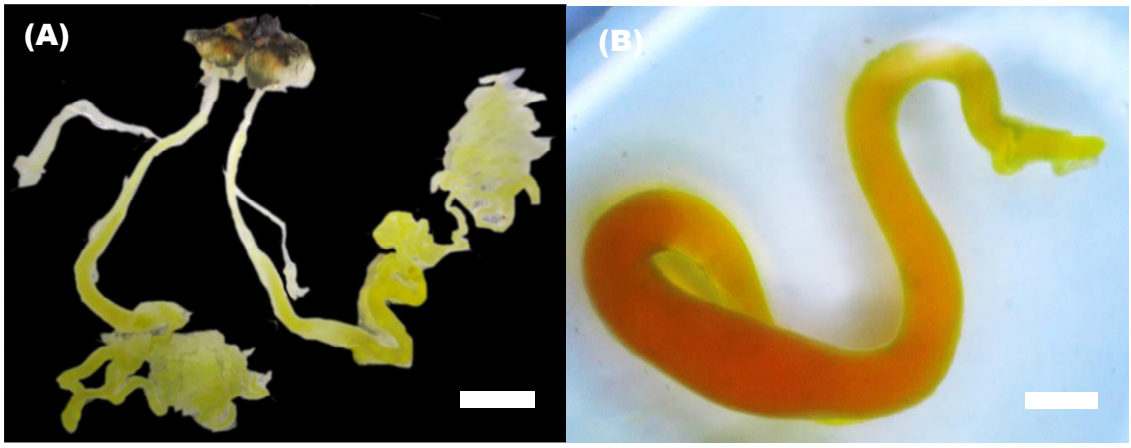


Fig. 2.2 (A) Dissected major ampullate glands of Nephila edulis spider, showing (top to bottom) spigots and outer cuticle, ducts, accessory glands, ampulla and tail region, scale bar 2 mm. (B) Dissected major ampullate storage sac of *Nephila edulis* spider, scale bar 0.6 mm.

2.1.1.5. Spider gland dissection

Fig. 2.2 (B) shows a typical storage sac. The epithelium surrounding the dope was gently peeled away using a combination of fine tweezers, a new scalpel blade, and sharpened pins.

2.1.2. Silkworm

2.1.2.1. Silkworm rearing

Bombyx mori silkworms were reared in Padova, Italy, ICIPE, Kenya, and Shrewsbury, UK on a diet of either silkworm chow or fresh mulberry leaves.

2.1.2.2. Silkworm preparation

For morphological studies freshly spinning *Bombyx mori* silkworms were killed by confinement within a large petri dish with a sheet of paper soaked in chloroform.

2.1.2.3. Silkworm dissection

For morphological studies and to extract the silk dope the spigot, duct and gland were dissected out in distilled water by cutting along the dorsal side of the worm from the tail to through the head plate. Sericin was removed by immersing the entire gland in distilled water in a petri dish, placing

this dish on an ice pack and placing this on a rotator plate set at 60 revolutions per minute. The distilled water was replaced with fresh every 15 minutes, for three washes.

2.2. Duct and capillary measurement

The slide with the duct was placed onto a microscope sample stage and the focus plane of the microscope image was set to half way through the duct, verified by sharp focus of the wall edges. This allowed the inner and outer diameter of the duct walls to be observed as shown in Fig. 2.3 (A). As the duct thickness increased along its length, the focus plane of the microscope was adjusted manually to keep the wall cross section in focus. Digital photomicrographs along the length of initial ducts were taken with bright field illumination through a 10x magnification objective on a modified microscope by a 576x768px monochrome digital camera (Oxford Cryosystems Metripol), with fiducial markers for later alignment. Later sequences were taken using a microscope with a motorised stage (Thermo Nicolet Nicplan), which enabled imaging at regular intervals and therefore made alignment easier, a change with no apparent loss of accuracy but an appreciable increase in productivity.

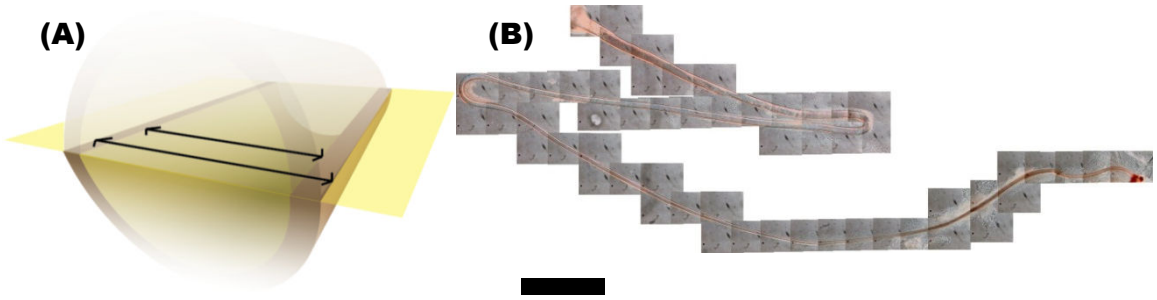


Fig. 2.3 (A) Representation of the focus plane (yellow) a microscope adjusted to a height midway through the duct (brown tube) to give a clear view of the inner and outer diameter of the duct walls (black arrows). (B) Photomontage of whole mount of unfurled spinning duct, scale bar 0.90 mm.

Aligned photomontages of the entire duct (such as Fig. 2.3 B) were prepared in Photoshop CS4 (Adobe Systems Incorporated) then imported into Illustrator CS4 (Adobe Systems Incorporated) to measure internal and external diameters along the duct. Duct diameters were measured perpendicularly to a line drawn down the centre of the duct, sampled at markers drawn by the software, at regular intervals that were specified by s shown in Fig. 3.3.

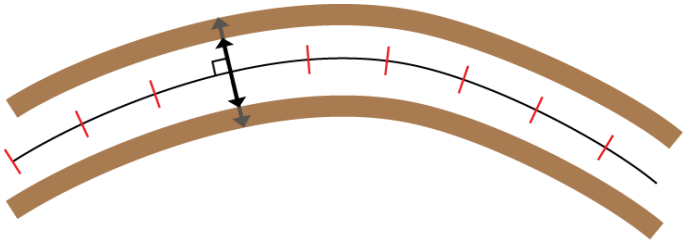


Fig. 2.4 (A) Schematic demonstrating how duct (brown lines) inner and outer diameters were sampled perpendicular to centre line of duct, at regularly specified intervals. (B) Schematic demonstrating how duct spigot diameter was measured

2.3. Fibre testing

2.3.1. Fibre collection

2.3.1.1. Spider

To measure the diameter of silks produced by the spiders, the spider was secured to a raft of expanded polystyrene under a fine nylon mesh, with a small fenestration to allow access to the spinnerets. After allowing thirty minutes to allow the effects of CO_2 to dissipate, (Madsen and Vollrath, 2000) at 22 ° C a single fibre from one of the two major ampullate ducts was collected onto custom reels powered by an electric motor, speed controlled using a custom motor controller.

2.3.2. Fibre mounting onto frames

Paper frames with a gauge length of 5 or 10 mm ± 0.2 mm were cut from 250 gsm card (Canson Bristol) with a laser cutter (HPC LS 3040). Fibres were fixed using cyanoacrylate glue, left to dry overnight in a dry environment.

2.3.3. Tensile testing

Tensile tests were carried out on a tensile testing machine (Instron model 5542) calibrated automatically, at a rate of 50 % per minute with a 5 N load cell and custom clamps, or a tensile testing machine (Zwick/ Roell Zwicki Z0.5) at a rate of 1mm per minute with a 5 N load cell

(Zwick KAP-TC) and film clamps. The engineering stress was calculated from the force and the initial cross sectional area of the fibre.

2.3.4. Fibre cross section measurement

Cross-sectional area of fibres for stress calculations were calculated from measuring the diameter of fibres first sputter coated with 7 nm of gold-palladium and then imaged with a scanning electron microscope (Jeol Neoscope JCM-5000) calibrated using standard EM grids.

2.3.5. Fibre solubility

Solubility of fibres was tested by immersion in 0.3 ml drops of distilled water at room temperature. Time till dissolution of the fibres was defined as the time taken until the fibre within the droplet of water was no longer visible through a dissecting microscope at a combined magnification of 40x (Olympus SZ4045), measured using a standard lab stopwatch.

2.3.6. Fibre polarization

Fibre polarization was measured using a Metripol quantitative polarization microscope (Oxford Cryosystems). The Metripol measures $|\sin(\delta)|$ where the retardation δ is equal to $L(n_2 - n_1)k$. Here, $k = \frac{2\eth}{\lambda}$ where λ was the wavelength of the light (Geday et al., 2000). True birefringence for orientated samples $\Delta n = n_{|} - n_{\perp}$ with the refractive index parallel and perpendicular (Holland et al., 2012a). The Metripol uses a deconvolution algorithm using a maximum of 3 wavelengths to calculate the extent of the retardation δ.

Experimentally, dry fibres were measured through a 10x objective at wavelengths of 550, 580 and 600 nm which were subsequently combined in the microscope's software to calculate the absolute value of polarization, delta, in accompanying software.

Chapter 3. General investigation into silk spinning gland morphology

3.1. Introduction

This chapter first looks at the morphology of the spinning gland, mainly in spiders, and then looks at how silk changes from a solution to a solid fibre as it flows through the gland, more specifically in a silkworm. Although Chapter 1 gives a detailed literature survey of previous studies on natural silk spinning, after a brief overview of the spinning process, it is important here to give a more specific review on gland structure and morphology. This forms the basis of the work undertaken in this project.

Silk filaments from silkworms and spiders are produced by largely similar processes (Vollrath and Knight, 2001), in spinning organs with similar morphology and properties (Fig. 1.2). The principal silk proteins have a high molecular weight of around 400 kDa and are secreted by cells lining the long tail of the gland and are stored in the lumen of the silk gland as a concentrated aqueous silk dope solution (Prudhomme and Couble, 1979, Sponner et al., 2005), and their rheology is remarkably similar (Holland et al., 2006a). When required for spinning, the proteins are moved from the lumen of the gland through a short tapered structure with a thick cuticle (the funnel in the spider (Knight and Vollrath, 1999) and an unnamed section in the silkworm) to the spinning duct, a progressively narrowing hyperbolic tube, which is folded into an S-shape in spiders (Knight and Vollrath, 1999) and many times in silkworms (Akai, 1983) probably to permit a long duct to fit within the available space (Bell and Peakall, 1969).

In the duct, the application of strain and shear, together with changes in ionic composition within the duct's length, are thought to convert the silk dope solution into a solid filament (Dicko et al., 2004b, Chen et al., 2002a, Vollrath et al., 1998). At a certain point along the duct, rather than flowing in contact with its inner lining, the silk dope becomes sufficiently gelled to sustain tension, and pulls away from the wall of the duct in a draw down taper (Knight and Vollrath, 1999). Within this drawdown, the protein molecules orient and align, expelling water that is

subsequently removed by specialised epithelial cells covering the outer surface of the cuticle lining of the duct. The removal of water by drawing initiates the formation of beta sheet crystallites, as a sort of physical 'crosslinking', interspersed with disordered regions that gives silk its particular properties (Knight et al., 2000). In the duct, the filament moves through a structure (often called valve in spiders or silk press in silkworms (Akai, 1983)), which is thought to act as a clamp and perhaps a micro pump (Vollrath and Knight, 1999). Further drawing takes place after the silk is pulled by the spider's legs or weight of the body (Vollrath and Knight, 2001), or the figure-of-eight movement of the silkworm's head, through the tight cuticular nozzle of the spigot, initiating further water loss and beta sheet formation (Riekel et al., 2000).

A key general aspect of gland morphology is size. The spider's spinning duct must be fully functional in even the smallest spiders, as all instars are able to spin safety lines and webs. However, to date, no work has been reported on changes in the size and shape of the gland or spigot with the growth of the spider. How the duct is able to grow and continue to produce silk fibres with properties that are reported to be identical (Ortlepp and Gosline, 2008) is of particular interest, as the entire spinning apparatus is formed anew before each moult (Townley et al., 1993b). The images of the spinning duct in the literature include some hand drawn images of the duct join with taper of *Araneus diadematus* and *Araneus cornutus* (Foelix, 1971a), and *Nephila edulis* (Knight and Vollrath, 1999). Low-magnification photomicrographs of glands and ducts exist of *Araneus cavaticus* (Tillinghast and Townley, 1986), (Tillinghast and Townley, 1987), (Townley et al., 1991a), *Araneus diadematus* (Vollrath et al., 1998), *Araneus seraticus* (Bell and Peakall, 1969), *Nephila clavipes* (Ortiz et al., 2000, Lefèvre et al., 2008), and the funnel-web spider *Agelena limbata* (Park and Moon, 2008).

However, the only dimensions known of the duct are from measurements of single final instar specimens of the spiders *Nephila edulis*, *Araneus diadematus* (Knight and Vollrath, 1999) , and *Nephila clavipes* (Kojic et al., 2004), a graph of the lumen diameter against distance from the start of the duct and a 3D reconstruction of the silk press in *Bombyx mori* (Asakura et al., 2007a) and the same for *Samia cynthia ricini* (Asakura et al., 2007b). These profiles have been used to predict

fluid flow using finite element analysis (Breslauer et al., 2009) and finite element methods (Moriya et al., 2008a). However, with only a single organism providing the dimensions for each duct profile, the results are unlikely to be an accurate representation of the ducts' capabilities. To supplement the limited reported observations, I present detailed measurements of spinning ducts of female *Nephila edulis* spiders, from a range of stages of spider development. These measurements should enable a better understanding of the flow of the silk fluid in the duct, which could improve the design of apparatus for spinning artificial fibres.

Although duct size and shape could be measured after dissection, this would not tell us the shape of the turns of the duct *in situ*. Therefore, the aim of the first section of this chapter was to measure the size and shape of the duct along its length, without first dissecting the spider. This formed the basis of the preliminary aim, to visualise the size, position and shape of the spinning duct within the spider by using paraffin sectioning to make a 3D reconstruction of a spider duct within the spider. This method would also give quantitative data towards the internal duct cross section, since there has been some discussion about whether the internal duct shape at the silk press of the silkworm is circular in cross section or otherwise (Moriya et al., 2008b); only a single cross section through a spider duct, that of *Nephila clavata* shows the duct has circular cross section (Moon et al., 1988), and only at this one sampling point. Ultimately this preliminary approach was unsuccessful, as will be described, so a method was found to measure the shape of the ducts *in vitro*. This second method, measuring the ducts of female *Nephila edulis* spiders, forms the bulk of this chapter.

Compared to the final instar female spiders, which are usually the basis of study, adult male *Nephila* spiders are very much smaller and lead a kleptoparasitic existence on females' webs, rather than spinning their own webs on which to catch prey. There does not appear to be any comparison studies between the duct sexual dimorphism of spiders or silkworms in the literature. I therefore hypothesized that the size and shape of the web silk producing (major ampullate) ducts of male and female spiders would be dissimilar, and that the silk would also be different. Sexual dimorphism of duct size was investigated in this work by selecting males of similar body size to

females, and comparing the duct sizes and shapes of males and females. Similarity between the ducts may indicate that the evolution of silk fibres as a safety line is more important than web production.

The largest part of the spinning gland is the duct, and the wall of the duct is likely to be the mediator of the chemicals that diffuse into the silk dope and also the removal of water. At the same time, the duct must prevent abdominal pressure from forcing dope from the ampulla into the duct and abrasion against other internal organs. It must resist the tension of the silk at the drawdown and the clamping forces of the valve, both of which pull the duct in a distal direction towards the spigot. In particular, thicker walls around the clamp and spigot may indicate mechanical strengthening, as the drawdown occurs in this region and is likely to require resistance to the radial pulling this creates. Despite the great importance of the duct to the spinning process, there appears to be no studies of the duct wall thickness and its associated flexibility in the literature. To test whether wall thickness is greater in some regions, wall thickness was measured at points along the length of the duct.

Leading on from studies of the duct wall thickness, larger heavier spiders spin at faster rates as they escape on their dragline fibres (Ortlepp and Gosline, 2008). This capability would be expected to manifest itself by an increase in the duct thickness and, therefore, resistance to pulling forces and increase in capability to change properties within the duct. However, as with wall thickness variation along the length of an individual duct, there does not appear to be any studies of the duct wall relative to the spider size and therefore spider development. I hypothesized that the wall thickness would increase as a function of spider size. To test this hypothesis I studied the relationship between thickness of the duct wall and the stage of spider development as indicated by spider size.

After the duct at the end of the spinning process, the sclerotized spigot is the only component of the silk production that is moulted (Townley et al., 1993b). As the sole externally visible component of the silk production system, it would be useful to link its size to the rest of the silk

production system. Studies of the spigot in the literature fall into the following categories: cataloguing the number of spigots during development (Coddington, 1989, Townley et al., 1991b, Townley et al., 1993a, Park and Moon, 2008), the arrangement of spigots on spinnerets (Townley and Tillinghast, 2009, Eberhard, 2010, Moon, 2012), or detailed studies of the spigot (Coddington et al., 2002, Knight and Vollrath, 2002b, Hajer et al., 2013). Unfortunately, of the three studies of the spigot, two are on the *Loxosceles* spider, not an orb weaver, and the third is only a brief mention. Published data on the relationship between the spigot and the associated silk product concern the spider *Loxosceles*, which spins a highly specialised, flat ribbon of silk (Coddington et al., 2002, Knight and Vollrath, 2002b), cribellate spiders (Opell, 2002, Park and Moon, 2009), or are just a brief overview of both (Hajer et al., 2013). From the literature, the relationship between the spigot and the diameter of silk fibres produced by orb weaving spiders has not been described. This relationship between the size of duct, spigot and fibre is an important step towards describing the spinning system in its entirety. I hypothesized that the sclerotized spigots would grow in size as a function of spider size. This hypothesis is tested in this chapter by comparing the size of the spigot against other spider size parameters.

The final part of this study on spinning gland morphology is how the silk fibre develops as it flows through the gland. Care must be taken when interpreting observations from dissected ducts, as semi-formed silk fibres can become damaged by dissection, for example silk within a duct dissected from an *Araneus diadematus* showed coiling and detritus (Wilson, 1962a) and coiling in *Nephila edulis* (Vollrath and Knight, 1999). The preliminary study reported in this chapter showed that full 3D reconstruction at a resolution to capture both the duct and its contents was unlikely to be successful within a reasonable time with the equipment available. Instead, to image the contents of the duct during the spinning process, the whole organism was frozen as quickly as possible, sectioned and laid out onto slides whilst still frozen (following established technique (Toma et al., 2002)), and the size of the fibril was measured. The model silkworm *Bombyx mori* was used for this study, as spiders have a very complicated internal structure with many glands and accompanying ducts in comparison with the silkworm's two mirrored ducts.

Unlike spiders, silkworm larvae spin fibres into cocoons during their final instar, so their silk gland may not need to be fully functional until pupation. Attempts have been made to model the process in which silk filaments are formed in spiders *in silico* (Kojic et al., 2004, Breslauer et al., 2009) and silkworms (Moriya et al., 2008a) but models require a strong understanding of both the dimensions and rheology of the problem to be solved. The dimensions on which these simulations are derived from the limited observations mentioned above. Empirical data is still lacking on the precise interaction between the dimensions, geometry and role of lining of the duct, and the rheology of the concentrated spidroin solution during the spinning process. Based upon these previous analyses, a hypothesis to be tested in this section is that the drawdown occurs close to the clamp. To test the hypothesis, the duct was imaged without prior dissection using cryosectioning of frozen silkworms.

A key part of the spinning process in the gland is the silk dope itself. Some of the effects of changing silk dope properties have been studied *ex-vivo*, such as the effect of shear stress upon the viscosity of reconstituted silk (Chen et al., 2001), the viscosity of recombinant silk (Rammensee et al., 2006), the viscosity of diluted silk (Hossain et al., 1999, Ochi et al., 2002a, Chen et al., 2002b, Ochi et al., 2002b) or the viscosity of native silkworm dope (Terry et al., 2004, Holland et al., 2006a), the viscosity of spider silk (Kojic et al., 2006) and degree of protein confirmation in reconstituted (Boulet-Audet et al., 2011) and native silk fibroin (Boulet-Audet et al., In preparation). The dope as a nascent fibre was previously studied within the dissected duct of the silkworm *Bombyx mori* by longitudinal imaging of a dissected duct and transverse sectioning of a silk press (Asakura et al., 2007a) and the dope surrounded by sericin within the duct considered schematically (Magoshi et al., 1994). In spiders, the nascent fibril is surrounded by flocular material and drawdown occurs in the distal third section of the duct before the valve (in the spider *Araneus diadematus,* described from thin transverse sections, though with no quantitative data) (Vollrath et al., 1998). Additionally the ionic content of frozen sections of a dissected *Nephila edulis* duct was determined by cryoSEM- energy dispersive X-ray (EDAX) (Knight and Vollrath, 2001).

Although it has been reported that spiders of a given species produce fibres with identical tensile strengths and elasticity (Ortlepp and Gosline, 2008), there is also an indication that these fibre properties are a function of reeling speed, with faster reeled fibres decreasing in extensibility and are weaker (Vollrath et al., 2001). In addition, if the ducts of spiders at different stages of development are of different shape and size, as suggested above, it is likely or at least possible that their differently sized and shaped ducts should produce fibres with different properties, due to the different rheological flow profiles. For example, larger, heavier spiders may need to produce fibres that require more force to break than smaller, lighter spiders. To reconcile these observations, a hypothesis was made that the silk produced by larger ducts becomes more disrupted at higher forced reeling speeds, relative the silk produced by smaller ducts. To test this hypothesis, tensile tests were performed upon fibres force reeled from different ducts at different speeds.

In summary, there are few quantitative literature reports on the morphology of spinning glands in spiders and silkworms. Therefore, this chapter first describes a study of the gross size and shape of the ducts of the major ampullate gland in the model spider *Nephila edulis*, with the aim of understanding the relationship between spiders of different sizes and the tensile properties of the silk they produce at different spinning speeds. The size and shape of the spinning ducts, spigot size, silk fibre diameter and spinning duct wall all need to be correlated with the spider size. Second, the development of the solid silk fibre as it passes along the spinning gland and the location of the fibre drawdown within a non-dissected duct of the model silkworm *Bombyx mori* was investigated using survey cryosections, and the result compared with conventional understanding of this part of the silkworm anatomy.

3.2. Methods development

3.2.1. Preliminary study

To make a 3D reconstruction of an organism, there are two types of possible methods: non-destructive and destructive. Non-destructive methods include micro computerized tomographic,

magnetic resonance or confocal imaging. These methods have the advantages of not damaging the tissue and being generally quick to make a scan. The foremost disadvantages are limited availability, inadequate resolution for measuring the duct inner diameter, and difficulties with low contrast specimens. Destructive methods use sectioning of the material with some kind of knife, then imaging stained sections through a microscope. This has the advantages of being able to be done with little equipment, and the disadvantages of being slow and difficult.

At the time of the study, post-doc Dr. Katrin Kronenberger was investigating the possibilities of non-destructive methods, but with limited success. In the literature, there were two examples of successful reconstruction of ducts within whole specimens after sectioning, those of *Helicoverpa armigera* (Sorensen et al., 2006) and *Cupiennius salei* (Hilbrant, 2008), so the destructive method was chosen. To section and then reconstruct a specimen requires a number of steps, each of which must be chosen to be compatible with the specimen and each other. These steps can be split into two sections: sectioning and reconstruction. The stages of sectioning are specimen immobilization, fixation, dehydration and clearing, infiltration and embedding, sectioning, mounting, staining. The stages of reconstruction are image acquisition, image processing, and 3D reconstruction. These relatively conventional methods are described in Appendix 1 for reference.

3.2.2. Spider morphology study

Nine *Nephila edulis* specimens weighing 0.05 g to 1.59 g (Fig. 3.1) were reared and prepared as detailed in section 2.1 of Chapter 1. Spider mass, fibre diameter and cephalothorax width were measured as detailed in section 2.1 of Chapter 1.



Fig. 3.1 An illustrative sample of cephalothoraxes of the spiders used for duct size measurements, encompassing spiders with cephalothorax widths from 2.16 mm to 8.98 mm. Scale bar: 5 mm

After imaging, weighing and silking, each specimen was instantaneously killed by crushing of the cephalothorax between a blunt instrument and hard surface.

Each leg was removed at the coxa (Fig. 3.2 (A)) and photographed through a stereo microscope (Olympus SZ4045TR) with a digital camera (Canon Powershot A640) on a flat surface against a known scale (Fig. 3.2 (B)). Some legs did not lie flat, so, to enable an accurate length measurement, they were cut into multiple sections that each would lie flat. The images were imported into SolidWorks (Dassault Systèmes), and the length of each leg measured as a compound curve drawn from tip of the tarsus to the end of the trochanter.



Fig. 3.2 (A) Schematic diagram of walking leg, reproduced from (Kaston and Kaston, 1953) Ta = tarsus, Mt = metatarsus, Ti = tibia, PT = patella, FE= femur, Tr = trochanter, Cx = coxa. (B) Representative photograph of whole and divided legs as used for leg measurements. Scale bar 6 mm.

The two major ampullate glands from each spider were dissected out as detailed in section 2.1.1.4 of Chapter 1. Each duct was transferred to a walled microscope slide and bathed in spider Ringer solution (Groome et al., 1991), whereby the translucent sac surrounding the duct was removed using sharpened pins and the three limbs of the duct were gently unfurled to prevent overlap during imaging.

Spider ducts were measured as described in the Methods chapter section 2.2. The distance between sampling points was 30 μm for the first four spiders' ducts, but measurements took a very long time, so the sampling interval was increased to 460 μm with no noticeable loss of clarity of data. To compare the size and shape of each duct, the centre of each duct valve was set as the origin of the x-axis and the radius of each duct plotted at known distances away from this point. The valve is the closest feature to the position at which draw down occurs and therefore the size of the duct just proximal to the valve is the most relevant to the spinning process. To prevent variations in size due to humidity, each duct was measured whilst immersed in spider ringer.

The diameter of the spigot was measured in Photoshop at a quarter of the distance from the tip to the base, as from inspection of each image it could be seen that this position between the final tip and the widening at the base of the process is most constant in diameter in the whole spigot (Fig. 3.3). A collation of these images is shown in Fig. 3.4.

Fig. 3.3 Schematic diagram showing how the location at which the diameter was measured on the spigot was calculated

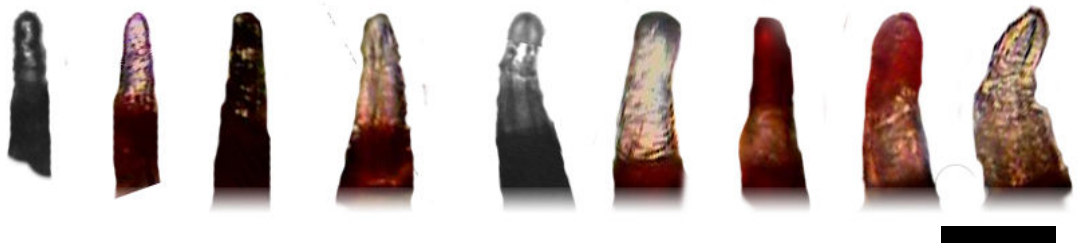


Fig. 3.4 Collated spigot images. Scale bar length 50 microns

The mean length of the two ducts of each spider was calculated to avoid pseudo-replication when comparing against other features. Relationships between the mean duct length and each feature

were calculated. To test the hypothesis that the length of the spinning duct is positively correlated with spider size, spider duct length was compared with (i) cephalothorax width, (ii) length of each pair of legs, (iii) average length of the legs of the spider, (iv) mass of the spider.

To test the relationship between duct length, spigot size and spider size, each was plotted as a function of cephalothorax width. The relationship between average duct length and each parameter for each spider was calculated using a standard linear regression analysis with Excel (Microsoft). To test the hypothesis that dragline-silk production takes precedence over web-silk production (and therefore ducts are optimised for fast spinning), duct length was plotted against cephalothorax width of male spiders. Most Male *Nephila* are too small to dissect and measure ducts using the method used here. At the time of the study only two males were large enough to be successfully dissected and have their ducts measured, so only these were used.

To test the hypothesis that the duct wall changes in thickness along its length, internal and external diameters of the duct were measured at the same regularly spaced points from the spigot to the funnel as described in section 2.2 of the Methods chapter. A single wall thickness of the ducts from above was calculated at each measurement point to be half the difference between internal and external diameters. To examine whether duct wall thickness is correlated with the developmental stages of a spider, the wall thickness measurements for spider cephalothorax width were normalised and then plotted against distance along the duct with the clamp valve as zero on the x-axis. A linear regression of thickness against spider size was modelled in JMP 10 (SAS Institute Inc.) with a null hypothesis that there was no relationship between the thickness of the duct and the spider size. The model was tested by an analysis of variance.

There were two problems to be overcome before duct wall thickness could be compared between spiders: first, an overall positive gradient in the duct wall thickness, and, second, minor fluctuations in thickness measurements over small lengths. To compare ducts of different shapes, my initial approach was to normalise the lengths of the ducts to unity, and to compare the wall thickness values of each of the normalised length ducts. Due to the particular shape of the ducts,

where each has a similar gradient though with different lengths (Fig. 3.5(A)) I quickly realised that normalising the duct length to unity would mean comparing the wall thickness of ducts of different diameters and would not be a valid test (Fig. 3.5 (B)), since the wall thickness also increases as a function of duct diameter. Instead, the ducts were not normalised in length to compare wall thickness, but compared 'as is', for the linear section of the duct only. As there were minor fluctuations in thickness of the duct wall along the length of the duct, the mean wall thickness was calculated for 2 mm long bins, up to the maximum length of 'linear' region of the duct wall of the smallest duct (Fig. 1.6 (C)).

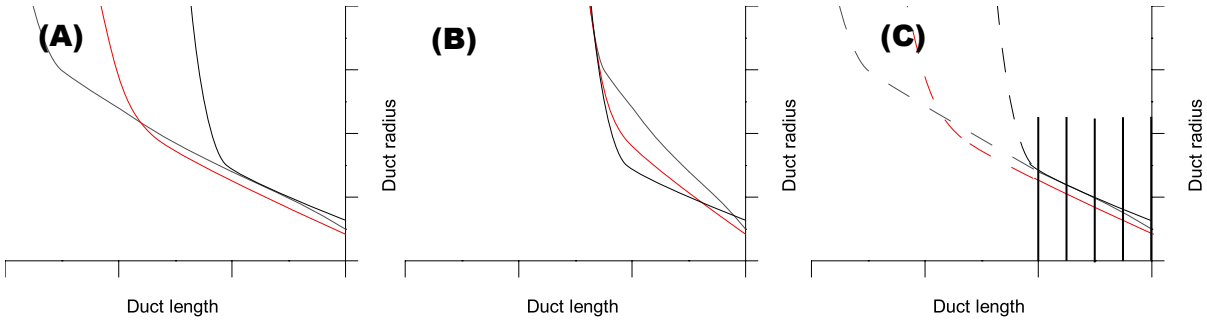


Fig. 3.5 A visual explanation of the rationale for binning. (A) Spider wall thickness profiles, (B) normalised in x-axis to length of small spider duct results in different gradients and comparison of different parts of the duct. (C) Using original data, but truncated to the length of the smallest spider, allows a valid comparison of wall thickness. Dotted lines indicate data not used in the comparison.

3.2.3. Sectioned silkworm duct study

Bombyx mori silkworms were reared to final instar and allowed to spin the construction part of their cocoon.

The next step was to rapidly freeze the whole specimen whilst it was still spinning. Dropping the sample whole into liquid nitrogen was attempted, but the extremely rapid freezing ruptured the wall of the glands, destroying the delicate silk draw down morphology to be studied.

Instead, the spinning worm was snap frozen using a modified form of an established technique (Toma et al., 2002) by immersion in a weighing boat filled with Optimal Cutting Temperature (OCT) formulation (VWR BDH Prolabo), within a beaker of isopentane, on a bed of dry ice. The

whole setup was placed in an insulated sample bucket with the lid on (whole schematic Fig. 3.6) and left for ten minutes to freeze completely.

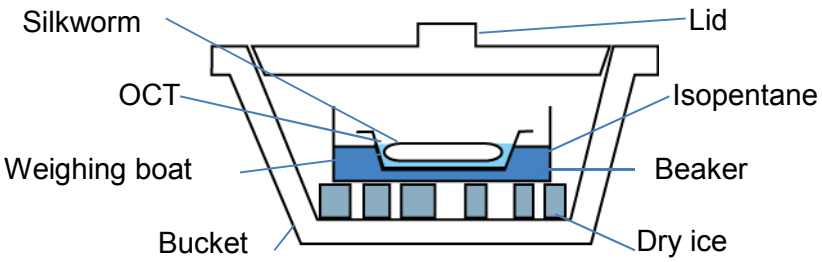


Fig. 3.6 Schematic of worm freezing process, showing worm immersed within OCT floating in a bath of isopentane on a base of dry ice

The OCT block was removed from the boat within a sample chamber (maintained at -18 ° C) of a cryostat microtome (Model CM3050 S, Leica Biosystems). The cryostat works in a similar way to a conventional rotary microtome, in that it moves the sample mounted on a stub past a stationary blade, which slices a thin section from the sample. This presents a problem: the extreme length to width ratio of the silkworm would result in large forces being generated at the anchor point when cut by the knife, probably breaking the sample from the cutting stub. To prevent this breaking, the sample was cut into three thick sections, each roughly cubic in shape, then each frozen to sample stubs with OCT.

When ready, each stub-mounted sample was placed in the chuck of the microtome and sections cut (Fig. 3.7 (A)). Cutting 10 µm sections through the whole ~50 mm long worm would require 5000 sections. Instead, repeated sequences of five 10 µm thick sections were made in a row, followed by a 950 µm thicker section. In this way, the internal structure was sampled every millimetre, with five samples together to ensure that at least one would be viable for imaging. These sections were then recovered from the microtome onto polysine coated microscope slides (Menzel-Gläser, Germany).

Each section was imaged with a digital camera (Canon Powershot A640) mounted upon a dissecting microscope (Olympus SZ4045TR), so that the overall structure of the duct could be studied (Fig. 3.7 (B)). The digital images were stacked and aligned in Photoshop CS4 (Adobe

Systems Incorporated), which allowed the location of the glands and ducts throughout the body of the silkworm to be tracked. The duct sections were imaged at 100x magnification on modified microscope by a 576x768px monochrome digital camera (Oxford Cryosystems Metripol) (Fig. 3.7 (C)). From these images, duct wall internal area, inner and outer diameter, inclusion diameter and area were measured in ImageJ (NIH).

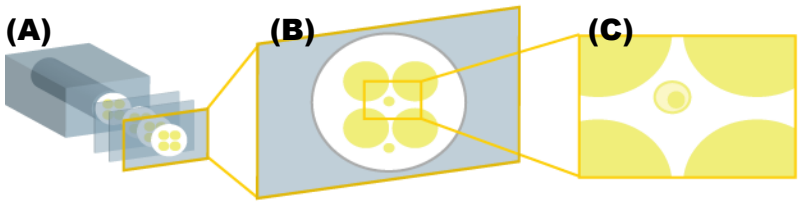


Fig. 3.7 Schematic of block sectioning process. (A) Worm within block of OCT is sectioned. (B) Each section was imaged at low magnification, showing the location of the glands and ducts. (C) The ducts were imaged at medium magnification, showing the nascent fibril within the duct walls.

Finding the location of a certain section within the block by calculating the number and thickness of previous sections is not recommended when sectioning, since the block can change shape due to humidity. An alternative method was needed to plot the location of each section along the duct. The ducts were dissected out from a worm of comparable size, and the outer diameter measured along the length of the duct. The radius of the duct sections was used as the metric of comparison, due to their use in previous work on duct size, included earlier in this chapter. This profile of duct radius against length of duct was used to locate the position of the duct sections. Inclusions with irregular cross section posed a problem in defining the radius size. I therefore assumed that the original shape of the nascent fibril was circular and that processing distorted its shape. Their areas were measured in software (NIH ImageJ), and the radius calculated of an equivalent circle with this equivalent area using Excel (Microsoft) (Fig. 3.8).

Fig. 3.8 Schematic demonstrating the method of standardization of irregular inclusions due to their assumed circular origin: area of the inclusion was measured, and the radius calculated if this area was a circle.

3.2.4. Silk properties

Five silk fibres were reeled at 10 mm s^{-1} ± 0.1 mm s^{-1} for 10 minutes from each spider before they were killed. The diameters of the silk fibres were determined using the method described in section 2.3.4 of the Methods chapter. The relationship between cephalothorax width and fibre diameter was analysed using a standard linear regression model using Excel (Microsoft).

A further six spiders were reared, collected and anaesthetized, massed and cephalothorax imaged as detailed in section 2.1.1 of the Methods chapter. They were secured to a raft of expanded polystyrene under a fine nylon mesh, ventral side upwards, with a small window in the mesh, positioned to allow access to the spinnerets. After allowing thirty minutes to allow the effects of CO_2 to dissipate (Madsen and Vollrath, 2000), a single fibre from one of the two major ampullate ducts was collected onto a reel powered by an electric motor at an ambient temperature of 22 ° C. Using the custom motor controller and methods described in section 2.3.1.1 of the Methods chapter, silk fibres were reeled at 0.1, 0.5, 2.0, 10.0, 20.0 and 40,0 mm s^{-1} for 5 minutes at each speed.

Reeling speeds were initially randomised, but it was found that the silk fibres frequently broke inside the spider if the first speed to be reeled was 40 mm s^{-1}. Internal breakage necessitated removal of the spider from the investigation to allow it to restart spinning (Vollrath et al., 2001). Therefore, spiders were each reeled from slowest to fastest rates, which did not break the fibre.

Resistance by the spider during silking was measured by an analytical balance (Sartorius BP121S) recording the reduction in mass of the spider as the spider was pulled upwards towards the reel (see Fig. 3.9), and was logged as a function against time in data logging software (A&D Company RSWeight).

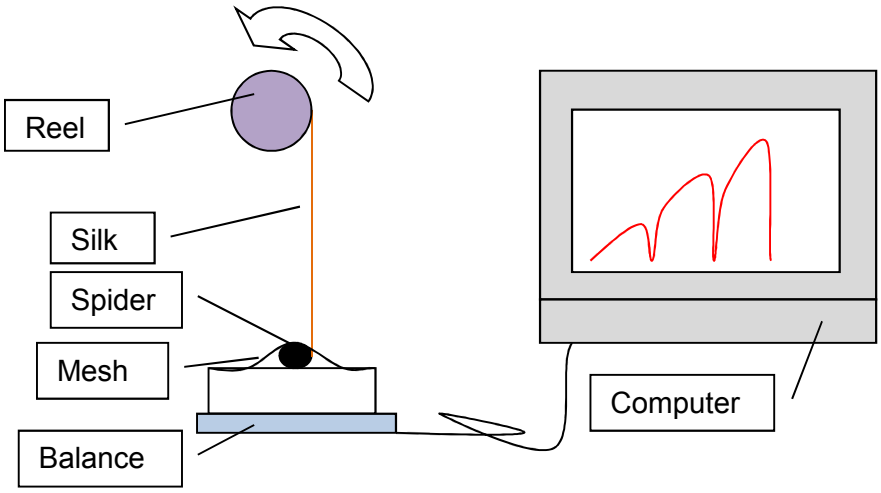


Fig. 3.9 Schematic diagram of spider being silked upwards whilst pinned under a plastic sheet, all on an analytical balance. Data from the analytical balance of change of mass of spider was recorded

Five fibre samples were collected from the last part of the fibre spun at each reeling speed for each spider and mounted on 10 mm gauge length card frames as detailed in section 2.3.2 of the Methods chapter. Tensile testing was undertaken at 22 ° C, 40% humidity and 50% per minute strain rate as detailed in section 2.3.3 of the Methods chapter. The cross-sectional area of fibres was measured as detailed in section 2.3.4 of the Methods chapter. Error bars for each data point were calculated from the standard error of the averaged samples.

3.3. Results and discussion

3.3.1. Preliminary study

After fixing, dehydration of the silkworm specimens seemed to dry out the unspun silk stored in the silk glands. Rather than filling with liquid and paraffin, the two silk glands became an empty void within the body cavity of each worm. When cutting the paraffin block with the microtome, rather than creating one smooth section, the part with the void collapsed, thereby distorting all the

tissue of the section. This was then unusable for sectioning. Fluid could not be injected into this cavity to prevent drying without thoroughly destroying the tiny specimens.

It was not possible to fix or infiltrate paraffin into large spiders, even by making copious invaginations through their cuticle. A small spider, a juvenile *Xysticus* was successfully sectioned into 280 slices and reconstructed. Fig. 3.10 shows the opisthosoma after reconstruction, the well-defined cuticle and showing that the outer cuticle is well aligned.

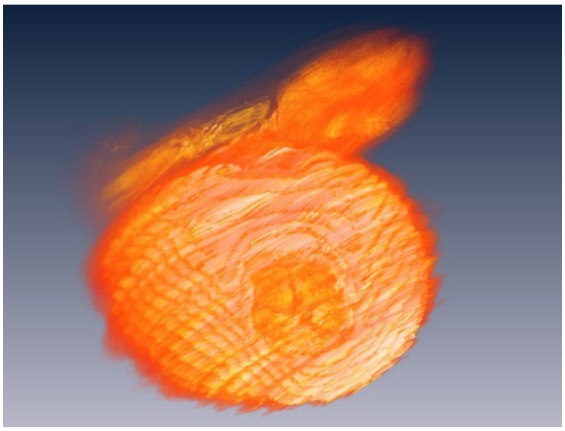


Fig. 3.10 Reconstructed outer cuticle of crab spider, ventral view

The results of highlighting and reconstructing the internal structures can be seen in Fig. 3.11. These images show two or possibly three recognisable silk glands (blue, green), with ducts that taper towards the front of the spider and then return towards the spinneret. Further towards the midline of the reconstruction are structures (pink) that have a tubular appearance, which taper distally towards the spinneret and then abruptly changes from a backwards to a dorsal direction. At the centre of the dorsal side is a thick tapering tube (purple), which reaches from the proximal to the distal ends of the image and is interpreted to be the heart. In the centre of the ventral side of the reconstruction are a large number of small discrete structures (yellow) of mainly homogenous size, which become larger and more clustered towards the distal edges. A fairly regular shaped structure in the centre of the reconstruction (red) connects via a fine tapering tube to another sac-like structure at the back edge, which is interpreted to be the digestive system and storage sac.

The results show the relative sizes and locations of the biological organs within the juvenile spider, but not to a high definition; either in-plane or within section thickness. The resolution is insufficient to identify the path of the spinning duct from either the main glands or the small aggregation glands to the spinnerets.

Although using paraffin embedding and Amira software has previously shown positive results (Hilbrant, 2008), in this case, the results were not of high enough resolution to be of use to meet the aims of the study. What started as a preliminary study had a large number of problems: the infiltration did not work on fully mature spiders, or at all on silkworms; performing the techniques well enough to get a whole specimen's worth of sequential sections for adequate reconstruction took a long time, even for very small specimens, with very steady hands and extreme patience; imaging and processing of files, although semi-automated, still had to be done for every section; to fit a whole specimen's stack of images into Amira without running out of memory meant that the resolution of each image had to be reduced to a low level of typically 30% of the native output of camera; after loading into the computer, the contrast between the duct and the surrounding tissue was too low for automatic area selection so had to be done for each duct by hand.

Due to the large number of difficult steps that were required for each specimen, even if a better imaging program could be found, the time involved would not be decreased significantly. The time that would be required to increase the resolution would be unacceptable, even before extending the study to a larger number of specimens for a degree of statistical relevance.

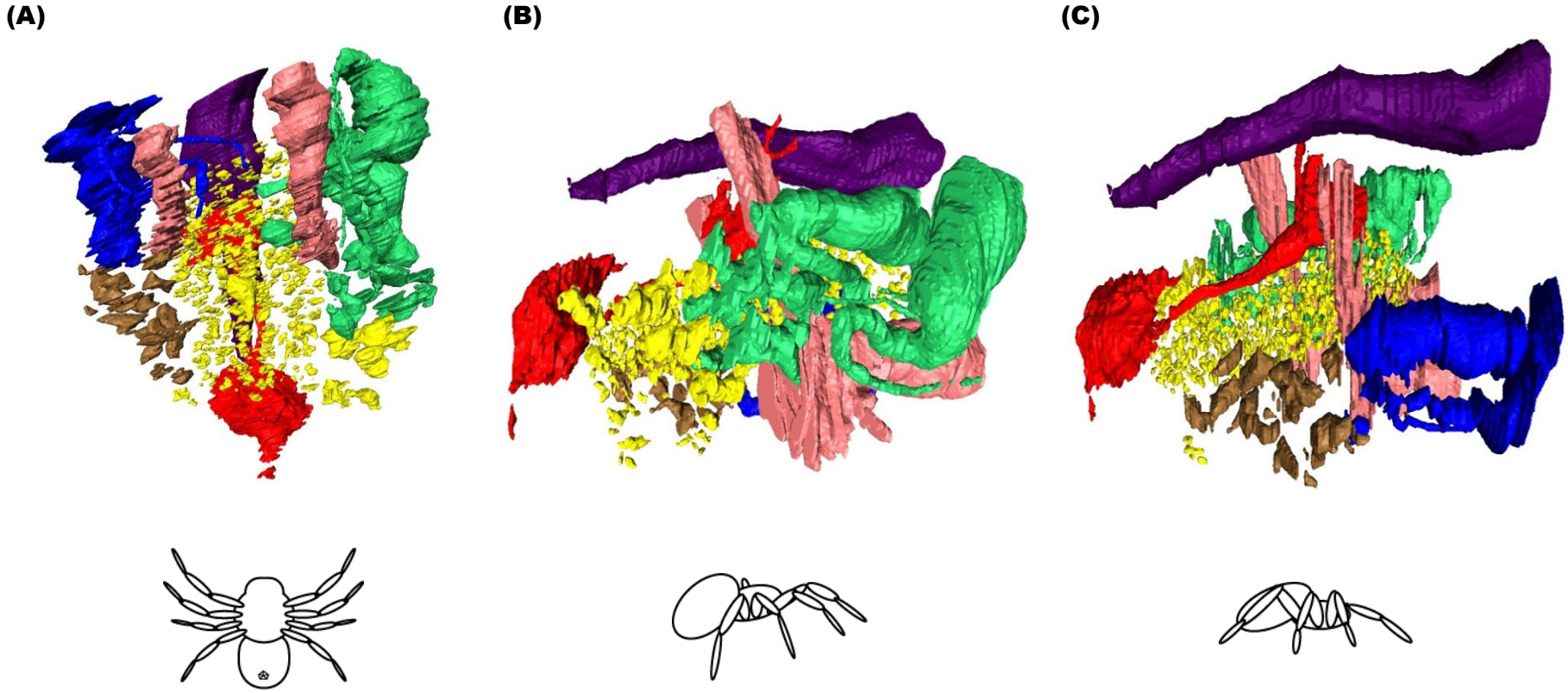


Fig. 3.11 Reconstructed internal structures of crab spider opisthosoma, with schematic of spider position to aid interpretation. (A) ventral view, (B) three quarters rear view, (C) side view. Green and blue: major spinning gland and ducts. Purple: heart. Red: digestive system. Pink: structural section. Yellow and brown: other glands.

3.3.2. Spider morphology study

3.3.2.1. Duct profile along length

This section describes the results measured from the ducts of dissected spiders. Fig. 3.13 shows a comparison of the measurements of the inner radius of the duct against length along the duct for different sized spiders with those of previous studies (Knight and Vollrath, 1999, Kojic et al., 2004). In the figure, the radius of the funnel, and then of the duct, initially decreases rapidly from left to right towards the origin, to an inflection point demarcating the start of the approximately linear distal portion of the curves. This has been described previously as a two stage hyperbolic function (Knight and Vollrath, 1999). The duct of *Nephila edulis* was described in that paper to closely fit a two stage hyperbolic profile, but the equation was not given. However, the equation governing this curve has been calculated elsewhere as

$$r(z) = ae^{bz} + ce^{dz} \qquad \text{Equation 3.1}$$

where a=-0.004886 μm, b=0.0003718 μm^{-1}, c=53.52 μm, d=-9.989x10^{-5} μm^{-1} (Breslauer et al., 2009). The shape of the spinning duct of the spider *Nephila clavipes* was also published (Kojic et al., 2004), although an equation governing the shape was again not published. To quantify the shape, the graph of the duct shape from that paper was imported into OriginPro 8 software (Origin Lab), and the curve digitized with 140 points.

A difficulty with using the two curves from the literature was that neither the origin of their x-axis was not specified, nor how close to the spigot the duct diameter was measured. Therefore, the curves from the literature were aligned approximately to the linear distal portion of the curves recorded in this study. The position along the duct at which the curve becomes linear depends on the size of the spider, generally commencing further from the spigot with increasing spider size. Despite a dramatic increase in duct length from moult to moult, the slope of the linear regions was closely similar in all eleven spiders studied, independent of the spider's size.

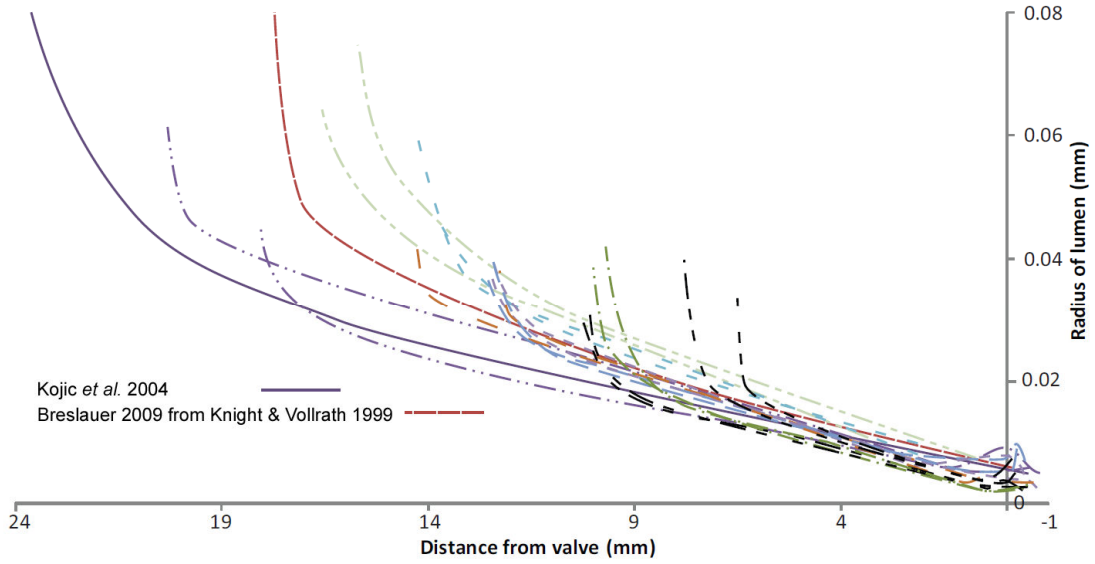


Fig. 3.12 Plot of the inner radius of duct against distance from valve to end of funnel. Data from this study is overlaid with *Nephila* data from previous studies ((Kojic et al., 2004), (Breslauer et al., 2009) from (Knight and Vollrath, 1999)), showing distal near-linear region with closely similar slope and Y-interception in all specimens. Duct pairs from each spider have same colour and dash patterns. N= 18 ducts from 9 spiders + 2 profiles of individuals from the previous studies noted in the legend

Measurements of spinning duct size and shape showed a hyperbolic linking region, followed in all spiders by the same essentially flat hyperbolic (effectively linear) gradient in the distal part of the duct. This profile maintains an effectively constant linear extensional flow rate (Chen et al., 1992) down the length of the duct. This may act to avoid imperfections introduced by transient flow instability. The progressive tapering of the duct probably allows the balance point for the transition from shear flow to extensional flow for internal draw down to shift along the duct to accommodate different spinning rates (see discussion, section 3.3.4). Given the sensitivity of the silk spinning-dope to shear and/or rapid extension, it is not surprising that, from the data presented here, it seems that a spiders' extrusion die has evolved to prevent premature beta sheet formation in the duct while optimizing flow parameters.

Regenerating the geometry of the distal portion of the duct to have a similar or constant gradient from instar to instar is a not an inconsiderable feat for the spider, as the entire spinning apparatus is formed anew before each moult (Townley et al., 1993b). This remarkable conservation of the

geometry in the distal part of the duct where the initial drawdown occurs (Knight and Vollrath, 1999) suggests that geometry is a key active part of the organism, in particular the spinning process.

A table of fits of each of the curves in is included on the following page. Parameters a, b, c, and d are as in equation 3.1.

black dashes 2	3.93E-18	5.477	0.004024	0.227	0.9797
black dashes 1	0.004074	0.2086	1.87E-16	4.129	0.9979
long dark dashes 2	0.002246	0.2297	0.000739	0.1476	0.959
long dark dashes 1	0.003599	0.1899	-0.06474	-3.447	0.9356
purple dashes 2	0.006315	0.1394	-0.002	-0.556	0.9849
purple dashes 1	-0.1351	0.1777	0.1406	0.1767	0.983
dark blue dashes 2	2.69E-18	2.889	0.006606	0.1204	0.9977
dark blue dashes 1	-0.00022	0.1742	0.005885	0.1419	0.9744
light blue short dashes 2	0.009226	0.1096	-0.00921	-0.4429	0.9902
light blue short dashes 1	1.82E-13	1.775	0.008472	0.1127	0.9992
dark green dashes 2	2.81E-14	2.801	0.003316	0.2048	0.9946
dark green dashes 1	8.04E-18	3.509	0.003806	0.1833	0.9895
light green dashes 2	1.71E-18	2.347	0.00891	0.1188	0.9977
light green dashes	0.00798	0.1205	-0.00877	-0.7433	0.9872
dirty orange 2	-	0.08162	1.93E+12	0.08162	9.52E-01
dirty orange 1	0.007491	0.111	-0.00715	-0.3786	0.984
purple double dots 2	0.005609	0.1058	-0.00695	-1.346	0.9678
purple double dots 1	0.008116	0.09165	-0.01391	-0.7634	0.9646
	A (µm)	B (µm)	C (µm)	D (µm)	R^2

3.3.2.2. Relative dimensions

Table 3.1 demonstrates that for each of the characteristics of the spider measured, cephalothorax width has the highest and most significant correlation coefficient with duct length (R2 = 0.946, p< 0.001). Thus, the cephalothorax width of spiders in this size range may be considered the best physical attribute of the spider from which to make an estimate of silk properties.

Table 3.1 Regression analysis of various features with duct length, N = 8 spiders.

Feature	R^2	Significance (%)
Leg 1 average length	0.796	0.122
Leg 2 average length	0.693	0.536
Leg 3 average length	0.203	22.354
Leg 4 average length	0.485	3.723
All legs average length	0.729	0.339
Spider mass	0.858	0.096
Silk fibre diameter	0.596	4.185
Cephalothorax width	0.946	0.001

Fig. 3.13 supports the hypothesis that length of the duct, as well as spigot diameter and silk filament width, all increase at a linear rate with spider cephalothorax width. However, the rate of increase of fibre diameter (gradient of 0.7) with cephalothorax width is considerably less than that of spigot diameter (gradient of 2.4). However, when normalised (by the point at x=5 divided by the corresponding y-axis measurement), the three sets of data have a mean normalised value of 3.69 with a standard deviation of 0.68. This normalised value indicates that, despite a range of sizes and gradients, the relative rate of growth between the three bodily parameters is very similar.

The total duct length, and diameter of the spigot show a strong correlation with spider size, measured as the width of the cephalothorax (<0.01 significance; R^2 values respectively 0.946, 0.917, F statistic 96.0, 49.3) in Fig. 3.13. This indicates that that both length of the duct and spigot diameter increase linearly with spider cephalothorax width. Duct length is unlikely to be affected by the very small extra length required to reach between old and new cuticle during ecdysis

(Townley et al., 1993a). The inter-cuticular distance at the major ampullate spigots was 0.2 mm on their photomicrograph of a 7th instar orb-weaving barn spider, *Araneus cavaticus*.

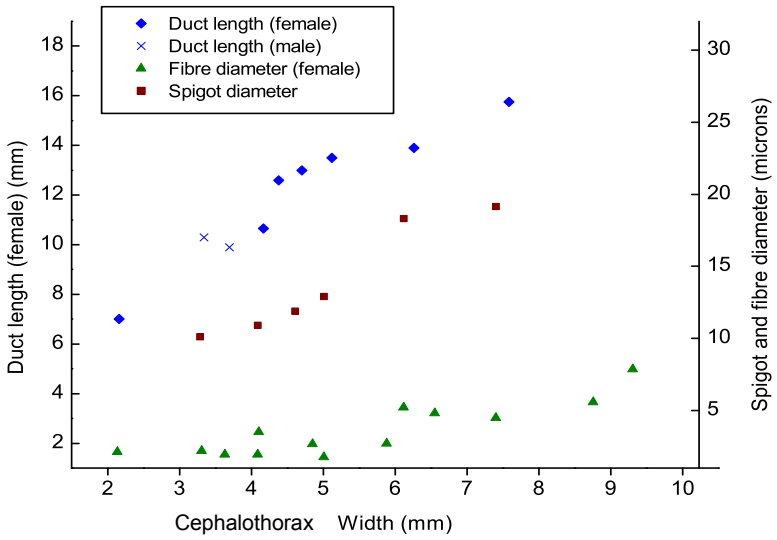


Fig. 3.13 Plot of duct length, spigot and fibre width against cephalothorax width. Data shows correlation with better than 0.01 significance for each feature. N=9 spiders for duct length of which 6 spigots could be measured, 12 spiders for fibre diameter

An analysis of total duct length against size of the two largest male spiders in Fig. 3.13 showed that the duct lengths of males lie upon the same line as those for females with no discernible difference in data for the two sexes. Duct size increases in the same proportion to body size in both males and females. This may be because both sexes spin safety lines, and the requirements for safety lines may be the primary constraint on fibre production, and hence duct size. This result suggests that male spiders may be able to spin dragline silks with similar tensile properties to those of the females. In general, larger adult spiders produce larger diameter fibres than smaller spiders (Fig. 3.13), and it has been reported that all the fibres have comparable normalised tensile properties (Ortlepp and Gosline, 2004). As the mechanical properties of the silk fibres are the same throughout spider growth and development (Ortlepp and Gosline, 2008), this suggests that the overall flow history that determines the molecular structure of the silk fibres should be equivalent. This flow history is determined by a combination of gland dimensions and spinning

speed, and so the effect of spinning speed on some spun silk properties is considered below for spiders of different size.

3.3.2.3. Wall thickness

Visual comparisons of short sections of duct showed little difference in wall thickness, as shown in Fig. 3.14. When plotted as a function of duct length an overall trend emerged: close to the funnel, the wall thickness appears constant or gently decreasing in thickness. This continues until an inflection point two millimetres from the valve at which the wall thickness then increases rapidly, as shown in Fig. 3.15.

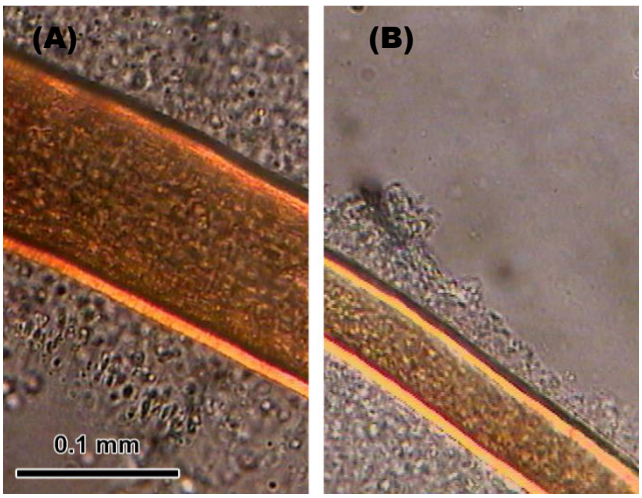


Fig. 3.14 Representative comparison of wall thickness at two different distances along a single duct showing little discernible variation in wall thickness (A) just distal of the funnel; (B) just proximal of the funnel. Scale bar for both images: 0.1 mm

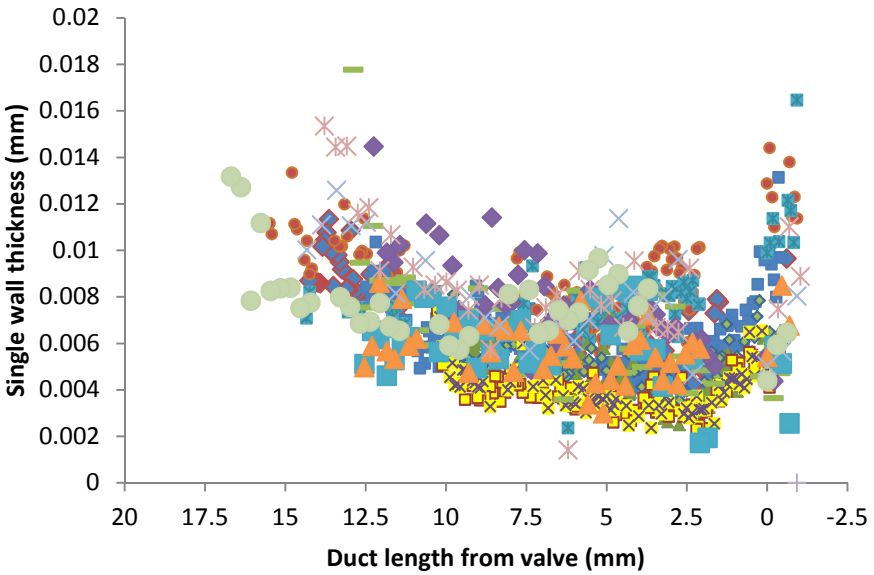


Fig. 3.15 Plot of duct wall thickness as a function of duct length. Symbols of the same colour and shape denote measurements along the length of a single duct. N= 9 spiders

Linear regression analysis of binned data of duct wall thickness and spider development confirmed the hypothesis that, for this spider species and data set, duct wall thickness does indeed increase as a function of spider cephalothorax width (R^2= 0.40, F = 35.2, p< 0.0001).

Superposition of the traces for each wall thickness from Fig. 3.15 suggest that the relationship between duct size and wall thickness also follows a similar pattern irrespective of spider size. These data were normalised by the diameter of the duct at that point and also the overall cephalothorax width of spider as a measure of spider development (shown plotted in Fig. 3.16). The figure indicates that there may be a generic relationship between spider size and the thickness of the duct. The figure shows that wall thickness increases slowly as a proportion of the duct's width along the length of the duct towards the valve, increasing rapidly 2 mm before the valve, and then abruptly decreasing again after the valve.

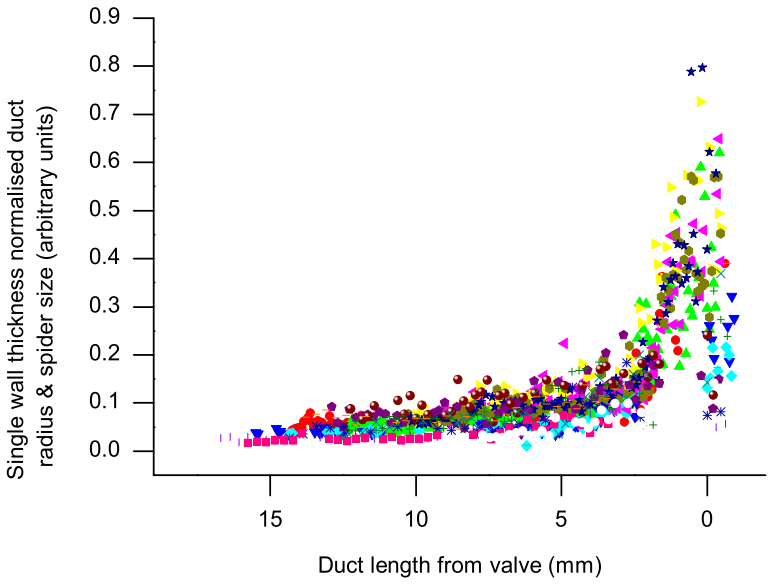


Fig. 3.16 Plot of duct wall thickness normalised by the internal duct diameter at that point and spider size, as a function of duct length. Each point represents a single measurement of wall thickness, and points of same colour and pattern come from the same duct. N= 9 spiders

The silk dope draw down occurs 2 – 4 mm from the valve (Vollrath and Knight, 1999, Knight and Vollrath, 1999) and moves proximally along the duct with increased reeling speed (Work, 1977). It is likely that, as the draw down moves further up towards the funnel, the larger diameter of the duct will be more susceptible to collapse from increased compressive stress. Therefore, to prevent duct collapse, the stresses are countered by a proportionally thicker wall than at smaller diameters. Just proximal of the valve at about 2 mm length, I observed a rapid increase in wall thickness around the point where phase separation of the silk proteins and water occurs.

The data presented here provides a measure of the combined cross section across both the extracellular matrix and the cells that compose the duct, and it is not possible to use it to differentiate between whether one or both the extracellular matrix and the cells composing the duct are changing in thickness. These modifications may increase the duct's ability to control the ionic environment, increase water uptake, and/or may improve the mechanical properties of the cuticle lining to permit spinning of larger diameter fibres and spinning at faster rates. This could be due to an increase in radial (bursting) stresses as water is released at higher rates and a larger filament is pulled more rapidly through the narrowed distal part of the duct. These requirements

might help to explain the gradual decrease followed by rapid increase in wall thickness observed in each of the ducts studied, but detailed effects such as these are beyond the scope of this work.

3.3.3. Sectioned silkworm duct study

The cryosections made along the silkworm duct show the change in radius and location of turns of the glands and ducts. Some of these sections with ducts showing can be seen in Fig. 3.17.

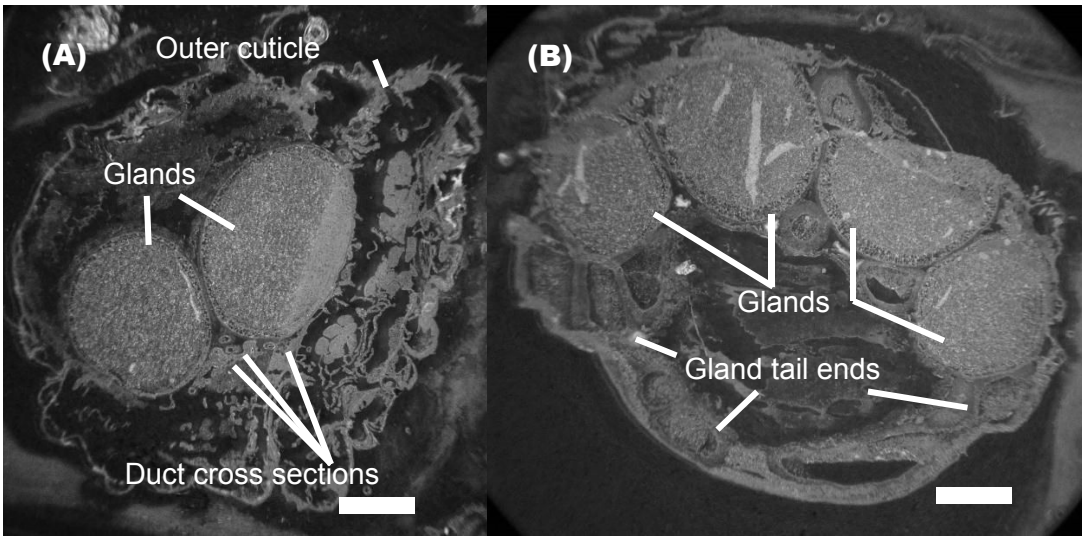


Fig. 3.17 10 µm survey cryosections through a *Bombyx mori* silkworm. (A) Section from middle of the organism, showing multiple duct cross sections and two gland sections. Scale bar 1 mm. (B) Section from posterior end of the organism showing folded glands represented by the four large areas of homogenous flocular material, and multiple circles from the tail, protein secreting end of the gland. Scale bar 1 mm.

The ducts and storage sacks were followed through the sections, to give a picture of their shape within the specimen. The 'map' (Fig. 3.18) shows that each duct is folded six times before reaching the storage sac (section 725 of gland 1, section 726 of gland 2), which is folded twice more. The circles in the diagram give the section number in which the measurements were taken, and circles with a letter and a number indicate a specific fold in two different glands.

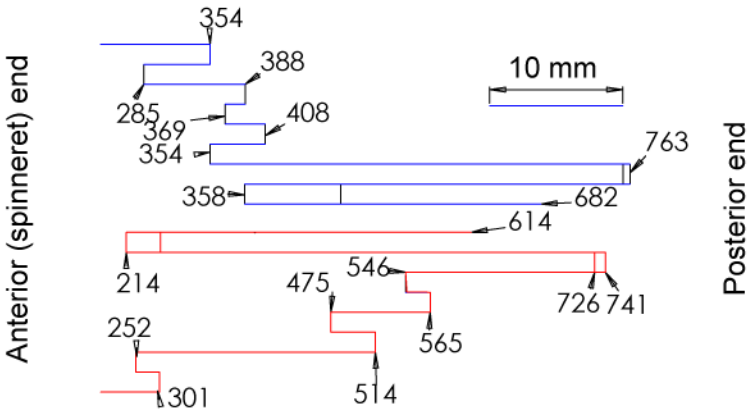


Fig. 3.18 Map of silk gland and duct folding, with the location of the fold indicated by section number.

Sections through the duct (Fig. 3.19) clearly showed the duct, surrounding epithelium, and the contents of the duct with a visible separation between a dense and lighter section. The wall of smaller diameter ducts was sometimes split in one or two places, for example Fig. 3.19 (B).

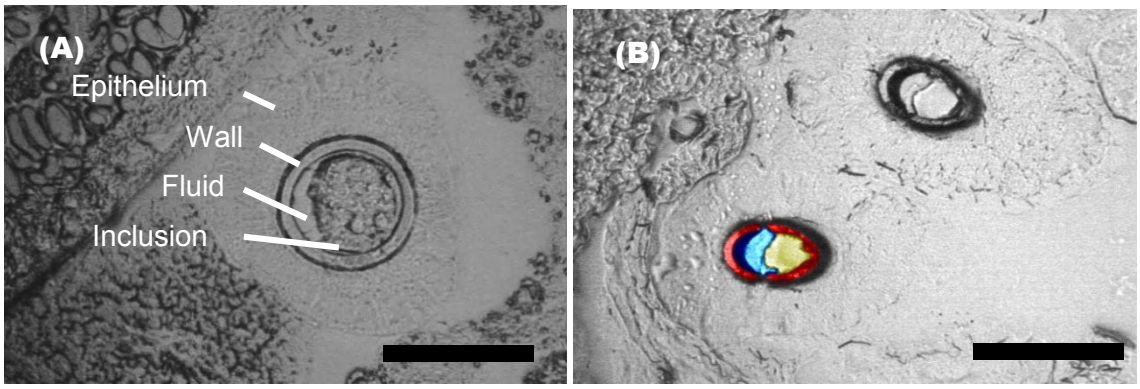


Fig. 3.19 Moderate magnification photomicrographs of duct sections showing surrounding epithelium, duct wall, surrounding fluid and internal inclusion. (A) single circular duct cross section from posterior side, scale bar 10 µm. (B) two ducts with artificial colour showing duct wall (red), surrounding fluid (blue) and inclusion (yellow), scale bar 10 µm.

It was not possible to view sections of the joining of the duct, the silk press or further distal features of the duct visible in Fig. 3.20, probably because they are extensively sclerotized and therefore do not cut well. In the sections with smaller diameter ducts the duct wall was sometimes split in one or two places, for example Fig. 3.19 (B). This is probably due to the pressure from water freezing into ice upon the small ducts, an increase in volume of 9 %. The small circumference of the duct in this distal location may not be sufficient to resist the increase in

volume, or the material near the spinneret may not be as extensible as the material closer to the storage sack.

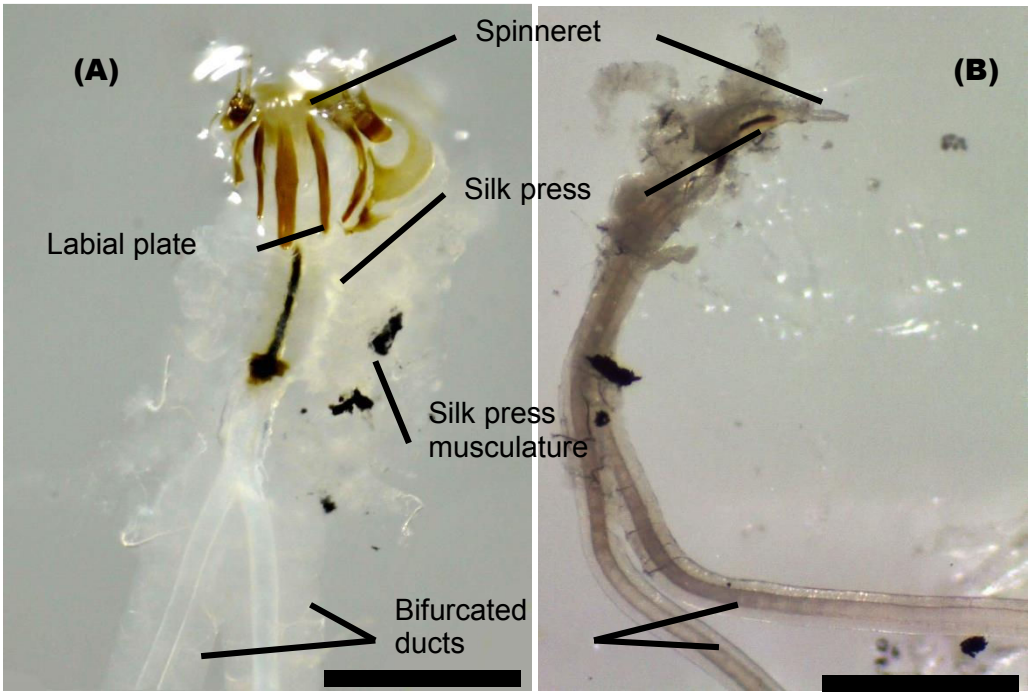


Fig. 3.20 Photomicrographs of joining of the duct, silk press and spigot (A) with labial plate present, Scale bar 1 mm. (B) with labial plate removed. Scale bar 1 mm.

The internal diameter of the duct walls is 0.1 mm at a distance of 18 mm proximal of the spinneret, which decreases in a fairly linear manner until 4 mm proximal of the spinneret, after which the slope increases in gradient (Fig. 3.21). The inclusion within the ducts goes from a radius of roughly 0.05 mm at a distance of 17 mm from the spinneret, and decreases very gradually to a distance of 3 mm before the spinneret. Like the duct radius, this then decreases at a faster rate for the last 3 mm before the spinneret.

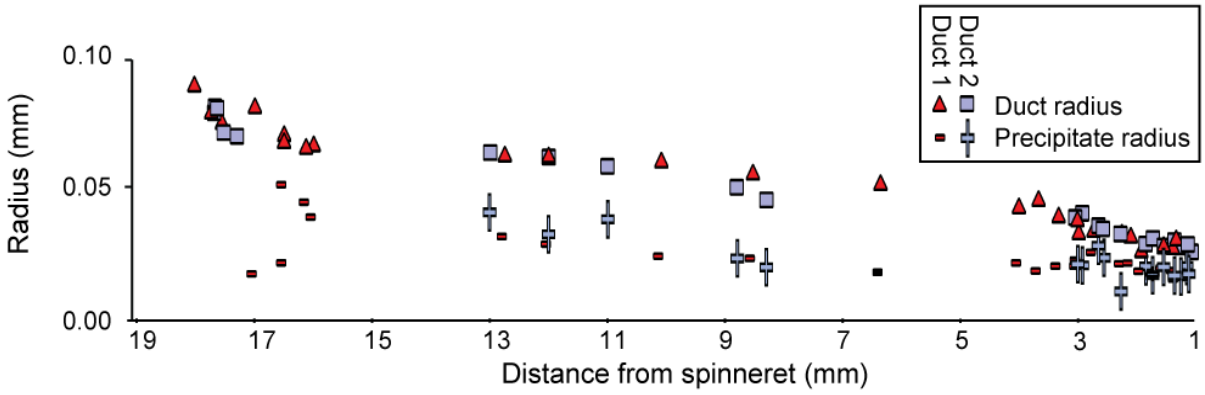


Fig. 3.21 Data from duct size, with the precipitate radius denoted by dashes and crosses, and the radius of the duct lumen by triangles and rectangles

This data was more easily visualised in Fig. 3.22, in which the wall of the duct, the inclusion and the surrounding area are shaded. The inclusion is drawn emerging from the storage sac on the left hand side of the diagram. Sections more than 17 mm from the spinneret were not available due to the cutting method using separate blocks, so data points for this section are not available.

The parameters for the curves of the silkworm duct from Fig. 3.21 when fitted to Equation 3.1 are noted in the following table:

Table 3.2 Fitting parameters for silkworm duct geometries

	Red triangles	Blue squares
A (μm)	0.03809	0.03531
B (μm)	0.04141	0.04311
C (μm)	-0.03881	-0.02385
D (μm)	-0.6832	-0.77549
R^2	0.92382	0.96394

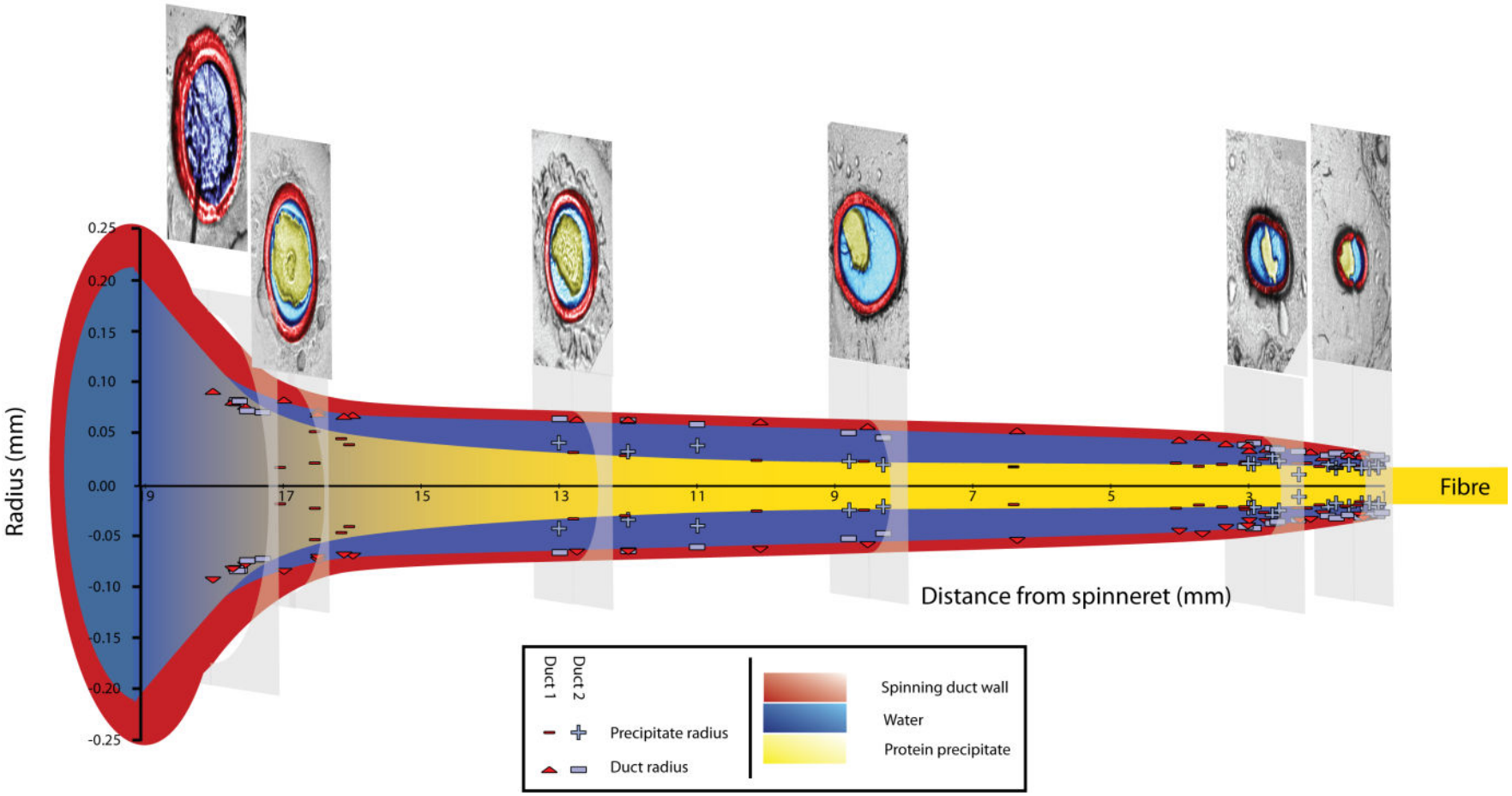


Fig. 3.22 Data overlaid with colours accenting contrast and location of nascent fibril within duct

The cryosection study suggests that the silk fibril coalesced at a position in the duct much further proximally than previous studies using ducts dissected in the normal way have shown. If this proximal location of the draw down is an accurate observation, it may indicate that the nucleation and formation of silk fibril is due to elongational rather than shear stress in the duct, facilitated by chemical changes in the fluid. This hypothesis is proposed because the nascent fibril does not appear to touch the wall of the duct any closer than 17 mm from the silk press, thereby removing the condition for shear flow, that the material has intimate contact with the walls of the flow channel.

The test does not prove conclusively whether the dope has phase-separated sooner than expected previously in the duct, so the results must be taken with caution. The next stage of this study, for which I ran out of time, would be to perform the same method of cryosectioning the worm, but to use micro-FTIR to probe the degree of beta-sheet formation. This could be compared against the results from Rheo-FTIR (Boulet-Audet et al., 2011) to quantify how far the feedstock has turned into a fibre. In addition, perhaps x-ray micro-tomography of non-frozen spinning glands could be performed might give an independent observation of these silk phase separation effects.

Silkworms differ from spiders in that they are fibroin, rather than spidroin, and also spin at one stage of development only, and within a much smaller range of speed than occurs in spiders. Additionally, the proteins of silkworm silk are co-extruded with a coating of sericin so may be prevented from touching the walls of the duct entirely. Therefore any comparison of the drawdown position between spiders and silkworms must be made with care.

3.3.4. Silk properties

Fibre diameter was positively related in Fig. 3.13 to developmental stage and size, represented by the width of the cephalothorax (<0.01 significance; R^2 values 0.732, F statistic, 33.8). This demonstrates that the corresponding silk fibre thicknesses all increase at a linear rate with spider cephalothorax width. It is interesting now to look at properties of the silk fibre as a function of spinning speed for the different sizes of spider to see if there are any trends that might provide insights into the production of silk in the glands, which would be useful later for artificial spinning. Fig. 3.23 (A), (B), and (C) shows three plots of fibre diameter, breaking stress, and resistance force to spinning as a function of spinning speed, respectively.

Fig. 3.23 (A) illustrates the diameters of fibres spun by the spiders at varying reeling speeds, and shows that the fibre diameter increases with spider size. The two larger spiders produce fibres that appear to increase in diameter as the reeling speed increases to 2 mm s^{-1}, whereupon the diameter seems to decrease again with reeling speed, though with a very small sample size. The two smaller spiders' fibre diameters, in contrast, seem fairly constant with perhaps a slight increase in diameter as the speed increases.

The convex shape of the curve in Fig. 3.23 (A) suggests that the diameter of all of these spiders' fibres builds to a local maximum at natural spinning conditions, reducing in diameter again as reeling speeds increase up to a certain speed limit. The speed limit may have been reached in the spider with a cephalothorax width of 3.1mm, indicated by red circles. The silk diameter increases at a spinning rate of 40 mm s^{-1}, much as described in earlier work (Vollrath et al., 2001) in which speeds above a limit seemed to produce increasing diameter fibres.

Fig. 3.23 ((B) shows that, for the gravid adults of cephalothorax width 6.2 and 7.7 mm, there seems to be a constant tensile (breaking) stress throughout the speed range. For the small spiders, we would expect higher breaking stress due to thinner fibres (Porter et al., 2013), and breaking stress seems more variable and rapidly drops off at 40 mm s^{-1}. This may indicate that the duct has exceeded its capability to produce fibres with functional tensile properties.

Fig. 3.23 (C) shows a fairly constant resistance to silking for the two larger spiders, with a possible slight increase in resistance with speed. The two smaller spiders both show an increase in resistance to reeling throughout the speed range, with the smallest spider having the largest forces proportional to its mass at each speed. Between 20 and 40 mm s^{-1}, the resistance to reeling of the smallest spider appears to drop sharply from 2x spider mass to 1.2x spider mass, possibly as at this speed the spider becomes unable to resist reeling with the silk duct, as has been witnessed previously.

The maximum resistance to silking of these fibres did not approach the previously published Ortlepp and Gosline 2004 value of three or more times spider body mass (Ortlepp and Gosline, 2004). The highest resistance observed was two times body mass (see Fig. 3.23 (C)). These data, when combined with that in Fig. 3.23 (A) may indicate that at speeds of 40 mm s^{-1}, the spider is no longer able to resist reeling, resulting in an increase in the diameter of the fibre and therefore reducing the amount of post draw brought about by stretching the fibre.

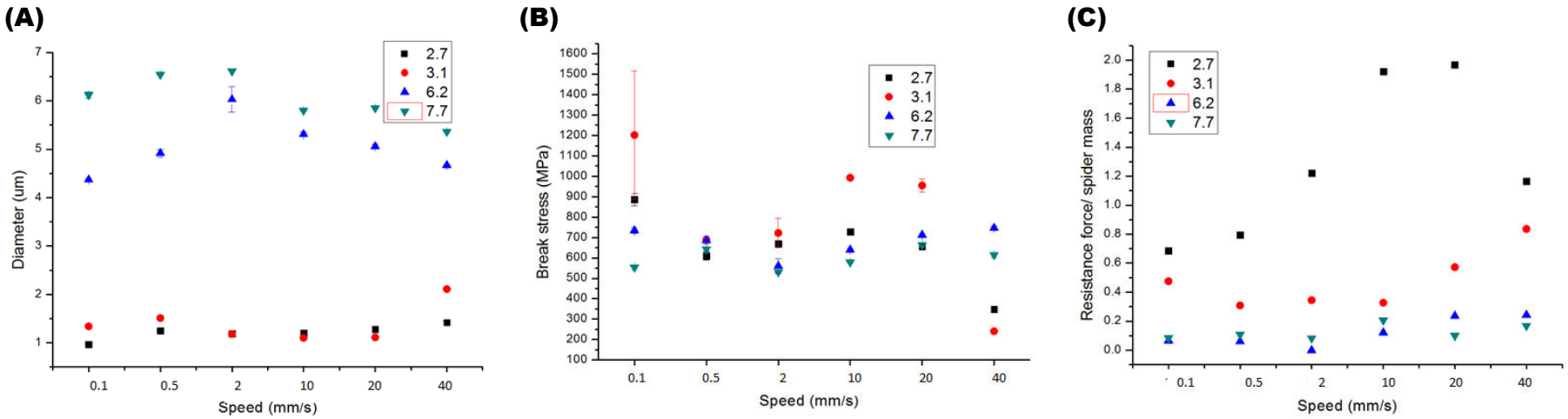


Fig. 3.23 Fibre diameters of spiders of different sizes, spun at different speeds. Error bars are calculated from standard deviation of values. Key indicates size of spider as measured by cephalothorax width. (B) Mean break stress for each fibre spun from different sized spiders at the range of speeds, with error bars of standard deviation. Key indicates size of spider as measured by cephalothorax width. N= 5 samples per speed per spider. (C) Resistance to silking by each spider, normalised by mass of spider

While more studies will be needed to draw firm conclusions about the effects of reeling speed and duct length on fibre properties such as tensile strength, the results described here may tentatively support the hypothesis that the increased duct length of larger spiders (illustrated in Fig. 3.12) enables the position of the draw down in the duct to move closer to the funnel. This would allow the same flow history to be applied to the developing fibre with the increased flow rate associated with larger diameter fibres, without moving the start of drawdown backwards to a point before the location of chemical modifiers, which are reported to play a key role in fibre spinning through the ionic environment (Knight and Vollrath, 2001, Dicko et al., 2004b, Dicko et al., 2004a). These ionic changes may also be exaggerated if the duct is unable to recover water normally at very high (or exceptionally slow) spinning rates (Vollrath et al., 1998, Vollrath and Knight, 1999, Tillinghast et al., 1984).

This is consistent with the commencement of the draw down process tending to move back along the linear portion of the duct as reeling speed increases (shown schematically in Fig. 3.24), as has previously been reported (Work, 1977). Importantly, the gradual tapering of the duct allows the location at which the draw down commences to be varied 'automatically' by the spider. Moving the location of the draw down accommodates the variations in the draw rate and force produced by spinning at a given developmental stage and still produces a fibre with the same amount of mechanical work.

Thus, the progressive elongation of the quasi-linear region of the duct as the spider passes through successive moults may allow for a greater range of draw rate and drawing force with the growth of the spider than would be possible without a quasi-linear duct region, while still maintaining the same fibre properties. This is essential, since the size, weight and strength of the spider increases by orders of magnitude as the spider develops. Similarly in speed, since a final instar (adult female) spider needs to produce strong silk at natural draw rates ranging from a few millimetres to 1 meter a second (Knight et al., 2000, Vollrath et al., 2001).

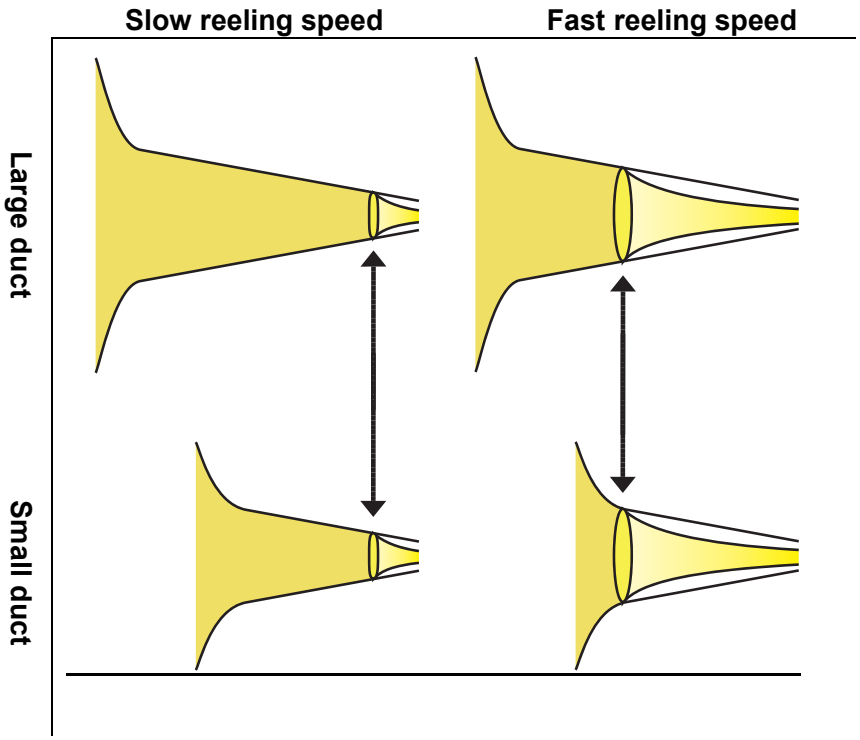


Fig. 3.24 Schematic diagram of internal draw down within the duct of small and large ducts, as a function of reeling speed. Location of internal draw down within distal part of the duct varies rapidly with relatively small variations in reeling speed. Equivalent drawdown locations correspond to different absolute locations in ducts of different sized spiders. In each image the long axis is compressed for convenience

3.4. Summary and conclusions

This study has looked at the morphology of spider and silkworm spinning glands, how the silk fibre develops as the dope flows through the gland, and the relation between silk fibre properties and both gland morphology and spinning speed. The study described in this chapter focused on the duct at a macro level. The composition and the structure of the duct wall are both likely to contribute to fibre properties, so are covered in the next two chapters.

The first important observation on morphology was that internal diameter of the distal part of the major ampullate silk gland duct is highly conserved in the spider *Nephila edulis* as the spider grows. This supports the hypothesis that the geometry of this region of the duct, in which the silk is initially drawn down into a filament, is crucial for the spinning of strong threads. The study also showed that the linearly tapered region of the duct both elongates and increases in diameter as the spider grows. This might enable the spider to adapt the position of the commencement of the

internal draw down to the increasingly wide range of draw stresses and strains encountered as the spider grows. Second, it was found that the wall thickness is a function not only of duct diameter but also increases with spider size.

Survey cryosections of the drawdown and phase change of the silk dope within the duct of the Chinese silkworm *Bombyx mori* indicated that this location was more proximal than previously thought.

Reeling silk from a range of spiders indicated that the control of tensile and other mechanical properties deteriorates as the reeling speed increases. It was tentatively shown by preliminary study that the reeling speed at which silk deteriorates is lower in spiders with smaller ducts.

The improved understanding from this work of the way in which the shape and size of the spider's duct changes as the spider develops should help in modelling the spider's sophisticated spinning process in different size spiders and at different draw rates. This will help in the design of biomimetic extrusion devices for native and regenerated silk proteins and other polymers.

From a project perspective, unfortunately, the preliminary study into imaging ducts *in* vivo had to be abandoned due to too ambitious objectives with insufficient technological support. However, as a preliminary study, I learnt a lot of biological and imaging techniques, and learnt that it is better to abandon a project if it is taking too long for poor returns than to blindly persevere. Ultimately, the lessons learned in the preliminary study were put to good use in the design of the remainder of the work in this chapter, which reduced the number of aims to some that were still both unstudied and relevant to the spinning process.

Chapter 4. Extracellular morphology of the silk duct

4.1. Introduction

Hypotheses as to the origins of the spigot and gland have generally fallen into one of three categories (Craig, 1997), (Sutherland et al., 2009): first, that the glands evolved *de novo* (Craig, 1997); second, from dermal layer structures such as from epidermal invaginations (Kovoor, 1987), limb buds or coxal organs (Shultz, 1987), or fluid-secreting setae (Young and Merritt, 2003); third, from non-dermal structures such as egg sacs (Kovoor, 1987), as some insect spinning glands appear to be modified salivary glands or malpighian tubules (Craig, 1997).

Arthropod sensory setae have ionic gradients across their cuticular intima that induce fluid flow into their inner surfaces in a manner similar to the way silk proteins are secreted via the silk duct (Phillips and Vandeberg, 1976). Inspired by the induced fluid flow, which may be more than a similarity, my hypothesis was that the spider duct developed from dermal structures. The primary aim of this chapter is to test this hypothesis by detecting cuticular materials in the duct.

Arthropod cuticle, including setae, is largely composed of relatively decreasing proportions of polysaccharide, chitin, structural proteins and calcium carbonate (Wainwright et al., 1976b), and arthropod sensory setae are composed of chitin. Therefore chitin, a D-glucosamine with functional acetamide group (Muzzarelli, 1977) shall be the material for which to test in ducts.

If chitin were found in silk duct walls, in addition to the evolutionary significance, its significance to silk production would also be of great interest. Chitin behaves like a viscoelastic polymer (Ruiz-Herrera and Martinez-Espinoza, 1999), which means it is very strong, pliable and flexible, whilst being very insoluble in water due to its high crystallinity (Pillai et al., 2009) and also great hydrophobicity (Ravi Kumar, 2000), properties likely to be highly pertinent for silk production due to the precise folding of hydrophobic around hydrophilic regions of the silk protein (Jin and Kaplan, 2003).

Silk production in spiders and insects is a classic example of convergent evolution, whereby two independent organisms evolved a very similar process (Vollrath and Knight, 2001) with a very similar output (Craig, 1997). Assuming that the presence of chitin is important in silk production in spiders, then, due to the similarity already known in silk production, chitin is also likely to be found in the duct walls of silkworms. Silkworm ducts are highly unlikely to have evolved from sensilla hairs, despite a suggestion to that effect (Young and Merritt, 2003), due to their derivation from the insect labial gland (Snodgrass, 1935). Thus, the presence of chitin in silkworm ducts would be an interesting example of convergent evolution in silk production.

The first part of this study, therefore, set out to test for the presence of chitin within the silk ducts of spiders and silkworms. Absence of chitin in the duct walls would make the hypothesis that ducts are derived from chitinous hair less likely and would have been a definite indicator that chitin is not required for spinning. The presence of chitin was tested using histochemical methods, and the evidence corroborated by Fourier transform infrared spectroscopy (FTIR) by comparing putative duct wall chitin both against other parts of the organism known to contain chitin, and against purified chitin.

The second part of this chapter set out to test whether the length of the duct containing chitin is constant or varies with duct length in spiders. The length of duct containing chitin was ascertained in spiders of the same species at different stages of development, and compared to the known total length of their ducts. There were several possibilities for the distribution of chitin within the duct, each of which would have different implications for silk spinning.

The length of spider's ducts are known to increase linearly with spider development, as shown in Chapter 3. A duct wall containing chitin for a proportion of the duct that scales with duct length would indicate a functional significance of chitin in the spinning of silk fibres. A duct wall wholly composed of chitin may indicate that the material is always required for spinning silk, or that it is not possible to build a duct without the presence of chitin. The extent of chitin was compared

against the position within the folded limbs of the duct, and whether it is the linear or hyperbolic regions of the duct profile.

The model organism the edible golden orb weaving spider *Nephila edulis* was used to test for the presence of chitin in spider silk duct walls, as *Nephila* has highly developed silk glands capable of producing silk fibres with excellent tensile properties (Vollrath and Knight, 2001). The model silkworm *Bombyx mori* (Xia et al., 2004) was used to test for the presence of chitin in insects as it produces silk of great commercial importance (Vollrath and Knight, 2001). For verification, these experimental results were compared with data from powdered purified chitin.

4.2. Methods

4.2.1. Specimen preparation

For electron microscopy of the duct *Nephila edulis* specimens weighing from 0.16 g to 1.48 g were reared, weighed, cephalothorax width measured and ducts dissected as detailed in section 2.1.1 of the Methods chapter. Final larval instar *Bombyx mori* silk ducts were prepared as detailed in section 2.1.2 of the Methods chapter.

Purified and powdered shrimp shells (Sigma Aldrich CAS 1398-61-4) were used as a reference sample for chitin for both histochemical and spectroscopic examinations.

4.2.2. Histochemical detection of extent of chitin along the duct

The established protocol for histochemical detection of chitin at the light microscopical level (Campbell, 1929) was followed, though a modified version to preserve fragile samples such as rotifer cuticle (Ravindranath and Ravindranath, 1975). The method involves treatment of the sample with potassium hydroxide (KOH) to partially deacetylate the chitin to chitosan and remove non-chitinous matrix components, followed by washing in EtOH, and acidification and staining with iodine to produce a purple to rest-red colour. Chitosan is soluble in acetic acid so the purple to rust-red colour produced gradually fades, but the structure itself does not solubilise as there is likely to be substantial amounts of un-acetylated chitin remaining (Peters, 1992).

Photomicrographs of the ducts (N = 5 silkworms, 8 spiders) were taken before and after testing the histochemical reaction with a digital camera (Canon Powershot A640) mounted on a stereo microscope (Olympus SZ4045TR). From these photomicrographs the duct length was measured from tip of spigot to proximal end of funnel with imaging software (NIH ImageJ). From these measurements, the proportion of the length of the duct that remained after the histochemical procedure was calculated.

To search for chitin-containing fragments released during the destruction of the proximal part of the spider's duct the entire histochemical procedure including digestion by KOH, washing in EtOH, acidification and staining was carried out in a silicone grease compressorium (4 ducts from 2 spiders) viewed with bright field illumination (both 10x and 100x oil immersion objective) on a modified microscope (Oxford Cryosystems Metripol).

The shape of the length of the duct that remained after the histochemical treatment and stained with iodine was estimated by plotting the duct radius profile for the spider size obtained from Chapter 3. This was used to estimate how far along this profile this portion of the duct extended.

Purified powdered chitin from shrimp exoskeleton (Sigma Aldrich) used as positive control stained a deep purple which faded slowly.

4.2.3. Spectroscopic detection of chitin

For spectroscopic examination, five replicate samples were taken and the mean spectra calculated for each of the following tissues: four silkworms' spigots, head plates and silk gland ducts; the extreme proximal and distal ends of four spiders' ducts (as the proximal third behaved differently to the remainder of the spider duct in the histochemical test), their spigots, cuticles, and midgut. The cells from each were removed by soaking overnight in aqueous 0.1 % Tween 40 (Sigma Aldrich) solution on an orbital shaker plate then washed thoroughly in distilled water. To demonstrate the effect of the detergent solution upon the duct, the mean spectra was calculated from four silkworms' ducts rinsed in distilled water rather than Tween solution but otherwise

treated identically. The effect was not expected to be different in spiders as they have remarkably similar ducts (Vollrath and Knight, 2001). 0.1 % Tween 40 was also probed in the same manner.

Spectra were measured on a Nicolet 6700 Fourier transform infrared spectrometer equipped with a liquid nitrogen cooled mercury–cadmium telluride (MCT-A) detector used with a 'Golden Gate' single bounce diamond attenuated total reflectance (ATR) sampling accessory (Specac Inc., USA). The diamond's internal reflectance element (IRE) had a refractive index of 2.417 with a 45 ° angle of incidence. To ensure contact of with the sampling window of the spectrometer, the specimen was transferred wet to the ATR cell. Water was then removed under vacuum to leave the sample stuck to the diamond window. Reference samples of commercial purified chitin (Sigma Aldrich) were compressed between the sample window and the anvil of the ATR cell until a good signal level was acquired.

Spectra were analysed with Omnic 7.3 software (Thermo Scientific, USA). The Omnic 'Correlation' algorithm which removes offset and eliminates variation in the baseline, was used to compare spectra from different specimens.

ATR microscopy may have given better results but unfortunately this facility was not available.

Any treatment is unlikely to remove all highly bonded protein from chitinous structures, so some protein is likely to remain after the treatment, preventing acquisition of pure chitin.

4.3. Results

4.3.1. Presence of chitin

4.3.1.1. Spider

After performing the histochemical test, whole mounts prepared from the major ampullate duct connected to the spigot showed that the proximal part of the duct had been destroyed leaving only a short length of the distal part of the duct still attached to the spigot, both of which stained a purple/ rust red colour (Fig. 4.1 (A)). This colour gradually faded as chitosan is soluble in acetic

acid, but the structure itself did not dissolve probably because deacetylation in KOH was only partial (Peters, 1992).

After performing the test extremely gently within the compressorium, no remaining components of the proximal part of the duct within the surrounding fluid were found even at high magnification.

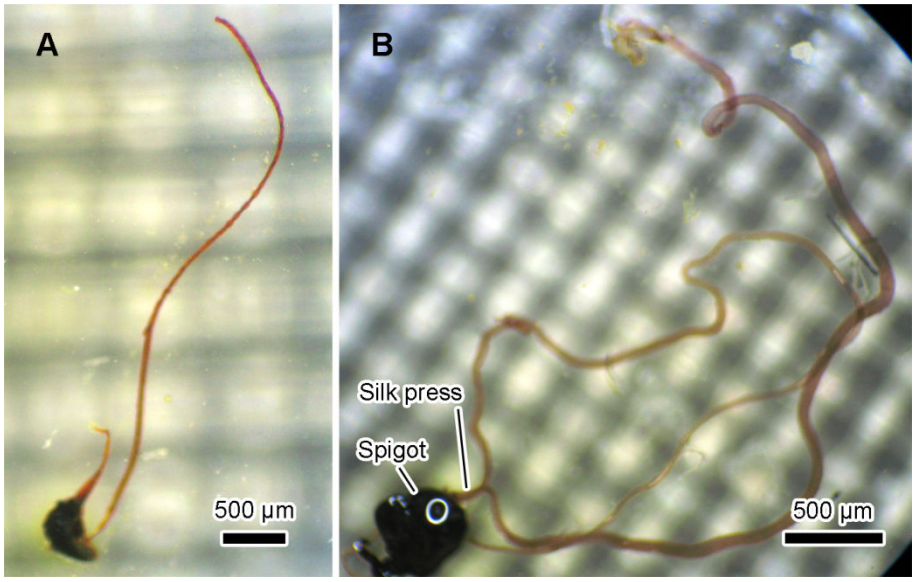


Fig. 4.1 Micrographs of ducts testing positively for chitin, (A) *Nephila edulis*, showing outer cuticle of spinneret and duct, scale bar 500 µm. (B) *Bombyx mori*, showing spigot, silk press and duct join, then both ducts stained. Scale bar 500 µm. Images brightened and contrast adjusted to improve contrast with background. Negative tests resulted in solubilisation of sample.

4.3.1.2. Silkworm

The entire length of the cuticle lining of the silkworm duct from the distal end of the anterior division of the silk gland to the outer tip of the spigot including the silk press survived KOH treatment and stained purple/ rust red colour with iodine in all specimens as illustrated in Fig. 4.1 (B).

4.3.1.3. Reference sample

When the same assay was performed on a reference sample of powdered chitin from purified shrimp the same deep purple was obtained, and faded over time in the same manner as the colouring of the ducts.

4.3.2. Longitudinal distribution of chitin

4.3.2.1. Spider

The length of the spider duct before the histochemical treatment was a linear function of cephalothorax width ($p > 0.01$; $R^2 = 0.9141$, n=8). After the chitin test, the length of the remaining duct was also a linear function of cephalothorax width ($p > 0.01$; $R^2 = 0.8759$, n=8) (Fig. 4.2).

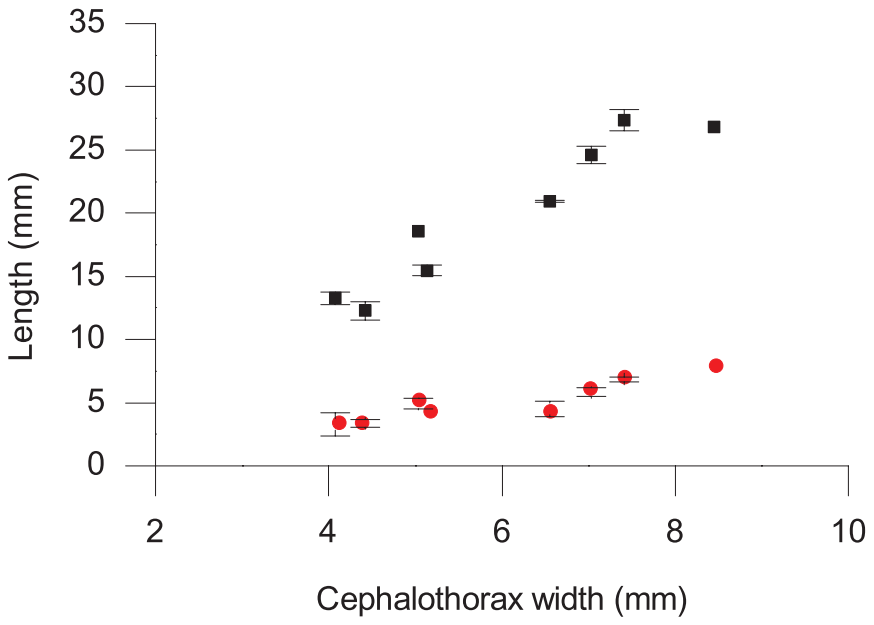


Fig. 4.2 Original length of spider duct and portion testing positive for chitin plotted against cephalothorax width. Original length of duct (black squares), portion testing positive for chitin (red circles) . Error bars show standard deviations of length measurements. N=16 ducts from 8 spiders.

The proportion of the length of the duct that survived the treatment and stained remained fairly constant as the spider grows.

4.3.2.2. Location of chitin in spider duct wall relative to duct limbs

For each of the spider duct studied, the portion remaining after KOH treatment and staining was found to extend from the tip of the spigot to a point approximately half way along the final limb of the three folded limbs of the duct. This location is shown in Fig. 4.3 (A), in which the portion of duct wall testing positively for chitin is shown superimposed on a traced image of the entire duct.

The graph Fig. 4.3 (B) shows the shape of the ducts in both an early and late development spider using data taken from Chapter 3. The section of the duct that tested positively for chitin lies within the part of the duct that decreases linearly in diameter for both early and late instar spiders.

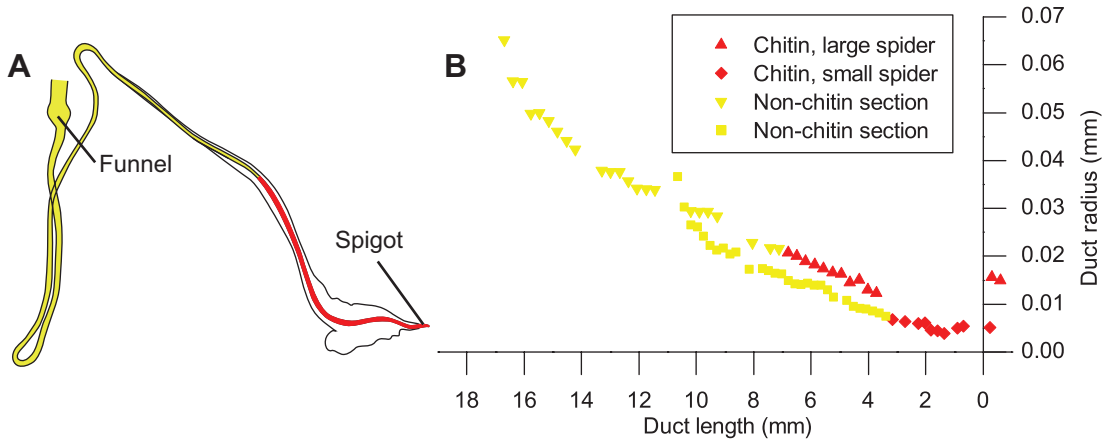


Fig. 4.3 Chitin location within the spider duct. (A) Tracing of spider duct, showing portion solubilised by acid in yellow and section remaining after KOH treatment and testing positive for chitin highlighted in red. (B) Duct profile of both and early and late spider instars from Fig. 3.12 in Chapter 3, with valve positioned at x=0. The symbols (red diamonds early instar; red triangles late instar) are for the part of the duct that stains for chitin and the yellow from the remainder of the duct that is destroyed in the test. This indicates that the surviving region is confined to the section of the duct that narrows linearly in both early and late instar spiders.

The results from spider ducts indicate that the length of the duct wall staining for chitin increases during organism development and is confined to the linearly narrowing distal section of the duct. as discussed in Chapter 3, experimental evidence suggests maintenance of the geometry of this part of the duct is crucial for silk spinning in the spider.

4.3.3. FTIR spectroscopy of ducts

4.3.3.1. Comparisons between the spider proximal and distal duct sections

The averaged FTIR spectra of the proximal and distal sections of the spider duct shown were similar to each other in shape and scale, with high intensity peaks at 3292 cm^{-1} indicative of the OH bond stretch (Libowitzky and Rossman, 1997), 3080 and 2926 cm^{-1} indicative of CH symmetric stretching (Ibrahim et al., 2005), followed by distinctive peaks at 1648 and 1536 cm^{-1} of amide I and amide II (Barth and Zscherp, 2002) (denoted on Fig. 4.4 (A)). A comparison of these peaks to the spectra of chitin is given below. There was little difference between the spectra

of the two duct sections, with only a slight decrease in intensity for the distal duct for peaks at wavenumbers below 3080 cm^{-1}. The quantitative similarity algorithm in the software calculated a very strong similarity of 94.2 % between the two sections of the duct.

4.3.3.2. Comparisons of duct with known chitin-containing spider body parts

Fig. 4.4 (B) shows the averaged spectra acquired from the ducts, cuticle, midgut lining and spigots of the spiders. The only difference (apart from slight differences in intensity of the signal given by the thick and relatively hard cuticle sections compared with the thin lining of soft internal organs) was a slight shift in the amide I peak from 1648 cm^{-1} in the duct to 1619 cm^{-1} in the spider cuticle and to 1626 cm^{-1} in the spigot. The quantitative similarity algorithm in the software calculated an 87.6 % similarity between the duct and the spigot, and 58.2 % similarity between the duct and the cuticle.

FTIR results for the lining of the midgut in the spider gave a different spectrum to the ducts, cuticle and spigot, with a broad peak at 3239 cm^{-1} due to hydration (Libowitzky and Rossman, 1997) despite extensive drying of the sample before spectral acquisition. It also showed an additional peak at 1744 cm^{-1} probably due to C=O stretch indicating lipid (Nzai and Proctor, 1999), and a very low intensity amide II band at 1536 cm^{-1}. Spectra from the duct and the midgut showed 66.3 % similarity. The difference in both hydration and in the carboxyl residue between the spectra of the thoroughly washed and dried midgut and the ducts suggests that the latter structures in the spider are not derived from an internal organ unlike the dermal silk glands present in some insects that are related to the reproductive tract in females (Sutherland et al., 2009).

4.3.3.3. Comparison of silkworm duct, spigot and head plate

FTIR of the silkworm duct showed (Fig. 4.4 (C)) a large band at 3279 cm^{-1} indicative of the OH bond, a shoulder at 3080 cm^{-1}, a fairly strong band at 2923 cm^{-1} and single amide I and II bands at 1639 and 1537 cm^{-1} respectively, a marked similarity to spectra obtained from silkworm pupal skin (Paulino et al., 2006). The spectra from the silkworm head plate and spigot were also very

similar to both each other and the duct. The spectra from untreated ducts showed the peak at 2926 cm^{-1} to be almost absent, reduced intensity at 1536 cm^{-1} and other smaller peaks, and the peak at 3292 cm^{-1} was more intense. The similarity in mean spectra with treated silkworm ducts was calculated to be only 52.41 %, which demonstrates that treatment with detergent had a large effect upon the ducts. The addition spectra from 0.1 % Tween 40 and the untreated duct (not shown) showed a similarity of 48.44 % with the treated ducts. A comparison of this addition spectra with that of the Tween-extracted duct and the untreated duct suggests that effects of Tween treatment are more likely to result from the removal of cellular materials and the luminal contents of the duct rather than the simple addition of the surfactant.

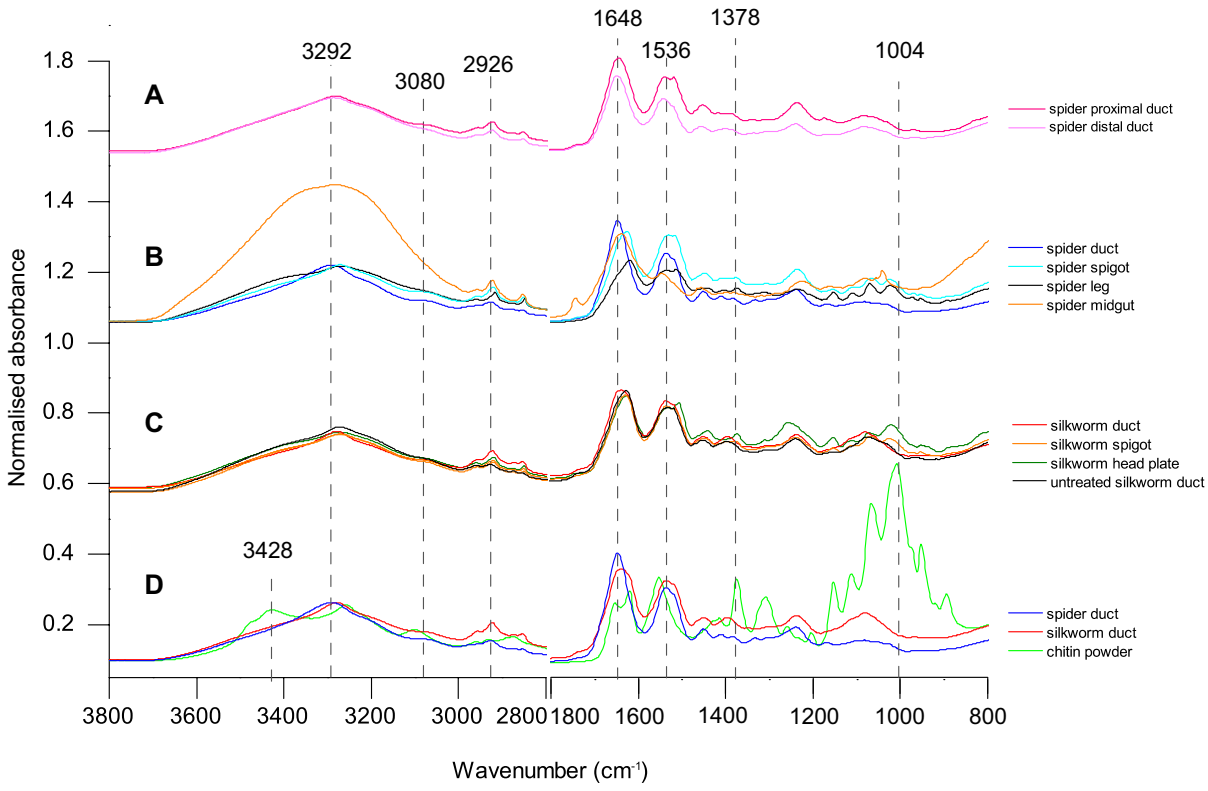


Fig. 4.4. Spectroscopic data with normalised absorbance. (A) Spider proximal and distal ducts, (B) spider duct average, spigot, cuticle and midgut, (C) silkworm duct, spigot, head plate and untreated ducts, (D) spider, silkworm and purified chitin showing great similarity between results of chitin containing parts of both animals. N= 5 replicates of each location, measured from 4 silkworms, 4 spiders

4.3.3.4. Comparison of silkworm and spider ducts with the chitin reference sample

Fig. 4.4 (D) shows the spectra of the spider and silkworm ducts overlaid with the spectra acquired from powdered commercially available chitin. Although the ducts' single large peak at 3292 cm^{-1} were replaced in the purified chitin by double peaks at 3428 and 3258 cm^{-1}, the shoulder peaks at 3101 and 2877 cm^{-1} were common to both samples. The sharp peak at 1648 cm^{-1} in the ducts was split into a doublet with peaks at 1655 and 1621 cm^{-1} in the purified chitin and the peak at 1536 cm^{-1} in the latter had shifted to 1553 cm^{-1}. In addition, there were a number of peaks including at 1378 and 1004 cm^{-1} in the purified chitin that were not visible in the duct spectrum.

Averaged spectra from spider duct and silkworm ducts showed 87.8 % similarity while purified chitin powder gave a calculated similarity of 26.3 % with spider proximal ducts, 25.3 % with spider distal ducts, and 26.8 % with silkworm ducts.

The amide I band distinguishes between α- and β-chitin, with a doublet of peaks at 1660 and 1627 cm^{-1} in α-chitin, β-chitin a single peak identified at 1656 cm^{-1} (Cardenas et al., 2004) or 1650 cm^{-1} (Jang et al., 2004). This difference in amide I peaks at 1648 cm^{-1} is attributed to hydrogen bonding between the main chain and side groups in α-chitin, but includes longer bonds that reach between β-sheets in β-chitin (Tanner et al., 1990). A similar pattern emerges for the part of the spectrum between 3000 and 3500 cm^{-1}, in which α-chitin has a shoulder at 3479 cm^{-1} that is not present in β-chitin, and instead has bands at a lower frequency (Focher et al., 1992). Comparing the peaks from the ducts to those of resilin, the structural protein associated with chitin in some regions of insect cuticle (Weis-Fogh, 1960) showed differences in wavenumbers and shape of both the amide I and amide II bands between 1800 and 1200 cm^{-1} (Tamburro et al., 2010), (Qin et al., 2012) but no data outside this region.

The spider and silkworm ducts exhibited many of the hallmarks of β-chitin including high intensity single amide I and II bands at 1648 and 1536 cm^{-1}. In highly crystalline forms of β-chitin, the OH band around 3485 cm^{-1} is often weaker or absent but the OH band around 3445 cm^{-1} remains (Parker and Rudall, 1957), comparable to the single peak at 3292 cm^{-1} in our samples.

The spectrum below 1500 cm^{-1} showed very little detail in the spider and silkworm ducts in contrast to the commercial α-chitin, confirming that the use of the amide III bands of this region as an indicator is problematic (Jackson and Mantsch, 1995).

The purified chitin powder had a doublet amide I band with peaks at 1655 and 1621 cm^{-1}, a shoulder at 3428 cm^{-1} in addition to a peak at 3258 cm^{-1}. Allowing for the variability in the location of the peaks reported in the literature and the frequency shift in spectra obtained from the diamond ATR (Boulet-Audet et al., 2010) the commercial sample was identified as containing α-chitin and show that the spider and silkworm ducts contain β-chitin. The sharp peaks and reduction in the proportional reduction in intensity of the amide groups and increase of the amine groups indicate that the sample is hydrolysed.

4.4. Discussion

4.4.1. Correlation between chitin histochemistry and FTIR spectroscopy

Both spectroscopic and histochemical tests gave similar results for the spinning ducts of *Nephila edulis* and *Bombyx mori*, and the purified reference sample of chitin from shrimp shells also gave positive reactions for chitin.

As the spectra of the detergent treated spigots and outer cuticle of both animals (composed largely of chitin (Wainwright et al., 1976b)) were so similar to the spectra of the ducts, and corroborated the histochemical tests for chitin, it was concluded that the duct walls of both spider and silkworm contain β-chitin. The calculated similarity between the spectroscopic results of natural ducts and purified chitin powder was less than the 85 % customarily taken to indicate similarity. This disparity may be explained by the vigorous extraction methods used in the 'spowdered samples' purification, which may have broken chemical bonds within the molecule.. The main difference between spectra from purified chitin and the natural samples was the spectrum below 1500 cm^{-1} already mentioned as problematic, and the increased width of the –OH peak at 3400 cm^{-1}, which

may depend on the degree of acetylation in chitin from different sources (Muzzarelli, 1977) rather than a fundamental difference in composition between the ducts and chitin.

4.4.2. Chitin presence in silk duct walls

Although the histochemical test appeared to detect chitin only in the distal end of the spider duct, spectroscopy indicated that both the distal end of the duct and the proximal end which dissolved in the KOH both contain chitin and had 94.2 % similarity. This data suggests that in the proximal part of the spider's duct, the chitin-containing structures are held within a matrix which is broken down by the powerful reagents used in the histochemical test thus releasing the chitinous component(s). This suggests that the distal end of the duct remains intact after digestion either because the matrix is more heavily stabilised or because the chitin nano-components are contiguous rather than encased by a matrix from which they can be released. The difference in matrix between the proximal and distal regions of the duct may relate to subtle differences observed in their FTIR spectra.

4.4.3. Relevance of chitin in silk spinning

Pure chitin behaves as a viscoelastic polymer (Ruiz-Herrera and Martinez-Espinoza, 1999), making it very strong, pliable and flexible , whilst being very insoluble in water due to its high crystallinity (Pillai et al., 2009). However chitin intimately mixed with matrix proteins that are strongly stabilised by hydrophobic interactions and oxidative phenolic tanning can provide very stiff and tough cuticular structures (Vincent, 2012).

The drawdown taper in both spiders and silkworms occurs in the distal part of the duct in spiders (Vollrath and Knight, 1999, Knight and Vollrath, 1999) and silkworms (Asakura et al., 2007a), so therefore within the region of chitin that cannot be extracted with KOH in the spider. It is likely that these regions in both spiders and silkworms must be kept stiff to prevent variations in the internal draw down rate (and ratio) brought about by unwanted extensional and/ or bending forces applied to the duct lining. These occur for example when the spider spins in a strong wind or when a silkworm bends its head from side to side during spinning (Magoshi et al., 1994).

In addition, the start of the draw down taper is just proximal to the clamp in spiders (Knight and Vollrath, 1999, Vollrath and Knight, 1999) and to the silk press in silkworms (Asakura et al., 2007a). These structures may generate extensional forces in this crucial part of the duct when they clamp down on the silk thread (Fu et al., 2009). Thus the arrangement of chitin and heavily stabilised matrix protein in this part of the duct may help to prevent unwanted deformations of this region of the duct whose geometry is thought to be vital for spinning (previous chapter).

4.4.4. Relevance of chitin to origins of silk ducts

Detection of chitin in the cuticle lining of spider and silkworm spinning ducts and the close similarity of the FTIR spectra of these structures with that of exoskeletal structures in the respective species adds credence to the suggestion that silk glands in both glands are dermal in origin.

The silk apparatus consisting of a secretory sac connected to a hollow chitin tube, surrounded by ion transporting epithelium and in turn connected to a spigot in essence resembles the ion transporting (Habel, 1963) and fluid secreting trichogen tormogen complex (Phillips and Vandeberg, 1976) of hollow arthropod spines. The ability of this trichogen tormogen complex to secrete a non-Newtonian, rheopectic fluid would have been advantageous to locomotion while selection for an increase in the mechanosensitivity of such a fluid could eventually have led to the ability to form solid silk threads. Thus the spider's silk secreting apparatus may have evolved from simple hollow chitinous spines (Craig, 1997).

Silkworm ducts are thought to be derived from the labial (salivary) glands, with the silk press a combination of the hypopharynx and prementum (Snodgrass, 1935) subsequently modified for silk production (Yonemura and Sehnal, 2006). As in the spider's clamp valve this silk press may have evolved from the trichogen and tormogen of hollow chitinous spines mounted on the head capsule near the mouth. In the case of the silkworm the non-Newtonian behaviour of the secretion from these spines may have had advantages in sticking together either the food for swallowing or

components of a primitive cocoon made from extraneous natural materials and been the starting point for the development of solid threads.

The observation that many of the cuticular proteins associated with chitin in arthropod cuticle are, like silk fibroins, β-sheet protein (Vincent 2012) supports the trichogen tormogen theory for the origin of arthropod silk glands. Thus silk proteins may have arisen from the ability of certain tormogen cells to secrete silk-like proteins derived from arthropod cuticle into the lumen of the hollow cuticular spines. Further investigations are required to differentiate between the hypotheses presented here and the hypothesis that spiders' silk ducts are lined with chitin due to the developmental constraint of their being attached to the chitinous outer cuticle. These investigations could include using studies of the molecular origins of silk to further the analysis.

4.5. Conclusion

Histochemical and spectroscopic investigations into the silk ducts of both the spider *Nephila edulis* and the silkworm *Bombyx mori* strongly indicated that they both contain β-chitin, despite an evolutionarily distant common ancestor. The results suggested that the arrangement of the chitin in the distal end of the duct may be different from that in the proximal end in the spider but not in the silkworm. In both species the chitin-protein composite lining of the duct may help to resist unwanted deformations of the duct wall and highly mechanosensitive silk dope.

In both species, the close spectroscopic resemblance of the cuticle lining of the silk duct with exoskeletal structures, and the presence of β-chitin in both suggested that arthropod silk duct and gland may have evolved from the trichogen and tormogen of a hollow cuticular spine capable of secreting a non-Newtonian fluid derived from a cuticular protein.

The presence of chitin in silk spinning organisms from separate lineages may indicate a subtlety in mechanical and physical properties of the duct that have been hitherto overlooked but are essential for spinning fibres with silk-like properties. The absence of these physical and chemical

properties in previous synthetic spinning attempts may explain their relative lack of success to date.

Chapter 5. Internal Microstructure and function of the silk duct

5.1. Introduction

5.1.1. Context

Little is known about the structure of spinning ducts (see section 1.2. Natural silk spinning). This chapter addresses the question of whether and how the duct wall itself has become specialized to produce silk fibres. The silk duct is likely to be optimised to perform its role in spinning as efficiently as possible within biological constraints: in particular, the opposing requirements of structural rigidity and permeability.

5.1.2. Structural rigidity

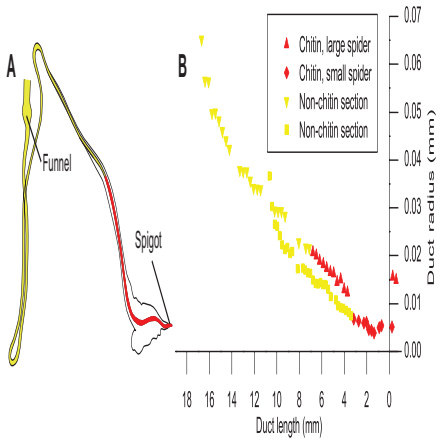


Fig. 5.1 (A) Spinning duct dissected from a gravid adult *Nephila edulis* spider.

It is important for the duct wall to have structural rigidity because of the extreme sensitivity to shearing forces of silk dope (Holland et al., 2012c), in particular because the duct has two sharp turns along its length, as illustrated in Fig. 5.1. If, for example during rapelling, the duct was to become blocked by buckling, the premature solidification of dope due to increased shear stress would permanently prevent silk fibre production. Silk dope is so sensitive to heightened stress fields that any buckling that occurs and therefore prematurely solidifies silk into a blockage within the duct would have disastrous consequences for the spider. This is particularly likely to

happen when silk is being drawn at great speed (e.g. when a spider is rappelling) and the drawdown has moved some distance proximally up the duct. There is always some silk in a major ampullate gland even during moulting (Townley et al., 1993) as evidenced by spiders hanging by a fibre during moulting.

However it seems that the duct has a good resistance to buckling of this type, as evidenced from the fairly tight radius turn that the duct can withstand when pulled between two pairs of fine forceps, as depicted in Fig. 5.2.

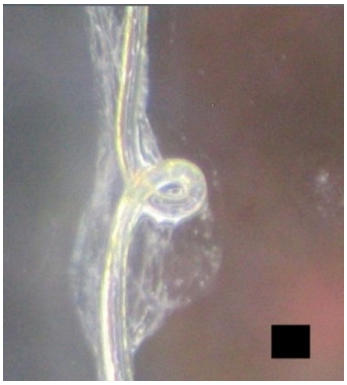


Fig. 5.2 Duct deformed by stretching between two pairs of fine forceps. Scale bar length= 100 µm

5.1.3. Diffusion across the duct

Chemicals need to be transported across the duct wall along its length to permit the transformation of silk dope into silk. Water, sodium, chlorine, potassium, phosphorus and sulphur ions , transported by osmosis or active transport, control the folding of the proteins required to produce silk fibres (Knight and Vollrath, 2001). Both osmosis and active transport would require that the duct wall be thin.

5.1.4. Literature relevant to the duct in relation to structure and diffusion

To date no studies have directly addressed the question of how the duct wall is adapted to balance the structural and transport requirements for silk production, although there are some descriptions of the duct lining. These brief observations have included a banding pattern visible in transmission electron micrographs of the *Araneus sericatus* (Bell and Peakall, 1969), in which

they described as “tubular or vesiculate structures”; a single image of a section through the duct wall of *Araneus cornutus* (Foelix, 1971b), in which the apical wall is described as ‘acellular’; a study of *Araneus diadematus* (Kovoor and Zylberberg, 1972), in which the features of the duct wall were described as having a spiral arrangement; and the most detailed observations, though still from a single image, in which the structure of the cuticle lining the duct of *Nephila edulis* was said to resemble a sophisticated version of a manmade hollow fibre dialysis membrane (Vollrath and Knight, 1999). Vollrath and Knight’s studies also suggested that some features of the duct wall that might provide structural rigidity extended some way distally along the length the duct (Vollrath and Knight, 1999), (Vollrath and Knight, 2001), but the material of which these structures comprised was unknown.

5.1.5. Specific aims of this chapter

This chapter describes an investigation of the ultrastructure of the *Nephila edulis* ampullate duct wall, with a view to discovering to what extent it is adapted to maximise resistance to compression while permitting adequate diffusion of chemicals. I used three different approaches to shed light on the question.

1. Unpublished and unanalysed transmission electron microscopy (TEM) and cryogenic scanning electron microscopy (cryoSEM) images of the duct wall, kindly made available by Dr David Knight, were examined in detail to provide a comprehensive view of the internal physical structure of the duct wall.
2. Light microscopy was used to discover whether the structural features observed in Knight’s electron micrographs might be composed of chitin, and might therefore be the source of the chitin found in the duct wall which was described in Chapter 4.
3. Finite element analysis was used to model the resistance to compression of a chitinous duct wall at a range of wall thicknesses (and hence permeabilities). This was done by modelling stress in the walls of incremental thicknesses, to seek the optimal balance of strength and permeability.

4. Finite element analysis was used to model stress in the wall of the optimum thickness in the above section, with and without ribs to determine the detrimental effect of ribs upon mechanical strength.

The results of the modelling were compared to data from the real duct to test whether the two parameters of resistance to compression and permeability were adequate to describe the situation observed in the real duct and hence to what extent the real duct achieves optimum permeability for a given thickness.

5.2. Biological imaging: Methods section

5.2.1. Ultrastructure of the cuticle lining of the duct

Dr David Knight used conventional TEM, freeze fracture TEM and cryoSEM to image the duct wall sections of the spiders at high resolution. Comparison of images from the three different approaches allowed me to ensure that any structures I considered were not an artefact of a particular preparation method. The methods described in sections 5.2.1.1-5.2.1.4 are published (Knight and Vollrath, 1999) and further detail here was communicated by Dr Knight.

5.2.1.1. Specimen preparation

Nephila edulis specimens were reared in the same way as detailed in section 2.1.1.1 of the methods chapter.

Adult female *N. edulis* with abdomens 14-18 mm in length were fixed by gentle perfusion for 30 minutes at 4 ° C and immersion (3x 12 h) in a modified Karnovsky fixative (Schartau and Leidescher, 1983) immediately after at least 4m of silk had been drawn artificially at ca. 100 mm s^{-1}. The fixative contained final concentrations of 2 % glutaraldehyde, 2 % formaldehyde, 0.1 M sodium cacodylate, 0.01 M calcium chloride and 0.35 M sodium chloride and was adjusted to pH 7.4 with hydrochloric acid.

5.2.1.2. Conventional TEM

After post-fixing in cacodylate buffered osmium tetroxide solution and embedding in Epon, sections were cut longitudinally through the wall of the duct with a diamond knife and stained with uranyl acetate and lead citrate in order to visualize a cross section of the duct. Ultrathin sections were imaged using a Philips 300 TEM operating at 80 kV.

5.2.1.3. Freeze fracture

Specimens were fixed in the same modified Karnovsky fixative as above. They were then frozen using liquid nitrogen and freeze fractured using a Balzers freeze fracture device with a rotary cold stage. The fracture surface was shadowed obliquely with platinum and directly with carbon, and replicas were separated after digestion of tissue with sodium hypochlorite solution and mounted from below on uncoated hydrophilic grids for TEM (see standard procedure (Severs, 2007) for producing replicas). Ultrathin sections were imaged using a Philips 300 TEM operating at 80 kV.

5.2.1.4. CryoSEM

Unfixed glands were rapidly removed from fresh spiders, quenched in slushed liquid nitrogen and after fracturing, etching and lightly coating with gold, transferred via an Oxford cryotransfer chamber to the cold stage of a Camscan SEM operated at 10 kV.

5.2.2. Light microscopy of the cuticle lining of the duct

The histochemical chitin test for chitin as described elsewhere (Ravindranath and Ravindranath, 1975) was performed on four ducts from two spiders were digested in a silicon grease compressorium to protect them from mechanical damage. The parts of the duct remaining after this procedure which is thought to remove all non-chitinous tissue components were observed and micrographed using a x100 oil immersion objective on a modified Prior MP 3500 microscope (Oxford Cryosystems) and a 576x768 pixel monochrome digital camera.

5.3. Biological imaging: Results

5.3.1. Ultrastructure of the cuticle lining of the duct

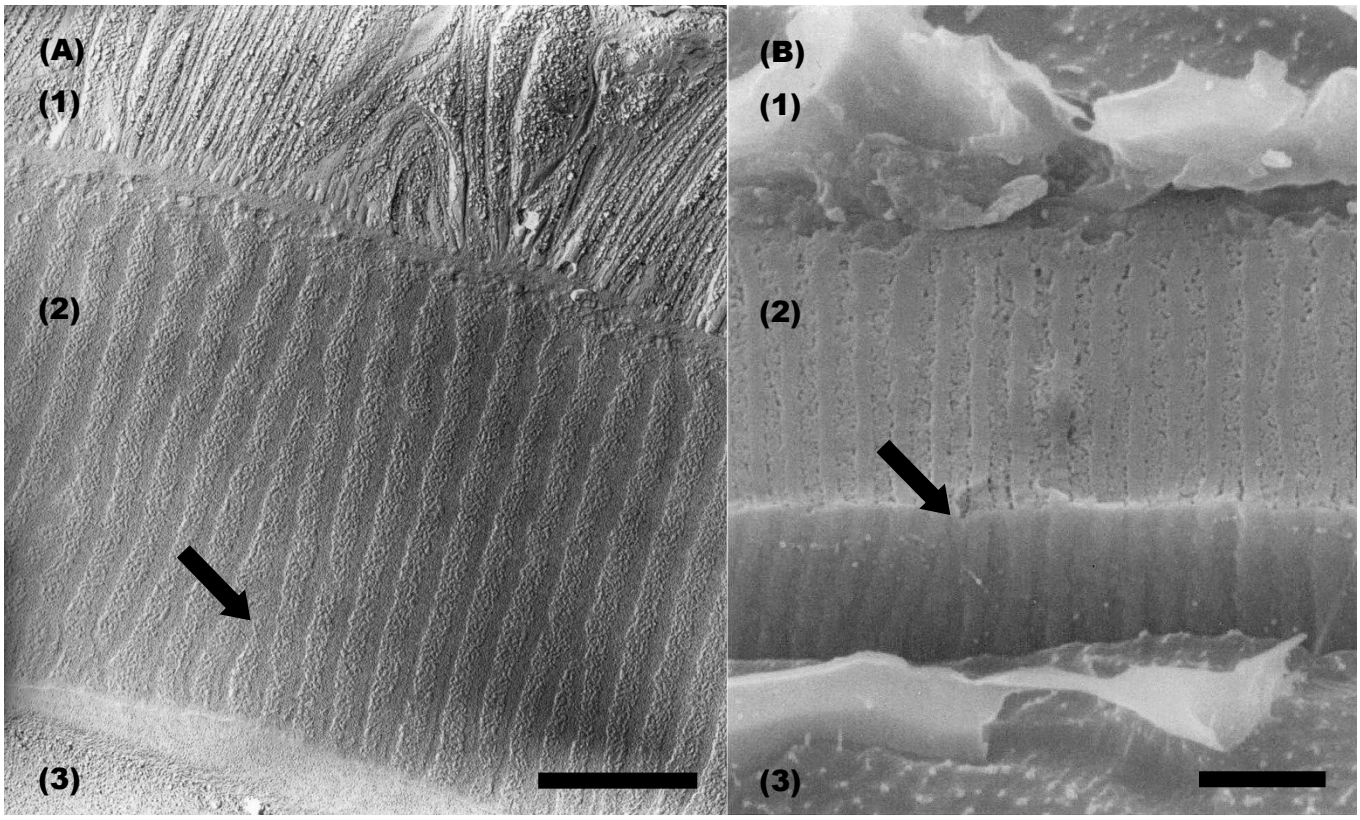


Fig. 5.3 Longitudinal fractures of the proximal end of the third limb of the duct. A. TEM of freeze fractured and etched replica; scale bar 2 µm. Fig. 5.3B CryoSEM of a freeze fractured and slightly etched preparation; scale bar 2 µm. In both micrographs (1) The apical part of the columnar epithelial cells surrounding the duct cuticle, (2) cuticle lining and (3) luminal contents (silk dope) In Fig. 5.3 B the contents of the lumen have pulled away from the luminal surface during preparation to reveal the luminal surface of the cuticle (arrow).The arrows in Fig. 5.3 A and B show respectively transverse and longitudinal disclinations in the banding pattern. Original photomicrographs courtesy of David Knight and Fritz Vollrath.

Micrographs from both freeze-etch replicas and fractured and etched cryoSEM preparations of the duct are shown in Fig. 5.3 (A) and (B). Fig. 5.4 shows a TEM of an ultrathin longitudinal section of aldehyde-fixed Epon embedded material taken from the same region. Both images show the longitudinally sectioned cuticle lining of the duct, which can be divided into three distinct layers.

The top of the images (layer 1) shows the apical component of the epithelial layer. This is joined via a thin electron-dense membrane to layer 2, the cuticle lining. Layer 3 is the contents of the lumen.

The luminal surface of the cuticle (layer 3) is completely covered by a thin inner lamina (approximately 70-90 nm thick) of moderately electron dense amorphous material. This is in turn lined on its luminal face by a thin bilayer resembling a cell membrane but with a somewhat greater thickness (about 30 nm) thick consisting of two electron dense layers separated by an electron lucent layer.

Longitudinal sagittal sections of the duct cuticle lining (layer 2) show a remarkable centrosymmetrical lamellar pattern. This pattern is built up from two alternating bands of approximately equal width I termed P- and Q- bands (named to avoid confusion with A- and B-zones of silk secretion), giving an axial period of 400 nm. In an ultrathin longitudinal ultrathin section (Fig. 5.4), the P-bands are relatively electron dense compared to the very weakly staining Q-bands and appear to contain a high density of tortuous tubules with a somewhat variable diameter of about 240 to 450 nm also seen in these bands in Fig. 5.3 (A) and (B). The Q-bands in ultrathin sections of all but distal part of the distal limb of the S-shaped duct are very weakly staining and appear to be constructed from of a finely granular amorphous material (Fig. 5.4). In contrast, in the cuticle of the distal part of the duct the peripheral parts (those furthest away from the lumen) of the Q-bands appears to be constructed from an alternation of thin (approximately 40 nm), electron dense laminae separated by thin (200 nm) virtually unstained laminae. The laminae appear to extend radially throughout the thickness of the Q- band and to be roughly aligned along the long axis of the duct.

In both the distal and proximal part of the duct the adjacent P- and Q- bands superficially resemble a series of separate discs stacked along the length of the duct. This model is a simplification as close inspection shows that the material of the discs frequently branches in both longitudinal and transverse planes in a similar way to the disclinations seen in liquid crystals (See arrows in Fig. 5.3 (A) and (B)). Although Kovoor and Zylberberg (Kovoor and Zylberberg, 1972) suggested that the banding pattern spirals around the duct, the images display no evidence for this.

The Q-band in etched preparations (Fig. 5.3 A and Fig. 5.4) show a relatively smooth fracture surface compared with that of the densely packed tubules of the P-band. The fracture surface of the Q-band is raised above that of the P-band suggesting that the former shrinks less than the latter band during etching and is therefore likely to have a lower water content than the P-band. This is supported by the observation that the P-band contains a large number of tubules likely to contain water in life.

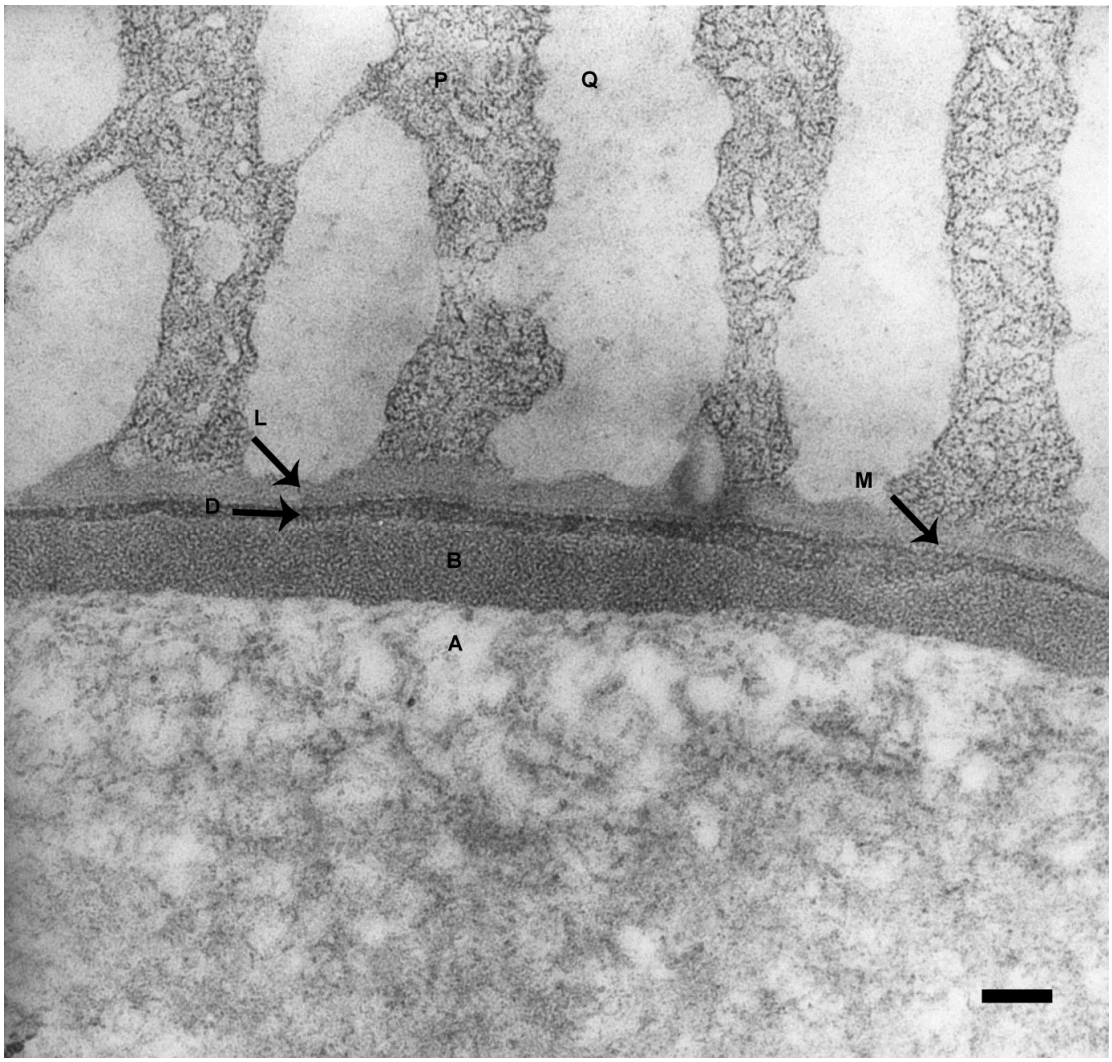


Fig. 5.4 TEM conventional ultrathin section of material fixed in glutaraldehyde/ formaldehyde mixture and embedded in Epon showing longitudinally sectioned or fractured cuticle lining of the proximal end of the third limb of the duct. The P-bands contain a high density of nanopores while the Q-bands show a smooth fracture surface. The apical P- and Q-bands are coated by an inner lamina, separated the inside of the duct by a bilayered membrane. Inside the duct a gland cell lines the bilayered membrane. At the bottom of the image, the B zone and A zone secretions of the ampulla can be seen in the duct. Scale bar 100 nm. Original photomicrograph courtesy of David Knight and Fritz Vollrath.

Proximal from the valve (also known as the clamp), the inner lamina covering the luminal surface (layer 3) of the cuticle is very thin (Fig. 5.4), compared with the much thicker inner lamina seen distal to the valve (Fig. 5.5). Its structure also differs in the two regions. In contrast to the amorphous appearance and uniform density in the inner lamina seen before the valve, that after the valve appears to be constructed from dense material with a finely granular or micellar texture together with occasional much larger dense spherical droplets. Moreover, while the luminal surface of the duct before the valve appears remarkably smooth (Fig. 5.4), the surface after the valve shows numerous fine longitudinal ridges with a separation of approximately 200 nm (Fig. 5.5).

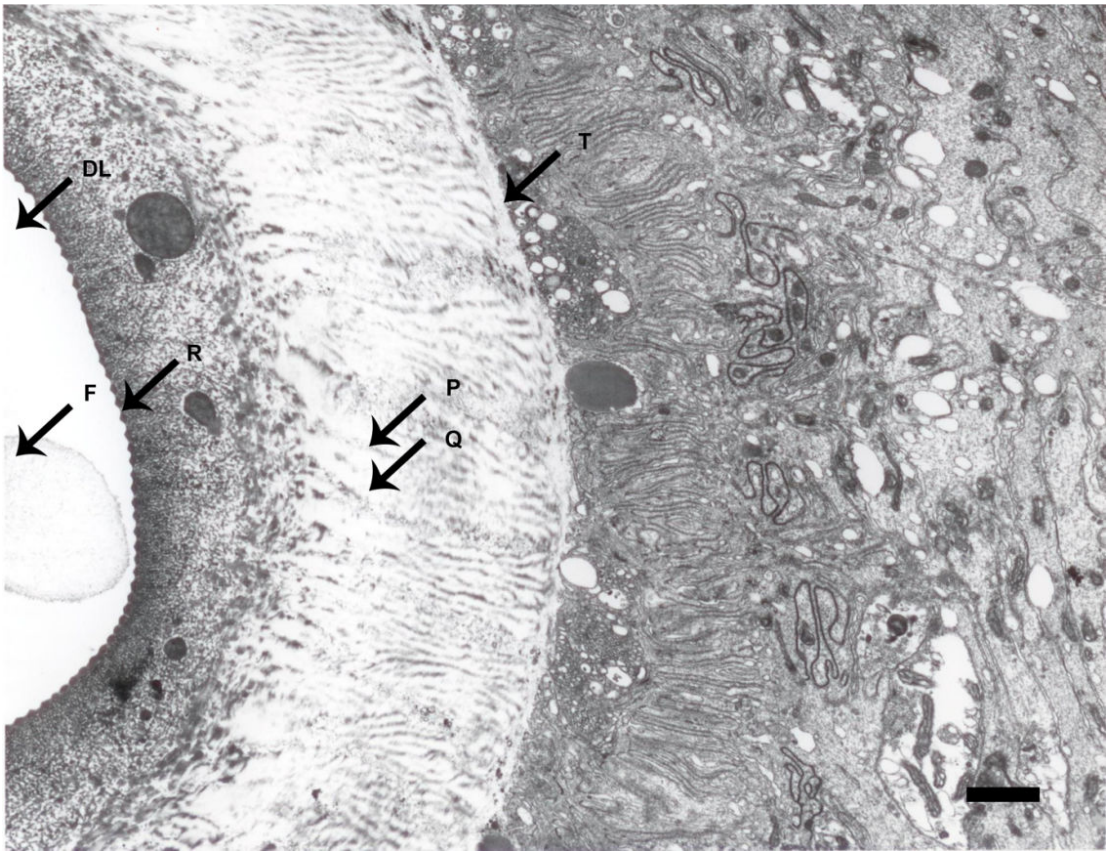


Fig. 5.5 A TEM of ultrathin of Epon section of the of the third limb distal to the valve (clamp) containing a nascent fibril (F) in the duct lumen (DL). The P- (P) and Q-bands (Q) are is lined with a ridged inner surface (R), encircled by a darker layer homologous to the inner lamina in Fig. 5.4, surrounded by a lighter zone of longitudinally orientated lamellae or fibrils. Where the outer surface of the duct lining joins the apical microvilli of the epithelial cells there is a thin amorphous non-cellular layer of slight electron density (T) surrounding the P- and Q-bands. Scale bar 1 µm. Original photomicrograph courtesy of David Knight and Fritz Vollrath.

5.3.2. Light microscopy of the cuticle lining of the duct after chitin test

The structure of the duct wall was examined after the chitin test which digests and solubilises material which is not chitinous. The presence of P- and Q-bands in the material remaining after the test would therefore indicated that the bands themselves were chitinous.

The light micrograph Fig. 5.6 (A) clearly shows the P- and Q-bands encircling the duct with (B) showing a transverse view of an undigested whole mount. This is confirmed by the fairly homogeneous orientation of the polarization Fig. 5.6 (B) in the same area of the duct image, as would be expected by light polarized by lamellar repeating structures, in comparison with the surrounding unorientated material. In contrast to the bands, which are clearly visible, the apical cellular layer surrounding the bands visible in layer 1 in Fig. 5.3 (A) and (B) is not apparent which means the cellular layer does not contain chitin. From these images and those of the other ducts it can be concluded that at least one of the P- and Q- bands contains chitin, though differentiation between the two is not possible at this magnification.

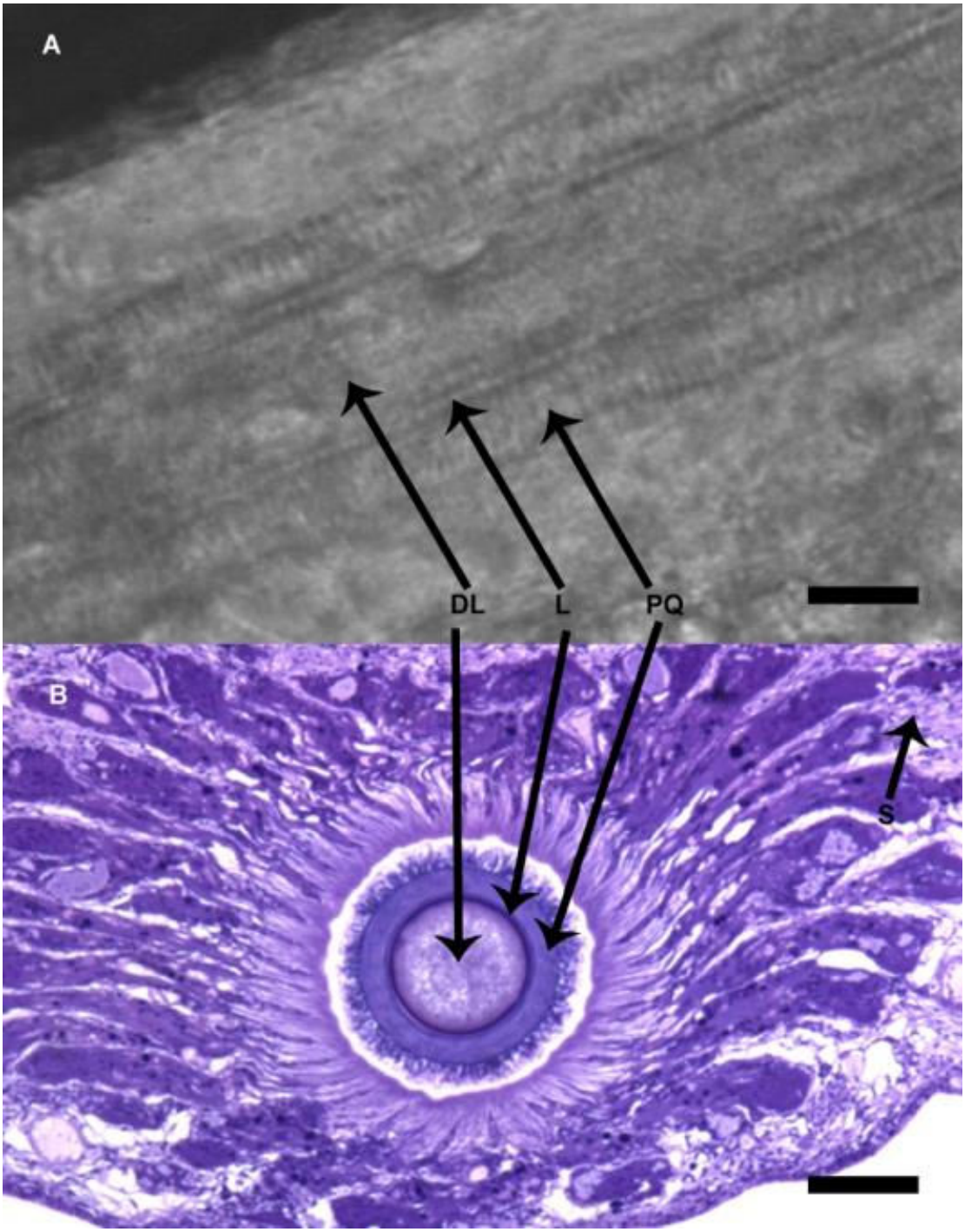


Fig. 5.6 Light micrographs of the final limb of the spinning duct about 5 mm proximal to the valve. (A) Longitudinal whole mount of the duct after digestion with KOH, treatment with acid and staining with iodine. Scale bar: 15 µm. (B) Transverse section of a 1 µm survey section stained with toluidine blue, original photomicrograph courtesy of David Knight and Fritz Vollrath. Scale bar: 15 µm. Duct lumen (DL); Inner lamina (L); Position of the P- and Q-bands (PQ); Brush border of the tall columnar epithelium (E) underlying the cuticle lining of the duct; Sheath containing droplets that stain with basic fuchsine (S). Scale bar: 15 µm.

5.4. FEA: Methods section

5.4.1. Introduction to FEA use

The heterogeneous nature of the cylindrical duct wall (Vollrath and Knight, 1999) prevented the application of a simple analytical method to model the wall's yield stress at different thicknesses.

FEA is a numerical computer modelling technique that provides an approximate answer when analytical methods are unable to provide a solution to a particular problem (Krishnamoorthy, 1994) and was therefore used to model yield stress of the duct wall.

FEA works by first modelling the shape that is wished to be investigated. The shape is then split into a mesh of elements of a small but finite size, each of a shape that may be determined. Material properties are assigned to the model, and a load is applied to a selected part. The external interactions are specified, often as restraints, and the linear equations for each element are then solved. Because each element is very small its linear equation is relatively simple to compute. The result is then passed on as an input to the surrounding elements, and their equations can then be calculated in turn.

FEA has advantages that arbitrary shapes can be modelled which analytical solutions cannot or will not solve, and for linear problems accurate solutions can calculated within a reasonable amount of time (Akin, 2010).

5.4.2. Shape and parameters assumed by FEA

To build a model of the duct to test by finite element analysis (FEA), 37 micron longitudinal sections of the duct were modelled in 3D in the computer aided design (CAD) software package SolidWorks 2008 SP3 (Dassault Systèmes) from measurements taken from the electron photomicrographs using ImageJ (NIH) and listed in Table 5.1. For each dimension a minimum of ten measurements were taken from each photomicrograph from a minimum of two photomicrographs except the lumen radius which used the mean from Chapter 3, 4 mm proximal to the valve.

Table 5.1 Measurements used for FEA models taken from electron photomicrographs, definitions as in Fig. 5.8 (A)

	Measurement	Mean length (μm)	Standard deviation
a	Bilayer thickness	0.10	0.014
b	Band spacing	0.416	0.154
c	Band width (proximal)	0.186	0.079
d	Band width (distal)	0.235	0.084
e	Height	4.120	0.098
f	Lumen radius	14.848	-

The FEA model assumed that the duct was a cylinder representing the main wall of the duct, with the ribbed banding pattern described in the results section.

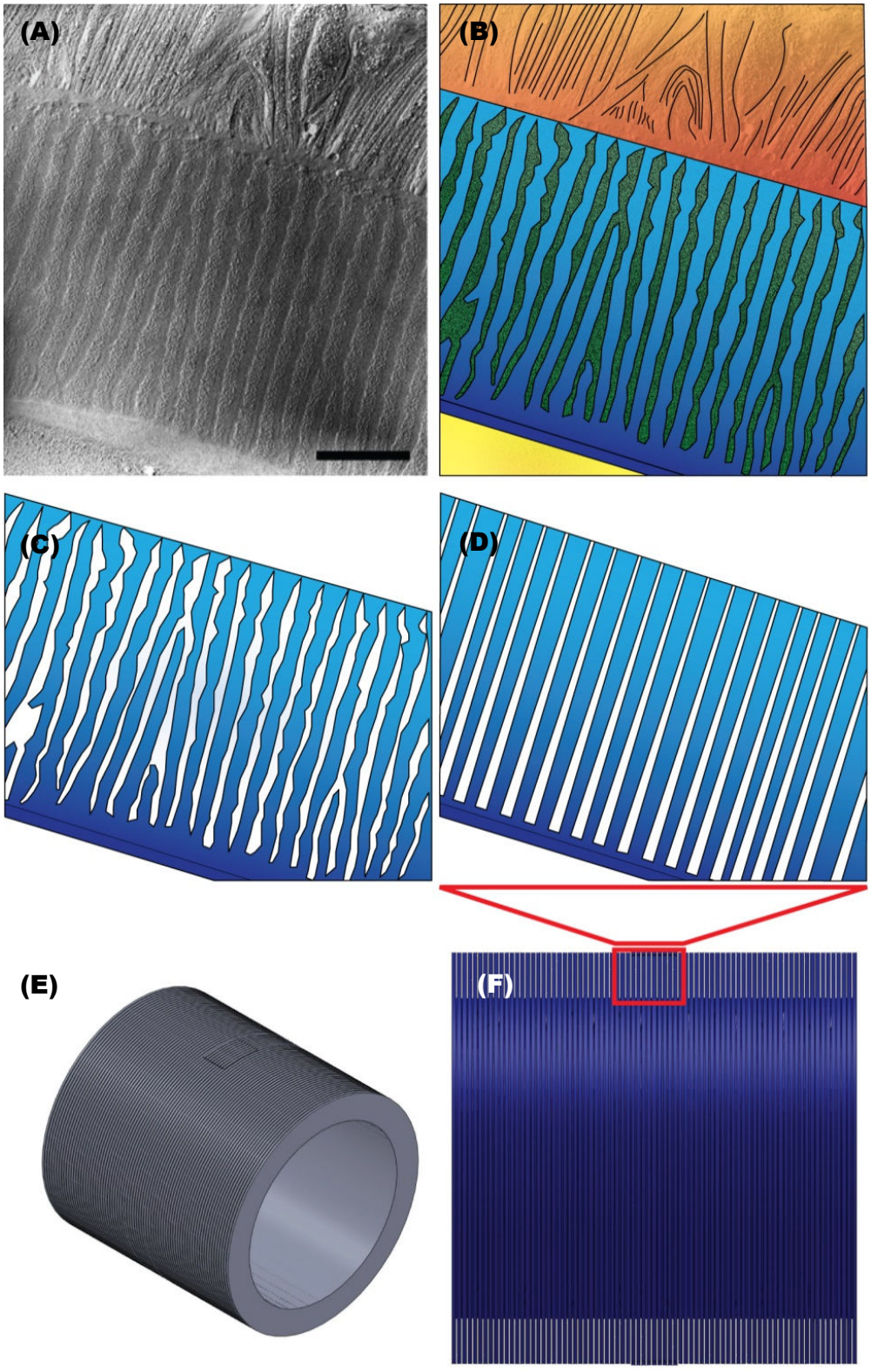


Fig. 5.7 Development of FEA model from observations. (A) TEM of ultra-thin section through spider duct wall reproduced from Fig. 5.3, showing from top to bottom: apical cell lining, chitin structure of interest, silk in lumen of duct. (B) Image vectorized, with the blue and green areas highlighting the chitin structure. (C) Apart from the electron-dense solid chitin section, all other material removed. (D) Structure is simplified to regular shapes. (E) SolidWorks FEA model in isometric projection. (F) Structure from (D) extended and revolved around to form cylinder with discs.

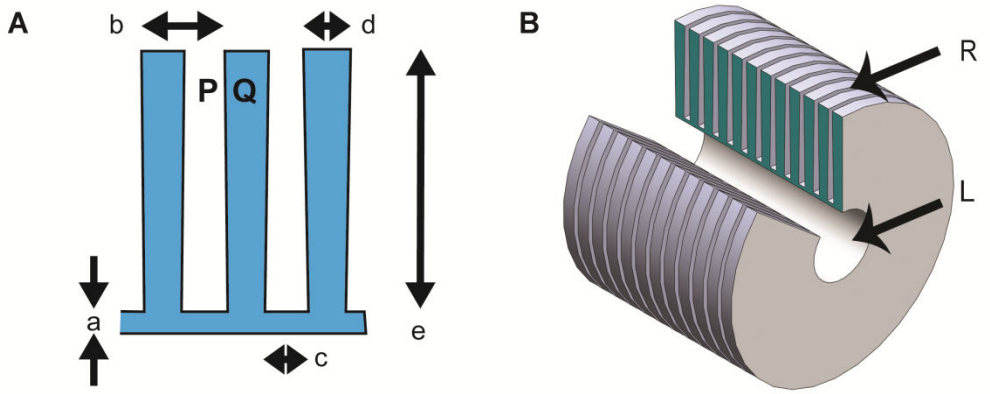
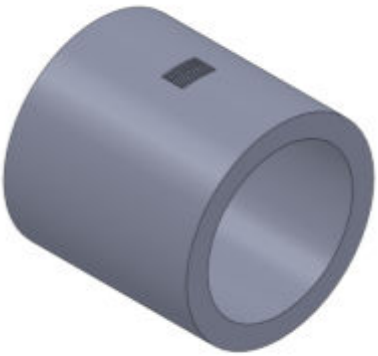


Fig. 5.8 (A) A longitudinal section of part of the simulated wall of the spider's duct with P- and Q-bands marked. The height e) of the rings was varied from 2 to 8 µm to simulate observed variations in thickness of the wall from region to region. (B) The 3D model of silk duct (not to scale) was formed by extending the sagittal longitudinal cross section of the wall (parameter a) in (A) to 37 µm and rolling it into a cylindrical tube with rings (R) pointing outwards, (L) duct lumen. The FEA model assumed that the duct was a cylinder constructed as above from the banding pattern described in the ultrastructural results section.

The duct was modelled as a shell in the form of a hollow tube with radial rings. Mean wall thickness (dimension (e) in Table 5.1) was varied between models from 2 µm to 8 µm in 0.5 µm increments.

In order to test the resistance of the duct without discs, sections of tube the same length as above were tested with the same force as above, with the following wall types displayed in Table 5.2: (a) no discs at all, (b) discs 4.31 µm tall, and (c) a solid wall 4.31 µm tall.

Table 5.2 Models used to test presence of discs upon wall strength

	(a) Thin uniform wall	(b) Stacked discs	(c) Thick uniform wall
Isometric view of model			
Wall thickness	0.10 µm	4.31 µm	4.31 µm

5.4.3. Materials assumed for FEA

Chitin-protein materials have reported elastic modulus values from 60 MPa to 20 GPa depending on the specific material structure and its state of hydration (Vincent and Wegst, 2004), so the material properties used for the models were those of chitin-protein composites most appropriate for the application from the literature and then checked for internal consistency as shown in Table 5.3.

Table 5.3 Material properties used in the finite element analysis

Material property	Value	Source
Elastic modulus	6.1E9 N m^{-2}	(Wainwright et al., 1976a)
Poisson's ratio	0.25	(Kesel et al., 1998)
Mass density	1425 N m^{-2}	(Carlstrom, 1957)
Yield strength	1.7E7 N m^{-2}	(Hepburn and Ball, 1973)

5.4.4. Test constraints

The most suitable method to model forces that would initiate kinking was to use compression from the outside, as modelling an actual bend of the tube would not be possible using the small displacements that can be calculated using FEA. Therefore the test of yield stress was performed by simulating duct compression by indentation at a given point on the wall with a known force.

To calculate approximate stresses in the duct wall, the model was exported to the COSMOSWorks FEA software within SolidWorks. Duct compression was simulated using a standard linear elastic material model as this is a simple model which is likely to give a result with less error than a more complicated model would for complicated geometry.

A simulated dorso- ventral compression with a force of 10 μN (chosen to induce very small strain without damage) was applied radially to a square area of 22.8 μm^2 on the central upper surface of the duct. All degrees of freedom of the indenter were constrained except the vertical

displacement. An identical area at the bottom of the duct was constrained in all degrees of freedom, simulating a rigid fixed support.

The program was directed three times to create a high quality mesh which contained between 20000 and 75000 elements, and the maximum stress value in the duct for each simulation was recorded. The location of this maximum stress shown on the model duct wall for each run was noted, and the average and standard deviation of the stress for each Q-band was calculated in Excel (Microsoft).

5.5. FEA: Results

The maximum von Mises stress was calculated by the FEA software for a structure with material properties corresponding to chitin, and the location of this maximum stress shown on the model duct wall. In each of the models the predicted maximum stress occurred on the outer surface of the duct wall in the region of the indenter.

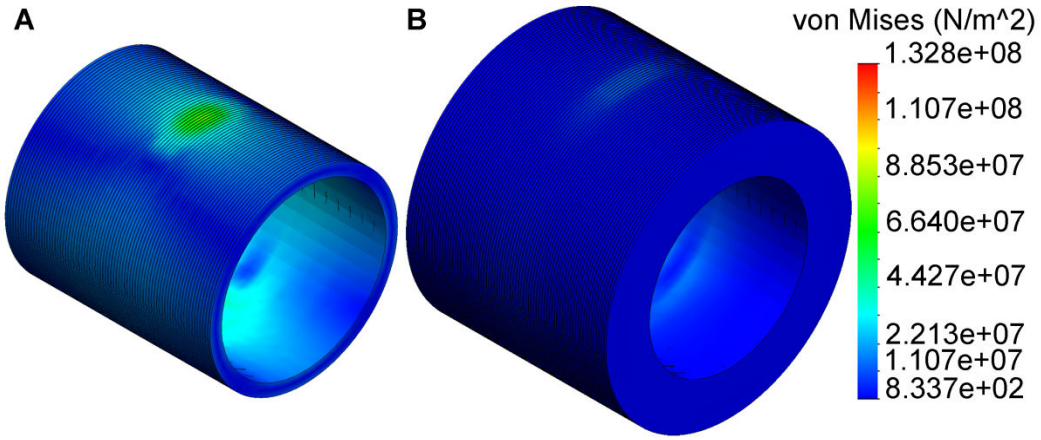


Fig. 5.9 Result of FEA on two ducts with different rib heights. (A) Duct rib height: 2 µm, (B) duct rib height: 8 µm. Colours indicate the von Mises stress for each point in the structure, ranging dark blue with a value of 0.3e2 to red with a value of 1.3e8.

Fig. 5.10 shows the maximum von Mises stress in the walls found in each of the modelled ducts. The graph shows that the maximum stress in the duct is highest in the duct with Q-bands 2 µm tall, and decreases with increasing height of Q-bands, albeit in a non-linear fashion. The stress drops rapidly from approximately 120 MPa until the duct model is a thickness of 4 µm and

thereafter is maintained at approximately 50 MPa through increasing wall thickness. The error bars indicate a small degree of error for each data point, with some increase in error for the ducts with Q-bands thicker than 7 μm.

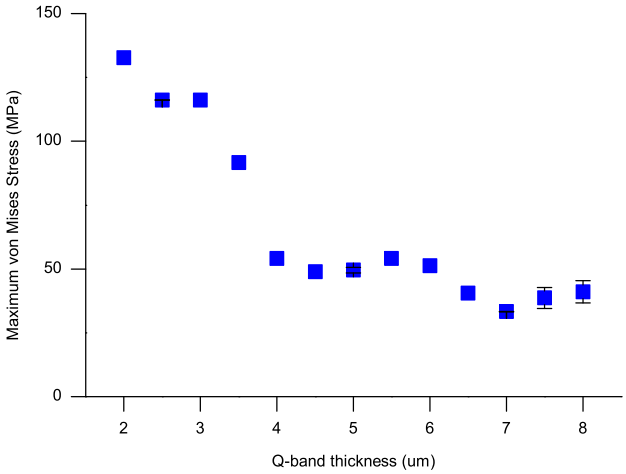
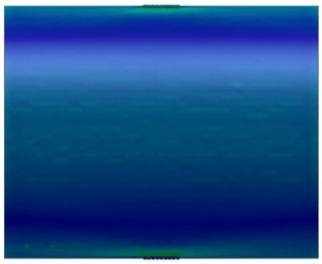
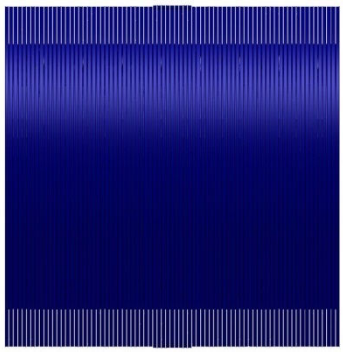
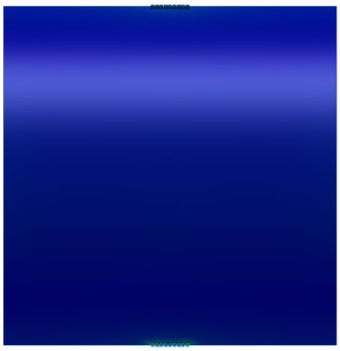


Fig. 5.10 Maximum stress in each duct wall as a function of wall thickness. Error bars show standard deviation from the mean. N= 3 runs per data point, 13 data points.

The predicted maximum stresses at failure for the three model ducts used to predict the influence of the ducts upon wall properties is shown in Table 5.4. The duct with stacked discs (b) had a predicted failure stress two orders of magnitude higher than the thin walled duct (a). Replacing the porous P- bands between the structural Q -bands with solid material to form a thick uniform wall (c) produced a small reduction in the stress to failure compared with the stacked disc model.

Table 5.4 Images of duct portion models and FEA stress plots where red corresponds to a maximum stress of 16.6 mN and blue to a minimum stress of 0.0001 mN.

	(a) Thin uniform wall	(b) Stacked discs	(c) Thick uniform wall
Side view of result			
Max stress (MPa)	0.01763	0.0001590	0.0001087

5.6. Discussion

5.6.1. Ultrastructure and material of the cuticle lining of the duct

The banding pattern previously observed at low resolution by other researchers (Bell and Peakall, 1969), (Foelix, 1971b), (Kovoor and Zylberberg, 1972), was imaged here at high resolution with different techniques at different locations indicating that the cuticle lining of the duct is not spiral but appears to be constructed from an alternation of porous and non-porous discs connected together in places by- like similar to the representation in Fig. 5.11.

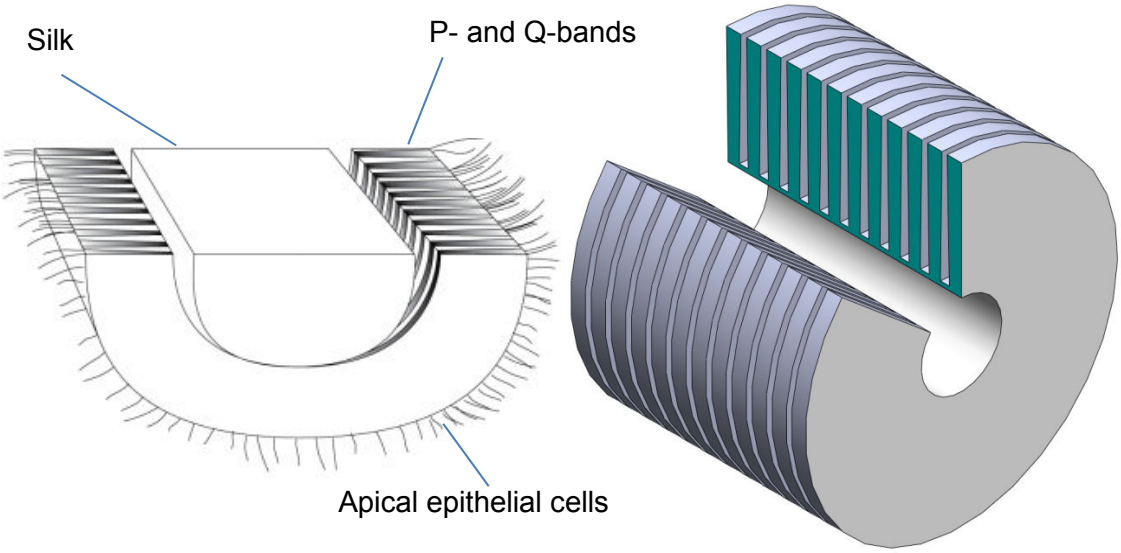


Fig. 5.11 Representation of discs forming the duct wall, with silk feedstock within lumen. Thin external lines represent the apical epithelial cells lining the duct.

The lamellar banding pattern is visible in images of the duct both before and after acetylation and solubilisation of the duct with acid, which suggests that at least one of the bands contains chitin. In Chapter 4 no discs apart from the intact duct were detected in the liquid after the chitin test, which can be explained by the very small feature size of the discs shown here.

The lamellar banding pattern and the existence of the disclinations may indicate that the chitin-containing cuticle lining has a monodomain, lamellar liquid crystalline construction. This is intriguing because chitin in arthropod cuticle and in many other locations shows a cholesteric rather than lamellar construction (Bouligand and Giraud-Guille, 1985). However, numerous lamellar biological chitin-protein composite structures are known (Ghiradella, 2010). These have axial periodicities in the range of that of the P- Q- banding pattern extending down to that seen in the lamellar substructure structures seen within the Q- band in the distal part of the duct cuticle and in the surface ridges seen in the cuticle lining in this region. If the silk gland duct lining does indeed arise from a lamellar liquid crystalline phase, the molecular director of the mesogens from which it is constructed would lie rather accurately parallel to the long axis of the duct.

The high density of nanopores in the P-bands shown in Fig. 5.4 and the thin layer covering the inner surface of both P- and Q-bands are likely to be important for the rapid and selective permeability of the cuticle lining. Incidentally, the gel-filled sheath (part of which is seen in Fig. 5.6 (B)) encasing the three limbs of the duct (Knight and Vollrath, 1999) may also play a part in both ion and water transport and selective permeability.

This study confirms that the structure of the cuticle lining along a large proportion of the final limb of the duct resembles a sophisticated version of a manmade hollow fibre dialysis membrane (Vollrath and Knight, 1999). It appears to consist of nanoporous discs alternating with non-porous structural discs, the whole structure lined at the luminal surface by a thin membrane. A remarkably similar banded arrangement is seen in the cuticle lining of the silk duct in the silkworms *Bombyx mori* (Sehnal and Akai, 1990) and *Diatraea saccharalis* (Victoriano and Gregorio, 2002). This arrangement is likely to provide the ducts of spiders and silkworms with a combination of mechanical integrity together with high and selective permeability to water, ions and possibly other low molecular weight solutes. The structure is also likely to provide resistance to kinking in the two rather tight hairpin bends of its S-shaped construction and the many tight turns of the silkworm duct (in the manner of a ribbed vacuum cleaner hose). The mechanical integrity of this construction may enable compact storage of the long duct required for conditioning and spinning the silk dope. Although not possible here due to time available, it may prove rewarding to study the structures the make up the duct walls at further locations along the length of the duct.

5.6.2. Finite element analysis

The theoretical maximum stress sustained within the wall drops rapidly between a wall thickness of three and four microns thick, which suggests that to minimise the risk of wall rupture the wall should be thicker than this. Measurements of the duct wall thickness from images Fig. 5.3 and Fig. 5.4 suggests that the actual wall thickness in life lies between 4.0 μm and 4.3 μm, a value

remarkably close to the minimum wall thickness possible as predicted by the model to maintain a low stress in the duct.

The location of maximum stress as calculated by FEA was situated approximately midway between two ends of the duct models, indicating that the stress was derived from the constriction force from the indenter rather than from an interaction with the boundaries with the duct model. That the location of this maximum stress value at the middle of the length modelled is unlikely to change with a longer duct modelled, suggests that the length of duct modelled is sufficient to avoid errors arising from conditions at the boundaries of the model.

The increase in size of error bars at higher Q-band thickness is likely to be due to the discs interfering with each other due to the larger diameter of the duct, but even the largest error bars do not alter the conclusions of this part of the study.

Modelling of the duct wall with and without ribs entirely showed that with just a thin walled tube, the duct stress was two orders of magnitude higher than in a duct with ribs of a height found in nature. Modelling the duct as a solid wall with a thickness comparable to the height of the natural ribs showed only a small decrease in stress from the model with ribs present. This small increase in stress is likely to be a trade-off with the 42 times shorter diffusion length to the apical wall layer that the ribs permit.

5.6.2.1. Problems with FEA modelling

As with any situation in which a computer is used to predict conditions in the real world, care must be taken when interpreting FEA results. In this case, there are a number of factors that could lead to the result being unreliable.

1. The model of the system did not take into account the material properties of the sponge-like material of the P-bands, which may contribute structurally to the duct in addition to their possible role in diffusion.

2. The model was not able to account for the contents of the duct - any compression in real life will be resisted by the hydrostatic forces within the duct, though in practise this may result in increased flow or premature gelling.
3. The size range of the duct being modelled is very close to the minimum that the FEA analysis software is capable of resolving, and as feature size decreases, the results become less reliable. However, the results of the models described here are supported by the duct thickness predicted by the model, which is comparable with the duct wall thickness found experimentally.

5.7. Conclusions

The structure of the cuticle lining of the duct of the model spider *Nephila edulis* consists of nanoporous discs alternating with non-porous structural discs, and the whole structure is lined at the luminal surface with a thin membrane. A remarkably similar banded arrangement is seen in silkworms. This structure is likely to provide a combination of mechanical integrity together with high and selective permeability to water, ions and possibly other low molecular weight solutes. Modelling optimum duct wall thickness when taking into account its requirements for permeability and resistance to kinking resulted in a value very close to the wall thickness measured in micrographs. The construction of the duct may enable compact storage whilst retaining the length required for conditioning and spinning the silk dope, suggesting that the duct is highly specialised to handle the spinning of silk fibres.

Chapter 6. Bioinspired silk spinning: Strategy and device development

The thesis up to this point has looked at the gross morphology, materials and ultrastructure of the spinning glands of the model spider *Nephila edulis* and the model silkworm *Bombyx mori*. The following chapters describe a series of developments made towards the synthetic spinning of silk fibres, building upon existing literature and insights gained here through observation of the natural glands. The main insight applied in this part of the project was to use flow fields that are likely to be present in spinning glands of spiders and silkworms and in device geometries that are based upon these glands. The aim was the design of a device for dry spinning of fibres that requires minimal or no post treatment, from small quantities of native silk dope. Considerable experience with handling the feedstock and incremental device development was required towards achieving this aim.

This section of the thesis is split thematically into four chapters, each of which describe a different aspect of the development of a spinning device. This first spinning chapter chronologically describes the incremental development of methods and devices developed during the course of the investigation. Devoting this chapter to development of the spinning device then permits the subsequent chapters to concentrate on the results of spinning trials, without the distraction of details of engineering device optimisation.

Before embarking on the design of a synthetic spinning device, I first needed to develop my experience of rheology-based devices and the general processes likely to take place in a spinning device. Thus, the second spinning chapter describes an investigation into the behaviour of silk dope using a novel capillary and centrifugal rheometer. The aim of this investigation was to formulate a model of the capillary and motive force provided by a centrifuge, and then validate the model by experiment. The same apparatus was used additionally to test whether dissected native dope could be moved along and through a glass capillary. A by-product of this process was that short fibres were spun on the device and were characterized.

The third spinning chapter describes initial attempts to spin long fibres from native dope, using flow fields similar to those likely to be present in spinning glands of spiders. Flow fields were insufficient to induce gelation, so alternative methods for fibre gelation were explored. After characterizing the fibres, these explorations were declared a limited success, insofar as fibres were spun. However, the spinning process itself was far different from that for native fibres.

The fourth and final experimental chapter describes a method based upon the observational sections of this thesis to permit better control of the spinning process and therefore to allow long and controlled fibre spinning, based upon a novel and key feature of the final stages of the native spinning glands. The fibres from this successful controlled spinning were again characterized and conclusions drawn, with important general conclusions for future work to develop better spinning devices.

As described in the outline above, the remainder of this chapter describes the practical development of the fibre spinning device. The main components of this device are shown in Fig. 1.1 and consist of the following: a movement generation apparatus to move the feedstock through the assembly; a tapered spinning nozzle from which fibres are produced; a gelation initiator, to start gelation of the silk dope (not always used); the fibre that emerges through the capillary and then needs to be collected, either by a batch or continuous method such as the collecting rod in the diagram; a collecting rod rotator to rotate the collecting rod; and a horizontal movement driver to move the collecting rod horizontally to present more collecting rod onto which to collect fibre.

Having introduced the main components of the assembly, a chronological development of each component is given below, with some technical details given in Appendix C Spinning device development for clarity.

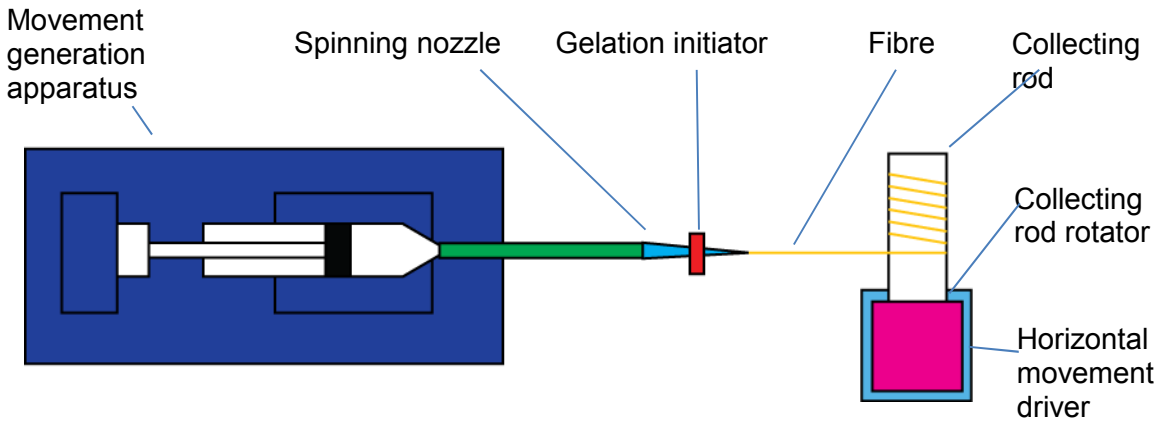


Fig. 6.1 Planar Schematic overview of components used in the spinning device

6.1. Movement generation apparatus: syringe pump

A method was required to assist movement of the silk dope through the capillary, since the natural pulltrusion process of pulling the dope out of the capillary nozzle behind solid spun fibres did not generate enough force before the developing fibres broke. A single- syringe infusion pump (Cole Parmer EW-74900-05) provided motive force for spinning. This was selected due to its simplicity of operation and previous documented use in other silk spinning systems (Liivak et al., 1998, Seidel et al., 1998, Trabbic and Yager, 1998, Seidel et al., 2000, Arcidiacono et al., 2002).

6.2. Spinning nozzles

6.2.1. Laser engraved

The first attempt at making a spinning nozzle with dimensions approximating a natural spinning duct was by laser engraving the shape into an acrylic chip (Fig. 6.2). Unfortunately, the laser cutter (HPC LS 3040) was unable to reproduce the details on a scale approaching the dimensions in nature, as the laser cutter was unable to cut any line thinner than 0.5 mm.

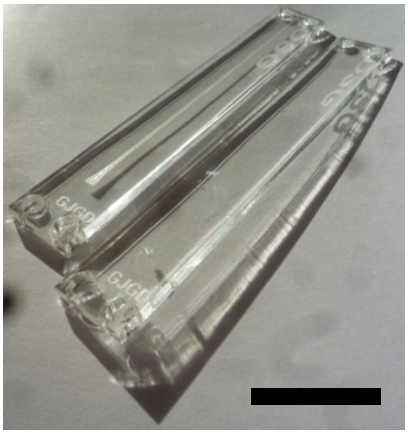


Fig. 6.2 A prototype spinning chip, with laser engraved shape at the top of the image and lid at the bottom of the image, scale bar 20 mm.

6.2.2. Glass capillaries: hand pulled

Glass capillaries were held over the hot flame of a Bunsen burner and the ends of the capillary were pulled apart. Although many different tapers could be produced, including those with curves that superficially resembled the turns of a natural spinning duct (Fig. 6.3 (A)), they were not reproducible (Fig. 6.3 (B)).

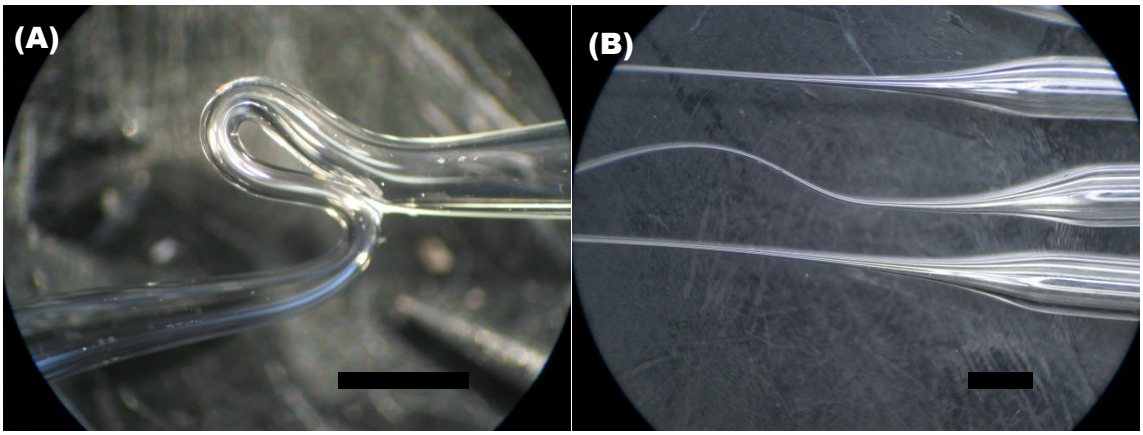


Fig. 6.3 (A) Glass capillary with s-shaped duct, scale bar 1 mm (B) Making tapers with reproducible dimensions was not possible by hand pulling over a Bunsen burner, scale bar 1 mm.

6.2.3. Glass capillary puller

Glass capillaries were pulled into a taper using a micropipette puller (Sutter P80/ PC). Borosilicate glass capillaries with 1.0 mm outer and 0.78 mm inner diameter (Campbell Inc.) were chosen, as these had the smallest internal diameter of any capillary available. It was hoped

this small diameter would make it easier to pull very long thin tapers than would be possible with a larger diameter capillary. After experimentation with settings described in Chapter 8, instrument settings of heat 550, pull 20, velocity 180 and time 8 (arbitrary units) were thereafter used in subsequent chapters for spinning all silk fibres.

6.2.4. Epoxy chip mount for capillary

The aim here was to design a chip which could allow the contents of a tapered glass capillary to be pressurized by an external source to force the dope slowly through the capillary, whilst protecting the capillary from rupture from the high pressure and without restricting visualization of the contents with a microscope.

This design was superseded after silk dope could not be pulled through.

The final design (Fig. 6.4) was a tapered glass capillary embedded into a transparent epoxy resin support between glass slides as optical boundaries and acrylic walls. Epoxy resin served to resist high pressure capillary rupture without restricting the light path. The chips were designed to be modular and stackable for incorporation into larger apparatus at some later stage. A female barbed Luer fitting with the barb removed was chosen as the high pressure connection (>300kPa (1996)) and glued at the proximal end of the spinneret. The internal dimensions of each capillary were measured in the same manner as used for measuring dissected silk ducts as described in section 2.2., Duct and capillary measurement.

Fig. 6.4 Components of epoxy chip device

Fig. 6.5 shows an early model chip before filling with epoxy resin, which can be compared to the design presented in Fig. 6.4. After some modification of the epoxy mixing and pouring protocol to prevent opaqueness due to micro bubbles in the epoxy, the chip design could be made fairly rapidly, with many in parallel (Fig. 6.6 (A)) and with fair reproducibility (Fig. 6.6 (B)).

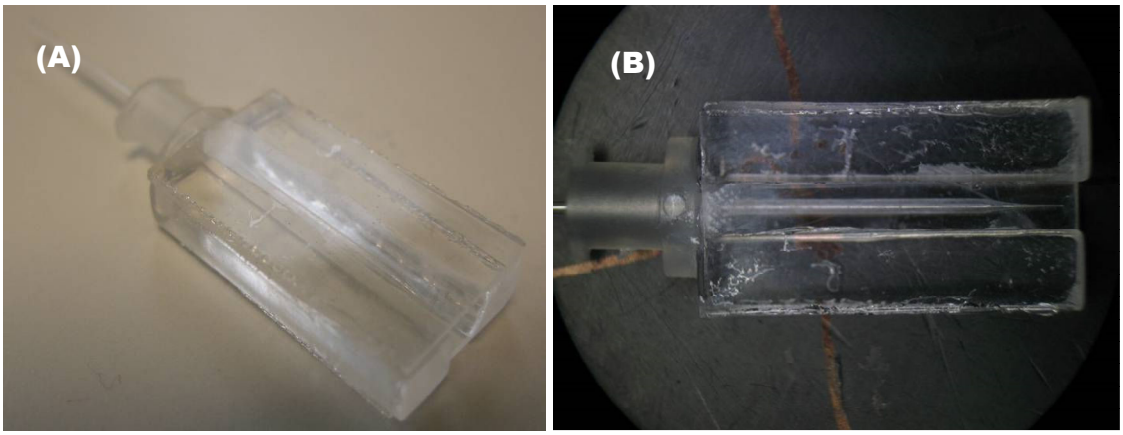


Fig. 6.5 (A) isometric view of device (pre-epoxy) (B) top down view of device (pre-epoxy)

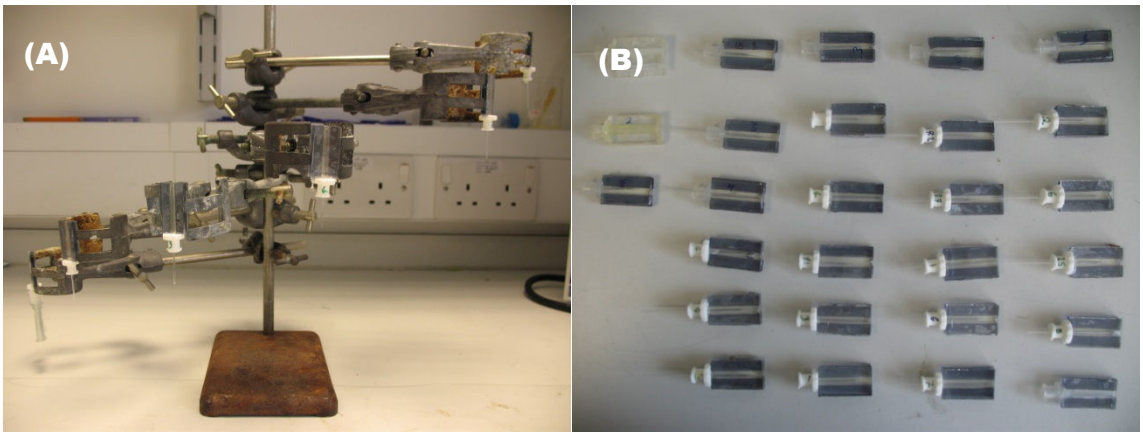


Fig. 6.6 (A) Six chips with capillaries inserted waiting for epoxy to cure, held within a lab clamp stand. (B) 27 chips showing reproducibility of method (prototype top left).

The flow rate of water powered by compressed air (Jun-Air OF302-25) through chips containing capillaries of different tapers was measured and compared to theoretical rates calculated from measurements of the internal dimensions of each capillary. Although preliminary results indicated that the relationship between theoretical and experimental results was fairly positive, it was found that if a capillary containing distilled water was allowed to dry out, contamination would clog the

taper, thereby preventing the chip from re-use. Attempts to avoid contamination using filters were not successful, so a full comparison between theoretical and experimental flow rates of capillaries with different tapers, and the flow rates of capillaries with the same taper, could not be made.

6.2.5. Epoxy chip hybrid

Although flow rates of distilled water through the epoxy chips could not be quantified, as described in the previous section, an attempt was made to spin silk through an epoxy chip containing a capillary with a taper similar to natural ducts. In order to draw silk dope through the capillary, an additional female Luer connector was glued to the taper end of the epoxy chip, and a syringe used to pull dope into the capillary. The main body of the Luer was then removed, and the silk dope within the capillary was pressurized using a single-syringe infusion pump (Cole Parmer EW-74900-05) attached to the original Luer adaptor.

Using a pair of tweezers, silk was pulled from the tip of the capillary, as shown in Fig. 6.7. The remaining collar of the Luer connector made it difficult to access the tip of the capillary protruding from the epoxy chip. The method of manufacture was also wasteful of materials, as many components were required to build each chip, none of which could be reused.

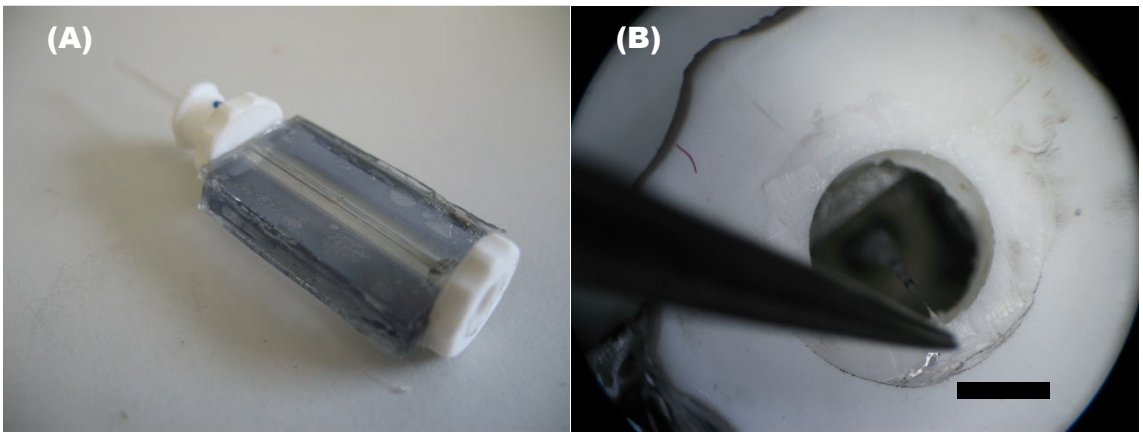


Fig. 6.7 (A) Image of an epoxy chip hybrid. (B) First silk dope pulled from a tapered capillary. Image shows the tip of a pair of tweezers pulling silk dope from a capillary pointing almost directly towards the camera, all surrounded by the Luer ring. Scale bar = 1.5 mm.

6.2.6. One Luer, one seal

As each epoxy chip took more than 12 hours to make, allowing for the epoxy to cure, and did not seem to add any functionality at this laboratory stage of investigations, spinning with just a capillary was attempted. The capillary still needed some method of filling and of attachment to the syringe pump, so a seal and Luer combination was used as shown in Fig. 6.8 (A).

This nozzle had the advantage of very quick manufacture, and if the capillary tip became blocked a length of glass could be removed to access the dope behind the blockage. The main disadvantage was that very many capillaries were broken during sample loading when trying to remove the loading syringe. Details of making and using this device are given in Appendix C: Spinning device development.

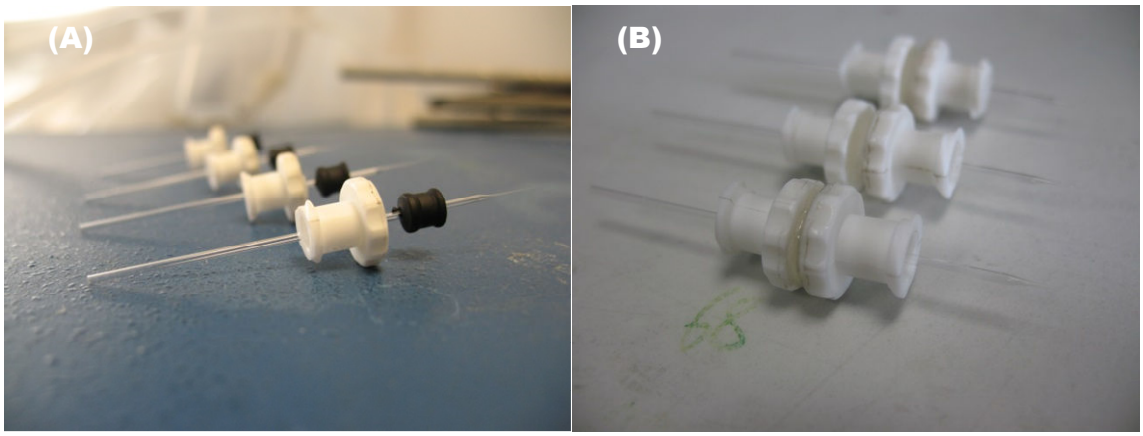


Fig. 6.8 (A) 'One Luer, one seal' nozzles (B) 'Two Luer' nozzles

6.2.7. Two Luer nozzle

At this stage of development it was discovered that the Luer connectors from broken capillaries could be cleaned and reused. Therefore, the next generation of nozzles replaced the problematic seal and replaced it with an additional female Luer connector, glued back to back with the original as shown in Fig. 6.8 (B). Details of making and using this device are presented in Appendix C Spinning device development.

This nozzle was very versatile and was used for the majority of spinning experiments. It had the disadvantage of requiring a relatively large amount of dope. It was previously found necessary to entirely fill the capillary with feedstock before applying compressed air. If the capillary was only partially filled, the viscous feedstock would be moved out of the stream of air preferentially to passing through the tip. Air would then flow freely through the capillary but the feedstock would not.

6.2.8. Shortened Luer nozzle

In order to spin very small volumes of feedstock such as spider dope, the volume of the capillary had to be very much smaller than the normal nozzle. Therefore, two developments were introduced almost simultaneously. The first involved cutting one Luer connector to be as short as possible, whilst still preserving the taper for interfacing with the sucking capillary and the back flange for mounting the capillary. The second involved creating the nozzle in two parts. This enabled a smaller capillary volume to be used than would be possible if the capillary had to be longer than the mounting Luer connector. Details for making and using this device are given in Appendix C Spinning device development.

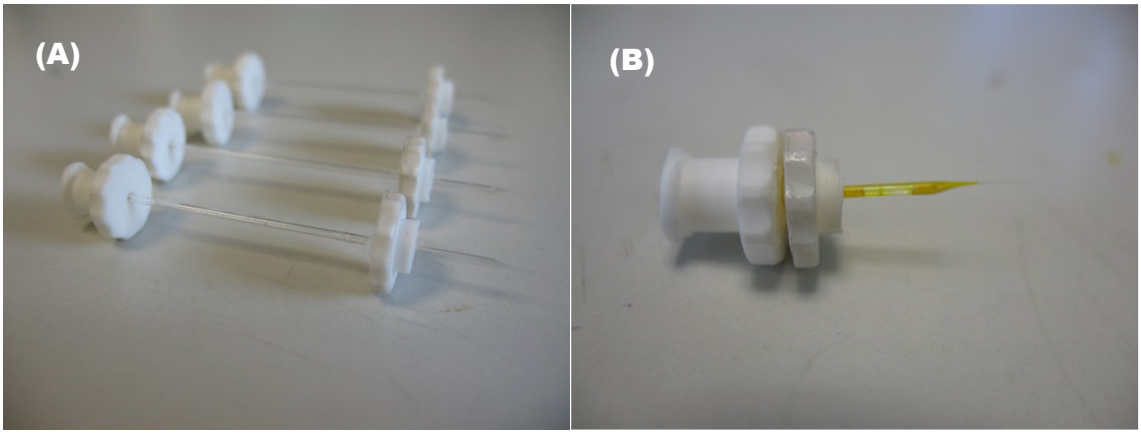


Fig. 6.9 (A) the first stage of using the shortened Luer nozzle, showing normal length Luer connectors glued to the capillary on the left ready for sucking in surface treatment, and shortened connectors on the right ready for sucking in feedstock. (B) a completed 'shortened Luer' nozzle, partially filled with feedstock.

6.3. Gelation initiator: capillary heating

A specific requirement for the spinning trials was to heat a short section of the final capillary between room temperature and 55 ° C, in a novel attempt to induced controlled destabilisation of the spinning dope prior to the final draw down of the fibre, as described in detail in Chapter 9 and more specifically in Section 9.3.2.

6.3.1. Temperature measurement

In order to measure the temperature of the heated section, a thermocouple was chosen, since thermocouples do not require an external power source. Temperature was read from a custom circuit capable of reading two thermocouples. New T-type thermocouples with 0.2 mm probe diameter (RS 621-2164) were chosen for their suitable temperate range, compatibility with the custom circuit and small size, and were calibrated within a thermo-gravimetric analyser (TA Instruments Q500 TGA) to a three-point calibration curve.

6.3.2. Humidifier annulus

The first heating method used a thermally controlled humidifier (Setaram Wetsys S60) powered by an air compressor (Jun-Air OF302-25) to pump hot humid air through an annulus, through which the capillary passed. The hollow annulus was constructed of two large zinc-plated washers spaced apart by several layers of hot glue, with Luer connectors either side to allow connection to the humidifier. The device was mounted via a custom Lego arm to a micromanipulator (Leica 116595), which allowed precise positioning of the annulus around the fragile glass capillary.

Fig. 6.10 shows a schematic of the spinning system. A syringe pump is connected to the Luer connectors that mount the capillary. Around the taper of the capillary is the heating annulus with tubes to conduct the heat to and from the device. At the end of the capillary a fibre is drawn. An image of the spinning device including annulus is shown in Fig. 6.11.

Unfortunately the humidity device was not able to provide heat at a sufficient rate to achieve the required range of temperatures, so another heating solution was attempted.

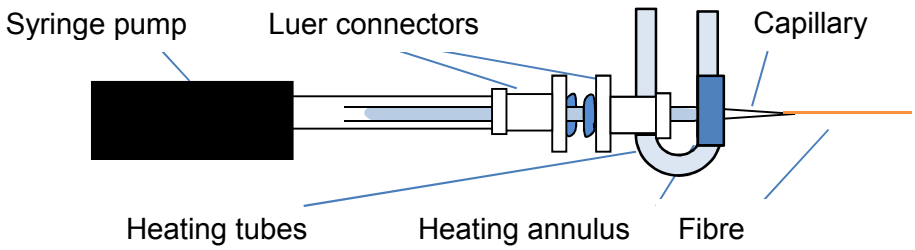


Fig. 6.10 Schematic of setup using annulus around capillary

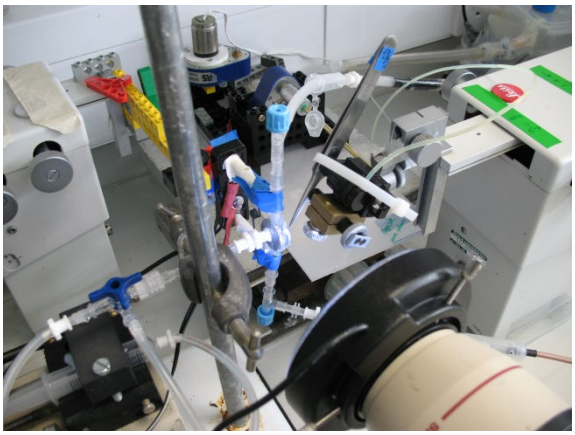


Fig. 6.11 Humidity controlled heating setup, showing air feed tubes to annulus, surrounding a 'two Luer' nozzle.

6.3.3. Hot coil

A logical alternative to the humidifier annulus shown in Fig. 6.11 was an electrical heating coil around the capillary. To do this, the heating coil and stand from a broken micropipette puller were removed, and attached on the Lego arm in place of the humidifier annulus. This coil (Fig. 6.12 (A)) was chosen as it was designed to heat capillaries and the existing electrical connections could be adapted safely.

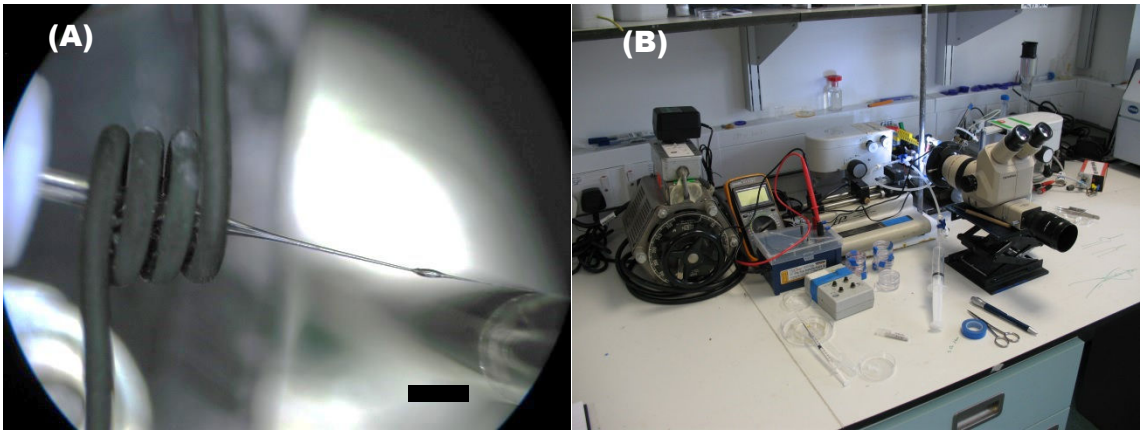


Fig. 6.12 (A) The heating coil, with a capillary protruding through, scale bar 2 mm (B) The initial heating coil setup.

Although fibres could be spun at higher temperatures through the coil, the precision of the temperature control was found to be inadequate at ± 2 ° C. This meant that there was uncertainty about the temperature at which fibres were spun within the critical temperature instability range. Therefore, the system needed upgrading again.

6.3.4. Peltier

A Peltier heating plate was then used to control the temperature of the capillary. This Peltier was controlled using custom equipment, with a rotary dial permitting temperature selection in the range 0-50 ° C. The Peltier required some modification to work for the spinning application, as described in more detail in Appendix C Spinning device development.

With the original Peltier set-up at full power, the capillary could only be heated to ~43 ° C. To increase the temperature range of the controller beyond that accessible with the rotary dial, a voltage was applied to the Peltier controller, which required an additional power supply. Although this extra power supply could be controlled manually, it was immediately upgraded to use computer control as described in the ‘Computer interface’ section below.

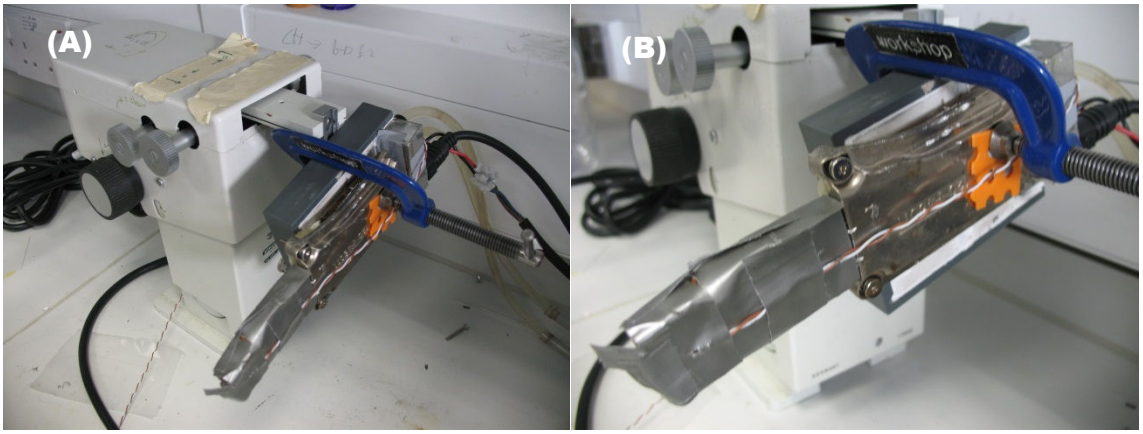


Fig. 6.13 Peltier plate and distance piece clamped to micromanipulator

6.4. Fibre collection from nozzle

To start spinning fibres required pulling on the dope or fibre that emanated from the tip of the nozzle. Then, the fibres needed controlled pulling and collection on a reeling device.

6.4.1. Fibre pulling

The first technique to pull the dope from the nozzle was simply to pull using a pair of fine tweezers. Simple manual pulling with tweezers had multiple disadvantages, including shaking induced by my hands, not being able to pull at a steady rate, and not being able to use the hand for any other adjustments whilst pulling fibres. To overcome these problems, a pair of tweezers was hot-glued to a pair of dividers and mounted horizontally upon a micromanipulator (Leica 100870). Using the micromanipulator, the tweezers could be moved into position around a droplet at the end of the capillary, and then clamped using the dividers. The micromanipulator could then be retracted to spin fibre, as shown using a 'one Luer one seal' nozzle in Fig. 6.14 (A).

Although an improvement over no clamping at all, the dividers still had to be closed by hand, introducing vibrations sufficient to break nozzle tips. Therefore, the tweezer clamp dividers were upgraded to a remote control hydraulic microdrive (Narishige MO-22) designed for microinjection manipulation. The combination of Microdrive and micromanipulator allowed

remote actuation of the tweezers' opening and position, removing all operator shake from the system and allowing very precise positioning of the tweezer tip.

This iteration was used in the final setup to initially draw fibres from the tip of the nozzle.

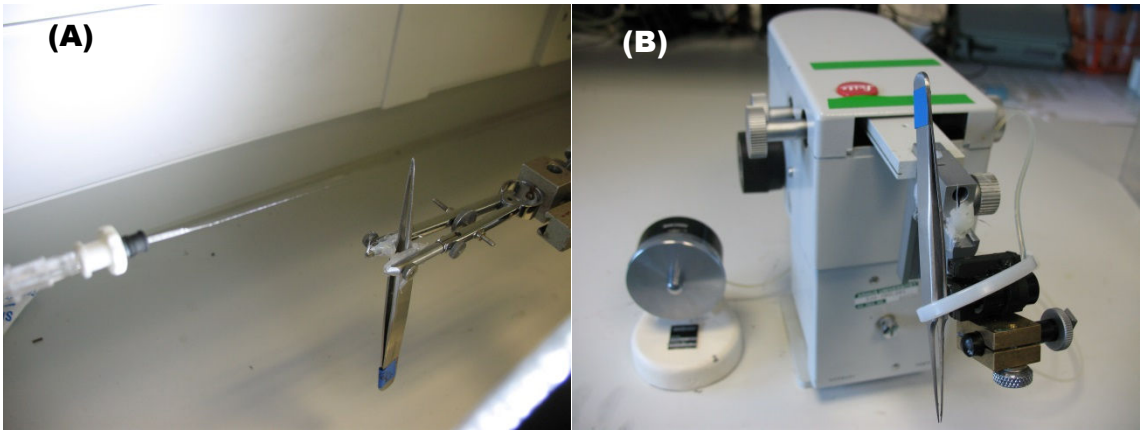


Fig. 6.14 Fibre collection devices (A) Tweezers on dividers, (B) Tweezers on oil cylinder.

6.4.2. Collecting rod rotation

Although the fibre could be collected from the nozzle, the length of silk that could be spun was limited by the distance the micromanipulator could move, which was about 50 mm. Therefore, a continuous method to collect fibre was needed. A collecting rod was chosen.

To rotate the collecting rod at a controlled speed required a system that consisted of three main components- a motor, a fine speed controller, and a power supply. These are described in detail in Appendix C Spinning device development.

6.4.3. Fibre collection rods

To collect fibres being spun from the tip of the nozzle, rotating collection rods were used. These needed to be removed easily from the spinning device to mount fibres onto frames. These required some development as described in Appendix C Spinning device development., but the final setup used a long metal rod either 4 or 10 mm in diameter.

6.4.4. Horizontal movement driver

Fibres were spun onto the collection rods, which needed to be moved horizontally to avoid fibres being deposited on top of each other. The development of this displacement device is described in detail in Appendix C Spinning device development. The final development shown in Fig. 6.15 permitted smooth horizontal movement of the rod, but the torque for continuous movement at slow speeds was more than the motor was able to supply. This limitation for continuous movement was overcome in the final spinning device by intermittent control of the motor via a computer interface.

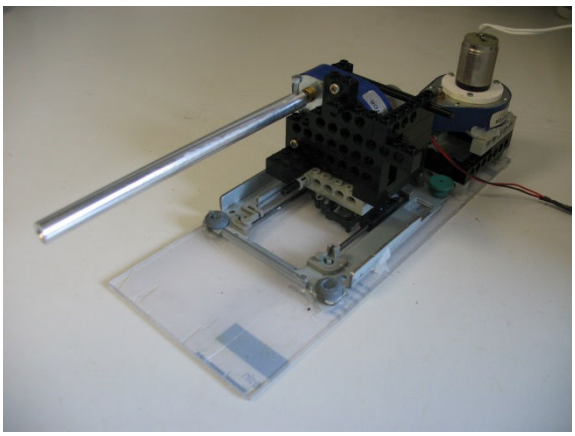


Fig. 6.15 Upgraded axial movement component

6.5. Computer interface

Both the Peltier and the collecting rod horizontal movement needed better control than was possible using the available manual controls. Therefore a computer system was devised and constructed which could control both to a better degree of accuracy.

The Peltier and horizontal reeling motor were controlled by a pulse wave modulation (PWM) circuit board with USB control (PC-Control Motorbee). The board was connected via a standard USB cable to a laptop computer (Dell Inspiron 8200). Power was provided to this board from a standard wall transformer (Moreal nap-2015-12v). To quickly alter the direction of the horizontal movement, a double pole single throw switch made from two single pole single throw switches

and a Lego block was placed after the PWM board to reverse the polarity of the power going to the collecting rod horizontal movement motor.

A simple piece of software (Fig. 6.16) was written to interface with the PWM board and thereby horizontal motor and temperature control. Although controlling two different pieces of hardware, the software was designed to allow quick modifications of spinning control without stopping spinning. This was accomplished using keyboard shortcuts. For details of how the software worked and the raw code, please see Appendix C Spinning device development.

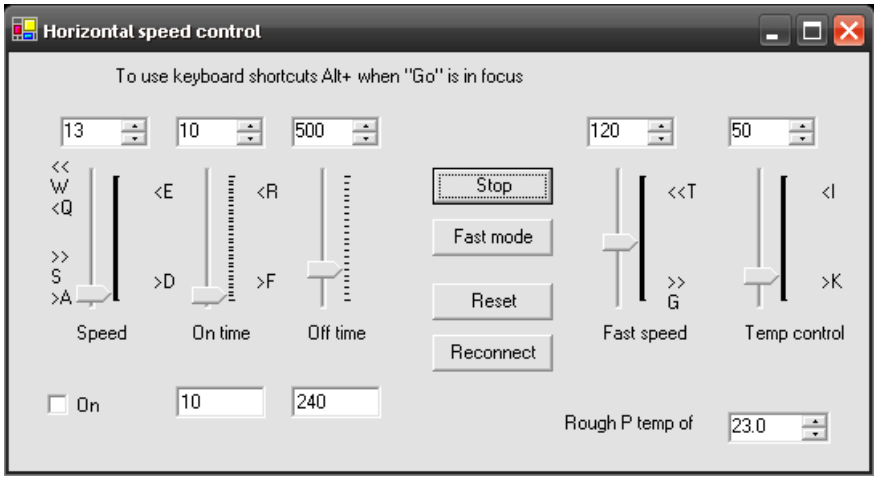


Fig. 6.16 Software interface

6.6. Fibre mounting

Initial fibres were pulled with tweezers and very short, so they were mounted straight onto card frames in the usual manner, as described in the Methods chapter section 2.3.2.

As longer fibres were spun on collecting reels, it was no longer practical to mount single stretches of fibre. Instead a frame was constructed from Lego to hold the spinning reel a small distance above the surface. Under a stereo microscope (Olympus SZ4045TR), the fibre was gently unwound, and repeatedly stuck to a strip of paper frames (Fig. 6.17). This meant that a fibre could be unreeled in one length, attached to the beginning and the end, and then glued to individual paper frames afterwards.

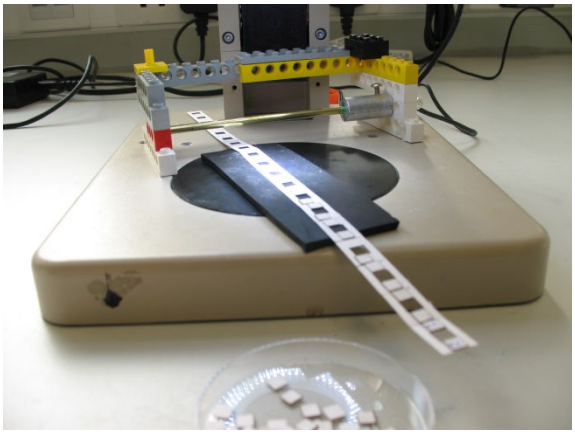


Fig. 6.17 Fibres glued to a strip of paper frames, underneath the unravelling frame, all mounted upon a stereo microscope.

6.7. Final setup

The figures Fig. 6.18 and Fig. 6.19 show a schematic of the spinning system, and Fig. 6.20 gives an impression of the final fibre spinning system.

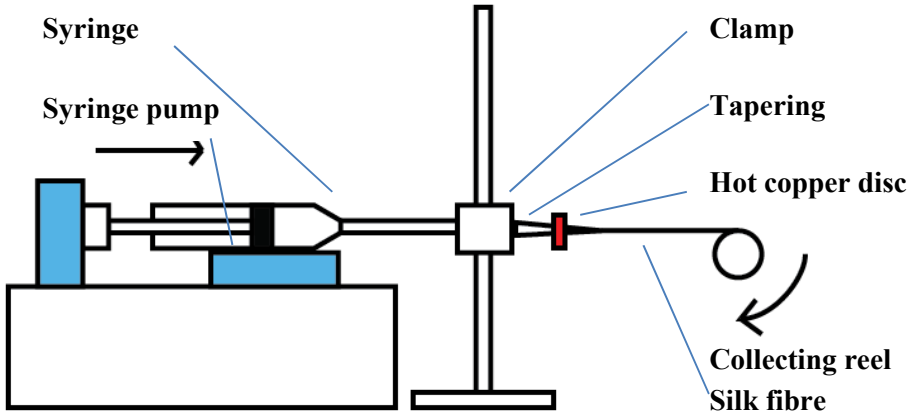


Fig. 6.18 Schematic of spinning apparatus, side elevation

Fig. 6.19 Schematic of spinning apparatus, plan view

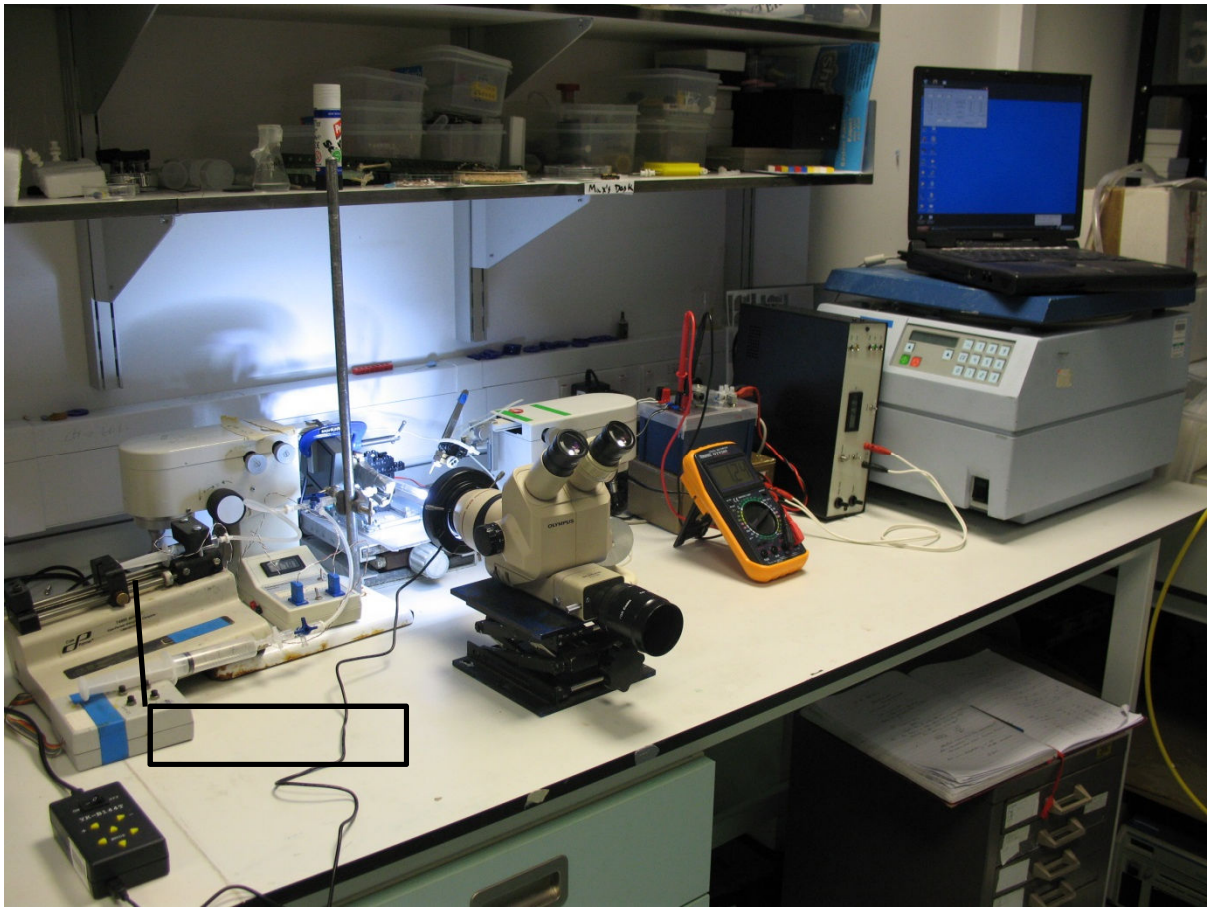


Fig. 6.20 Fibre spinning system, with components labelled

Chapter 7. Capillary rheology with centripetal force

7.1. Introduction

The aim of the work reported in this chapter was to design and test a device capable of moving silk dope through a small diameter capillary, similar in size to biomimetic spinnerets likely to be used to spin silk fibres, and also to learn quantitatively about the rheology of the feedstock. A secondary aim was to use shear forces generated within the device to induce gelation in the native dope, and thereby form fibres with similar properties to native silk fibres.

Spiders and silkworms produce silk fibres from their spinning ducts using pulltrusion. Namely, they do not use internal pressure to force their feedstock through the spinning duct. This is not surprising: a basic analysis may be performed to find the order of magnitude of pressure that would be required to perform such a feat; spiders resist silking with forces roughly 3 times the average body weight of 1 gram (Ortlepp and Gosline, 2004), and the final diameter of *Nephila* spider major ampullate silk is roughly 3-6 μm, so using approximate scaling

$$Pressure = \frac{Force}{Area} = \frac{3 * 0.001 * 9.81}{\pi * (3 * 10^{-6})^2} \approx 1\ GPa \qquad \text{Equation 7.1}$$

Therefore, assuming constant viscosity, the internal pressure required to push the dope through the spinning gland would be unrealistic. Instead, I tried to develop a novel method to propel the dope through a capillary that would also allow some quantitative indication of the rheology taking place during the flow, bearing in mind that consideration of the chemical modification of silk within natural glands (the subject of several studies (Vollrath et al., 1998, Knight and Vollrath, 2001)) was beyond the scope of this thesis work.

Instead of trying to push the fibre through the capillary from the far end, a method was proposed to mount a capillary orientated radially on the rotor of a spinning centrifuge. The centripetal force

involved would generate a force to act upon the entire length of the dope simultaneously. This is shown schematically in Fig. 1.1 (A).

Within the literature, the rheology and forces within a fast rotating horizontal tube are not well documented, but there is a body of work concentrating upon the behaviour during spin coating; a method of placing a feedstock on a rapidly spinning horizontal flat circular plate to enable fast and controlled coating of the plate. Some studies even derive a model for the spin coating (Lawrence and Zhou, 1991, Bludszuweit, 1995, Jang et al., 2003). Unfortunately, these models are of limited applicability due to the special case of constrained capillary flow here.

As no suitable equations could be found, a set of equations pertaining to the system in Fig. 1.1 were formulated by combining known model equations. The new equations were validated against results obtained from the spinning rheometer device using rheometer calibration oil of known properties. When the properties of the system were better understood, silk dope was used as a feedstock within the capillary. Native silk dope fibres were spun in the device, and the fibres characterized and compared against natural silk fibres.

Fig. 7.1 (A) Model of the centrifuge rotation rheology spinner apparatus, where r_0 is starting radius, ρ density of fluid, r final length of fluid, ω angular velocity of centrifuge, R radius of capillary. (B) Sectioned diagram of fluid reservoir.

7.2. Methods

7.2.1. Experimental apparatus

A plastic reservoir was made from a hose coupling and hot glue. The bottom of the reservoir was bored to a tight interference fit over the central retaining bolt of the rotor of a centrifuge (MSE Instruments Mistral 1000). The wall of the reservoir was drilled to snugly fit a glass capillary tube, which was attached facing radially out from the centre of the rotor. To prevent the capillary from moving away from the horizontal, it rested in a channel cut into the top of a 100 ml centrifuge tube, placed in the centrifuge rotor. An additional falcon tube containing water was placed on the opposite side of the centrifuge rotor as a counterbalance. The whole assembly is pictured in Fig. 7.2.

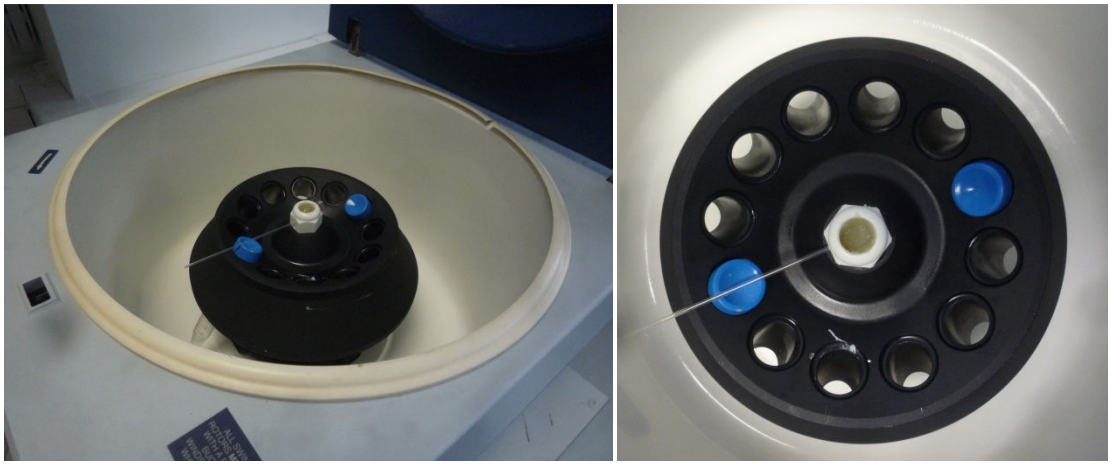


Fig. 7.2 Design of rotator apparatus for model testing

The fluid reservoir (sectioned view in Fig. 7.1 (B)) was shaped in such a way that the top opening was of a smaller diameter than the storage cavity within. This overhang prevented fluid within the reservoir from escaping in a vertical direction without needing a lid, thereby preventing a vacuum lock inside the vessel. The design included a raised central area, which directed the feedstock towards the capillary opening and reduced the volume of feedstock needed to perform a test.

The centrifuge allowed user selection of the rotational velocity and time of spinning. A digital readout displayed the current speed to the closest 25 RPM.

7.2.2. Materials

Rheometer calibration oil was used as a model calibration fluid, since it has known Newtonian properties. A small amount of oil was introduced through the top opening into the fluid reservoir. This was allowed to settle for a few minutes to allow air bubbles to escape. The main parameters for this investigation are given in Table 7.1.

Table 7.1 Parameters used to model length of oil column

Parameter	r_o	ρ	R	μ
Unit	mm	kg/ m2	mm	Pa s
Value	8	950	0.639	15

Chinese *Bombyx mori* silkworms were reared on white mulberry leaf until on the cusp of spinning, at which point they were transferred to an incubator maintained at 8 ° C until required. Silkworms were individually removed from the incubator, massed, and the silk glands dissected out using a dissecting microscope (Olympus Corporation, Japan). Having been transferred to another container, the glands were washed and peeled, leaving only the sericin-covered unspun silk dope. The sericin was washed off over a period of time, leaving only the pure silk protein. A full description can be found in the methods chapter, section 2.1.2.3. The 'pure' silk of two glands was then transferred to the clean fluid reservoir of the apparatus and left for thirty minutes to settle.

7.2.3. Preliminary calculations

From standard texts, the equation for centripetal force is

$$F = \frac{mv^2}{r} = mr\omega^2 \qquad \text{Equation 7.2}$$

which can be modified into a suitable form using the method described in Appendix B and cross checked using a simple dimensional analysis. This gave the equation

$$r = r_0 . e^{\rho \omega^2 \frac{R^2}{8\mu} t}$$ Equation 7.3

where r_0 is the starting radius, ρ density of fluid, r final length of fluid, ω is the angular velocity of the centrifuge, R radius of capillary, t time of spinning, and μ is the viscosity of the fluid. Fig. 7.3 shows the physical parameters of this model against a photo of the apparatus.

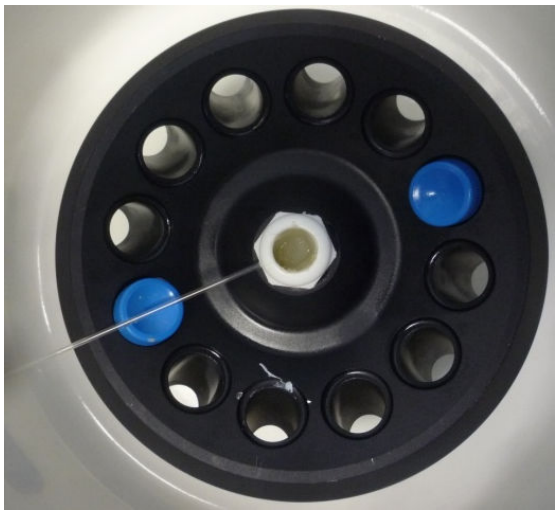


Fig. 7.3 Diagram of physical positions of factors used in equations

7.2.4. Experimental testing of analytical equation

A syringe was used to draw oil to the distal end of the capillary tube, and then the pressure was reversed to move the oil back along the capillary tube to the reservoir, but leaving some oil on the walls, as required by the Hagen-Poiseuille equation from standard texts. The centrifuge was then started. The length of oil that had flowed from the outer edge of the reservoir, r, was measured using a digital calliper (Mitutoyo Corp CD-6”CP). This test was repeated 10 times for each combination of top speed and length of time. A digital camera (Panasonic Lumix DMC-FX500) in ‘film’ mode was used to monitor the speeds throughout the test. By analysing the video footage, a record of the acceleration and deceleration was made (Fig. 7.4). This formed the basis of an estimate of the forces applied to the oil, and thus how far along the tube the oil flowed.

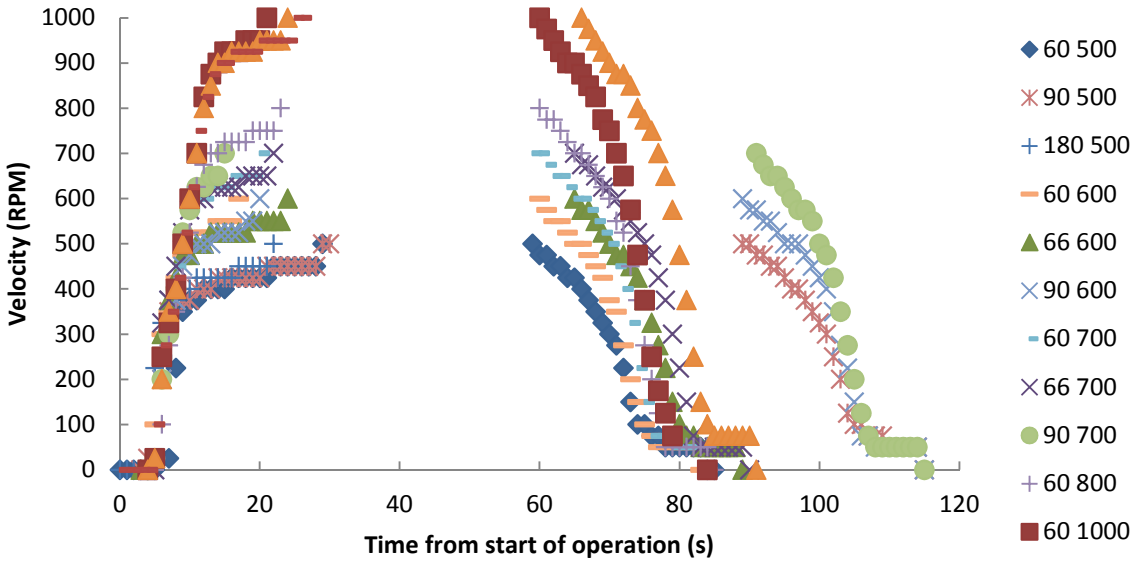


Fig. 7.4 Speed curves of the centrifuge. In legend, two digit number refers to programmed time and three or four digit number to maximum speed for each run. N= 2 repeats per run, 11 uns.

Using Fig. 7.3 in combination with simplified model equations for each speed setting on the centrifuge, predictions of the distance the fluid would flow were made for each speed. For the detailed development and the full set of equations for each run please refer to Appendix B.

7.2.5. Fibre Spinning

The fluid reservoir was secured to the centre of the centrifuge rotor, and a glass capillary introduced through the opening in the wall of the reservoir. The capillary was secured to the top of the falcon tube using a thermo softening plastic-based glue. The centrifuge was initiated along its pre-programmed speed curve and, when completed, any fibres produced were collected from the bowl using tweezers and placed in a clean petri dish. Due to the severely limited volume of samples available for testing, the result of one run was used to choose the next run's speed and time parameters. Between runs, the inner walls of the centrifuge wall were gently cleaned and dried so that any new fibres adhering to the walls in the next run could be noted and recovered.

Fibre samples were glued onto 10 mm gauge length paper frames as described in the Methods section 2.3.2. Samples were tensile tested as described in the Methods section 2.3.3. A 5 N load

cell was used to measure the forces at 50 % per minute strain. Fibres were imaged and the cross sections measured as described in the Methods section 2.3.4.

7.3. Results and discussion

7.3.1. Comparing model to experimental results

Using Equation 7.3, simplified predictions of the distance the fluid will flow for each speed were made and are reported in Table 7.2. The mean distance that oil flowed along the capillary was calculated for the 10 experimental runs for each speed and shown in

Table 7.3. Columns of oil that overflowed the 100 mm long capillary tube are marked "-". Tables 1.2 and 1.3 are plotted for comparison in Fig. 7.5. The figure shows that although the three green triangles that correspond to experimental flow lengths after 90 seconds look linear, in fact the green calculated line shows the relationship (including the forces during acceleration and deceleration of the centrifuge) is an exponential function, and the linearity is an observational artefact of too narrow a sample size.

Table 7.2 Predicted oil flow distance

	Time and Predicted r if r_0=8 mm			
RPM	60 s	66 s	90 s	180 s
500	13.7		19.3	48.5
600	19.2	20.2	29.3	
700	26.3	28.8	48.7	
800	36.2			
1000	83.4	106.2		11018.9
2000	55294.4			1.49E+13

Table 7.3 Experimental mean oil flow distance

	Time and Experimental r when r_0=8 mm			
RPM	60 s	66 s	90 s	180 s
500	29.5		57.0	-
600	61.2	57.2	77.4	-
700	74.8	70.5	91.3	-
800	83.3	-	-	-
1000	78.8	85.4	-	-
2000	-			

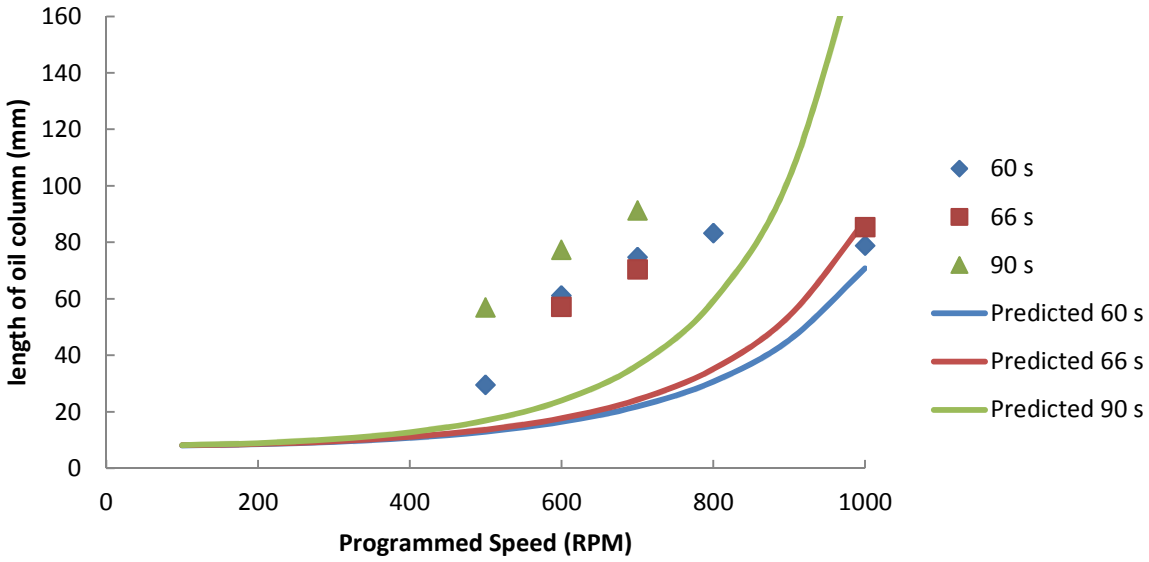


Fig. 7.5 Lengths of oil column as predicted by the model (lines) against experimental results (markers). In legend, two digit number refers to programmed time for centrifuge to run

From observation, oil moved along the capillary even when the centrifuge did not move. This might be explained by normal capillary flow alone but can be theoretically predicted. The equation for distance due to capillary pressure can be derived from the equation for pressure in a tube and combined with the Hagen-Poiseuille flow as described in more detail in Appendix B. This gives equation 1.4, which predicts the length of a fluid column in a static capillary tube after a certain time, given a horizontal tube and an infinite supply of fluid, with the new parameter Γ,

which is a surface free energy for the polymeric fluid. This equation is similar to one in the literature (Washburn, 1921).

$$\Delta r = \sqrt{\frac{\Gamma R}{2\mu}.t} \qquad \text{Equation 7.4}$$

For this investigation, it is not sufficient simply to add this extra length from Equation 7.4 to the length of the column as calculated by Equation 7.3, since the reference length of fluid decreases with the square root of time. Therefore, equation 1.3 must be adapted to the form

$$r = \left(r_0 + \sqrt{\frac{\Gamma R}{2\mu}.t}\right).e^{\rho\omega^2\frac{R^2}{8\mu}t} \qquad \text{Equation 7.5}$$

with parameter values given in Table 7.4, as referenced previously with the addition of the new parameter $\Gamma \approx 0.15$ N/m (Porter, 1995). This new formula can now be applied to the theoretical model equation curves. The result of these calculations is shown in Fig. 7.6 with parameters given in Table 7.4.

Table 7.4 Values of parameters used in Equation 7.5

Parameter	r_o	ρ	R	μ	Γ
unit	m	kg/ m^2	m	Pa s	N/ m
Value	8E-3	950	0.639E-3	15	0.15

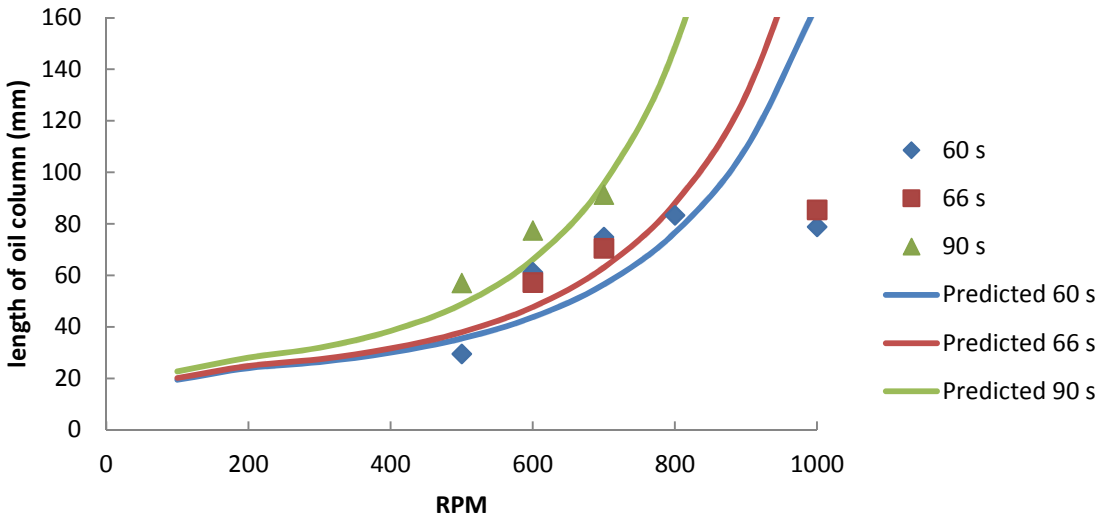


Fig. 7.6 Comparison between experimental data and model runs with capillary flow. In legend, two digit number refers to programmed time for centrifuge to run

The fit of the experimental results and the model is now reasonable for all runs, in particular for the 90 second run.

One important factor that has not yet been mentioned is the length of the capillary tube. The design of the apparatus meant that it would be difficult or impossible to monitor if any oil flowed from the end of the capillary tube. A monitoring capability of blue roll and then eppendorfs on the end of the capillary was trialled but was not successful as neither could withstand the centripetal forces invoked during spinning without becoming detached. It is possible that if oil flowed out of the capillary due to centrifugal forces, hydraulic forces meant roughly the same amount of oil always remained in the tube. This speculation could explain the reason that at 1000 RPM the distance extruded seems to have remained the same for the lengths of time explored.

Any further offset between the theoretical and experimental results may be explained by factors outside our experimental control. One possible factor is temperature fluctuations altering the oil viscosity and therefore how far it will flow, but was beyond the scope of this work.

7.3.2. Dope rheology

The aim of this section was to use the centripetal rheometer to test the rheology of silk dope. Theoretical values for distance travelled were calculated with the validated Equation 7.5 , with the parameters in Table 7.4 used for the properties of silk dope, with the exception of viscosity μ (the value 1500 Pa s from the zero-shear viscosity of silkworm silk (Holland et al., 2006a)).

The first speed and time combinations used were the same as used for the oil movement equations above. These 30 runs resulted in a mean predicted distance moved along the capillary of 9.8 mm with a standard deviation of 0.3 mm. These similar predicted distances were due to normal capillary flow for the length of time of each experiment, as the rotation was too low to result in silk dope movement due to centripetal forces. Instead to increase the variability between runs, higher speeds and longer times were chosen: The model for fluid flow developed above was use to select some speed and time combinations that the model would predict a range of distances moved by the front of the silk dope within the capillary. The shortest was predicted to result in a final distance of 10 mm, whilst the longest was predicted to result in a final distance of 90 mm along the 100 mm capillary.

Silk dope was loaded into the apparatus which was set to run for equivalent times to the model. At the end of each of the experimental runs, rather than feedstock remaining in the capillary as was the case of the oil runs, there was no silk dope left in the capillary and for four of the six runs, fibres had been spun. Table 7.5 shows the theoretical and experimental results for each of the runs.

Table 7.5 Results of theoretical and experimental silk dope centripetal runs

Run	Predicted length (mm)	Centrifuge speed (RPM)	Run time (minutes)	Fibres spun?

1	9.8	1000	1	Yes
2	14.8	3000	2	Yes
3	19.5	4000	2	No
4	27.7	4000	3	Yes
5	28.7	6000	1.5	No
6	90.5	6000	3	Yes

These results show that unlike the rheological calibration oil used in the formulation and calibration of the model, silk dope does not flow in a Newtonian manner. It appears that once flow has initiated it continues even with small forces. This suggests silk dope acts as a Bingham fluid (similarly to non-drip paint), as in there is no flow until under pressure flow conditions. Therefore, the viscosity during flow was much lower than expected and the predicted models formulated using silicone oils were no longer applicable.

Unfortunately, the experiment essentially failed to measure the detailed rheological properties of the silk dope, since the flow appeared to operate in a highly nonlinear on-off mode, rather than flowing as a Newtonian fluid. However, the results showed it was possible to flow silk dope through capillaries and, since silk fibres had been spun, they were collected and were characterised as the first examples of fibres spun in this thesis work.

7.3.3. Fibre characterization

The longest fibres were also the thickest- these adhered to the walls of the centrifuge bowl, and took a longer time to dry. The finest fibres were also the shortest and most difficult to test. The majority of fibres spun had very high width to depth ratios as can be seen in the SEM images (Fig. 7.7), as though they had been forced against the wall of the centrifuge at high speed.

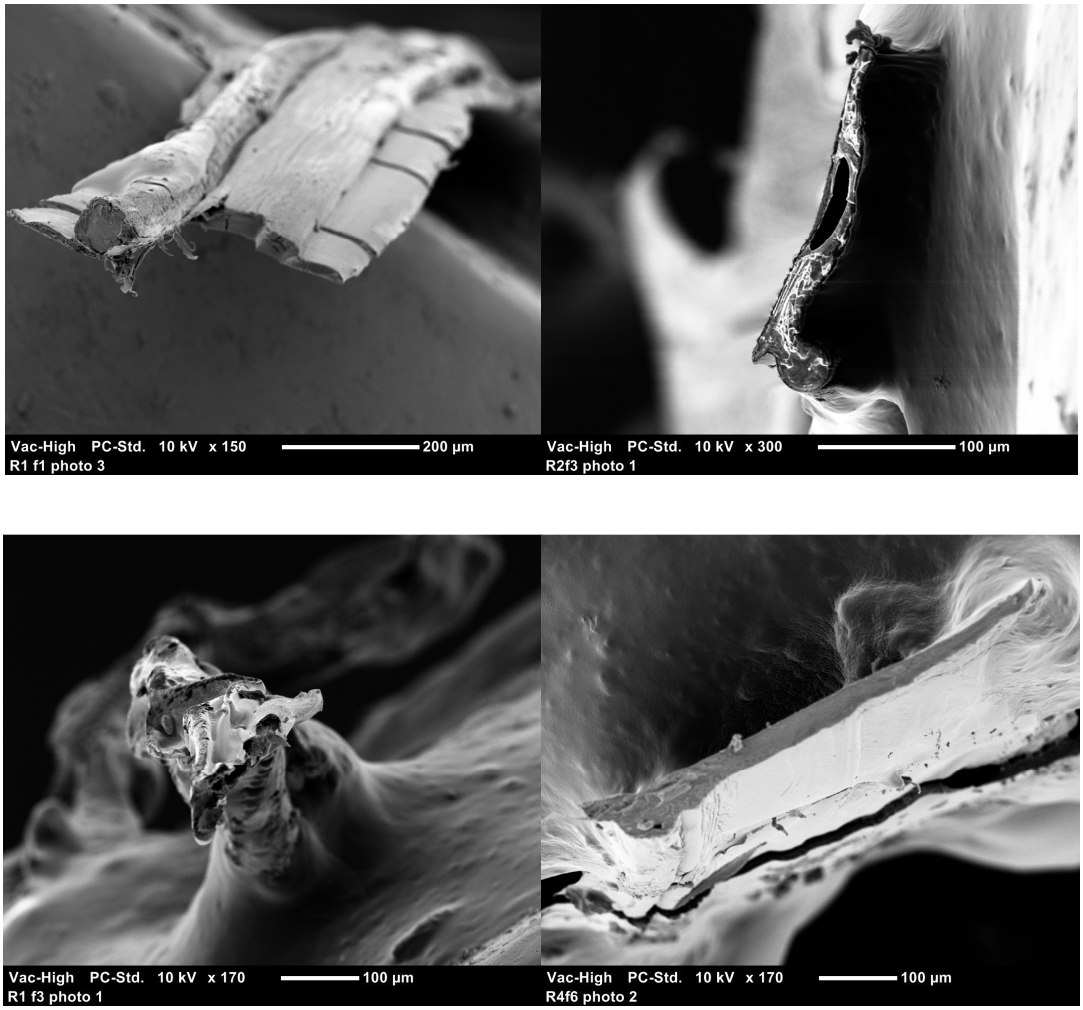


Fig. 7.7 SEM micrographs of fibre morphology, scale bar noted on each image

Although the apparatus had been used to form fibres from natural silk dope, when compared to each other and to natural *Bombyx mori* silk fibres, it can be seen from the tensile results in Fig. 7.8 that the fibres spun using the centrifuge did not have high breaking stress nor strain. The results of tensile tests upon the spun fibres are shown in Fig. 7.8. Fibres had breaking stresses between 3.93 and 172.08 MPa, and initial moduli between 38.75 MPa and 9537.89 MPa. Some fibres exhibited a short plastic yielding behaviour, whilst some did not yield at all before breaking in brittle mode.

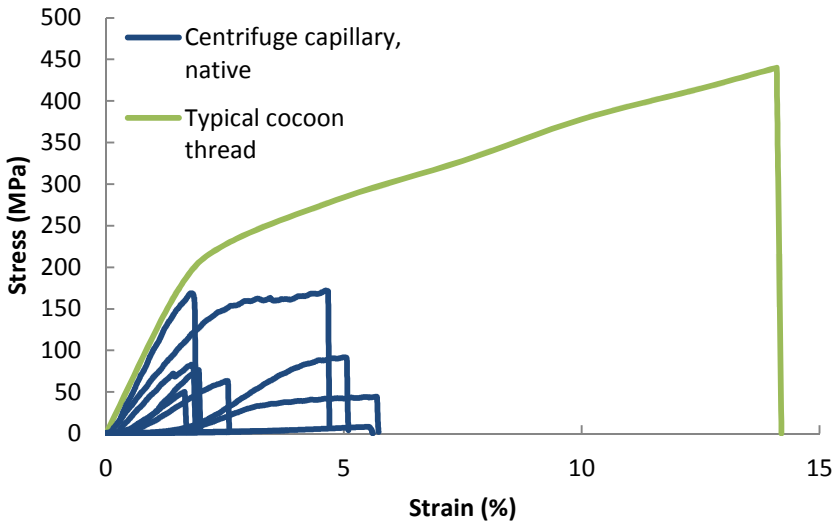


Fig. 7.8 Centrifuge spun fibre tensile results compared with *Bombyx mori* silk fibre results from (Shao and Vollrath, 2002)

As the stress and modulus values for the fibres are based on the very variable cross sectional area, some care must be taken when interpreting the results. Also, although the SEM used to calculate cross sections is calibrated, if the point at which the cross section is measured is not perpendicular to the fibre, the value is likely to be an over estimate.

The majority of fibres failed in a manner that is not characteristic of natural silk fibres, since they fail in brittle mode before yield. Since the fibres have so many cracks or inclusions likely to promote crack propagation, it is pointless here to speculate on the mechanism for brittle failure. However, the cross-sectional area of the cocoon fibre is more than an order of magnitude smaller than the fibres produced artificially in this set, so we would expect the natural fibre to be intrinsically much stronger (Porter et al., 2013).

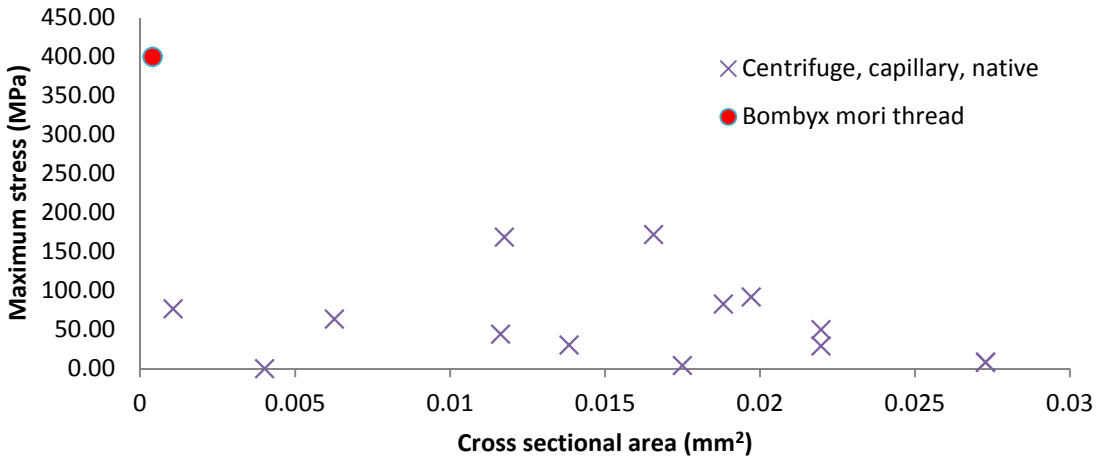


Fig. 7.9 Maximum stress vs. cross-sectional area of centrifuge spun fibres compared to natural *Bombyx mori* silkworm fibre. N=1 per point as tests were destructive.

7.4. Summary and conclusion

A novel 'centrifugal rheometer' was constructed to measure the flow of fluids in a capillary tube, as a preliminary exercise in understanding quantitatively the flow processes that are likely to take place in natural silk spinning glands.

An equation was formulated in terms of a small number of parameters to predict the distance that a feedstock will flow in a glass capillary within a centrifuge, including both acceleration and deceleration. This equation was further refined to take into account the surface tension of a fluid, and results for a model calibration fluid fit the experimental data well.

This model indicated that it was possible to use the centrifuge to move silk dope through a capillary of the size used here.

Using the same apparatus with native silk dope, fibres were spun and characterized as having variable but overall poor mechanical properties.

Due to the small amount of available natural dope sample relative to the large device volume, it was not possible to test dope rheology and spin large enough quantities of fibre for reliable testing. The device was, therefore, placed aside to concentrate on more direct spinning methods

through tapered capillaries with geometries more in line with natural spinning glands that was the specified aim of the project.

Chapter 8. Bioinspired silk spinning: synthetic screening trials

8.1. Introduction

The principle aim of the work reported in this chapter was to spin silk-like fibres using natural feedstocks, by mimicking one or more processes that are involved in the natural silk spinning apparatus. This chapter documents initial screening trials that were conducted in parallel with the development of the spinning equipment, reported in Chapter 6, to investigate some important factors for spinning.

The poor mechanical properties of synthetically spun RSF may be inherent to the feedstock, due to the severe structural changes and degradation of silk proteins that occur in its dissolution in aqueous salt solution (Holland et al., 2007), among several examples. The properties of the RSF feedstock then virtually eliminates key features of the silk spinning process, such as shear induced orientation and aggregation (Holland et al., 2006a), and the final fibres have a very different molecular level morphology to natural silk. From these unnatural processes, it is unlikely that a fibre can be spun that truly replicates the properties of natural silk, even under ideal natural spinning conditions.

This work investigates how processes from natural silk glands can be translated into synthetic spinning processes. Therefore, in this chapter to research the synthetic spinning process and avoid effects due to inferior or very different feedstock, silk dope dissected from silk spinners is used. If or when a feedstock that accurately replicates natural silk dope is produced by other researchers, the two streams of research can be combined to spin wholly artificial fibres.

The processing effects to be mimicked must be selected carefully. To exactly recreate the natural shearing and chemical conditions would require extremely complicated apparatus, far beyond the scope of this thesis. Tantalisingly, evidence indicates that an exact recreation of the chemical gradients within the duct to spin silk fibres may not be necessary, since silk dope has been shown to form fibrils purely on the application of shearing forces (Holland et al., 2012b), and become

liquid crystalline from drawing (Kerkam et al., 1991) although no fibres have been produced or tested by this means. This hypothesis is tested in this chapter.

The work reported in the first section tested the hypothesis that silk fibres can be spun using purely shearing forces. From the promising evidence in the literature, it was hoped that shearing forces could initiate gelation of the silk dope molecules, which would then be stretched by drawing the fibre. To do this, glass capillaries were moulded to a shape that replicates the morphology of the silk duct from data in Chapter 3. Native silk dope was then forced through these capillaries, and the emerging droplet at the tip of the capillary was drawn into fibres which were characterized. A transition from silk dope to a fibre with silk-like properties would convert the hydrolytically stabilising water-amide bonds into amide-amide bonds that irreversibly coagulate the silk macromolecules. This is experimentally testable, since such silk fibres made from native dope would transition from being very soluble in water to a relatively insoluble fibre, in which segments are not available to bond with water.

Results from the first section of this chapter indicated that shear stress alone was insufficient to form silk-like fibres in glass capillaries. Although it was possible to spin silk dope filaments from a droplet formed at the end of a tapering glass capillary, the protein molecules were neither orientated nor formed crystallites. Silk spinning organisms convert dope to fibre in a combination of internal draw-down and chemical modification from specialised cells linking the duct (Vollrath et al., 1998), (Knight et al., 2000). They appear to chemically induce some (unspecified type of) gelation to the dope, before stretching out the constituent molecules so that crystallites can form. Growing or harvesting cells that perform the natural functions within the duct is beyond the scope of this thesis. So, to achieve molecular conversion within a glass capillary, it was proposed to use shear forces in combination with another independent process to promote gelation of dope into fibres. The table below explores a number of natural and unnatural processes that may induce this gelation, with a discussion on the advantages and disadvantages of each.

Method to induce gelation	Discussion
Shear stress	This work tests the hypothesis that shear stress alone can destabilize a natural silk dope and induce gelation, which then facilitates the extension and orientation of the silk macromolecules and dehydration into solid silk fibres with properties comparable with natural silk. To do this, glass nozzles approximating the hyperbolic geometry found in spiders were made and natural silk dope was forced through the tapered capillaries by a combination of internal hydrostatic pressure and pulling the fibres out of the end of the capillary nozzle. However, natural spinning glands do appear to have (perhaps secondary) methods to induce gelation in the spinning gland to promote correct fibre formation, so alternative gelation mechanisms must be considered for the eventuality that shear stress alone is insufficient.
Chemical alteration	The chemical alteration of the dope within the duct and the effects of this on the silk dope have been studied (Knight and Vollrath, 2001). Although desirable, to make alterations to dope through the wall of a glass capillary would be challenging. The ideal piece of equipment to study fibre formation would be a dialysis membrane cast to the desired hyperbolic shape, or perhaps a tapering capillary drilled with micro holes. Even after constructing such a device, precise control of the pH in the duct would be complex.

Heat — It has been shown that at temperatures between 40 and 50 ° C, the modulus of silk dope increases by two orders of magnitude from base level of 10^4 to 10^6 Pa (Holland et al., 2006b). If controlled gelation can be achieved in this temperature range, the flow field may be able to orient the silk molecules more effectively to form crystallites in a more natural silk-like morphology. Control of the precise amount of heat that each molecule of fibre receives as a function of reeling speed may be difficult.

Light — Spectroscopy enables the vibrations of the bonds making up the dope to be quantified. The protein structure could be excited using infrared radiation of between 1100 and 1800 cm^{-1} (9000- 5500 nm) (Boulet-Audet et al., 2011) until specific bonds are altered or broken. This would require an accurate and controllable laser. Lasers of this wavelength range and accurate to ± 20nm are available, but at restricted frequencies. This may limit the bonds that can be targeted.

Magnetism — Magnetic fields have been shown to orientate molecules in the direction of the field, and it may be that a specific magnetic field can be designed that will orientate the silk protein molecules in a manner that creates better fibres. It is likely that very large magnetic fields would be required, and this is a little-studied area so would require significant background work.

For the purposes of the second section of this chapter, heat-induced gelation combined shear stress with the chosen method of delivery via tapering glass capillary was chosen as the simplest method likely to yield novel results. The aim was to test the hypothesis that heating a dope whilst it is sheared within a capillary can induce the conversion from silk dope to natural silk-like fibres. This conversion should then enable spinning of fibres with better tensile properties than fibres formed simply by drying thin filaments of silk dope. In the literature, there are many reports of

silk spinning, but none were found that use elevated temperatures to improve spinning. There are cases of using heat to stabilise (Weiguo et al., 2011), or to endow specific functions (Guohong et al., 2012) to post treat spun fibres. There are many reports of using heat to assist spinning of other materials, for example to electrospin gelatin-sodium-alginate-water by heating water at ~45 ° C to prevent premature coagulation (Moon and Farris, 2009), and conventional melt spinning of polymers, but in these cases the heat governs an entirely different process. Patent CN102181957, "Preparation method for regenerated fibroin fiber" relates to spinning regenerated silk fibroin (RSF) fibres using heat from 5-35 ° C, and patent CN102134757 "Preparation method of regenerated silk fibroin fiber and product thereof" relates to spinning RSF from 10-30 ° C using a microfluidic chip, but it is clear they are not using temperature to induce gelation of the protein from the temperature ranges employed.

To test the hypothesis, fibres were spun using the syringe pump and tapered capillary described in the previous Chapter 6, with the addition of heating a small length of the glass capillary. The resultant fibres were tested for solubility in water and tensile tested. Rapid solubility of the produced fibres in water indicates that the silk dope proteins have not been successfully converted to a silk-like confirmation, and this can be confirmed by tensile tests finding brittle fibres. A positive result would be insoluble fibres that exhibit both elastic and yielding behaviour when tensile tested.

The Chinese silkworm *Bombyx mori* was used as the source of silk dope rather than from other silkworms or spiders, due to the large volume of dope that can be extracted with fairly homogenous and widely-studied properties allowing for valid repeat experiments. *Bombyx mori* silkworm ducts were dissected as detailed in the methods chapter.

8.2. Methods

The spinning device consisted of the following distinct components pictured in Fig. 8.1: a movement generation syringe pump connected to a spinning nozzle containing feedstock, the taper surrounded by a gelation initiator. Feedstock emanating from the tip of the capillary was

reeled onto a collecting rod, made in such a way that it could be moved horizontally. Development and detailed descriptions of the components are in Chapter 6.

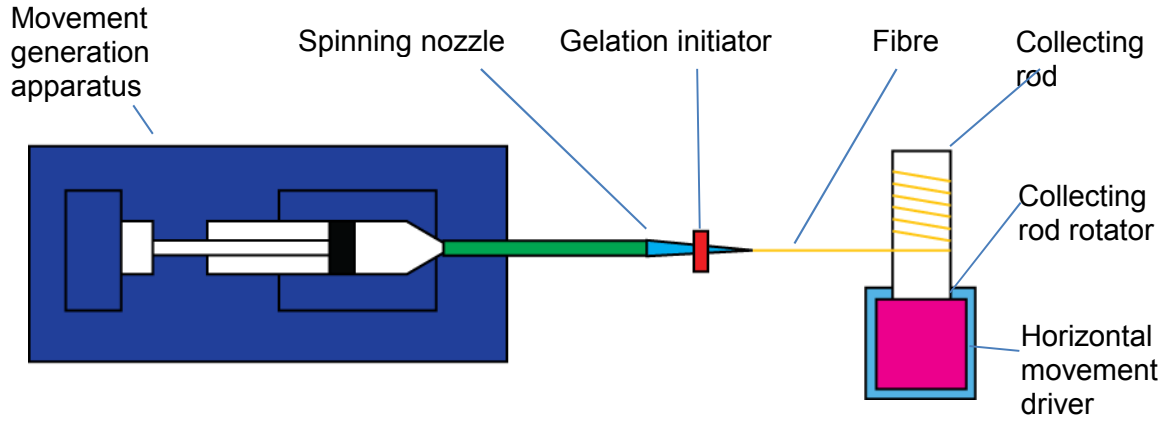


Fig. 8.1 Schematic overview of components used in spinning device

Bombyx mori silkworm ducts were dissected as detailed in the methods chapter. The proximal limbs of each gland storage sack adjoining the secretory tail were carefully peeled in distilled water, and the sericin-free dope within (Magoshi et al., 1994) collected into a 1 ml centrifuge tube and left overnight at 4 ° C to settle.

Borosilicate glass capillaries of 1mm outer and 0.78 mm inner diameter (Campbell) were pulled into tapers using a micropipette puller as described in the methods chapter. Capillaries were truncated at different lengths to find a length that would allow continuous spinning without drying of the dope, and subsequently imaged at 100x magnification.

As described in the development of the spinning device, Chapter 6, 'Hot coil 2' was used to heat the capillary. Fibres were reeled at the following temperature bins: ambient temperature, 40 ° C, 45 ° C, 50 ° C. The heating device was then upgraded from a heated coil to a Peltier plate. For a full description of the work that this upgrade required, is contained in the spinning development chapter.

Fibres were collected onto the 10 mm diameter rod at speeds noted in Table 8.1. At each of these speeds a fibre was first spun at room temperature, and then the temperature was incrementally increased and the speed and temperature combination for each given fibre was noted.

Table 8.1 Reeling speeds

Speed (mm/s)	0.38	0.45	0.52	0.58	0.65	0.79	0.92	1.05	1.19	1.21

Solubility of fibres was tested using techniques described in the methods chapter.

Spun fibres were unwound from the rod, mounted on 5mm gauge length card frames, tensile tested at ambient room temperature and humidity at a strain rate of 50% per minute and their cross sections were measured using techniques described in the methods chapter.

Fibre polarization was measured using a Metripol quantitative polarization microscope (Oxford Cryosystems). Dry fibres were measured through a 10x objective at three different wavelengths which were subsequently combined in the microscope's software to calculate the absolute value of polarization delta in accompanying software: see the Methods chapter for more details.

Scanning electron microscope (SEM) images were taken in a SEM (Jeol Neoscope JCM-5000) calibrated using standard electron microscope grids.

8.3. Results

8.3.1. Initial screening trials to scope problem.

The first test was whether a capillary was needed to spin fibres at all. This showed that simply pulling fibres more than 10 mm long from a droplet of silk dope with tweezers was not possible, as they broke before drying to solid fibres.

The shape of the capillaries made by the capillary puller was investigated and compared to published and my own data for spider duct dimensions from chapter 3 as shown in Fig. 8.2. The length of the 'long' capillary closely matched the length of spider ducts found in nature, and the distal 9 mm of this capillary closely matched the natural duct, although the initial radius of both capillaries was considerably larger to enable feedstock loading. Unfortunately, dope forced through the 'long' capillary taper (even with the distal 5 mm removed) or the 'short' capillary did not reach the tip of the capillary under the pressure from the syringe pump. However, for a 'short' capillary with the distal 1 mm removed, dope could be forced through the capillary and would form a droplet at the tip. Shorter but similarly tapered nozzles were subsequently investigated, as shown in Fig. 1.3.

Fig. 8.2 Dimensions of capillaries as compared to silk ducts from the literature (Kojic et al., 2004) and (Vollrath and Knight, 1999)



Fig. 8.3 Comparison of lengths of short capillary used for spinning. The dope could not be forced through capillaries the length of the top three, but would move through and form a droplet at the end of the bottom two capillaries. Scale bar: 0.5mm

When short capillaries were cropped very short, dope adhered to the capillary exit surface, resembling the 'Barus' effect or 'die swell' in conventional polymer extrusion. Known solutions to this problem are to increase the length to diameter ratio of the spinneret, or reduce the viscosity of the spinning solution (Matsumoto et al., 1996). Reducing the viscosity was not possible when using native dope, so a range of capillary lengths were investigated (illustrated in Fig. 8.3) before stable flow of dope was achieved by truncating the taper to 2 mm less than 'as-pulled', and pumping sufficient dope through to form a droplet around the tip. The larger surface area of the droplet dehydrated at a slow enough rate to allow filaments of wet silk dope to be drawn, from which the water subsequently evaporated to leave a fibre. This is shown in Fig. 8.4 (A), where a fibre is pulled from a 'one Luer one seal' nozzle using tweezers on a divider.

If the drawing rate was increased to be higher than the rate of dope flow through the capillary, the droplet formed at the capillary exit would be drawn into fibre and dope would come straight from the capillary. Unfortunately, spinning fibres more than 4 mm long from a capillary without a droplet at the capillary tip was not possible, since the drawn dope would dry to the capillary tip. Any further pulling would break the already existing fibre, rather than pulling away the dried dope from the capillary tip and pulling fresh dope from the capillary.



Fig. 8.4 (A) Image of fibre spinning from 'one Luer one seal' nozzle using tweezers on a divider (B) Image of mist to rehydrate the droplet being fed to the tip of the nozzle

In order to prevent the fibre drying onto the capillary tip, a mist of distilled water generated by a piezoelectric membrane (Maplin Mini-Fogger Mist Generator) was directed at the tip of the nozzle as shown in Fig. 8.4 (B). This technique was successful in rehydration for a short time, but the water within the dope would quickly evaporate again once the misting was halted. Also, it was not possible to spin simultaneously with even a little, highly directed mist, as the spun fibres became wet and broke, so the misting attempt was abandoned.

Although spinning from a droplet may result in any shear stress induced by the capillary being lost as the proteins relax to a quiescent state, there is evidence that fibrils formed from any shear that occurs above a certain threshold is irreversible (Porter and Vollrath, 2008, Holland et al., 2012b), so it was hoped that if shear above this threshold could be induced, spinning fibres from the droplet would be successful; seeing the droplet as a sort of hydration seal round the fibre.

Spiders spin at a range of speeds of at least 3 μm/s (Holland et al., 2012a) to 1.3 m/s (Ortlepp and Gosline, 2004), though this lowest recorded speed for spider spinning is almost certainly outside this normal behavioural range, as the alignment of the molecules is low at slow rates (Riekel et al., 2000), and the range is extended due to mechanical action of the spinnerets to enable spinning at slow rates (Riekel et al., 1999).

Fibres were drawn from the droplet at the distal end of the capillary at rates from 0.2 mm/s to 2 mm/s, rates within the range in which spiders are able to produce silk. To compare the flow

conditions between the natural and capillary flow, the Reynolds number Re can be used (Equation 8.1), since shear rate inside the droplet is not calculable. Table 8.2 gives the values of the parameters used, and the resultant Reynolds numbers.

$$Re = \frac{density.velocity.diameter}{viscosity}$$ Equation 8.1

Table 8.2 Comparison of rheological properties in spider and capillary

	Spider	Capillary	Spider data reference
Feedstock density	Equivalent		
Feedstock viscosity	Equivalent		
Feedstock velocity (m/s)	$3*10^{-6}$ – 1.3	$2*10^{-4}$ – $2*10^{-3}$	(Holland et al., 2012a), (Ortlepp and Gosline, 2004)
Fibre diameter (m)	$3*10^{-6}$	$1*10^{-3}$	(Vollrath and Knight, 2001)
Reynolds numbers	$9*10^{-12}$ – $3.9*10^{-6}$	$2*10^{-8}$ – $2*10^{-7}$	

The results of the calculation show that the Reynolds numbers used here in artificial fibre spinning are within the range of those successfully spun by spiders. Therefore, the capillary geometry that produced these values from instrument settings of heat 550, pull 20, velocity 180 and time 8 (arbitrary instrument units) described as the 'short capillary' in Fig. 8.2 was used for the remainder of the spinning experiments.

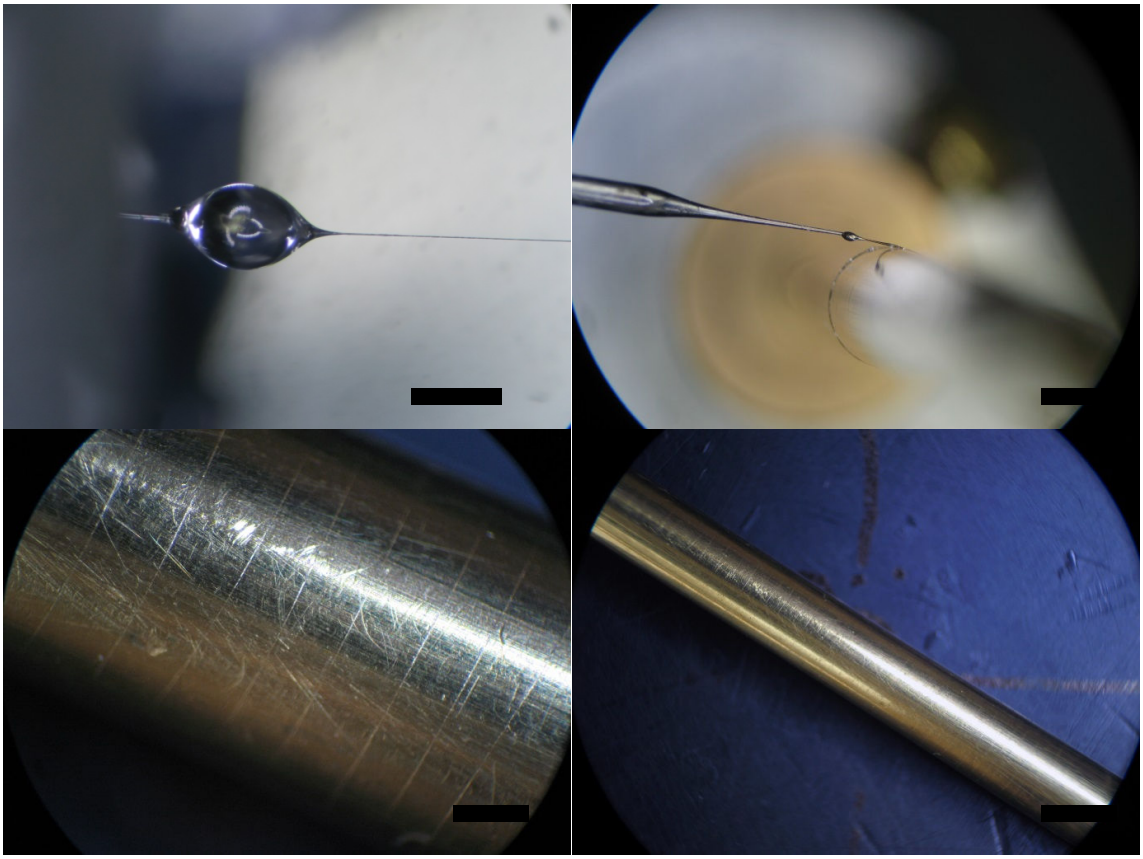


Fig. 8.5 Images of fibre spinning (A) Droplet emerging from capillary with fibre, scale bar 0.26 mm (B) Fibre pulled onto reel, scale bar 2.4 mm (C) Fibres on reel, scale bar 0.6 mm (D) Reel covered with fibres, scale bar 3.4 mm

The mechanical properties of the fibres are shown in Fig. 8.6. The figure shows fibres with low breaking strength of below 100 MPa (except just one extraordinary fibre which broke at 240 MPa), and brittle fracture at below 3 % strain. The resultant fibres were found to be soluble in water. The very short length of the fibres produced, their failure strength, and their solubility in water is an indication that the dope was not converted at the molecular level into true silk fibres.

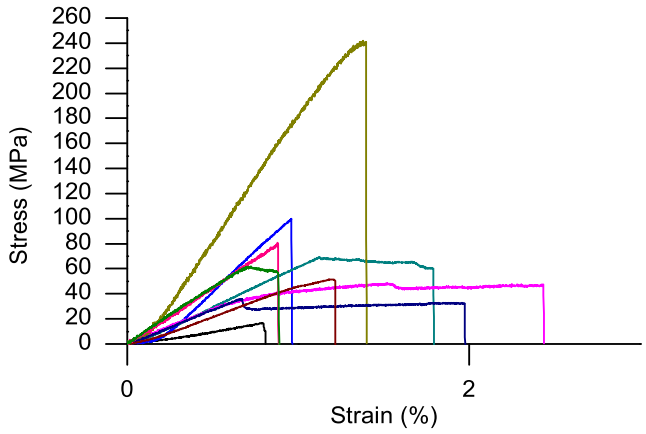


Fig. 8.6 Tensile properties of fibres spun from native dope, from a capillary with a droplet, at ambient temperature

8.3.2. Temperature augmented spinning

The next section describes the results of spinning with a droplet using heat to induce gelation of the silk dope in the capillary. Fig. 8.7 gives a schematic of the spinning device used.

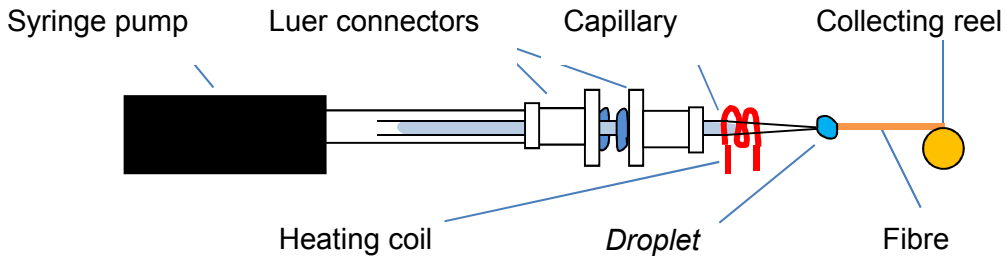


Fig. 8.7 Schematic of setup using heating coil around capillary

Using an electrical coil to heat the capillary, fibres were successfully spun through heated, tapered capillaries, into a droplet, and onto a reel. The thermostat regulating the temperature of the hot coil in which this trial experiment was only accurate to within ± 2.5 ° C, which was a problem if a precise measure of temperature at which fibres were spun was required. Therefore a Peltier device was used, which was capable of heating the capillary to within ± 0.1 ° C. Using the Peltier and copper disc to heat the capillary, over 10 m of fibres were spun from speeds of 0.38 to 1.21 mm/s and temperatures of 22 to 50 ° C, and mounted on paper frames. As the temperature of the hot

copper heating disc approached 50 ° C in each temperature ramp trial, the spinning process became increasingly unstable and the spun fibre became more brittle, until it finally broke. This demonstrates the consistent effect of heat induced denaturation on the properties of silk dope.

Fig. 8.8 shows the tensile results of fibres using a hot coil as the heating method formed by drawing from the droplet using tweezers mounted upon the micromanipulator. These show a wide range of tensile results, with little correlation between the breaking stress of the fibre and the temperature at which it was reeled. The lowest breaking stresses are 20 MPa with breaking strains of 2 %, while the highest breaking stresses are 120 MPa with breaking strains of 12 %.

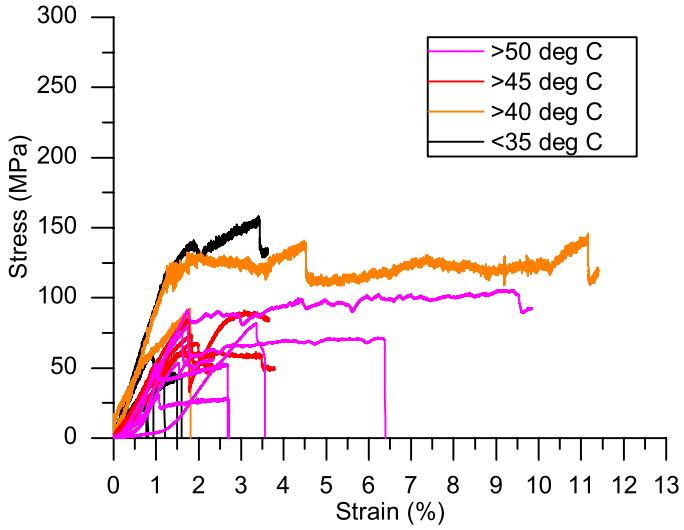


Fig. 8.8 Fibres spun by drawing by tweezers, variable temperature as marked in legend (° C)

Fig. 8.9 shows tensile results of fibres collected at constant speed onto the 4 mm diameter reel using the heating coil. Different reeling speeds were required at each temperature to counter changes in viscosity of the feedstock as the heat increased, as expected from the heating and viscosity profile of silk (Holland et al., 2006a). The tensile results are similar or exhibit slightly reduced failure stresses to the results in Fig. 8.8, though with one fibre that was spun at 45 ± 2.5 ° C had a remarkable and not reproducible breaking stress of over 500 MPa, and a strain at break of 25 %.

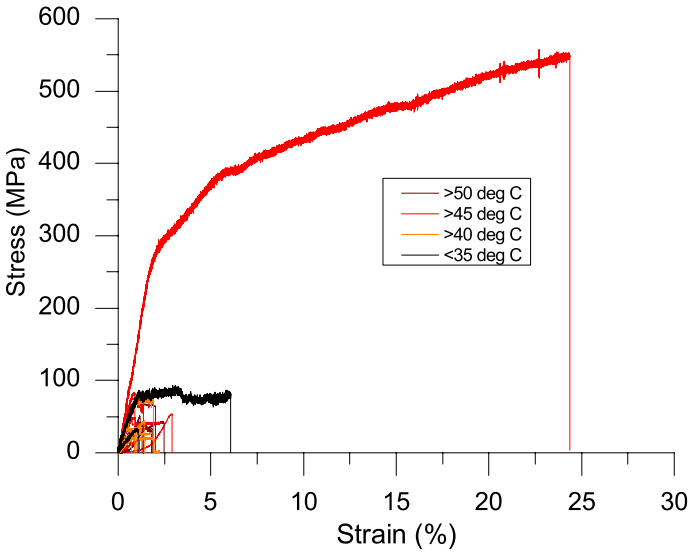


Fig. 8.9 Fibres reeled from droplet at constant speed, variable temperature as marked in legend (° C)

Fig. 8.10 shows the tensile results from a set of fibres all reeled at a constant speed of 0.5 mm s^{-1}. This was achieved by altering the pressure generated by the syringe pump to maintain a stable droplet. This figure shows that though the range of properties of fibres at 45 ° C is much wider, the maximum stress in fibres spun at 50 ° C is much lower than the average for fibres spun at 45 ° C. This suggests that denaturation of the silk proteins occurred, and the fibres produced consist of more disordered and less hydrogen bonded structures. This result shows that heating has an observable effect upon the properties of the fibres being spun.

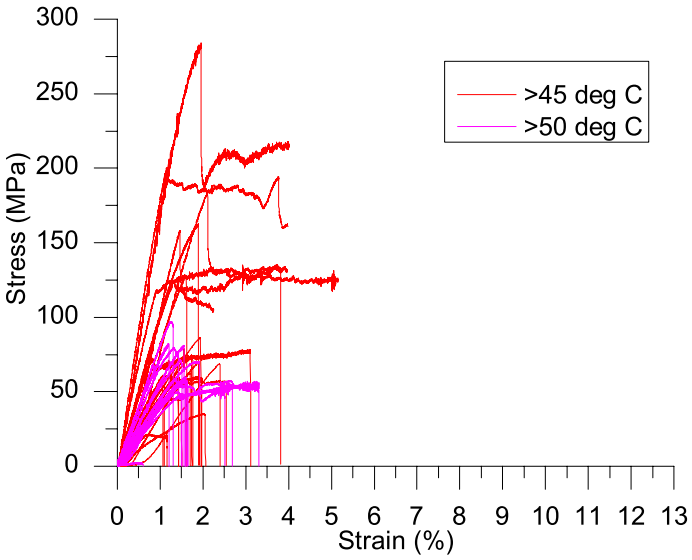


Fig. 8.10 Constant reeling speed for whole fibre, variable temperature as marked in legend (° C)

Although the majority of fibres spun using a capillary coil and droplet with gelation induced by a heated coil broke at stresses below 200MPa and 5% strain, a small number of fibres exhibited significantly better properties. Fig. 8.11 plots the best three fibres of Fig. 8.9 and Fig. 8.10 together, in comparison with fibres spun immediately adjacent to each of these fibres.

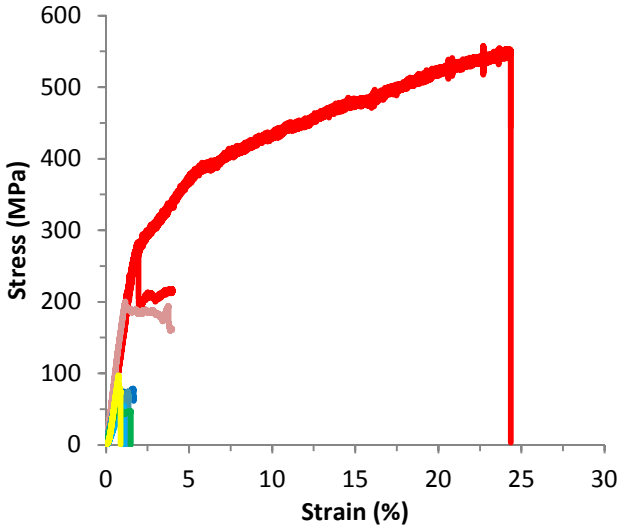


Fig. 8.11 Comparison of best fibres and their nearest neighbours, all spun at 45 degrees centigrade. Blue lines indicate results of fibres that were soluble in water, red that were insoluble. These results are taken from adjacent fibres, i.e. a fibre with properties marked by a red line was spun immediately before or after a fibre with properties marked in blue.

From observation the fibres in Fig. 8.11 can be separated into two different groups: fibres that broke at stresses above (red lines) or below (yellow and blue lines) 100 MPa. In this particular sample, fibres with low breaking stress all brittle fracture, whilst fibres with better than 150 MPa breaking stress exhibit some yielding before failure. As the difference in tensile properties between two fibres from adjacent frames appeared to be of such magnitude, it must be assumed that there is some mechanism that enables this step-change in tensile properties. The figure shows that fibres were created with breaking stresses above 150 MPa and strains of better than 3 % on multiple occasions from different feedstocks, but it is not clear what lead to these properties as the fibres surrounding them do not exhibit the same properties.

Producing fibres with exceptional properties could be very exciting, so care must be taken to verify results are not due to contamination. This verification was performed using other characterization techniques in this chapter.

Fibres spun through a heated copper disc from each of the combinations of heat and reeling speed were tensile tested, and the results combined in Fig. 8.12. The figure shows that none of the fibres had properties with breaking stresses of higher than 110 MPa or strain before breakage of more than 7 %. From observation there does not appear to be a correlation between temperature and either stress or strain of these fibres.

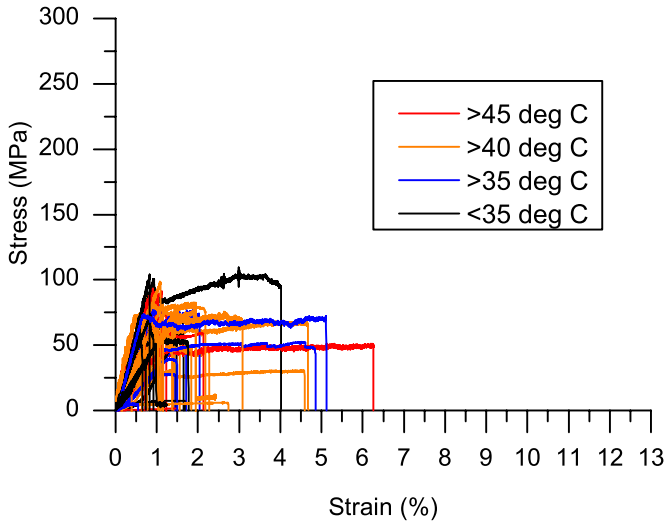


Fig. 8.12 Tensile results of fibres spun from a droplet through a capillary using a Peltier for heat generation, at a range of spinning speeds. Legend notes spinning temperatures.

8.3.2.1. Meta-evaluation:

To better visualise how the properties may arise from the combination of speed and temperature of the fibres spun from Peltier and hot copper disc, speed and temperature were set as the axes of plots, with the colour of the plot denoting the value of the data. If there were a specific combination of conditions that produced fibres with good properties, this would be shown on the graph by an area of one colour, surrounded by contours of decreasing properties. As shown in Fig. 8.13, there does not appear to be a correlation between speed, temperature and the maximum tensile stress of the fibre in the fibres reeled in this experiment.

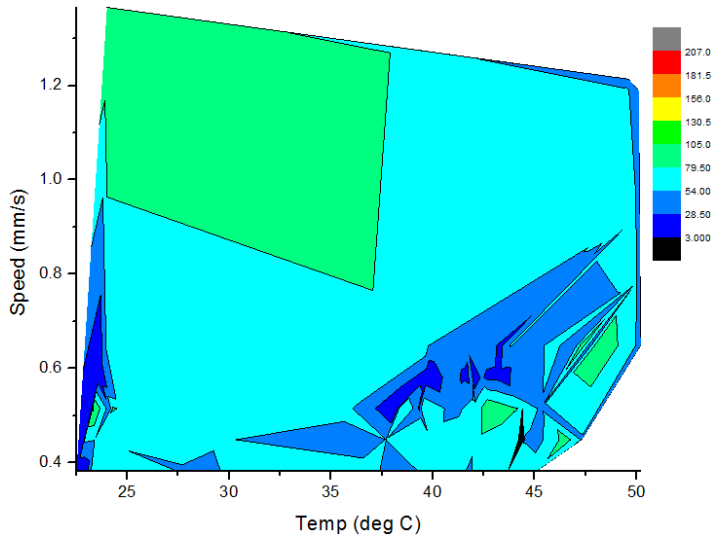


Fig. 8.13 Maximum stress in fibre (MPa) matrix as result of reeling speed and temperature

The plot for initial modulus, shown in Fig. 8.14 as a function of speed and temperature, has large areas of homogenous properties similar to the plot for tensile stress. In areas where a larger number of data points are present, specifically at a temperature of 46 ° C and a reeling sped of 0.5 mm s^{-1} there may be a point where fibres with better properties cluster. Unfortunately the best properties here did not come close to matching the properties of fibres previously produced, despite near identical spinning device and probable temperature range.

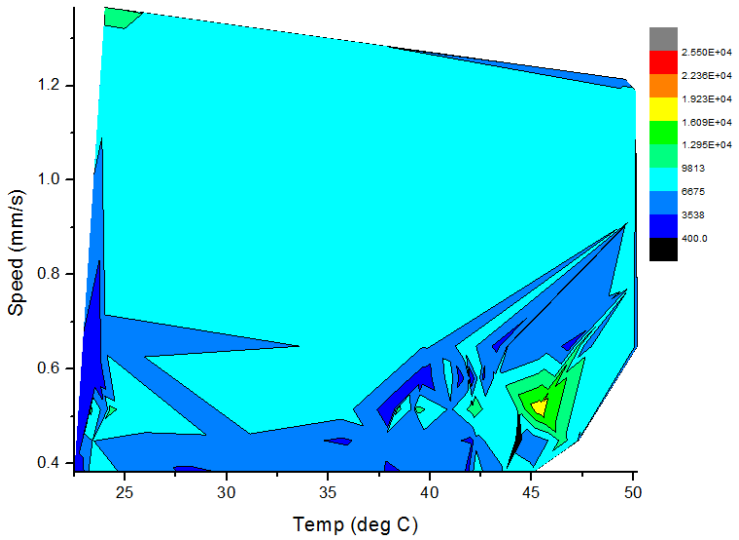


Fig. 8.14 Initial modulus (MPa) matrix as result of reeling speed and temperature

8.3.3. Fibre analysis

In general, the mechanical properties of fibres spun in these screening trials are highly variable and inconsistent, with no clear trends emerging to develop relationships between spinning conditions and properties. Additionally, the tensile results of fibres spun through a copper disc heated by a Peltier show mechanical properties that did not approach those of some of the fibres spun using the hot coil, or even without heating. Since the Peltier device was clearly giving a more reproducible heating effect, this suggests that some undefined aspects of the spinning process is giving an effect on fibre structure that can dominate heating and shear stress. Some spun fibres were analysed in a search for mechanisms that might affect properties.

A small number of fibres spun using the hot coil as a gelation initiator were tested for their degree of polarization. Images of two of the fibres are shown in Fig. 8.15 (A) and (B), for which the software calculated a delta value of 10 for the fibre pictured in the left hand image (breaking strength >450 MPa) and a delta of 2 for the fibre on the right (breaking strength <100 MPa, from stress strain curves shown in Fig. 8.11). Although only a preliminary polarization study, there appears to be a major difference in polarization between the fibres. This suggests that the stronger fibre is much more highly oriented at the molecular level.

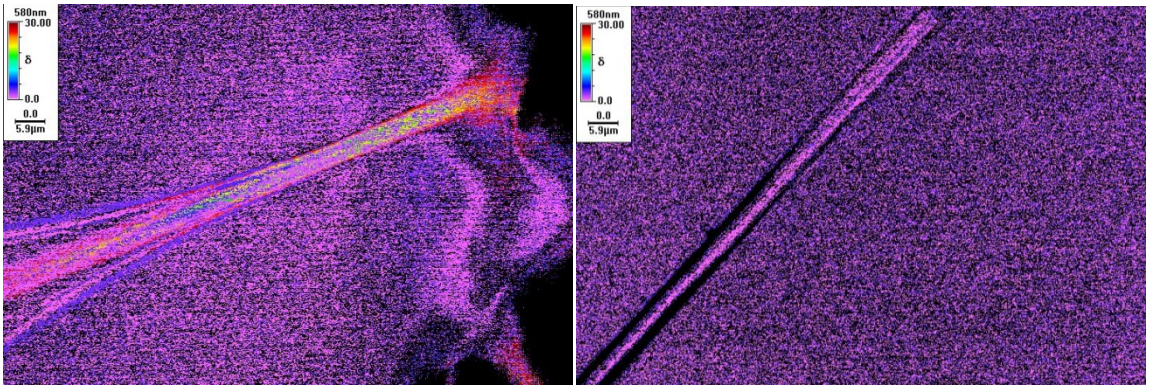


Fig. 8.15 (A) Fibre that failed at 500 MPa. Delta = 10. (B) Fibre that failed at ~50 MPa. Delta = 2

When tested for solubility the fibres spun with a breaking stress of less than 150 MPa dissolved in fewer than 10 seconds from the point of immersion in distilled water. Fibres with breaking stress of ~180MPa took 10 minutes to dissolve (plotted in red on Fig. 8.11), and the fibre which failed at

500MPa appeared to be insoluble. This result indicates that there has been a step change in material properties between the two groups of adjacently spun fibres.

Fig. 8.16 shows the breaking point of four representative fibres spun at 20, 40, 45 & 50 ° C. Despite the range of spinning temperatures, each have similar core-coat morphology similar to that of fibres spun from pure fibroin solution (Jin and Kaplan, 2003) and natural spider silks (Li et al., 1994), though unlike natural silk these layers are probably due to drying of the fibre (as the Barus effect removes most or all the effects of shear flow), probably resulting in the two stage tensile results. It may be assumed that the initial steep modulus section of the tensile test is due to forces being shared by core and coat combined, and the drop in stress occurs when the stiff outer coat fractures. The core then stretches without a corresponding increase in force.

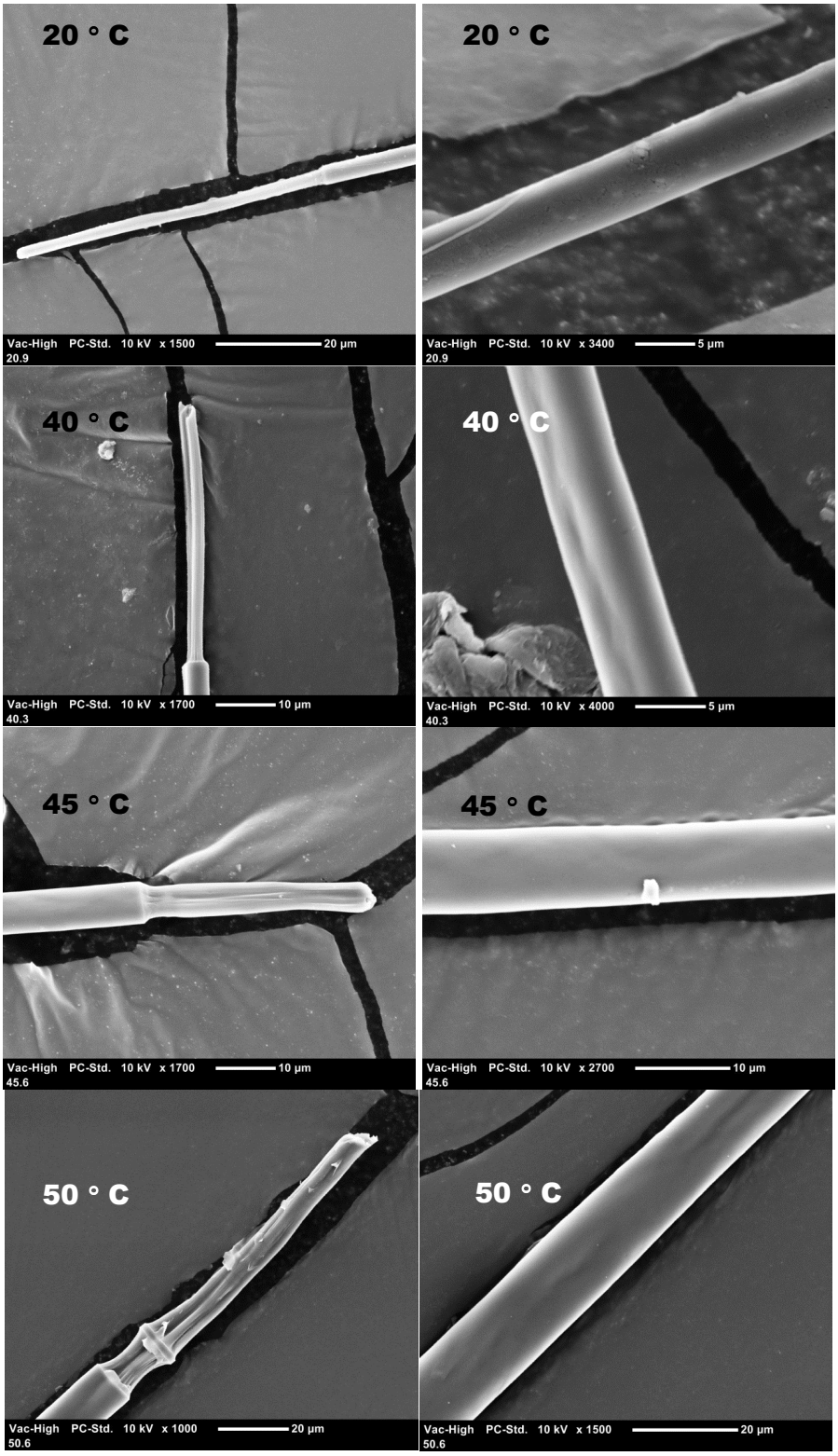


Fig. 8.16 Morphology of fibres spun at 20, 40, 45 and 50 ° C. Scale bar shown in each image.

In comparison with the previous fibres shown in Fig. 8.16, the fibres with the ‘step change’ in tensile results show markedly different morphology (Fig. 8.17, all fibres). The fracture surface does not show the core-coat morphology with extended lengthening of the core, but rather shows a fairly uniform break or very short core. The fibre itself appears extremely uniform in diameter and has a smooth surface, in comparison with the often bumpy outer surfaces of the fibres with poor tensile properties (Fig. 8.16, all fibres). The third fibre is the exception to this smooth surface, with some undulations detectable. These undulations present may help to explain why this fibre broke with the lowest breaking stress 200 MPa of the three ‘step change’ fibres.

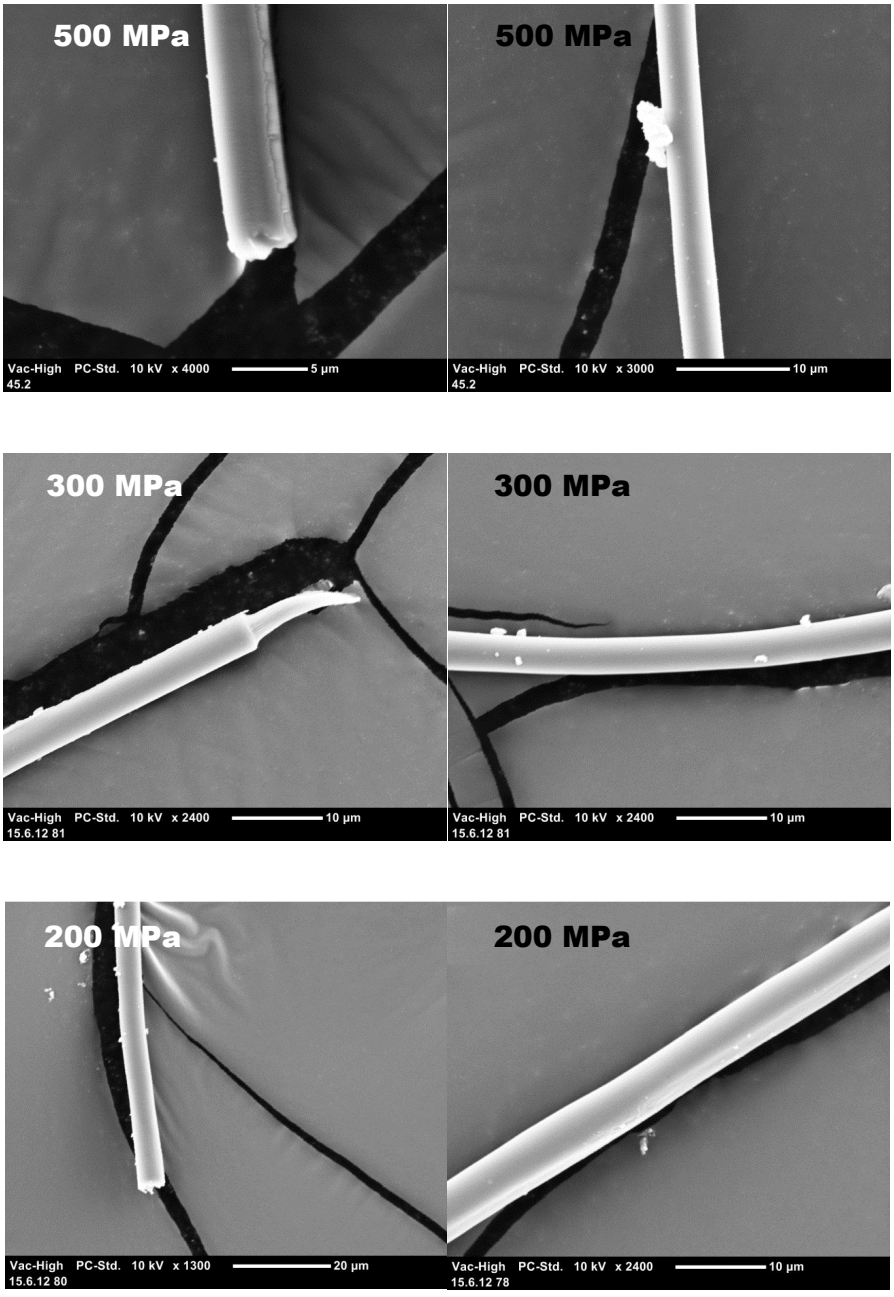


Fig. 8.17 SEM micrographs of the fracture surface and general morphology of insoluble fibres, with breaking stress noted.

Unlike the fibres that failed at a stress higher than 150 MPa with a fairly smooth fracture surface, the majority of the thin fibres fractured in two stages (shown in the tensile tests and SEM images): first, the stiff outer coat broke, followed by a stretching of the inner core at constant force. I hypothesized that the coat was transformed by the shear into material with good properties, but the inner was not transformed. To test this hypothesis, I calculated the relative strength of the

fibres' outer coat. Normal calculation of stress in a tensile test assumes homogenous material properties through the fibre, so the stress is calculated from the overall diameter of the fibre. Using ImageJ software (NIH), I measured the diameter of the outer coat of the best fibre from each speed from the SEM micrographs and from this calculated the cross section assuming a circular fibre. From these cross sections and the maximum force of the fibre from raw tensile data, I then recalculated the maximum stress on the outer coat. The results of this calculation are shown in the subsequent table.

This recalculation shows that the maximum stress that the material is able to resist before breakage (mean of 154.5 MPa) was still significantly below that of the strongest fibre spun with the hot coil (543.85 MPa).

Table 8.3 Recalculated stress values using only the outer coat cross section

Temperature spun	Speed spun (mm/s)	Coat diameter	Core diameter	Max force (N)	Area annulus (m^2)	Stress (MPa)
45.8	0.38	5.8	3.8	2.58E-03	1.54E-11	167.7
47.2	0.45	4.0	2.6	9.85E-04	7.70E-12	127.9
24.4	0.52	6.2	4.2	3.82E-03	1.62E-11	235.5
42.3	0.58	5.8	4.1	3.11E-03	1.34E-11	232.2
50.6	0.65	3.8	2.2	6.75E-04	7.38E-12	91.5
50.6	0.78	7.5	4.6	2.72E-03	2.76E-11	98.4
50.7	1.19	6.2	3.8	2.99E-03	1.92E-11	156.2
49.9	1.21	6.1	4.6	1.59E-03	1.26E-11	126.3

Mean	0.72	5.7	3.7	0.002309	1.49E-11	154.5
Std. dev.	0.3	1.1	0.8	0.001035	6.10E-12	51.7

8.4. Summary and discussion

This chapter documents a series of initial screening trials for bioinspired synthetic spinning of fibres from natural silk dope. These trials on spinning conditions were conducted in parallel with development of the spinning device hardware, reported in Chapter 6, and the results of both pieces of work are clearly linked inextricably together. Before a final series of 'controlled' spinning trials are reported, it is useful to summarise the results of the screening trials and see what lessons have been learned from experimental observations that can be generalised quite fairly as being very inconsistent and variable, with generally poor performance of fibres produced by spinning processes that were very different from those occurring in natural spinning glands.

The rheology and spinning processes observed in these extended spinning trials, both with and without heating zones, could not reproduce those in natural spinning glands, despite a comparable level of shear to that which occurs in nature. From the start, no internal draw-down of the fibres into the spinning capillary could be induced, and stable spinning without fibre breaking was only possible by pulling a fibre from a droplet formed at the capillary exit. In many ways, this would be expected to render the shear flow in the capillary largely redundant, since the droplet might be expected to consist of silk dope that has relaxed from its flowing state, back into isotropic dispersion. However, different conditions did have measurable effects upon fibre properties, albeit that the effects were highly variable, as discussed below.

A generalised spinning situation is shown schematically in Fig. 8.18, with the main variable parameters labelled for clarity.

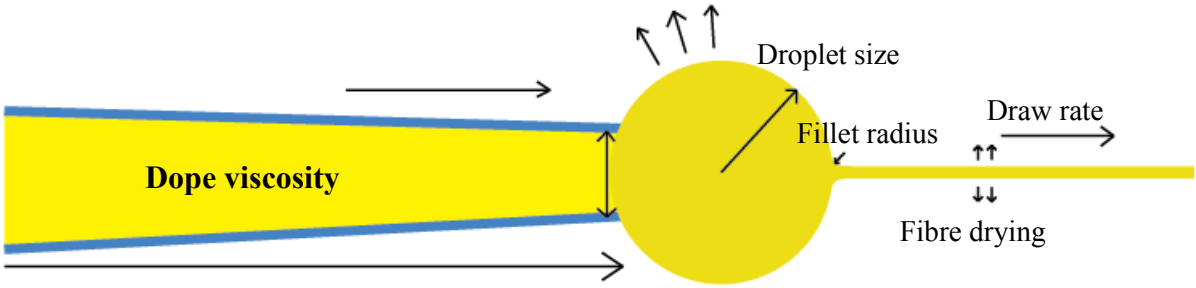


Fig. 8.18 Parameters involved in droplet spinning

Properties of fibres spun simply with various geometries of tapered glass capillaries under ambient conditions were consistently poor. They were easily soluble, had little birefringence, and had very poor mechanical properties; essentially they looked like fibres of dried silk dope. The provisional conclusion was that spinning simply with shear stress did not produce natural silk-like fibres, even under the same nominal flow rates as those in natural spinning glands.

The next step was to try to induce some sort of gelation in the silk dope during the shear flow in the capillary, with the aim of increasing macromolecular extension and orientation. Heating the dope to about 45 ° C did often induce stepwise changes in tensile, polarization, solubility and fracture imaging properties of spun fibres, which we assumed to be caused by the proposed gelation effect (Holland et al., 2006a). A small number of the fibres produced by heating with a hot coil had properties substantially better than the majority of spun fibres. The variation in properties between adjacently spun fibres may indicate that a narrow temperature range and heating duration is required to produce these desirable fibres, which the equipment used was unable to maintain.

In retrospect, I note that the very few fibres with good overall properties were spun with the heating coil arrangement, which was replaced by more stable and better controlled Peltier-disc device. The inability to re-spin fibres with desirable properties using only slightly modified heating equipment was surprising, given the multiple instances in which they previously occurred in uncontrolled circumstances from different feedstocks. The temperatures of the coil and the

Peltier-disc were calibrated to the best of the ability of the coil control, although there was a difference in heating volume (coil wrapped to surround a ~5mm length of the capillary as compared to the copper disc surrounding a ~1.5mm length of capillary). Heating had an effect on the rheology of the dope, so the flow rate increased thereby decreasing the exposure time of the dope to heat. This shows the system was very difficult to control. Since the precise effect that heating has on silk protein solution is unknown, it is possible that brief unstable periods of heat above a certain threshold may allow particular structures to be induced in the dope under shear that are advantageous for fibre properties, whilst prolonged exposure to the same heat simply induces general denaturation with structural disorder that cannot be manipulated under shear. This naturally leads to the hypothesis that the extended meta-evaluation of a wide range of heating conditions was intrinsically flawed by having too long a heating zone that denatured the silk dope into an inappropriate structure that could not be converted by shear flow into a good fibre structure. It may be that certain levels of stresses of multiple types is required to reach the threshold of gelation, and this requirement is not being met here.

Another possibility in these screening trials is that there were one or more factors that were not measured or controlled, but greatly affect the fibre properties. For example, one aspect which was observed to fluctuate was the size of the droplet from which the fibre was spun, which is controlled by many factors as shown in Fig. 8.18. It is likely that the size of the droplet and the speed which fibres are drawn from it has an effect on the core-coat morphology, due to the replacement rate of the fluid relative to the drying rate. To demonstrate this, the lifetime of an evaporating droplet can be evaluated using the following simplified relationship (Keyes et al., 2008),:

$$t \approx \frac{R^2 \rho}{2D\Delta C} - F \qquad \text{Equation 8.2}$$

with the following parameters: t time, R initial radius, ρ density of evaporating fluid, D diffusion constant of material in exterior gas, ΔC concentration difference between the centre and surface of the droplet, F is the volume of fibre removed. This simplified model shows that spinning

conditions are complicated by the silk dope on the surface of the droplet that dries to form a layer that inhibits further solvent evaporation and fibre production. The different states of the dope on the surface and interior of the droplets and the spinning fibres may be the cause of the core-shell fibre morphology observed in facture imaging, but was not investigated in greater detail.

Another problem may be that any orientation is not fixed: the droplet formation means orientation induced in duct flow is not retained- there is no intra-duct gelation to keep orientation in position. Whilst there is a formation of droplet due to die swell any orientation already present is lost.

In summary, these screening trials show that a way to spin fibres directly from the capillary tubes with internal draw-down is needed, without the intermediate step of pulling the fibres from a droplet of dope at the end of the spinneret. It was not possible to induce the correct form of gelation in the spinning dope by heating, which allows the correct protein structures to develop in the fibres during shear flow.

Chapter 9. Controlled shear spinning

9.1. Introduction

The previous chapter showed that inducing a droplet of native silk dope at the tip of a tapered glass capillary was required to spin fibres, otherwise fibres would dry at the capillary tip and break very quickly. However, fibres spun from a droplet have very different processing rheology to natural fibres and also resulted in highly variable fibre properties. Therefore, to spin fibres in a stable manner requires a method or treatment that would allow spinning without the need for a droplet.

Furthermore, in the previous chapter, it appeared that spinning at temperatures between 45 and 50 ° C could very occasionally result in fibres with mechanical properties that approached those of natural silk fibres. If a method could be found to spin fibres without a droplet, the heat instability experiment could be repeated to search for conditions that produce good fibres, but with controlled and flow conditions similar to natural silk.

The overall aim of this work was to use observations of natural spinning glands and processes to guide the development of synthetic silk spinning devices. Chapter 4 showed that the walls of both silkworm and spider spinning ducts contain chitin or chitosan, which are biological polymers that can be hydrophobic (Le Tien et al., 2003, Liu et al., 2003, Beppu et al., 2007). Therefore, a hypothesis was formulated that making the final stages of the spinning device hydrophobic would remove the intimate contact required for stress transfer in shear flow between the capillary walls, and thereby induce extensional flow and perhaps some degree of internal drawdown in the dope to nucleate fibre formation. If nothing else, it might inhibit sticking of the dope to the capillary and reduce the frequency of breaks in the fibre. A good indicator of this would be to eliminate the need for droplet spinning.

While there are numbers of references to hydrophobicity and silk fibres in literature (Tanaka, Inoue et al. 1999; Motta, Migliaresi et al. 2002; Geisler, Pirzer et al. 2008; Manoudis, Karapanagiotis et al. 2008; Lu, Zhang et al. 2011), there is little reference to the effect of hydrophobic surfaces on silk dope

itself, so the outcome of applying a hydrophobic treatment is hard to predict. Out of possible substrates, PDMS is the polymer most frequently used for making microfluidic devices (Zhou et al., 2010). This polymer is intrinsically hydrophobic (Bodas and Khan-Malek, 2007) and the hydrophobicity can be improved by surface treating PDMS using lasers to induce surface roughness (Khorasani et al., 1996) or applying NaCl (Khorasani et al., 2005). However, when used with silk, PDMS must be treated with a block copolymer to prevent the silk proteins sticking to the walls (Rammensee et al., 2008).

Instead, since borosilicate glass capillaries have been used in the previous spinning experiments in this work, it seemed appropriate to try to make the ends of the glass capillaries hydrophobic. Glass can be treated to be hydrophobic in a number of ways: a coating of hydrophilic silica (SiO2) nanoparticles within poly(methyl methacrylate) (PMMA) solution (Manoudis et al., 2008), polymeric coatings such as low density polyethylene treated with plasma (Fresnais et al., 2006), and using perfluoroalkylsilane (PFAS) and tetraethoxysilane (TEOS) (Jeong et al., 2001), for example.

In this work, a commercial perfluoroalkylalkylsilane treatment ('Aquapel' Pittsburgh Glass Works (Franz et al., 1996)) was used for its proven reliability and ease of use. The contact angle of distilled water on untreated and treated glass was measured as reported below which quickly showed that this treatment was simple and highly effective in making surfaces hydrophobic. The next step, to treat the previous glass capillary spinnerets, is reported below in terms of its effect on the flow of natural silkworm and spider silk dope to produce fibres.

The results of tensile tests (detailed below) showed these fibres to be extremely poor in comparison to natural fibres. In addition, the fibres were soluble in water which was hypothesized to be due to a lack of beta-sheet crystals. These attributes were hypothesized to be due to a lack of order within, unlike silk which has high orientation (Rousseau et al., 2009). Order (defined as the quantity and quality of hydrogen bonds within the material) can be increased by taking the material to its glass transition temperature (by using either or a combination of heat and humidity) to mobilise the disordered fraction of the protein and permit hydrogen bonds to form between chains (Guan et al., 2013). A set

of annealing processes were selected as a combination of humidity and temperature from this work. to try and produce some measurable change in the fibre properties.

The properties of fibres spun from capillaries treated with perfluoroalkylalkylsilane, both with and without heat instability treatment, were then tested in the usual way for solubility in water, birefringence, tensile properties and within a dynamic mechanical thermal analyser, DMTA.

In summary, this chapter tests the bioinspired hypothesis that using a capillary with a hydrophobic tip could permit fibre spinning with natural silk dope without the need for a droplet, and potentially induce internal draw-down in the capillary to produce fibres with improved, or at least less variable, properties.

9.2. Materials and methods

Adult *Nephila edulis* and sericin-free *Bombyx mori* silk dopes were obtained as described in the Methods chapter. *Bombyx mori* cocoon fibres for comparison were unwound from three typical cocoons, degummed by agitation at 60 ° C for 5 minutes per wash in two washes of sodium carbonate solution at 10 g per litre of distilled water, and rinsed in two washes of distilled water (Yamada et al., 2001).

For hydrophobicity tests, standard glass microscope slides (Menzel-Gläser) were cleaned in 70 % technical alcohol solution and after being allowed to dry were either left uncoated or were coated in a silica and perfluoroalkylalkylsilane solution (Pittsburgh Glass Works 'Aquapel') as per the manufacturer's instructions. Three 300 µl droplets of water were dispensed from a pipette (Gilson Pipetman) onto the centre of both uncoated and coated slides. Sessile droplets were imaged with a digital camera through a stereo microscope (Canon Powershot A640, Olympus SZ4045TR). Contact angle was measured from the images with ImageJ software (NIH).

Nozzles to be coated were immersed in Aquapel solution from the tip to the start of the taper, and using a syringe the solution was sucked into the capillary to the same depth. The nozzles were then

removed from the solution, and excess solution was blown from within the capillary using air at 1 bar supplied by a compressor (Jun-Air OF203-25).

Droplet adhesion to the capillary was tested by extruding a minimal amount of silkworm dope through the capillary, and the droplet imaged with a digital camera through a stereo microscope (Canon Powershot A640, Olympus SZ4045TR).

9.2.1. Fibre spinning

Artificial silkworm dope fibres were spun through treated 'two Luer' nozzles using the techniques and apparatus described previously. Artificial spider dope fibres were spun through identically treated 'shortened Luer' nozzles using a procedure modified to accommodate the very small volumes of feedstock as detailed in the methods chapter. Both sets of fibres were collected upon a 10 mm diameter polished aluminium rod at a speed of 0.3 mm s^{-1}. Spun fibres were unwound from the rod and mounted on 5 mm gauge length card frames as described in methods chapter.

9.2.2. Annealing

One quarter of the fibres were left as-spun (indicated in results by the initial 0), one quarter were humidity treated (indicated by the initial T), one quarter were heat treated (H), and the final quarter were both humidity and heat treated (TH). Humidified samples were left overnight in a plastic box at room temperature, supplied with humidified air via a tube connected to a gas bubbler filled with distilled water and powered by air pressure from a compressor (Jun-Air OF203-25). This resulted in the humidity within the box fluctuating between 80 and 86% as measured by a lab instrument (Oregon Scientific ETHG913R). Control samples were left in a box at equivalent temperature and duration.

Post 'humidity' treatment for the first set of fibres consisted of leaving them in a gentle stream of compressed air, resulting in a humidity of 30-35 % for 60 minutes. Control samples were left in a box at the same temperature for the same time. Post 'heat' treatment consisted of heating at 60 ° C for 20

minutes. Control samples were left in a box in a gentle stream of dry compressed air resulting in a humidity of 30-35 %.

9.2.3. Fibre characterization

Three fibres each of conditioned and non-conditioned treatments were tested for solubility in water as described in the Methods chapter. Fibre polarization was measured and calculated using a quantitative polarization microscope (Metripol, Oxford Cryosystems) as described in the Methods chapter. Fibre diameter was also measured with the quantitative polarization microscope, as this allowed rapid and non-destructive testing of the scarce fibres. Tensile tests were performed upon the Zwick tensile tester using the techniques described in methods chapter. Samples were tested at ambient room temperature and humidity at a strain rate of 1 mm per minute. Fibre cross sectional areas for stress were calculated from the diameter provided from the quantitative polarization microscope.

Fibres with a gauge length of 5 mm were tested on a dynamic mechanical thermal analyser (DMTA) (TA Instruments Q800) with a preload calculated using a specified stress multiplied by the cross sectional area of the fibre calculated from the diameter. The instrument moved with a frequency of 1 Hz, at an amplitude of 5 μm and was performed from room temperature to -100 ° C, left to stabilise for three minutes and then heated at a rate of 3 ° C per minute until the fibre stretched to a length of > 24 mm or broke.

9.3. Results

9.3.1. Hydrophobicity

Droplets of distilled water on the upper surface of a horizontal plate of uncoated glass had a measured contact angle of 55 ± 6 °, and droplets on coated (but otherwise identical) glass plates had a contact angle of 87 ± 2 ° (Fig. 9.1). When the glass plate was angled away from horizontal, the droplet on uncoated glass slid slowly away in a wide but shallow sheet of liquid, whilst the droplet on coated glass slid quickly off without losing its droplet form. The marked changes in droplet surface contact

angle and behaviour indicated that the hydrophobic coating was effective in increasing the hydrophobicity of the glass substrate. The contact angle measured was less than the angle of 150 ° required for superhydrophobicity (Wenzel, 1936), but was similar to recorded data of 90 ° for a drop of water on a flat horizontal surface facing upwards for hydrophobic surface treatment (Franz et al., 1996).

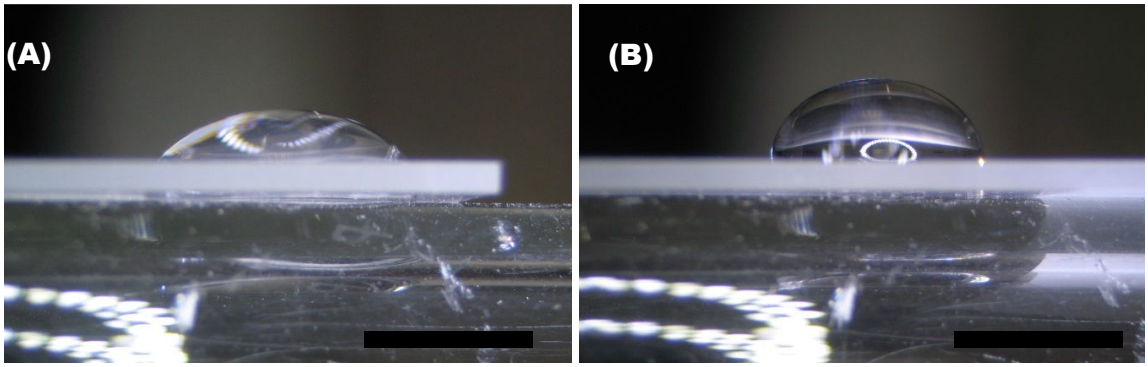


Fig. 9.1 Shape and contact angle of a single 300 µl droplet of distilled water at room temperature on (A) standard microscope slide, Contact angle 55 ° ± 6 (B) hydrophobically coated microscope slide, contact angle 87 ° ± 2. Scale bars 5 mm

Bombyx mori silk dope adhered to the outside tip of uncoated capillaries through which it was extruded, but did not adhere to the tip of coated capillaries. This behaviour is shown in Fig. 9.2 for an untreated capillary Fig. 9.2 (A), and treated capillary in Fig. 9.2 (B).

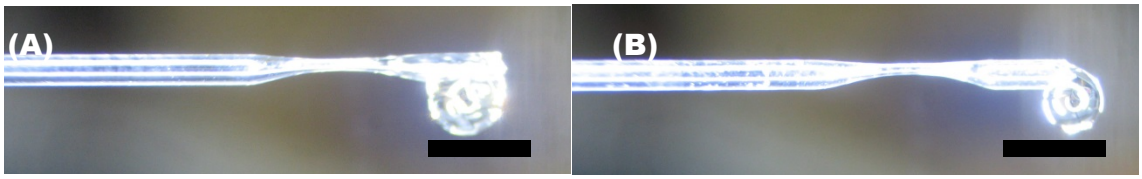
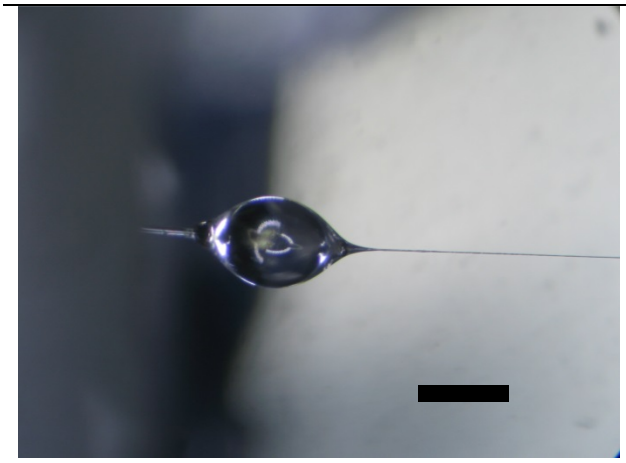
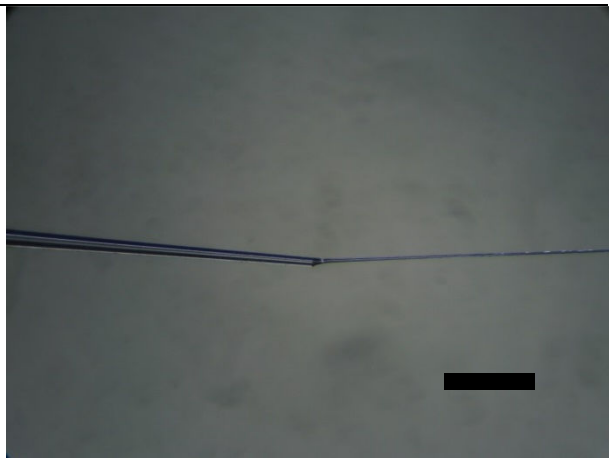


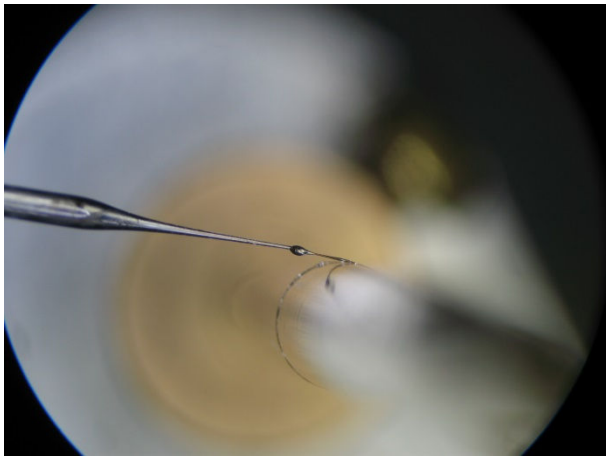
Fig. 9.2 Silk dope droplet adhesion with a borosilicate capillary by surface tension, (A) untreated capillary showing droplet attraction to the capillary. (B) Treated capillary with droplet repelled. Scale bars 3 mm.

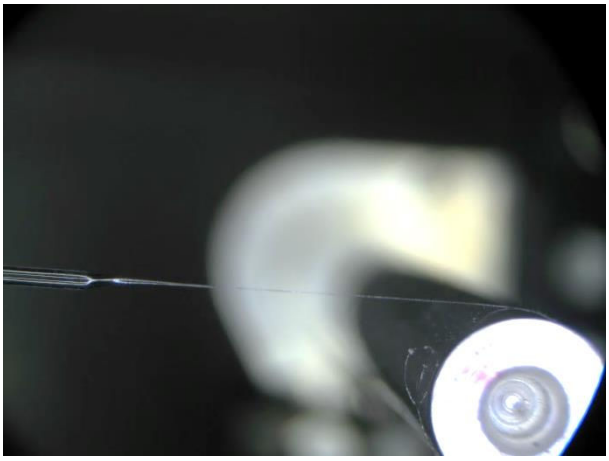
The droplet contact angle test showed that the coating imparted hydrophobicity, and extruding silk dope through uncoated and coated capillaries showed that the hydrophobic coating was capable of repelling *Bombyx mori* silkworm silk dope. From these positive results it was thought likely that the droplet could be eliminated from dope spinning and the hypothesis was tested in the next section.

9.3.2. Fibre spinning: silkworm dope

In contrast with previous spinning attempts, in which a fibre could not be spun straight from an uncoated capillary without using a droplet as a buffer, it was possible to smoothly and continuously draw fibres from the tip of a hydrophobic coated capillary without adhesion. In addition, in previous attempts, if a droplet became desiccated or spinning was paused for any reason, the capillary had to be discarded as it was not possible to pull dried feedstock from the tip. With a coated capillary, after spinning had been paused for some reason such as a problem with the spinning apparatus, dried feedstock could be pulled easily from the end of the capillary and spinning restarted. The removal of the droplet meant that spinning could be performed with relative ease, as the speed of the syringe pump, overall system pressure and reeling speed did not need constant adjustment to cope with varying droplet size and desiccation. Coating the capillary transformed spinning from being a difficult and time-consuming procedure fraught with uncertainty, to being a relatively straightforward endeavour. Contrasting images of spinning with and without droplets are in Fig. 9.3.

Untreated capillary	Treated capillary
	
Scale bar 0.26 mm	Scale bar 0.26 mm





Scale bar 2.4 mm

Scale bar 5 mm

Fig. 9.3 Comparison of droplet and non-droplet spinning

As-spun fibres dissolved in distilled water either immediately or within 10 seconds, which is a similar result to fibres spun from a droplet at room temperature, as described in the previous chapter. Therefore, it is unlikely that the fibres had been formed with a molecular structure any more sophisticated than dried silk dope. However, fibres spun from a coated capillary appeared thinner, had a smaller range of diameters (Fig. 9.4) and the smooth outer surface of the fibres suggested that the cross sectional areas were more regularly shaped than fibres spun from a droplet on the tip of an uncoated capillary (Fig. 9.5, Intensity).

In attempts to improve the properties of fibres spun from coated capillaries, fibres spun under ambient conditions were post-treated by annealing: first with high humidity of >80% for about 36 hours in order to try to exceed the local glass transition conditions in the silk fibre and encourage crystallisation; second with heat treatment at elevated temperatures of 60 ° C for 20 minutes. Note that control samples were left in a box in a gentle stream of dry compressed air, resulting in a humidity of 30-35 %.

In addition, the same treatments were applied to fibres spun from coated capillaries at temperatures between 45 and 50 ° C and were similar in diameter and appearance to those spun at room temperature, their diameter varied with a shorter periodicity and a larger number of the fibres had to

be discarded due to 'necking' of the fibre diameter present in the gauge length of the card frame, probably due to variability in the original feedstock or processing time of the dope.

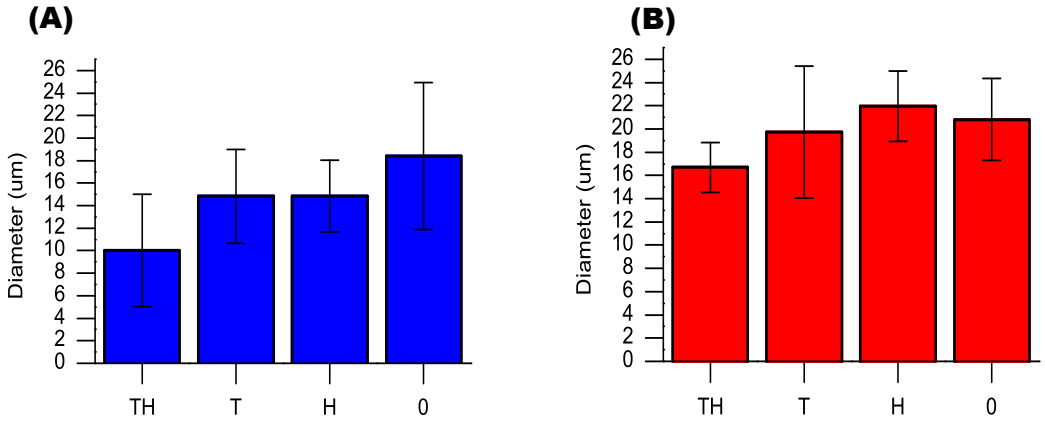


Fig. 9.4 Mean diameters after treatment of spun fibres spun at (A) ambient and (B) elevated temperatures (heated copper disc at 45 ° C), for each of the four treatments: humidity and heat (TH), humidity (T), heat (H), and none (0). Error bars represent standard deviation. N=3 fibres per treatment

All artificially spun fibres from coated capillaries were tested in comparison with degummed single *Bombyx mori* fibre brins, which were very much thinner, twisted with a periodicity of roughly 300 µm per 120 ° of twist, and with a cross section more triangular than circular.

9.3.2.1. Appearance

After humidity treatment, the fibres appeared to become more uniformly circular in cross section and had fewer obvious flaws than as-spun fibres from the coated capillary. Heat treating fibres re-introduced some flaws in the surface of the fibre, but not to the number or extent of the flaws in untreated fibres. Images of these fibres are shown in Fig. 9.5. Fibres spun at elevated temperatures showed the same pattern.

9.3.2.2. Solubility

Any humidity treated fibres and any fibres spun at elevated temperatures did not dissolve in distilled water even after repeated immersions, but instead became soft and flexible, and became stiffer again

when the water droplet evaporated. This suggests a greater fraction of beta-sheet crystallinity that is insoluble in water.

9.3.2.3. Polarisation

Of each of the treatments tested on fibres spun at room temperature, the heat treated fibres had the least orientation, followed by as-spun fibres, then fibres both humidity and heat treated, and the most orientated were fibres that were only humidity treated (Fig. 9.6). The standard deviation of each treatment was between 1 and 1.8 °. The graph appears to show that the heat treatment decreases the degree of polarization within each fibre, as heat treated and heat-and humidity treated fibres have lower values of polarization than their controls.

When fibres were spun at elevated temperatures, each of the treatments resulted in a broadly similar polarization value of approximately 4 (Fig. 9.5). The values are lower than for fibres as-spun at room temperature, and show that none of the treatments had more than a slight or negligible effect on the polarization of the fibres. These results may indicate that spinning at elevated temperatures reduces the fibres' ability to become orientated or become crystalline during treatment: a sort of heat-set of a disordered structure.

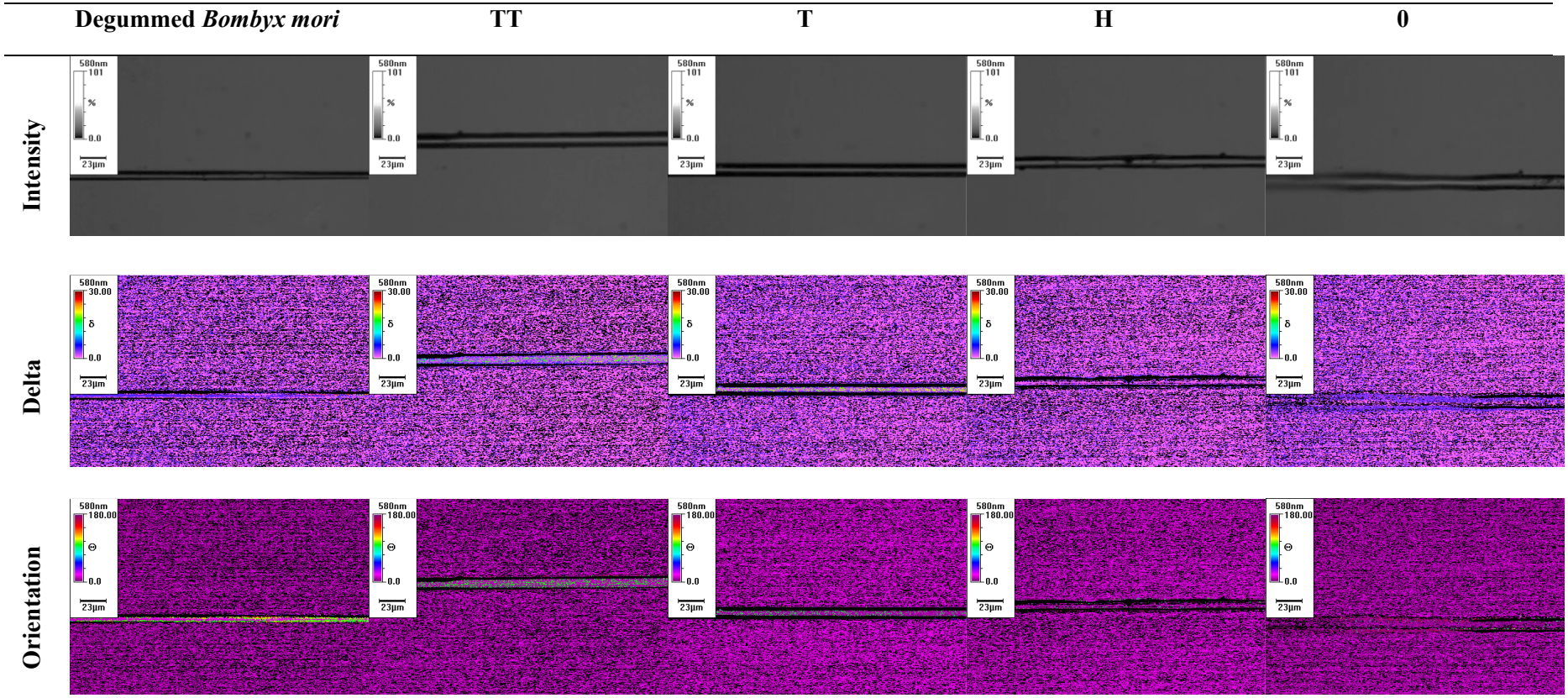


Fig. 9.5 Intensity, Delta and orientation comparison of treated fibres

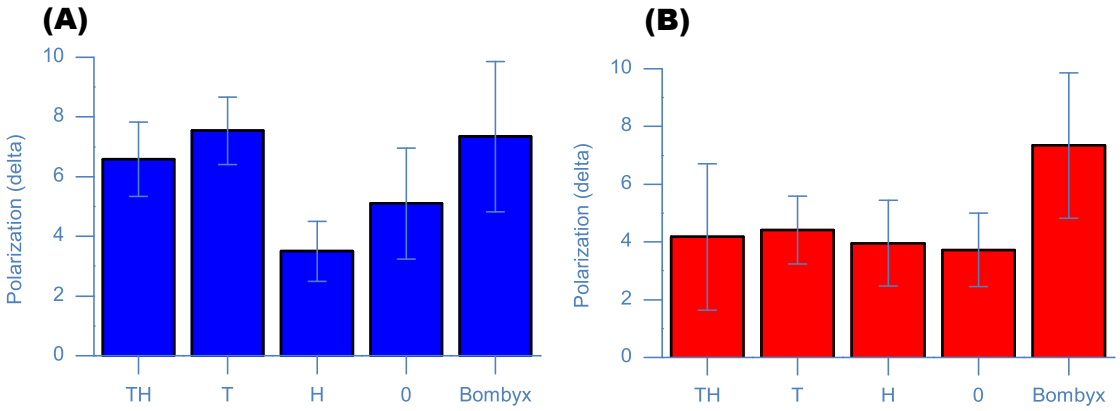


Fig. 9.6 Mean delta values for fibres spun at (A) room temperature, (B) at elevated temperatures, for each of the four treatments: humidity and heat (TH), humidity (T), heat (H), and none (0). Degummed single *Bombyx mori* fibres (Bombyx) are included for comparison. Error bars represent standard deviation. N=3 fibres per treatment

9.3.2.4. Mechanical Properties

The stress strain curves of fibres spun at room temperature without a droplet from coated capillaries had a characteristic shape of a linear but short initial modulus, followed usually by immediate brittle fracture (Fig. 9.7 (A)); only the humidity and heat treated fibres occasionally showed yield, with a short plastic flow. The different treatments resulted in modulus and maximum stress values that scaled linearly with respect to each other: humidity-and-heat treated (TH) fibres had the largest values, followed by humidity treated (T), heat (H) and finally as-spun fibres (Fig. 9.7 (B)).

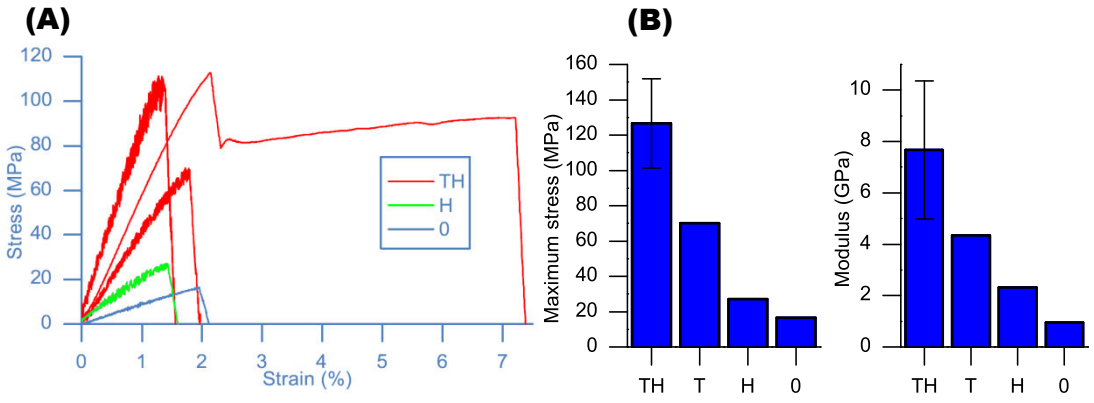


Fig. 9.7 Results of tensile tests upon fibres spun at room temperature, scales to match earlier graphs to aid comparison (A) comparative tensile curves of treated and untreated fibres, (B) comparative maximum stress and initial modulus of treated and untreated fibres. Error bars represent standard deviation. N=3 fibres per treatment for TH, 1 for T, H and 0

Fibres spun at elevated temperature without a droplet from coated capillaries had a similar characteristic shape to those spun at room temperature, but a larger proportion of the fibres exhibited a yielding section after the initial modulus and before fracture (Fig. 9.8 (A)). In contrast to fibres spun at room temperature, there was not such a clear distinction between the tensile properties of the differently post-treated fibres, with humidity-and-heat treated (TH) fibres having the highest values, but humidity treated (T) was within the standard deviation of these results for both maximum stress and initial modulus. Heat treated (H) and as-spun fibres had lower and similar results to each other (Fig. 9.8 (B)).

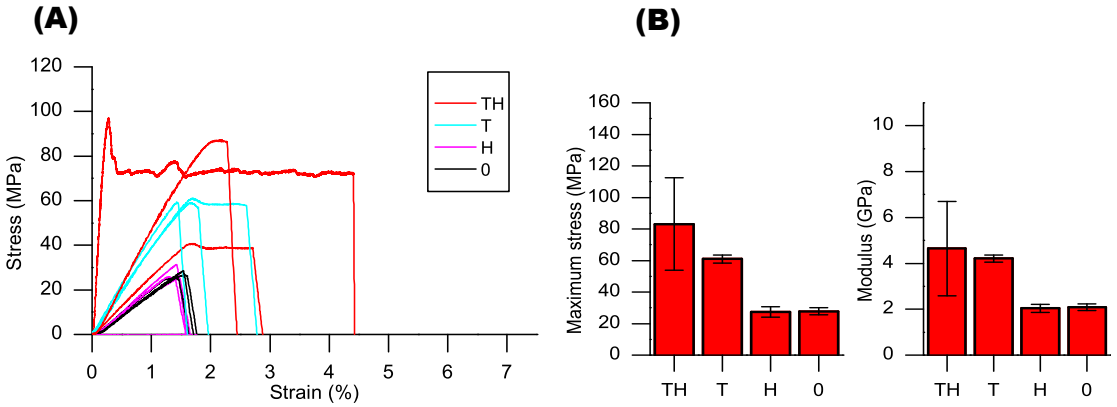


Fig. 9.8 Results of tensile tests upon fibres spun at elevated temperature, scales to match earlier graphs to aid comparison (A) comparative tensile curves of treated and untreated fibres, (B) comparative maximum stress and initial modulus of treated and untreated fibres. Error bars represent standard deviation. N=2 fibres per treatment

9.3.2.5. DMTA (tests performed in discussion with David Porter)

preload equivalent to a stress of 11 MPa (selected by calculation from tensile tests of a stress that would not break the fibres) was used for these treatments. Fig. 9.9 shows the temperature at which fibres broke in the increasing temperature ramp, and tended to occur at the glass transition temperature indicated by the peak of loss tangent and rapid increase in length due to softening under load. In this test, I also include an 'annealed' sample for room temperature spinning, where the sample was taken up to 150 ° C and then re-scanned with a fresh temperature ramp, which seemed to give improved mechanical properties, as suggested in a recent publication (Guan et al., 2013).

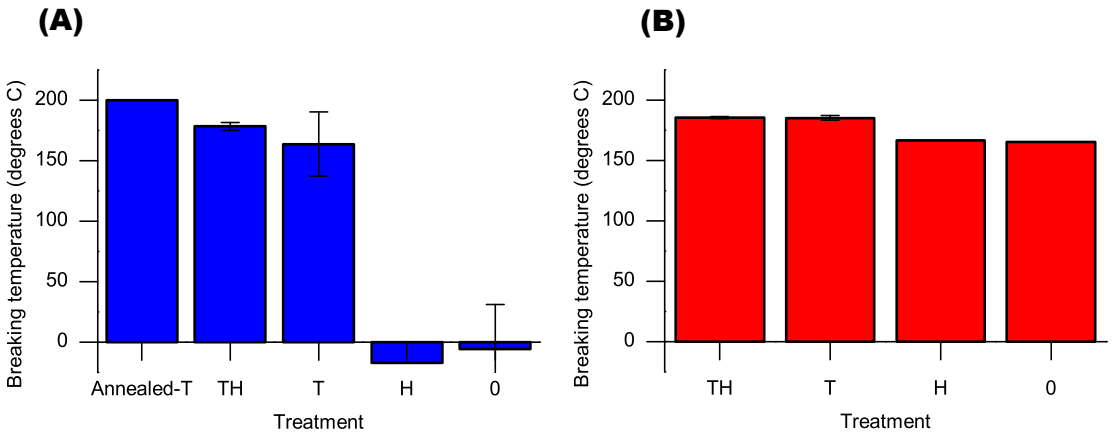


Fig. 9.9 Peak Tan delta values of DMTA tested fibres spun at (A) room temperature, with a preload equivalent to 30 MPa. (B) at elevated temperatures. Fibres with treatment TH and T used a preload equivalent to 30 MPa, treatment H and treatment 0, 11 MPa. Error bars represent standard deviation. N=1 or 2 fibres per treatment due to extreme scarcity of sample

Fig. 9.10 shows the loss tangent profile of fibres spun at room temperature with different post-treatments, and compared with natural force-reeled samples provided by Beth Mortimer that will be discussed later in this Chapter. The key point to note is that the best TH post-treated samples have a glass transition, Tg, at about 180 ° C, which indicates a relatively disordered and poorly hydrogen-bonded structure, but which can be made more ordered with a higher Tg by 'annealing' to just below the glass transition under load, or post-drawn at the initial Tg of about 180 ° C under static load by careful manipulation of the temperature ramping on the DMTA near Tg. Similar post-draw treatments have been used on reconstituted silk samples to dramatically improve mechanical properties (Yin et al., 2010, Wei et al., 2012). This, in addition to the much higher values of loss tangent through Tg relative to the natural silk fibres, indicates a much lower fraction of order obtained in the synthetic spinning process in this work.

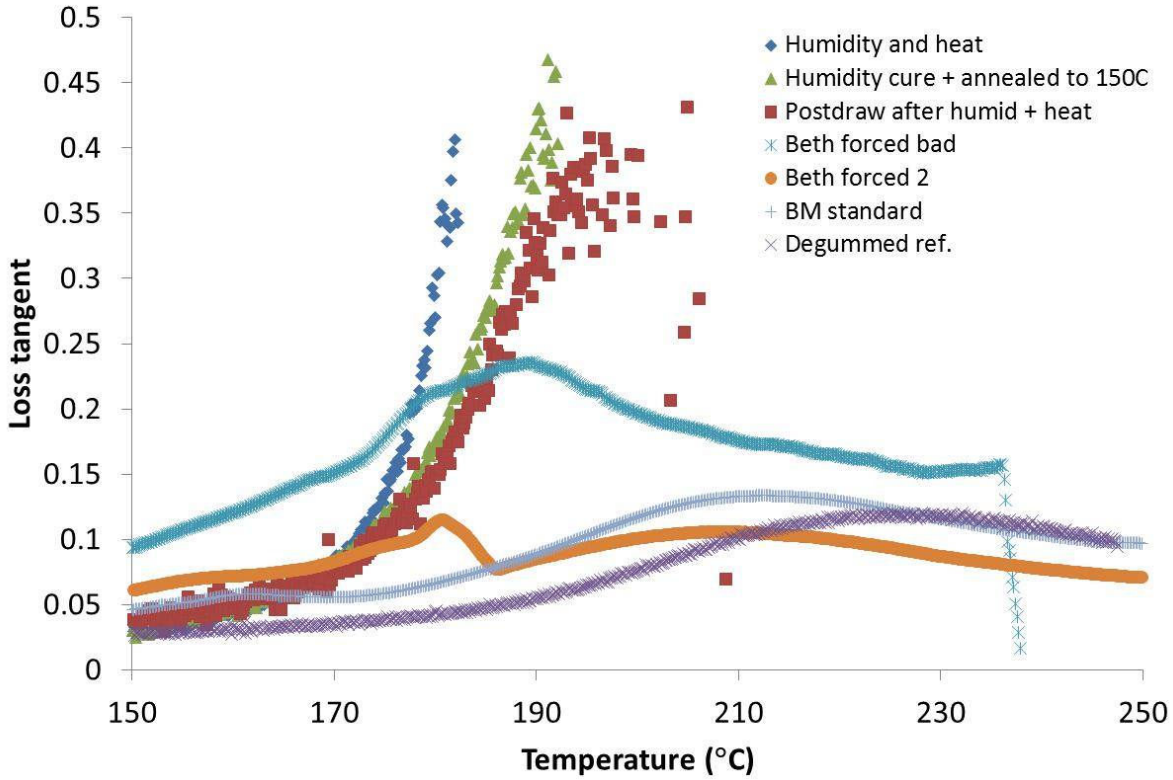


Fig. 9.10 Loss tangent of fibres spun at room temperature as compared to natural force reeled silkworm and degummed cocoon fibres, showing a clear distinction between the glass transition temperatures of fibres with different post-treatments. In the legend 'forced bad', 'forced 2' and 'BM standard' refer to silkworm fibres, 'forced bad', 'forced 2' force-reeled from silkworms by Beth Mortimer which gave poor dynamic properties for reasons not explainable at the time of thesis writing.

Fi. 9.11 shows loss tangent profiles for fibres spun at elevated temperatures with hydrophobic capillaries. The most important observation is that as-spun and only heat treated samples had a low Tg value in the range 160 to 177 ° C, which indicates a high state of disorder, comparable with RSF fibres (Guan et al., 2013) with little or no coherent secondary structure in the fibres. Fibres that had been humidity treated showed a significantly higher set of Tg values, more typical of (albeit bad) natural fibres, or RSF silk that has been post-treated to induce crystal structures by treatments such as immersion in ethanol-water mixtures (Guan et al., 2013, Yuan et al., 2010). Again, this suggests that synthetic spinning under the conditions used in this work were not able to recreate the macromolecular hydrogen-bonded structures and morphology obtained in the natural spinning process, which has very important implications for this work.

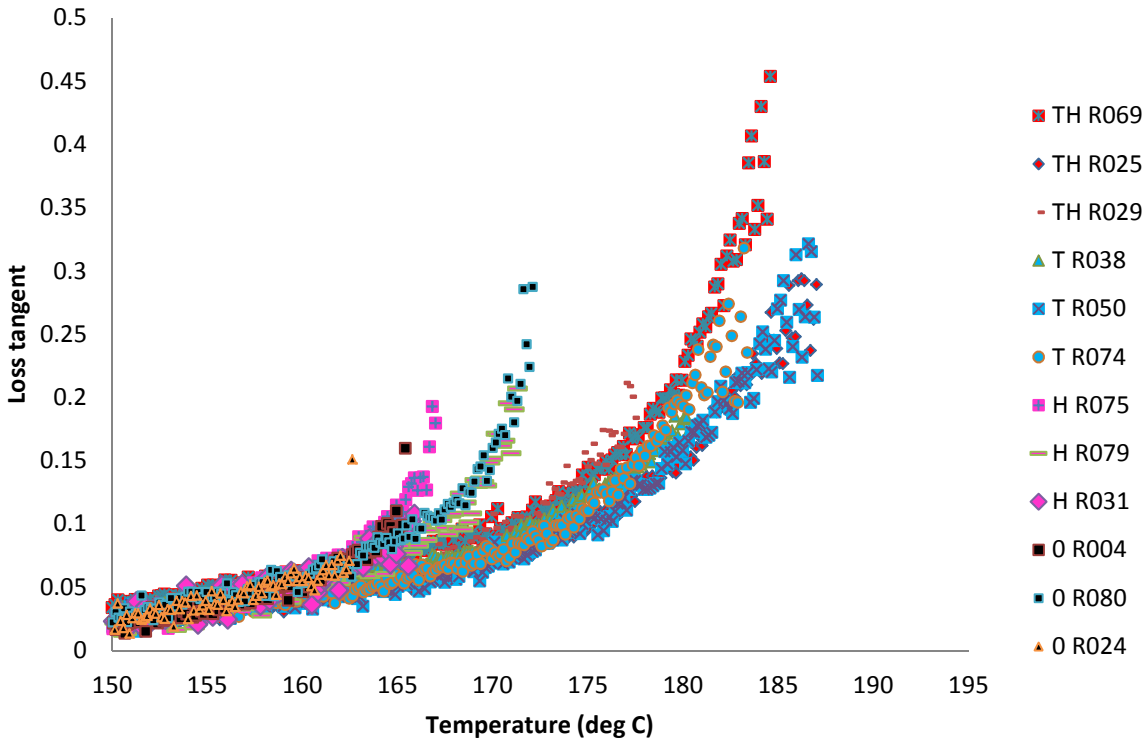


Fig. 9.11 Loss tangent of fibres spun at elevated temperatures, showing a clear distinction between the glass transition temperatures of fibres with different: humidity and heat (TH), humidity (T), heat (H), and none (0). R# indicates fibre number.

9.3.3. Fibre spinning: spider dope

Spider dope fibres were successfully spun from a coated capillary without a droplet at room temperature, without any adjustment of parameters required during spinning. Spinning speed was 0.5 mm s^{-1}, comparable to the forced reeling speed that results in spider fibres with the largest normalized breaking energy (Vollrath et al., 2001).

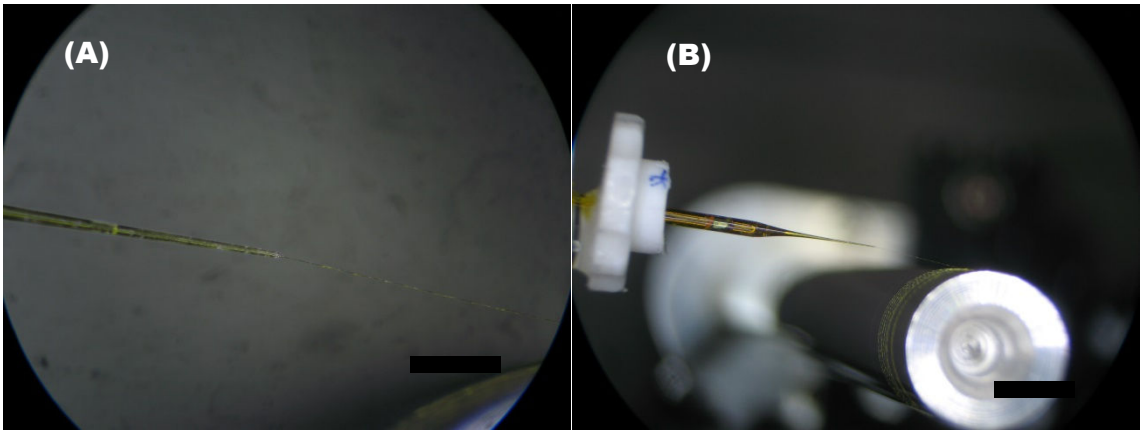


Fig. 9.12 Spinning spider fibre at rates comparable to natural fibres. (A) tip of the capillary with fibre being spun without a droplet. Scale bar 0.26 mm. (B) Overview of nozzle spinning multiple bands onto collecting rod. Scale bar 5 mm.

Unlike as-spun silkworm dope fibres which dissolved in water, as-spun spider dope fibres did not dissolve in distilled water, even after repeated immersions, but instead became soft and flexible, becoming stiffer again when the water droplet evaporated.

As-spun fibres spun from spider dope were not polarized above natural background polarization, similar to as-spun at room temperature fibres of silkworm dope.

Tensile tests of fibres spun from spider dope had a short initial elastic region, followed by a brittle fracture in a similar shape to as-spun at room temperature silkworm dope fibres (Fig. 9.13),. The maximum stress of 22.9 MPa was very low in comparison with natural fibres, as was the initial modulus of 1.3 GPa which indicates a very low fraction of hydrogen-bonded structures in the fibre.

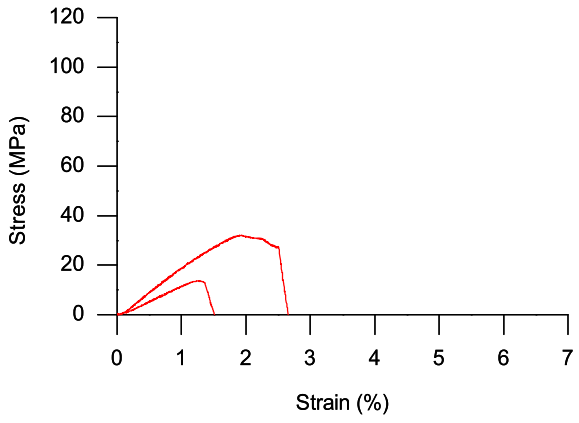


Fig. 9.13 Typical tensile results of spider dope fibres spun at room temperature.

Images of the fracture end of fibres used in tensile tests (Fig. 9.14) showed a brittle break, with no obvious distinction between core and coat of the fibre. With the maximum tensile stress of the fibre so low, it was not possible to perform a DMTA run on the fibres.



Fig. 9.14 Broken end of spider fibre after tensile test. Scale bar: 7 µm

9.4. Summary and discussion

A hydrophobic coating was applied to the inner and outer sides of a borosilicate tapering nozzle, preventing dissected silkworm and spider dope from adhering to the tip of the capillary, such that a droplet was no longer required. This allowed metres of fibre to be spun at biologically relevant controlled rates and conditions, and with a heated instability stage. The artificial fibres were characterized and compared against naturally spun fibres.

Despite spinning without a droplet and with biologically relevant conditions, including a gelation step, the fibres spun from native dope still had poor mechanical properties that were more similar to the fibres spun from regenerated silk fibroin than natural fibres. This tells us that combinations of shear stress and the heated gelation step during synthetic spinning did not produce fibres with the structure, morphology and property relations of a native silk fibre. Very occasionally, an exceptional fibre was produced with properties approaching those of natural silk fibres, but no sets of processing conditions or mechanisms could be linked in any way to these fortuitous events.

While the ‘bioinspired’ steps of being able to spin fibres using devices with geometries similar to natural spinning glands and hydrophobic exit regions represents a partial success for this DPhil work, since no other research groups have yet spun fibres with properties approaching those of natural silk, it is useful here to discuss possible mechanisms why the properties of these synthetic fibres are ‘poor’ relative to natural fibres. The first point is why the fibres are intrinsically brittle, and the second point is what can be done to improve the spinning process to remove this brittleness and allow the fibres to attain their potential strength (Porter et al., 2013).

Some materials are brittle because their constituent molecules cannot move relative to each other under load to dissipate mechanical energy by plastic flow, such that elastic energy accumulates and generates free surfaces or cavities that eventually join up to form a brittle fracture surface. Materials are ductile if their yield stress (at which point large-scale plastic flow can develop) is less than the brittle failure stress. Porter (Porter, 1995) has shown that the brittle failure stress can be quantified by the product of the elastic modulus and the loss tangent in a material, and for polymers the yield condition or loss tangent is equivalent to an elastic strain of about 0.025. This tells us that the polymer will be brittle if the value of loss tangent is below 0.025 under test conditions.

Tensile stress-strain observations on spun silk fibres shown in Fig. 9.7 and Fig. 9.8 show that the fibres break in brittle mode at strain values in the range 0.01 to 0.02. Fig. 9.15 shows DMTA temperature scans on two fibres spun under ambient conditions with heat-and-humidity and heat post treatments. Note that the value of loss tangent does not rise above 0.02 until the onset of the glass transition peak at low values around 150 ° C. Porter has shown that the elastic strain is equivalent to the product of temperature rise and thermal expansion coefficient, which is shown as a model line in Fig. 9.15 using the calculated value of 0.0002 K^{-1} for silk (Porter and Gould, 2009). The point where the model elastic strain line crosses the experimental loss tangent curves predicts the brittle failure point of the silk fibres, which lies in the observed range of 0.01 to 0.02 and is associated with a relatively low failure stress due to the modulus values in the range 2 to 5

GPa. This discussion is based upon literature models for post-drawn regenerated silk (Yin et al., 2010).

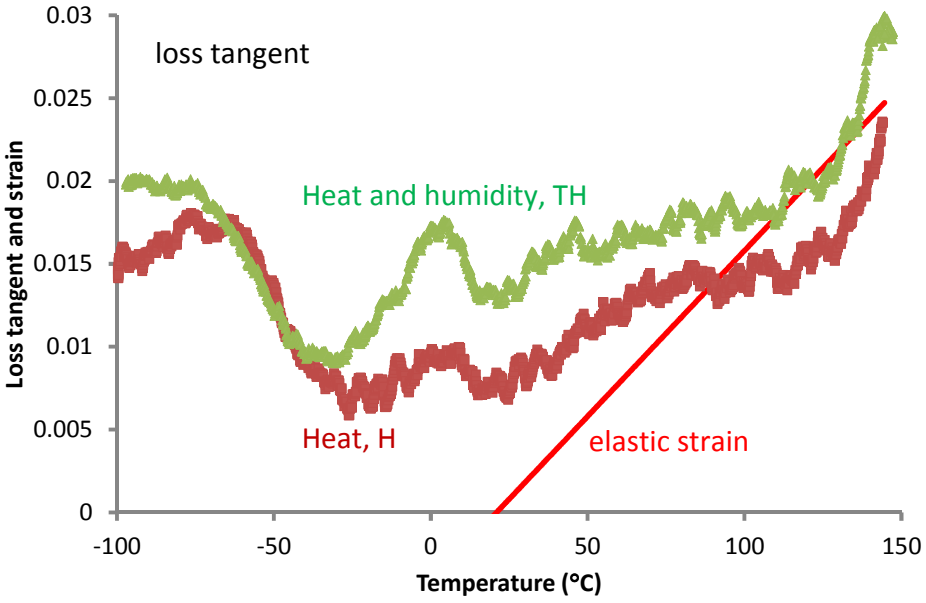


Fig. 9.15. DMTA scans of a heat and humidity (TH) and heat (H) treated fibres spun at ambient temperature

Low values of tensile modulus, loss tangent and glass transition temperature have been associated with poor hydrogen bonding in silk structures (Porter et al., 2005, Vollrath and Porter, 2006, Guan et al., 2013), so a general conclusion is that synthetic silk spinning gives a molecular structure with poor hydrogen bonding, which may be associated with highly disordered structures, such as regenerated silk (Yuan et al., 2010, Yin et al., 2010, Wei et al., 2012). In order to reduce disorder and increase interchain hydrogen bonding, the molecular chains must be at least partially aligned. This is how post-drawing reconditioned silk fibres under high humidity improves failure stress significantly.

The question now is how to align the silk molecules during spinning to remove the need for post-draw. Perhaps this requires the correct type or combination of gelation out of the possible types of entanglement, crosslinking, non-linear polymerization, crystallization, helix formation, , complexation, hydrogen bonding and covalent bonding (Jones et al., 2009). So how does natural spinning induce order and alignment with good hydrogen bonding between chains? Recently, two

papers were published back-to-back in Nature that suggested that the terminal groups in silk proteins are specifically destabilised by changes in pH and/or ionic concentration along the spinning gland to promote self-assembly for fibre formation (Askarieh et al., 2010, Hagn et al., 2010). This was followed quickly by a paper that suggested a specific alignment mechanism during spinning, whereby the terminal groups are destabilised by decreasing pH towards the end of the spinning gland and the middle section of the protein chains are then stretched and aligned in the flow field as the tethered ends are pulled apart, as shown schematically in Fig. 9.16 (Gaines et al., 2010).

Fig. 9.16 Proposed model for pH induced terminal group destabilisation resulting in stretching of the middle section of the protein within the duct. Reproduced from (Gaines et al., 2010)

Unfortunately these published suggestions came too late for testing in this work, and no experimental testing or validation of this proposed terminal group stretching mechanism has appeared in literature. Models have been published very recently (Gronau et al., 2013) to support the chain extension idea, and show how changes in chemical environment might induce specific gelation of terminal groups, followed by extension under flow, as shown in Fig. 9.17.

Fig. 9.17. Model of joining of the terminal groups of a silk protein to form a dimer, and computer models of silk protein stretching from the terminal groups. Both reproduced from (Gronau et al., 2013)

In retrospect, the decision to use impermeable glass capillaries with the addition of heat induced gelation conditions appears to have induced gelation indiscriminately in the silk proteins, which more recent publications have indicated are the opposite of what occurs and is required to produce fibres with natural properties. These results may indicate that, although shear force or heat induced gelation of silk dope is capable of increasing the modulus of the feedstock, the chemical process that occurs between the silk proteins is an indiscriminate gelation and therefore an inaccurate reflection of the conditions and processes that occur *in vivo*.

If spinning with an impermeable nozzle was continued, a new gelation method would be required that does not require a diffusion membrane as occurs in nature. Using pH change to mediate this gelation may not be successful, as without the particular secretion locations within the duct that a permeable duct wall allows, any gelation will be non-selective and may lead to similar results to those found here. Novel approaches will be needed to test these issues and suggest alternative controlled instability processes. For example, a new method to spin with an impermeable membrane may be to mix an agent into dope that thermally destabilizes below the thermal threshold of indiscriminate gelation explored in this thesis, but above silk dope stable temperature. Upon release of divalent ions such as organic calcium salts dissociated at 40 ° C, the result may be a terminal group gelation step, whereby further elongational stretching of the

molecules within the hydrophobic tip. This experiment would test the terminal groups gelation hypothesis, potentially producing fibres with silk like properties.

Future work will need to test aspects such as internal draw down during spinning, perhaps by scattering methods that could show phase separation in the dope (as suggested may be possible, Dr. Imke Greving personal communication), and also look at the structure of the fibres through FTIR, Raman, or x-ray scattering methods.

9.5. Conclusions

This chapter tested the hypothesis that a naturally inspired hydrophobic coating of the spinning device would permit the spinning of fibres from natural silk dope directly from the spinning capillary device. This would remove the need for a droplet to be formed at the capillary exit for stable spinning to occur and also to remove the intimate contact required between the dope capillary walls, and thereby induce extensional flow and perhaps some degree of internal drawdown in the dope to nucleate fibre formation.

The hypothesis was tested by spinning fibres from a hydrophobic nozzle tip, both at ambient and elevated temperatures. The results showed that, although the treatment eliminated the need for a droplet, it was not possible to produce fibres with similar properties to naturally spun fibres using either shear force alone or shear force and heat induced gelation. DMTA analysis strongly suggests that spun fibres have a low degree of order (orientation and crystallinity) and poor hydrogen bonding (low modulus and T_g).

Chapter 10. Conclusions

10.1. Thesis summary

This thesis, 'Natural and bioinspired silk spinning', describes an investigation into native silk spinning, with the objective of reproducing high performance natural silk fibres in the laboratory using a novel device based upon observations on natural spinning glands and processes. While the work is reported in two sections of natural and artificial spinning for convenience, these two aspects are inextricably interconnected, and the two parts of the work developed in parallel as observations from nature were used to guide the design of, and solve problems with, the bioinspired device.

After a brief discussion of the background to this work, the body of the Introduction presents an in-depth literature review of the natural spinning process in spiders and silkworms and the current status of artificial silk spinning. For natural spinning, the literature provides a great deal of fragmented data on different aspects of silk production, which allows the process to be visualised as a series of stages, from synthesis, storage, shear flow, destabilisation, draw down, and water extraction for conversion of the aqueous protein solution into a solid fibre. However, we still do not understand how the wide diversity of different silks of different functions is produced with consistent properties under a wide range of conditions, and by genetically diverse animals and insects whose sizes vary by orders of magnitude. Areas where the need for further information is particularly acute for artificial spinning include: the specific size of the spinning ducts and the size of these ducts relative to the final silk diameter and its properties; the importance of the composition of the walls of the duct and its interaction with the feedstock; the location and physical/chemical origin of the feedstock instability process and the subsequent drawdown of the fibre to its final solid form; and the process of development of the silk morphology during spinning that gives natural silk its excellent mechanical properties. These areas were, therefore, addressed in my work on natural spinning.

The literature confirms that the status of artificial silk spinning is poor. As a broad generalization, no artificial spinning has been reported to reproduce the properties of natural silk fibres. All types of artificial spinning seem to produce a highly disordered silk structure, with consequently weak mechanical properties of low strength and toughness due to brittle failure. The one way to improve fibre properties is to post-draw the fibre under high humidity to increase orientation and crystallinity of the silk molecules, but even after this the stress-strain profile remains very different from that of natural fibres. A key point is that the majority of artificial spinning attempts have not incorporated many aspects of the natural spinning process, which I hypothesized was some of the reason they have failed to make fibres with the required properties.

The first half of the thesis looks at natural silk spinning. The first experimental chapter considers the morphology of spider and silkworm spinning ducts, how the silk fibre develops as the dope flows through the gland, and the relationship between silk fibre properties and both gland morphology and spinning speed. The second experimental chapter describes histochemical and spectroscopic investigations of the silk ducts of both the spider *Nephila edulis* and the silkworm *Bombyx mori,* and showed that they both contain β-chitin, despite an evolutionarily distant common ancestor. The final observational chapter describes how the cuticle lining of the duct of the model spider *Nephila edulis* consists of nanoporous discs alternating with non-porous structural discs, and a model of the wall indicated that it appeared optimised for a combination of mechanical integrity together with high and selective permeability to water, ions and possibly other low molecular weight solutes.

The second half of the thesis is concerned with making a spinning device, in which the spinning feedstock was natural silk dope, mainly taken from the silkworm *Bombyx mori*. This feedstock provided adequate volumes of feedstock and eliminated complications arising from the major differences between reconstituted silk and the native material that had co-evolved with the glands that were studied as a guide. The first experimental chapter details the gradual development of the engineering aspects of the spinning device, which presented many practical difficulties that could be considered independently of the spinning investigation. The next chapter outlines the

development of a centrifugal capillary rheometer, which gave practical quantitative insights into rheological processes. Next, the spinning investigation is reported in two stages: first, the screening of spinning in glass capillaries based upon natural gland dimensions and flow rates that had been shown to induce fibrillation in silk dope in a rheometer, and also included initiation of instability through heat applied along the capillary; second, the final spinning evaluation, using lessons learned from all the screening trials throughout the project, but also including a key development of a hydrophobic coating on the capillary tip to inhibit droplet formation, which massively increased the process stability and ease of fibre production.

The main conclusions from this work are: first, that good silk fibre cannot be spun by shear stress alone; second, that heat instability induces the wrong kind of gelation in the silk to allow the correct molecular structure to be produced for good silk fibre properties. In addition, the body of work behind these conclusions provides fundamental background information and new insights that are likely to contribute to the next stages of development of artificial silk spinning, from obtaining a better understanding of the biology of natural spinning glands to the engineering difficulties of implementing the bioinspired principles.

10.2. Technical achievements

Although many reconstituted silk fibroin (RSF) spinning devices have been described, none could be found that permitted spinning from native dopes. Therefore, to test spinning hypotheses required significant and continuous technical advances concurrent with the experimental work carried out, as reported in chapter 6. Although many of these advances concerned rather prosaic collection and calibration of suitable components to make up the spinning device, some components were entirely novel for the application and had to be made from scratch.

The first significant technical achievement was the novel use of a glass capillary maker to make capillaries of a shape similar to the shape of ducts found in nature, to induce shear forces within the duct similar to those expected by natural ducts. By modifying the default settings programmed into the capillary maker, ducts of similar dimensions to those found in nature could be produced

with excellent repeatability. The only constraint to better similarity arose from the need to load silk dope into the proximal end of the capillary, solved by using a capillary with a larger inner diameter than the diameter of the silk gland storage sack at the proximal end though with a tip of natural size.

The second technical achievement was the development of a method to attach the capillaries to the spinning device that greatly increased the speed of experiments. Modified Luer adaptors allowed quick and easy connection to all manner of attachments, and even permitted reuse of the plastic components. The combined adaptor and capillary were later adapted to permit spinning from very small volumes of native spider dope, with no loss in functionality. The 'design specification' of natural silk spinning, compared to the technical achievements in this thesis are contained within the following table.

Table 10.1 Design specification for silk spinning

Parameter	Natural spinning	My design
Feedstock	Spider or silkworm dope	Spider or silkworm dope
Feedstock storage before spinning	Storage sack	Removed from dissected natural storage sack
Solvent	Water	Water
Dope gelation mechanism(s)	Ion concentration, pH, dehydration, shear stress, elongational stress (drawing)	Shear stress, heating, drawing
Duct geometry	Tapering tube	Tapering tube
Motive force	Fibre drawing	Pressure, fibre drawing

The third significant technical achievement was the ability to spin fibres from both native silkworm and spider dope, from a capillary but without an intermediary droplet from which fibres are pulled. The developments that led to this achievement will be discussed further in the next section.

10.3. Scientific findings and their implications

Measurements were taken of the internal and external diameters of the ducts of spiders at different stages of development, which allowed comparisons of the duct shapes to be made with the type of silk produced, and with other dimensions that quantify the development of spider growth. The main finding from this was that the gradient of the essentially linearly decreasing stage of the duct was essentially the same in a great range of spider sizes and stages of development. This finding was used later in the study to inform the design of the spinning ducts, where a larger capillary was used than previously published in the literature, but of similar shape. More detailed theoretical analysis of these results may be valuable in understanding the mechanisms for flow in the glands that allow silk to be spun under such a wide range of conditions (Dicko et al., 2008).

The material of the spinning ducts of both the silkworm *Bombyx mori* and the spider *Nephila edulis* was shown to be composed largely of the biopolymer chitin. This convergence in materials used, like the similar properties of the silks of these two animals, may be more than coincidence. Rather, it may indicate properties of the spinning duct that are essential to spin fibres with silk-like properties. The ultrastructure of the spinning duct of the spider was described, from which the properties of this structure composed of chitin were tested. These investigations showed that the wall appeared to be optimised for a balance between resistance against compression and potential for diffusion of substances through the duct lumen into the silk dope. Knowing that some chitins are hydrophobic led to the hypothesis that hydrophobic coating of a spinning nozzle facilitates fibre spinning.

This hypothesis formed the basis of, and was tested in, the artificial spinning experiments. All early attempts at spinning fibres from glass capillaries had to be executed via the intermediate of a droplet of dope at the end of the capillary, from which the fibres were pulled. Hydrophobic coating on the end of the capillary allowed spinning without a droplet, permitting controlled shear spinning from within the capillary for the first time.

Attempts to gel the silk dope using heat were based upon the hypothesis that gelation (usually by chemical means) may play an important role in developing the silk molecular structure during spinning, thereby eliminating the need for post-drawing that is used with reconstituted silk. Although heat was ineffective in improving the spinning process, it did demonstrate that indiscriminate gelling is counter-productive, and that more natural chemical approaches to gelation are likely to be needed, detailed below.

Modelling silk dope flow through a capillary being spun within a centrifuge required modification of standard equations of centripetal forces and capillary flow to derive a predictive model of Newtonian flow within the centrifuge, including the two stage acceleration and deceleration portions of the centrifuge program. This model was validated by calibrating the artificial spinning device with rheological calibration oils, but ultimately was not taken further due to the unpredictable characteristics of silk dope under these conditions. Nevertheless, this chapter represents the first instance of silk fibres being spun in this manner from native silk dope, although their properties were not good.

10.4. Suggestions for future developments

Both parts of this thesis suggest developments that could be made in the future. The aim of the first section of the thesis was to make a detailed investigation of the size, composition and ultrastructure of the spinning duct. These studies were performed mainly on the spider *Nephila edulis* and to a lesser degree on *Bombyx mori*, so it would be rewarding to extend these studies to other related species. Conservation of features across species would give further evidence of their importance, especially in relation to spinning.

Although some of the features of the natural spinning duct described here and by others were incorporated into the spinning device presented here, many aspects were not incorporated. It would be very interesting to test the hypothesis that duct length is correlated with maximum possible spinning speed, by using a variety of spinning duct shapes, in combination with an experimental and theoretical analysis of conditions required to induce dope instability. In

addition, construction of a duct tip from a material that allowed selective and controlled permeability with a hydrophobic coating would be my ultimate spinning device.

A development that may be easier to achieve would be to use the spinning device developed in this work with a destabilizing agent in the dope to change pH or introduce divalent ions to initiate gelation of the silk dope 'on command'. The interesting aspect of this approach is that the location and power of this gelation could be varied externally by exposure of the agent to appropriate light or heat sources, for example, permitting a full study of their effects with little other reconfiguration. Another method that may prove promising is the technique of electrogelation of silks (Yucel et al., 2010, Leisk et al., 2010), developed by other researchers at the same time as my studies. Although the most recent studies suggest that the structures formed by electrogelation are beta-sheets (Lu et al., 2011) and therefore likely to have similar results in fibre spinning to the methods I used, if better control of electrogelation were possible it may have significant uses in fibre spinning.

10.5. Final summary

The precept of this thesis was that to spin fibres with silk dope artificially, study of the biological system is as important as the spinning device itself. Without studying the biological system and using those observations, we are unlikely to reproduce the properties of native silk fibres by artificial spinning. This thesis documents my attempts at learning from nature in a systematic way. Although I was not ultimately successful in spinning fibres with fully silk-like properties, I suggest that this is due to the complexity of the system to be replicated in the limited time available, rather than a failing of the approach itself.

On a personal level, starting my DPhil from an undergraduate degree in engineering led me to think of a technical achievement as an end in itself. This work has gradually taught me the subtle difference between engineering and scientific achievements, and different approaches in the different scientific disciplines.

Appendix A. 3D section preparation

This appendix describes the protocols required for acquisition of a 3D image from paraffin sections. The main points are wax embedding protocols for spider and then silkworm, haemotoxylin and eosin staining protocol, a list of possible 3D reconstruction packages, and the protocol for using Amira for the desired result.

A.a. Overview

To make a 3D reconstruction of an organism, there are two types of possible methods: non-destructive and destructive. Non-destructive methods include micro computerized tomographic, magnetic resonance or confocal imaging. These methods have the advantages of not damaging the tissue and being generally quick to make a scan. The foremost disadvantages are limited availability, inadequate resolution for measuring the duct inner diameter, and difficulties with low contrast specimens. Destructive methods use sectioning of the material with some kind of knife, then imaging stained sections through a microscope. This has the advantages of being able to be done with little equipment, and the disadvantages of being slow and difficult.

At the time of the study, post-doc Dr. Katrin Kronenberger was investigating the possibilities of non-destructive methods but with limited success. In the literature there were two examples of successful reconstruction of ducts within whole specimens, those of *Helicoverpa armigera* (Sorensen et al., 2006) and *Cupiennius salei* (Hilbrant, 2008), so the destructive method was chosen.

To section and then reconstruct a specimen requires a number of steps, each of which must be chosen to be compatible with the specimen and each other. These steps can be split into two sections: sectioning and reconstruction. The stages of sectioning are specimen immobilization, fixation, dehydration and clearing, infiltration and embedding, sectioning, mounting, staining. The stages of reconstruction are image acquisition, image processing, and 3D reconstruction.

The two successful attempts in the literature used very different methods: one used an ethanol dehydration series, embedded in LR White resin, made 3 μm sections, and then reconstructed with Surf 3D software (Sorensen et al., 2006). The other embedded in paraffin, made 7 μm sections, aligned the images in Amira software, then segmented, 3D modelled and meshed in IMOD (Hilbrant, 2008). Of the two attempts, paraffin will be used in this study as it is much easier to handle and the facilities are available within the university.

A.b. Collection & Identification

Sites were identified as being typical habitats for a number of different spider species. Spiders were gathered from a number of wild sites using a spider pooter for collection, and identified through a dissecting microscope with a spider key (Roberts, 1995) and the help of experienced colleagues. Specimens were identified to species level in adults but only to family level in juveniles. The species of the specimens was confirmed by comparison with other images. The live specimens were kept separately in ventilated boxes ~200 x 150 x 100 mm.

Juvenile *Antheraea pernyi* and *Bombyx mori* silkworms were supplied in clean boxes by Silkworm Store Ltd (Essex, UK).



Fig. 10.1 Crab spider

A.c. Immobilization of specimen

Each specimen was carefully removed from its ventilated box and placed in a 50 ml tube. A piece of absorbent paper was dipped in ethyl ether, introduced into the 50ml tube and the lid sealed. The specimen was exposed to the ethyl ether for 30 seconds longer than the time it takes to stop moving. The specimen was then removed, paying attention that it did not come into contact with the liquid ethyl ether.

A.d. Fixing

A protocol was developed for fixing and subsequent steps and adapted to different samples. The text here provides an overview but for specific protocols please see Appendix A. Bouin's stock alcoholic solution was mixed with glacial acetic acid to form an active solution. Samples were immersed separately in sealed airtight glass vials, which were gently but continuously upended for the number of days specified on the protocol, regular observances ensuring that the fluid had not dried out and that the specimen was able to move freely within the fluid.

Some specimens required some level of dissection to permit full infiltration of the fixing solution. This was done whilst immersed in fixative solution to prevent drying of the specimen.

A.e. Dehydration & clearing

Samples were transferred in a fume hood to glass vials filled with solutions of ethanol and water, continually upended as before, over time transferred to solutions with increasing proportions of ethanol as specified by the protocols mentioned referred to above. The introduction of ethanol serves to dehydrate the tissues in preparation for infiltration of paraffin as detailed in Appendix A. Introduction of ethanol must be undertaken with patience at a rate suitable for the particular sample, as too rapid a dehydration will introduce shrinkage or wrinkles in the tissue.

The water in the tissues has now been replaced with ethanol. This ethanol must be 'cleared' from the tissues before the paraffin wax can be infiltrated into the specimen.

A.f.Infiltration & Embedding

As the outer surfaces of the specimens were extremely waterproof, extreme measures were taken to enable influx of paraffin. Therefore paraffin wax was combined in a vial with the Histoclear (National Diagnostics) in the proportion set out in the protocol, the combination giving a gradual change to the tissues. This mixture was gently heated in a water bath to 60 ° C, and the sample transferred to this mixture. The vial and mixture were subjected to a slight vacuum, which helps to remove any air in the sample and remove it with the liquid mixture. Finally the sample was removed from the mixture of wax and clearing agent, and replaced into a heated vial of pure liquid wax, under vacuum. After several different vials of pure wax the sample will not have any Histoclear residue, and can be embedded into a solid block of paraffin wax.

The sample was removed to a mould into which was poured liquid wax. The sample was orientated and the wax allowed to cool while mounted on to a labelled plastic cassette as shown in Fig. When the wax has cooled and solidified it was ready for sectioning.

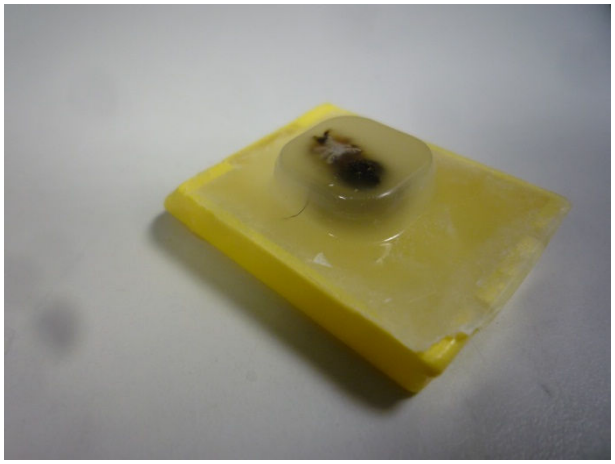


Fig. 10.2 Sample embedded into paraffin wax block mounted on plastic cassette

A.g. Sectioning

Samples were sectioned with an Anglia Scientific (Cambridge, UK) Type 300 rotary microtome. The plastic cassette with wax block attached was clamped into the microtome (see Fig. 10.3, Fig. 10.4). The microtome blade was washed with Histoclear and allowed to dry. The protruding edge of the block was aligned with the knife edge both so that the edges were parallel and also so that the knife made a clean cut across the block. Doing this ensured that when sectioning the block was not cut into a progressively smaller wedge shape, so that the cassette does not have to be moved to remove the very last residues of sample within the wax. The thickness of sections required was read from the protocols below and dialled into the microtome. The handle was used to move the block smoothly across the knife and advancing by the specified thickness after each cut.

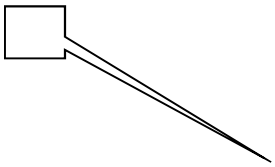


Fig. 10.3 Rotary microtome. A: Guide for ribbon paper. B: Knife holder clamp. C: Plastic cassette holding sample. D: Cassette clamp. E: Cassette clamp thumb screw. F: Vertical tilt adjustment thumbscrew. G: Flywheel locking mechanism lever. H: flywheel handle. I: Flywheel. J: Lid locating spur. K: Knife angle adjustment knob. L: Section cutting thickness adjustment knob.

Fig. 10.4 Rotary microtome detail, M: Horizontal tilt adjustment thumbscrew. N: Knife holder release lever. O: Knife assembly release lever. P: Knife assembly traversing ways. Q: Knife clamp. R: Knife. S: Palm rest. T: Knife holder.

When these instructions were followed correctly the sections attached together forming a 'ribbon' of wax which was then collected upon paper strips mounted in a guide as depicted in Fig. 10.5 (A). Ribbons were stored on clean strips of paper in drawers of a metal filing cabinet until required.

A.h. Mounting

The long ribbons of wax were mounted on glass slides before they can be handled due to their fragility and tendency to blow away in the slightest of air currents. To do this a bath filled with distilled water was heated to 40 ° C. The wax ribbons were cut into lengths equalling that of standard glass slides. These small lengths of ribbon were floated on the warm water until any waviness or other imperfections unfolded, at which point a slide was inserted into the water and moved under them. Once the end of the ribbon touched the slide it tended to stick, and the slide was removed from the water almost vertically allowing most of the water to run off but the ribbon remained attached. The slide was labelled with the date, sample identification, slide number and order of sections, and left inclined for the water to drain off to dry on a slide heater as depicted in Fig. 10.5 (B).



Fig. 10.5 (A) Ribbons of wax upon the paper ribbon guide. (B) Slides drying on a slide heater

A.i.Staining

Biological tissue has little contrast in light microscopy, so must be stained to reveal the structures it is made up of. This stage describes the steps required to stain the sections. Though the timings and order of the staining are detailed in Appendix A, the points and aims of the procedure will be discussed here.

The haemotoxylin and eosin stain was used. This is an extremely widely used stain, in which haemotoxylin stains cell nuclei a blue-black, and the eosin stains cell cytoplasm and connective tissue fibres pink, orange and red (Bancroft and Gamble, 2008).

Before starting, each of the solutions were prepared in separate canisters. The slides were put into a stainless steel holder which kept them upright for easy drying, and prevented them from touching each other, blocking contact with the solutions. The slides were first inserted into a solution of Histoclear which removes the wax infiltrated into and from around the specimen. Two different solutions of Histoclear were used to wash the slides. The slide holder was moved through solutions of ethanol and water, starting from 100% ethanol then gradually increasing the water content to distilled water. As in the dehydration stage this gradual dehydration helped to prevent adverse effects on the structure of the tissues.

The slides inside the slide holder were then moved to a solution of haemotoxylin. The holder was periodically rotated to agitate the fluid and allow fresh to come into contact with the slide.

The slide holder was then moved to a container with water running through it, at a pace gentle enough not to wash off the sections from the slide. This changed the sections from a dark purple colour to blue. Next was a container of acidic alcohol and then running water again. Eosin was the final chemical to be used, which changed the sections to a red- pink colour. The samples were dehydrated again so that they do not degrade or become mouldy during storage by briefly agitating the sample in each solution, from distilled water to pure ethanol. The samples were finally washed in the two solutions are of Histoclear.

Cover slips were laid out over the edges of a smooth board, and an amount of D.P.X. (Sigma Aldrich) was dispensed onto each and allowed to spread out. Slides were taken individually from the slide holder immersed in Histoclear, excess fluid from the underside was wiped away, and placed over the coverslips in such a way that most of the air was expelled leaving only a small number of small bubbles. Finally the slides with slide covers attached were transferred to a drying rack left in an oven at 37° C overnight.

A.j. Image acquisition

Images of sections were taken using a PZO microscope (PZO, Poland) under 100x magnification, using a Canon A640 camera in a room with constant light intensity. Notes were taken of any lost or deformed sections so this would not distort the thickness of the 3D reconstruction.

A.k. Image processing

Images were processed in Photoshop (Adobe systems) into a form that could be accepted by the 3D reconstruction software. This required removing all blank space around the file, increasing the contrast, inverting the colours, and removing any artefacts from the slide obviously not part of the section involved as shown in Fig. 10.6. The images are then in a format which can be used by image construction software.

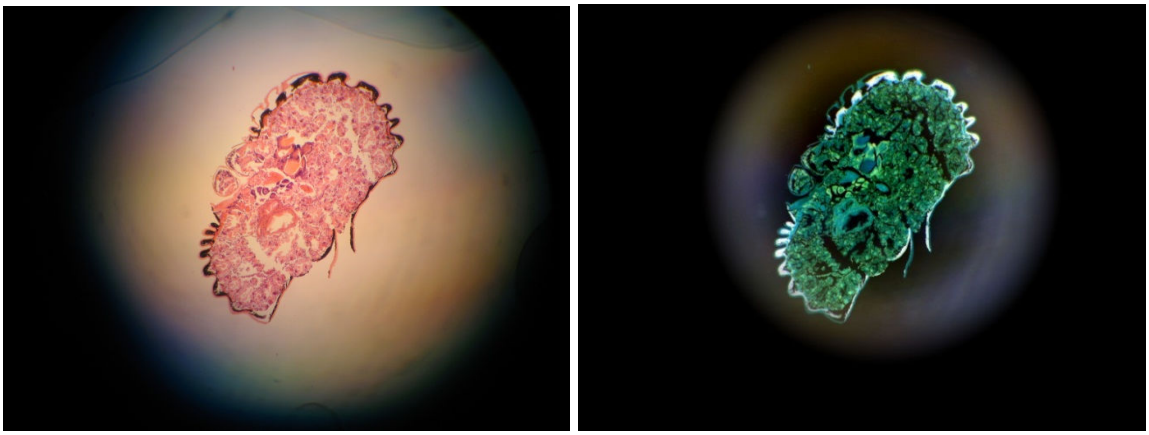


Fig. 10.6 Artefacts not part of the image before and after

A.l. 3D reconstruction

Various 3D reconstruction software packages were researched and evaluated for their suitability, and noted in Appendix A. The high-specification software package Amira (Visage Imaging Inc., CA, USA) was chosen at it was available including support at no cost within the university. Images were aligned and stacked using the automatic registration function and errors were corrected manually. As the program could not differentiate between the ducts and other low contrast areas of the section, the ducts were highlighted manually in each section. The software was then directed to assemble each of these highlighted sections. The specific steps taken are detailed in Appendix A.

A.m. Wax embedding protocol

(Under guidance of Katrin Kronenberger)

- Make sure all necessary solutions and equipment ready
- Everything must be labelled clearly
- Collect spider
- Soak a little piece of tissue with Ethyl ether, insert the latter into the vial containing the spider and wait until the spider stops moving
- Take spider out of vial, image animal and measure abdomen
- Under the dissecting microscope cut off/ separate cephalothorax from opisthosoma using a sharp blade and improve penetration of fixative, if possible inject very gently some of the latter
- Keep opisthosoma in solution and don't ever let it dry out
- Clear working place and dispose of any sharp objects in the sharps bin
- During the protocol rather change the solution the sample is in than moving the samples with tweezers from solution to solution to prevent damage to sample.

A.m.i. Fixation

Prepare from (stable) stock solution 14:1 just before dissection

Alcoholic Bouin's 24 hrs. RT, rotator

Transfer from fixative to dehydration solution preferably inside a fume cupboard

A.m.ii. Dehydration

At this point use agarose orientation sheets if required- one either side or required edges of sample, using agarose glue to glue together

30% EtOH 2 hrs., RT, rotator
50% EtOH 2 hrs., RT, rotator
70% EtOH 2 hrs., RT, rotator
Leave samples overnight in the fridge at 4 degrees C

96% EtOH 2 hrs., RT, rotator
100% EtOH 2 hrs., RT, rotator
100% EtOH 2 hrs., RT, rotator
Histoclear 2 hrs., RT, rotator
Histoclear 2 hrs., RT, rotator

A.m.iii. Infiltration

Histoclear/ wax 2 hrs., 60, vacuum
Wax 2 hrs., 60, vacuum
Wax overnight, 60, vacuum

A.m.iv. Embedding

These are dangerous chemicals, wear full lab protection including gloves and lab coat.

Prepare from (stable) stock solution just before dissection

EtOH 80% 7.5 ml
Formaldehyde 37% (Sigma, in methanol) 3.0 ml
Picric acid 70 mg
Acetic acid 0.75 ml

The points and aims of the procedure will be discussed here.

The haemotoxylin and eosin stain was used. This is an extremely widely used stain, in which haemotoxylin stains cell nuclei a blue-black, and the eosin stains cell cytoplasm and connective tissue fibres pink, orange and red (Bancroft and Gamble, 2008).

Before starting, each of the solutions were prepared in separate canisters. The slides were put into a stainless steel holder which kept them upright for easy drying, and prevented them from touching each other, blocking contact with the solutions. The slides were first inserted into a solution of Histoclear which removes the wax infiltrated into and from around the specimen. Two different solutions of Histoclear were used to wash the slides. The slide holder was moved through solutions of ethanol and water, starting from 100% ethanol then gradually increasing the water content to distilled water. As in the dehydration stage this gradual dehydration helped to prevent adverse effects on the structure of the tissues.

The slides inside the slide holder were then moved to a solution of haemotoxylin. The holder was periodically rotated to agitate the fluid and allow fresh to come into contact with the slide.

The slide holder was then moved to a container with water running through it, at a pace gentle enough not to wash off the sections from the slide. This changed the sections from a dark purple colour to blue. Next was a container of acidic alcohol and then running water again. Eosin was the final chemical to be used, which changed the sections to a red- pink colour. The samples were dehydrated again so that they do not degrade or become mouldy during storage by briefly agitating the sample in each solution, from distilled water to pure ethanol. The samples were finally washed in the two solutions are of Histoclear.

Cover slips were laid out over the edges of a smooth board, and an amount of D.P.X. (Sigma Aldrich) was dispensed onto each and allowed to spread out. Slides were taken individually from the slide holder immersed in Histoclear, excess fluid from the underside was wiped away, and placed over the coverslips in such a way that most of the air was expelled leaving only a small number of small bubbles. Finally the slides with slide covers attached were transferred to a drying rack left in an oven at 37° C overnight.

A.n. H&E Staining

(Under guidance of Richard Stillion in Pathology 7.15.10)

Filter Haematoxylin using filter paper and funnel into new glass container. Rinse old container with water in sink.
Move slides into stainless steel slide holder ready for processing.
Using a new filter, filter Eosin into a new glass container. Rinse old container with water in sink.
Meanwhile,
Slides in Histoclear to dewax slides for 10 mines
Then Histoclear again for 1-2 minutes
Then 100 alc , 96, 80, etc. etc. to distilled water for 1 minute each.
Haematoxylin for 3 minutes,
Running water to ‘blue the stain’ for 2-3 mins+, draining and rinsing until water clear
Acidic alcohol 30 seconds to one minute

Running water to ‘blue the stain’ to 1-2 mins+, draining and rinsing until water clear
Eosin a few dips
Water to ‘blue the stain’ to 3-4 mins+, draining and rinsing until water clear
Dehydrate again from distilled water up to 100% alc, to Histoclear, dipping this time. Tip rack to drain excess and pad on paper towels
Leave in Histoclear part 1

Using the black board, scrub with first Histoclear and then ethanol to clear the Histoclear. Lay out the number of coverslips required. These may slip due to static- slide a finger along to lay down a little grease and this should stop. On each coverslip dole out some DPX. Careful- this contains xylene.

Take slides individually from their slide holder still in the Histoclear. Wipe the reverse side on paper, and drop gently from one side onto the DPX covered coverslips.

Transfer slides w/ coverslips to over grill. Use reverse end of a paintbrush to push out bubbles, without pressing so hard as to squash the sections.

Move grill and slides to oven to be kept at 37 ° C overnight.

A.o. Image acquisition

Images of sections were taken using a PZO microscope (PZO, Poland) under 100x magnification, using a digital camera (Canon Powershot A640) in a room with constant light intensity. Notes were taken of any lost or deformed sections so this would not distort the thickness of the 3D reconstruction.

A.p. Image processing

Images were processed in Photoshop (Adobe systems) into a form that could be accepted by the 3D reconstruction software. This required removing all blank space around the file, increasing the contrast, inverting the colours, and removing any artefacts from the slide obviously not part of the section involved as shown in Fig. 10.7. The images are then in a format which can be used by image construction software.

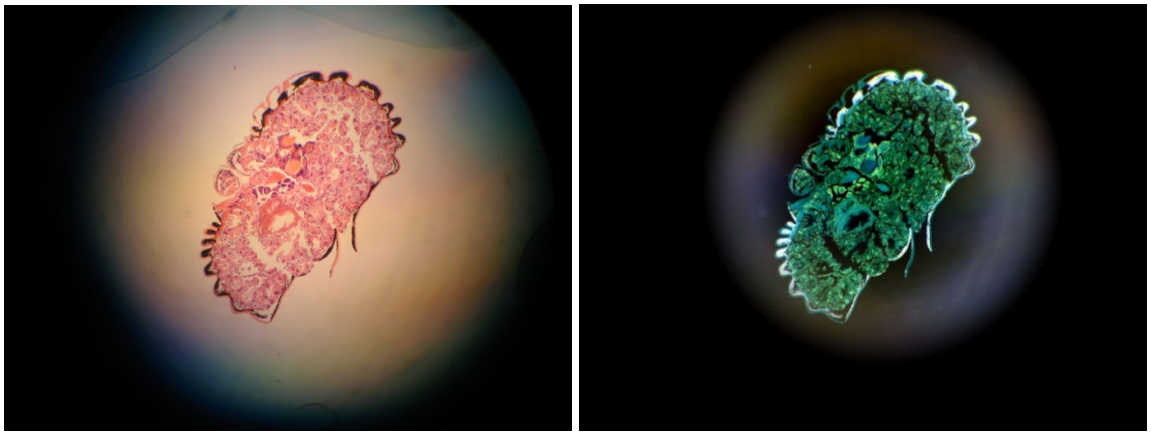


Fig. 10.7 Artefacts not part of the image before and after

A.q. 3D reconstruction packages

Table 10.2 shows a short list of available 3D reconstruction software packages.

Name	Cost	Website	Trial?	Notes	System
Amira	£££	http://www.amira.com/	Y	Mark Fricker has	all
BioVis3d		http://www.biovis3d.com/	y	Looks expensive	Win
Etdips	Freeware	http://sourceforge.net/projects/etdips/		Very undeveloped	Win 9x-2000
FreeSurfer	Free	http://surfer.nmr.mgh.harvard.edu/fswiki/SystemRequirements		For brains with good colour contrast	Max OS X/ Linux
imod	Free	http://bio3d.colorado.edu/imod/download.html		Looks complicated	all
OsiriX	free	http://www.osirix-viewer.com/		Dedicates for DICOM use	mac
Surf 3D				Used in (Sorensen et al., 2006), can't find	-
Tomovision	$4000	http://www.tomovision.com/		Mainly for whole body imaging	Win
TRI/3D-VOL		http://www.ratoc.co.jp/vlm_c.htm		Used in (Asakura et al., 2007b), in Japanese	-
Vis5d	Free	www.ssec.wisc.edu/~billh/**vis5d**.html		Last modified 2002	-
VolVis	Free	http://www.volvis.org/		Last modified some time ago	Unix
3dAcq		http://bio-imaging.liacs.nl/acquisition.html	n	Imaging Research Group of LIACS	
3d Slicer	Free	www.slicer.org		Looks ok	all

Table 10.2: Table of some available 3D reconstruction packages

The high-specification software package Amira (Visage Imaging Inc., CA, USA) was chosen at it was available including support at no cost within the university. Images were aligned and stacked using the automatic registration function and errors were corrected manually. As the program could not differentiate between the ducts and other low contrast areas of the section, the ducts were highlighted manually in each section. The software was then directed to assemble each of these highlighted sections.

A.r. Amira protocol

First, using an imaging program crop images to as close as possible, and adjust levels until background is black.

Reset Swatches, Set selection to around the circular bright area viewable by in the microscope photo. Inverse selection and delete. Change levels to give better contrast. Make new layer via copy. New layer. Hide background. Circular gradient tool from transparent to white, and do this so the darkness around the edges is cancelled out. Merge visible. Invert, crop out the black lines, Convert Mode to grayscale mode with merge and without rasterize. Save and close.

For this protocol images should be arranged by numerical or alphabetical order, and be equally spaced slices.

In Amira:

Open Data...

Select a medium number of images e.g. 150 and open them, or all if you are feeling brave

Right-click on the lozenge when loaded, and save as 2D Tiff. The #### in the filename are where Amira puts the names of the individual files. The images are now saved as an uncompressed Tiff stack, with a 'table of contents' in the .info file.

Right-click on the lozenge and click Compute/ AlignSlices. 'Edit' then align all the slices automatically using the multiple align stack function. After, go over and manually align any that are obviously miss-aligned. It's usually enough to just change the rotation/ flip to roughly correct and then press auto-align.

When all samples are aligned, press Resample then Close. To check the output if you like, on the lozenge press Display/ volren and the orange yellow result will be shown in the display window.

In the new lozenge, go Labels/ LabelField to be able to select separate regions of the sections. Use the label editor that appears, and using a brush or other selection tool highlight areas of sections. As long as the areas do not move a lot, it is possible to highlight two slices far apart and interpolate between them using Apple key+ I. Use the scroll wheel to move quickly between sections, and use the zoom tools to be able to see the parts needed. When all that is needed is selected, select the area you want to add these too on the top left e.g. Internal then use the + button to add the selected parts to the data. Save often. When everything required is selected, go back to tree view.

On the newly created labels lozenge hanging below the .align, right-click Compute/ Resample

A `Resample` lozenge should appear. Click on it and make it resample. On the `labels.resampled` lozenge that appears, click `SurfaceGen`. On the newly created lozenge `labels.surf`, click `Display/SurfaceView`

The partitions you have selected should now be visible in the view pane. You can rotate and zoom using the controls above the pane.

To export this separated data, right-click on Export then Save As. Save the file with an extension STT. This can now be viewable using SolidWorks.

Appendix B. Centrifuge model development

This appendix describes the development of some aspects of the centrifuge model in detail. The first section describes the derivation of the equations for flow, and the second describes development of the equations used for the capillary behaviour.

B.a. Derivation and analysis of equations

B.a.i. Centripetal force into capillary flow

This section describes how the standard equation for centripetal force was combined with the Hagen-Poiseuille equation to predict fluid flow through a capillary being rotated by a centrifuge. The resultant equation was used in the rest of the chapter.

From standard texts, the equation for centripetal force is

$$F = \frac{mv^2}{r} = mr\omega^2 \qquad \text{Equation 10.1}$$

Where F is force, m is mass, v is speed, r is radius and ω is angular velocity. However this equation is in a form that assumes a mass is involved. For the purposes of this investigation the equation should be in a form where the pressure of a fluid is used instead.

To convert a mass into a fluid pressure where m is mass, ρ is density, R is radius of capillary and l is length of capillary tube

$$m = \rho.\pi R^2.l \qquad \text{Equation 10.2}$$

$$\therefore p = \rho.\pi R^2.l\,.r\omega^2$$

$$\frac{\Delta p}{\Delta l} = \rho.\pi R^2.r\omega^2$$

To approximate flow through a capillary tube, Hagen-Poiseuille capillary flow from standard texts was used. This formula is

$$\Delta p = \mu l \frac{8Q}{\pi} R^{-4} \qquad \text{Equation 10.3}$$

Where Δp is the pressure drop, μ dynamic viscosity, l length of capillary, Q volumetric flow rate, R radius of capillary.

Rearranged in terms of Q

$$Q = \frac{dP}{dl}\frac{\pi R^4}{8\mu}$$

dP must be related to dl as dl=r-r_0 so by observation

$$Q = \frac{dl}{dt}.\pi R^4$$

equating,

$$\pi R^4 \frac{dl}{dt} = \frac{dP}{dl}\frac{\pi R^4}{8\mu}$$

$$\frac{dl}{dt} = \frac{dP}{dl}\frac{R^2}{8\mu}$$

Equating this with $\frac{\Delta P}{\Delta r} = \rho R\omega^2$ gives

$$\frac{dP}{dl}\frac{\pi R^4}{8\mu} = \rho.R.\omega^2\frac{R^2}{8\mu}$$

$$\frac{1}{r}\frac{dr}{dt} = \rho.\omega^2\frac{R^2}{8\mu}$$

$$ln\frac{r}{r_0} = \rho.\omega^2\frac{R^2}{8\mu}t$$

$$r = r_0.e^{\rho\omega^2\frac{R^2}{8\mu}t} \qquad \text{Equation 10.4}$$

B.a.ii. Dimensional analysis

This section describes a dimensional analysis performed upon the novel meant for predicting fluid flow through a capillary rotated within a centrifuge. A dimensional analysis is a standard technique used to verify whether the parameters in an equation are dimensionally consistent.

The fundamental dimensions of each parameter were noted in terms of the fundamental system of units length, mass, and time (Bridgman, 1922).

Table 10.3 Fundamental dimensions of parameters used in equation, where [L] is length, [M] is mass, [T] is time

Parameter	Symbol	Definition	Fundamental dimensions
Density of fluid	ρ	$\frac{mass}{volume}$	$\frac{[M]}{[L]^3}$
Radius of capillary	R^2	length^2	$[L]^2$
Angular velocity of centrifuge	ω	$\frac{1}{frequency}$	$\frac{1}{[T]^2}$
Time of spinning	t	time	[T]
Viscosity of fluid	μ	$\frac{force}{area}.time$	$\frac{[M].[L]}{[L]^2.[T]^2}.[T]$
Starting radius of fluid	r_0	Length	[L]
Final radius of fluid	R	Length	[L]

Arranging these fundamental dimensions and cancelling,

$$\frac{[M]}{[L]^3}.\frac{1}{[T]^2}.\frac{[L]^2.[T].[L]^2.[T]^2}{[M].[L].[T]} = 1$$

Thus the whole equation became

$$[L] = [L].e^1$$

Thus it was shown that the relation is dimensionally consistent. If the dimensions were not consistent the equation must be false.

Pressure in a tube

The following section describes a derivation of a formula to predict the rate of fluid flow within a static capillary that is laid horizontally, assuming an infinite source of fluid. This equation was used to refine the model described in the main chapter.

From standard texts pressure in a tube can be defined as

$$P = \frac{2\pi R\Gamma}{\pi R^2}$$

Where *P* is pressure, *R* is the radius of the tube and Γ is free surface energy of the fluid due to the circumference of the tube. This can now be shown as the rate of change of pressure as the distance from the centre of the centrifuge increases:

$$\frac{dP}{dr} = \frac{2\pi R\Gamma}{\pi R^2} = \frac{2\Gamma}{Rr}$$

Now, the flow rate through a capillary is defined as

$$Q = \pi R^2 \frac{dr}{dt}$$

We know Hagen-Poiseuille flow

$$Q = \frac{dP}{dr}\frac{\pi R^4}{8\mu}$$

So these equated are

$$Q = \pi R^2 \frac{dr}{dt} = \frac{dP}{dr}.\frac{\pi R^4}{8\mu}$$

Replacing rate of change of pressure from above and cancelling

$$Q = \pi R^2 \frac{dr}{dt} = \frac{2\Gamma}{Rr}.\frac{\pi R^4}{8\mu}$$

$$\frac{dr}{dt} = \frac{\Gamma}{r}.\frac{R}{4\mu}$$

$$\int r\,dr = \int \frac{\Gamma R}{4\mu}\,dt$$

$$\frac{r^2}{2} = \frac{\Gamma \mathrm{R}}{4\mu}.t$$

$$\Delta r = \sqrt{\frac{\Gamma R}{2\mu}.t}$$ Equation 10.5

This equation predicts the length of a fluid column in a static capillary tube after a certain time, given a horizontal tube and an infinite supply of fluid. This equation is similar to one in the literature (Washburn, 1921) though with parameters suitable for this application.

B.b. Development of model equation data

The following section describes the method used to find and understand the speeds used by the centrifuge, and simplify them to a form that would allow them to be inputted into calculations predicting fluid flow through capillaries. The successful equations were used to understand the fluid flow through capillaries being rotated within a centrifuge.

Control of the actual acceleration and deceleration curves was not possible with the centrifuge model used, but it was still possible to monitor these parameters via the readout on the front of the machine. The rotor decelerated until stationary, whereupon the lid was automatically unlocked.

User control of the instrument was limited to specifying a maximum speed and a time. When the machine was started it followed a pre-programmed acceleration curve until it reached the maximum speed. When the user-specified time elapsed, In order to predict how far the oil column will advance, it was not sufficient to use the maximum speed of the centrifuge as the only speed value used in Equation 7.3, as the acceleration and deceleration can make up a significant proportion of the total time of exposure.

Predictions of the distance oil moved were made from the curves in Fig. 7.4, acquired by monitoring the readout of the centrifuge. It can be seen from observation of the example speed setting of Fig. 10.8 that there were three characteristic modes of both acceleration and deceleration. The first is almost flat, the second rather steep, the third levelling off to programmed speed, fourth constant at programmed speed, fifth first deceleration, sixth is the second, steeper deceleration, and seventh and final is a slow pulling to a stop.

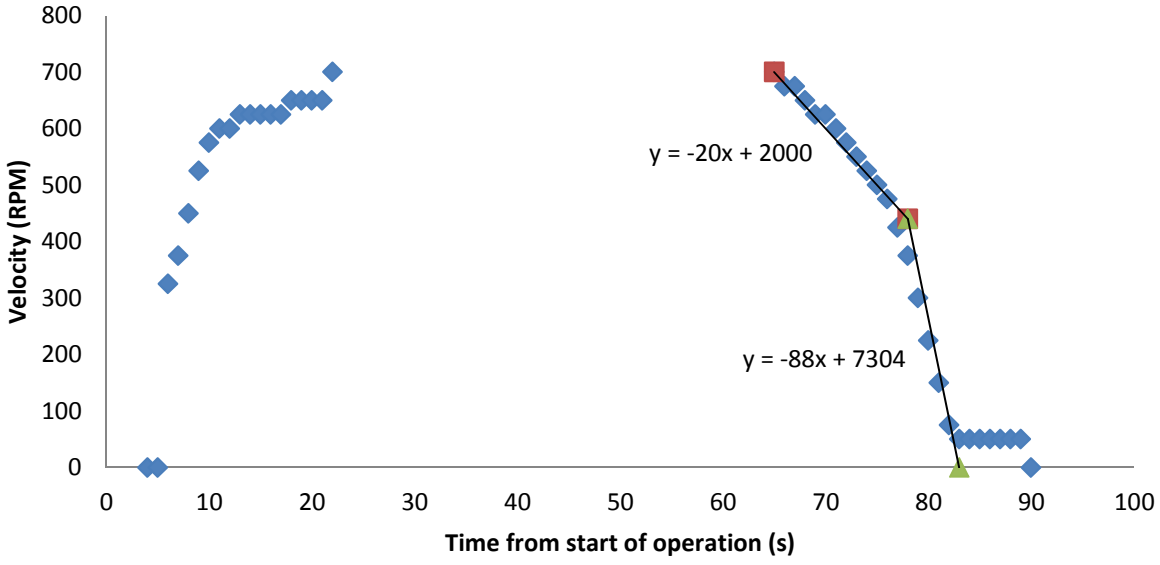


Fig. 10.8 An individual speed curve with model equations. Top speed 700 RPM, time 66 seconds

With the aim of building a simple model, trend lines were drawn along the four steeper modes, ignoring the mode with the smallest magnitude gradient (at the beginning of the acceleration and end of the deceleration). These trend lines were drawn on a graph to give a simplified model representation of the speeds during a run. Equation 7.3 was used to plot the length of the oil column for each point on this graph.

What follows is a general model in terms of time and speed specified, that is applicable for all observed curves, and allows curves for hypothetical combinations to be modelled. It is in five parts as discussed above. The equations and boundaries use a mix of time and RPM as waypoints, and thus cannot be interpreted as straight equations. Individual equations for each of the combinations of speed and time used are noted in Table 10.5.

RPM_C= current RPM (y)	t_C= current time (x)	RPM_S= selected RPM	t_S= selected time

Table 10.4

	Acceleration 1	**Acceleration 2**	**Constant speed**	**Deceleration 1**	**Deceleration 2**
Equation	$RPM_C=100 \times t_c - 400$	$RPM_C= 10 \times t_c + (RPM_S - 250)$	$RPM_C=RPM_S$	$RPM_C=-25 \times t_C + 25*t_S + RPM_S$	$RPM_C=-70 \times t_C + (t_S + 15)*70 +(-25*(t_S+15)+(25*t_S) + RPM_S)$
Boundaries	$0 < t_c < (RPM_S -250)$	$RPM_S-250 < t_C < RPM_S$ (this is $t_C \sim= 25$)	$25 < t_C < t_S$	$t_S < t_C < t_S + 15$	$t_S + 15 < t_C < RPM_C = 0$

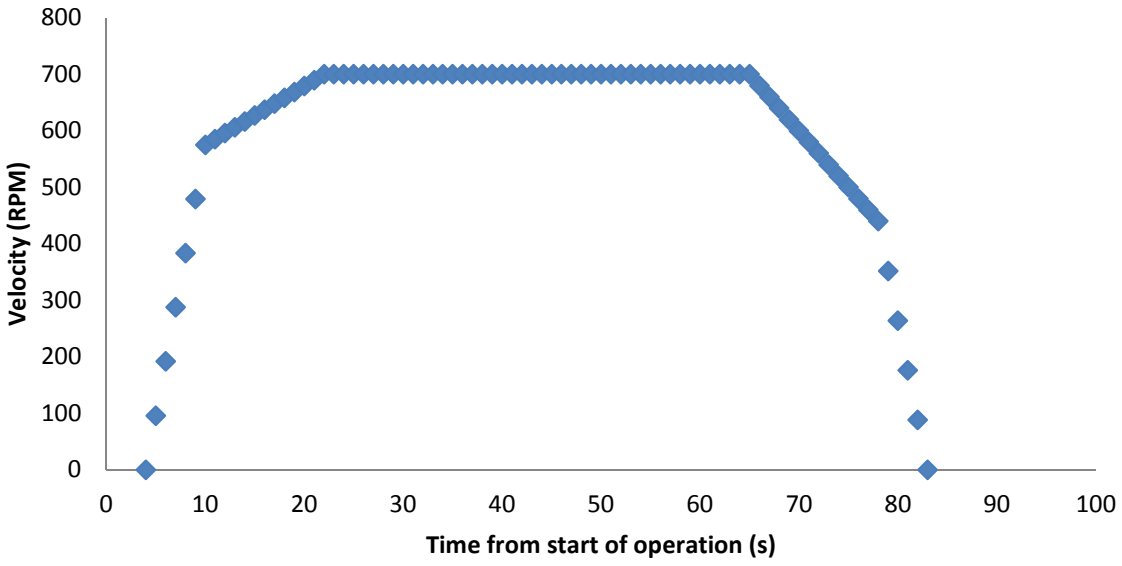


Fig. 10.9 Model representation of a run top speed 700 RPM, time 66 seconds

To test if the accuracy of the model is affected by this simplification, Equation 7.3 was used on the data in both original and simplified data for a run with top speed 700 RPM for 66 seconds. Fig. 10.10 shows the predicted length of column of oil per time for both sets of data.

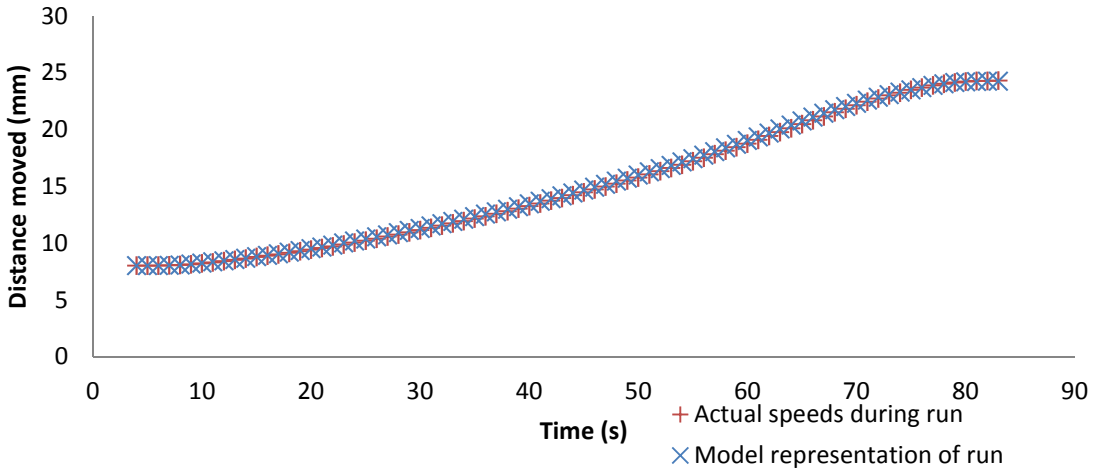


Fig. 10.10 Comparison between speed data and simplified speed model of lengths of oil column during spinning (700 RPM, 66 s)

It can be seen from Fig. 10.10 that the curves from actual runs and simplified run models are remarkably similar.

To find the offset, a wider set of predicted models was required to generate more data points.

Building upon the custom simplified equation versions of videoed runs, a generalised set of equations for any length of time and speed was formulated. Some example hypothetical speed time combinations generated using this method are shown in Fig. 10.11.

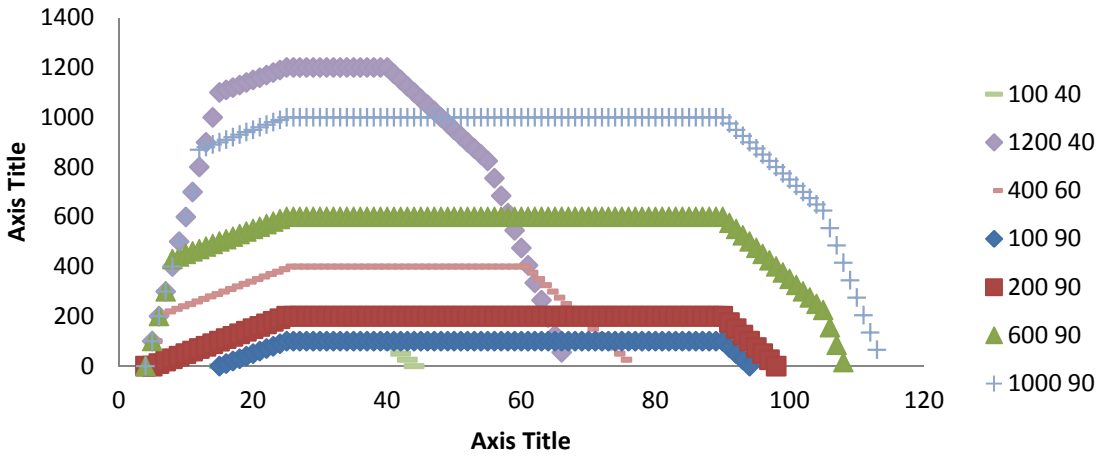


Fig. 10.11 Hypothetical combinations of speed and length of exposure

Using these curves, Equation 7.3 was used to plot how long an oil column would be if the centrifuge is set to run at any speed. From these a smooth curve was plotted over a wider range than would be possible with the equipment, allowing any effects that might not otherwise be visible to be shown.

Table 10.5 Model equation data for spinning curves

RPM	Time	Rise 1	Cords	Rise 2	Cords	Fall 1	Cords	Fall 2	Cords	Predicted r if r0=8 (mm)
500	60	y = 87.5x - 437.5	5,0 9,350	y = 7.5x + 282.5	9,350 29,500	y = -26.667x + 2100	60,500 75,100	y = -11.111x + 933.33	75,100 84,0	13.7249
500	90	y = 93.75x - 375	4,0 8,375	y = 5.9524x + 327.38	8,375 29,500	y = -16.667x + 1983.3	89,500 101,300	y = -50x + 5350	101,300 107,0	19.27559
500	180	y = 125x - 625	5,0 8,375	y = 8.3333x + 308.33	8,375 23,500	y = -28.571x + 5671.4	181,500 195,100	y = -10x + 2050	195,100 205,0	48.51462436
600	60	y = 117.5x - 470	4,0 8,470	y = 14.444x + 354.44	8,470 17,600	y = -20x + 1800	60,600 71,380	y = -63.333x + 4876.7	71,380 77,0	19.21796
600	66	y = 117.5x – 470	4,0 8,470	y = 8.125x + 405	8,470 24,600	y = -19.444x + 1863.9	65,600 74,425	y = -53.125x + 4356.3	74,425 82,0	20.17792
600	90	y = 94x - 376	4,0 9,470	y = 9.2857x + 386.43	9,470 23,600	y = -16.667x + 2083.3	89,600 101,400	y = -66.667x + 7133.3	101,400 107,0	29.2582
700	60	y = 95.833x - 383.33	4,0 10,575	y = 12.5x + 450	10,575 20,700	y = -17.692x + 1743.8	59,700 72,470	y = -58.75x + 4700	72,470 80,0	26.2600611
700	66	y = 95.833x - 383.33	4,0 10,575	y = 10.417x + 470.83	10,575 22,700	y = -20x + 2000	65,700 78,440	y = -88x + 7304	78,440 83,0	28.86265

RPM	Time	Rise 1	Cords	Rise 2	Cords	Fall 1	Cords	Fall 2	Cords	Predicted r if r0=8 (mm)
700	90	y = 110x - 440	4,0 9,550	y = 25x + 325	9,550 15,700	y = -20.455x + 2540.9	90,700 101,475	y = -79.167x + 8470.8	101,475 107,0	48.71401
800	60	y = 84.375x - 337.5	4,0 12,675	y = 10.417x + 550	12,675 24,800	y = -22.917x + 2175	60,800 72,525	y = -75x + 5925	72,525 79,0	36.23196
1000	60	y = 87.5x - 262.5	3,0 13,875	y = 15.625x + 671.88	13,875 21,1000	y = -25x + 2500	60,1000 70,750	y = -75x + 6000	70,750 80,0	83.36025
1000	66	y = 96.667x - 386.67	4,0 13,870	y = 11.818x + 716.36	13,870 24,1000	y = -25x + 2625	65,1000 77,700	y = -87.5x + 7437.5	77,700 85,0	106.1824
1000	180	y = 87.5x - 262.5	3,0 13,875	y = 9.6154x + 750	13,875 26,1000	y = -66.071x + 13091	183,1000 197,75	y = -9.375x + 1921.9	197,75 205,0	11018.92
2000	60	y = 98.684x - 394.74	4,0 23,1875	y = 9.6154x + 1653.8	23,1875 36,2000	y = -41.667x + 4500	60,2000 72,1500	y = -100x + 8700	72,1500 87,0	55294.38
2000	180	y = 105.56x - 527.78	5,0 23,1900	y = 5.5556x + 1772.2	23,1900 41,2000	y = -87.5x + 18013	183,2000 205,75	y = -10.714x + 2271.4	205,75 212,0	1.49E+13

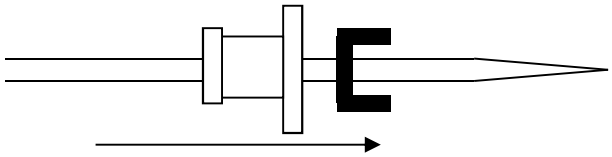
Appendix C. Spinning device development

This appendix describes detailed parts of spinning device development, including circuits of the device and code for the software that was written.

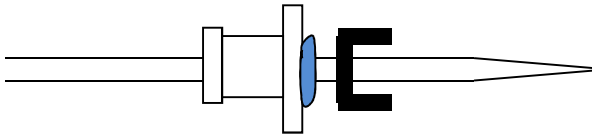
C.a. 'One Luer one seal' Nozzle spinning

The following method was used to make, fill and spin with this nozzle:

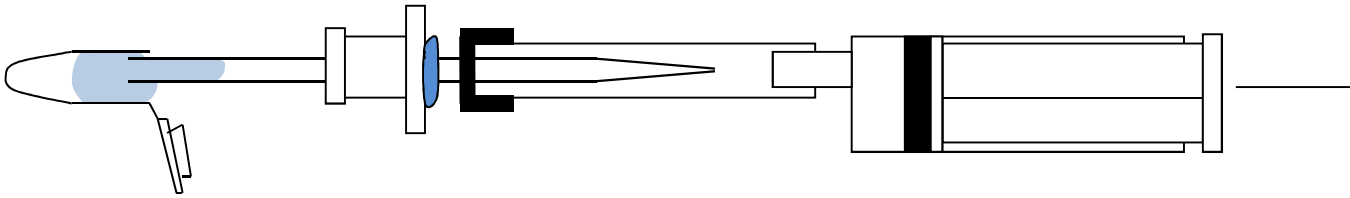
1. Slide 1ml syringe seal and female Luer connector onto capillary proximal end



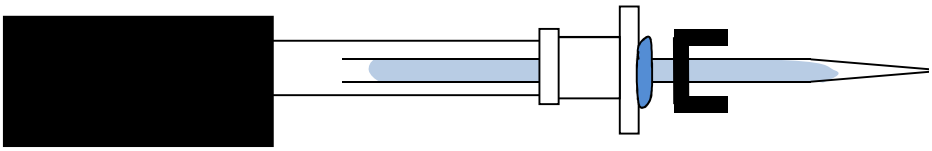
2. Superglue Luer connector to capillary and leave to dry
3. Remove tip of capillary



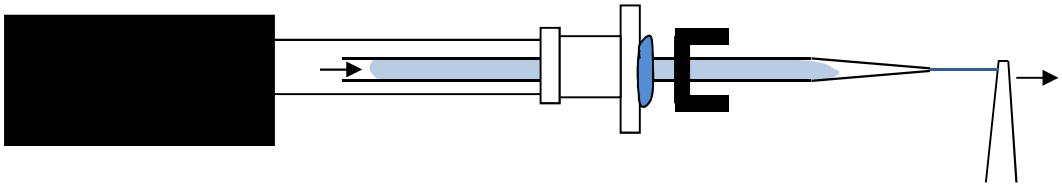
4. Attach syringe to distal end via extension tubes. Suck silk dope from Eppendorf



Remove extension tube, syringe, Eppendorf. Attach syringe pump to Luer connection via extension tube, pump gently



Use tweezers mounted on micro-manipulator to catch dope at end. Continue syringe pumping and pull away slowly to form fibre



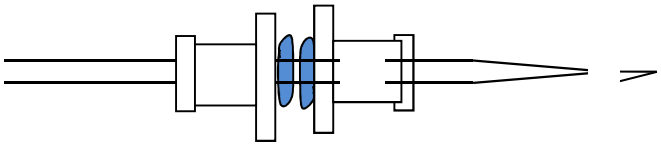
C.b. 'Two Luer' spinning instructions

The following method was used to make, fill and spin with this nozzle:

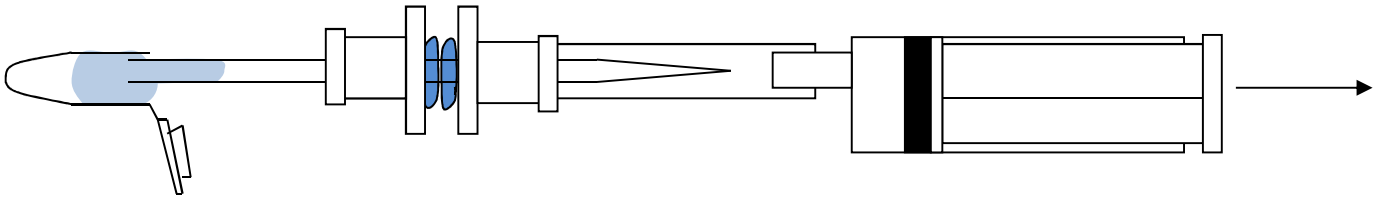
1. Slide female Luer connectors onto capillary proximal end, leaving 10mm gap before start of taper



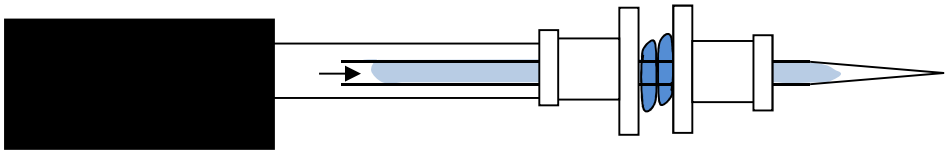
2. Superglue Luer connectors to capillary and leave to dry for > 1hour
3. Remove tip of capillary



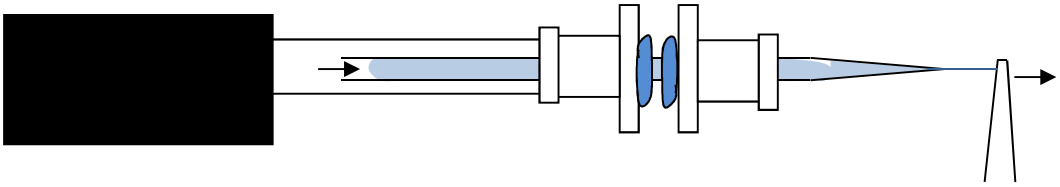
4. Suck minimal amount of distilled water into distal capillary end using capillary action
5. Attach syringe to distal end via extension tubes. Suck native silk dope from Eppendorf



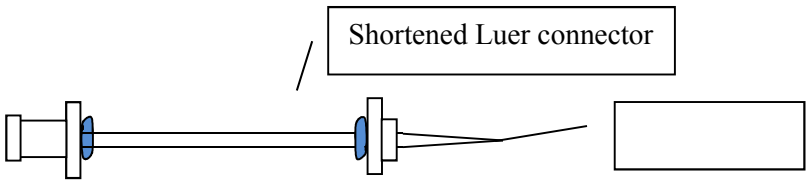
6. Remove extension tube, syringe, Eppendorf. Attach syringe pump to Luer connection via extension tubes, pump gently



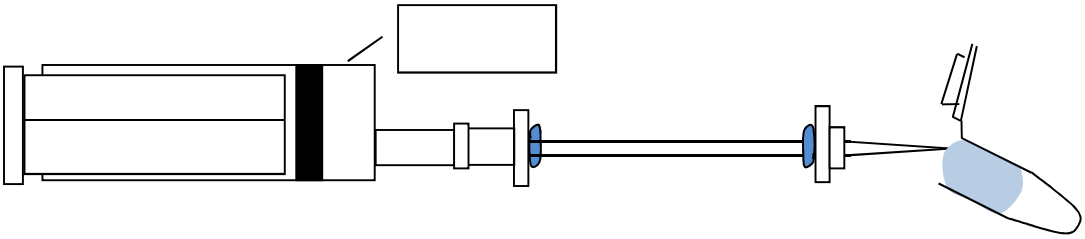
7. Use tweezers mounted on micro-manipulator to catch dope at end. Continue syringe pumping and pull away slowly to form fibre



C.c. 'Shortened Luer' spinning instructions



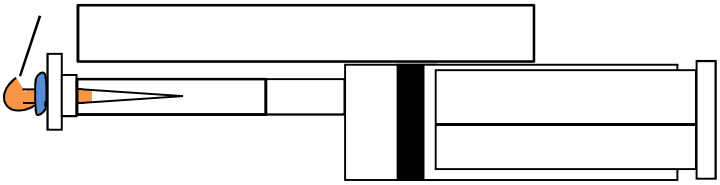
1. A nozzle was made up using one female Luer connector glued at the far end of the capillary, and a shortened connector glued next to the capillary taper



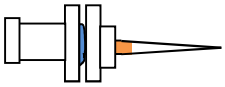
2. Any surface treatment was sucked by a syringe from a container into the taper, then any excess blown out using compressed air.



3. The capillary was broken away except for a very short distance protruding from the shortened Luer connector



4. Spider dope was sucked by a capillary from a container into the shortened capillary



5. Another Luer connector was glued back to back with the shortened capillary, forming the completed nozzle



6. The new Luer connector was connected to the syringe pump assembly as before and fibres spun onto the collecting reel.

C.d. Hot coil heating device

To control the temperature of the hot coil, a thermostat controlled heating kit (Velleman MK138) was built and tested. The original temperature range of the kit was less than required at 5-30 ° C.

This was modified to 20-70 ° C by arrangement and substitution of resistors. The hysteresis of the temperature control was altered to give better accuracy around a desired set point by similar (see Fig. 10.12 (B)) for circuit diagram and Table 10.6 for resistor substitutions). This setup allowed temperature control of the coil and capillary within.

The thermostat was calibrated by placing a thermocouple within a capillary, centred within the heating coil. The temperature measured within the capillary was measured from the digital readout, and the values marked on the control dial of the thermostat. Thereafter, temperatures could be selected by turning the dial to the required temperature.

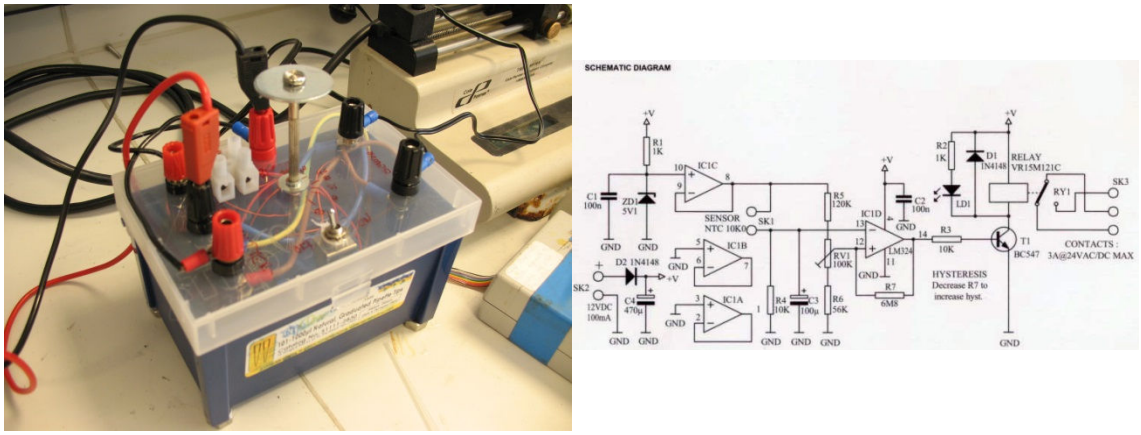


Fig. 10.12 (A) Hot coil 2 control box. (B) Thermostat circuit diagram.

Table 10.6 Resistors replaced in thermostat. Refer to Fig. 10.12 (B) for resistor designations.

Resistor	Original value (Ω)	Altered value (Ω)
R5	120k	15.4
R6	56k	120k
R7	6M8	14M

C.e. Peltier modifications

Initially, a flat strip of copper with a hole drilled in the end was used to transfer heat from the Peltier to the capillary. However, the drop in heat across the strip between the Peltier and the capillary was considerable, so it was not possible to heat the capillary to more than 35 ° C when the Peltier was at full power.

To reduce heat loss, a laptop heatsink was found and modified to remove almost all the cooling fins, leaving phase change copper heat pipes for efficient heat transfer. A copper disc with a hole drilled through for the capillary was soldered onto the end of the two heat pipes. One calibrated thermocouple was soldered just to the inner edge of the hole so that it measured the temperature at the capillary, and the whole assembly insulated with foam and then masking tape. This assembly was clamped (sandwiching in heat conductive paste (Arctic Silver)) to the Peltier plate, and onto

the micromanipulator (Leica 116595). This procedure reduced the temperature drop from the Peltier to the remote point from 15- 20 ° C to 8-10 ° C, dependant on external lab conditions.

C.f. Collecting rod rotation

The motor used was a security camera motor (RS precision motor 336-292) and gearbox (RS 336-286). These were chosen as the very low ratio gearbox meant a slow speed of rotation could be obtained. Motor speed was controlled by a switching 1 A power supply (Velleman P1823'2), which was built and interfaced to. Power to this speed controller was provided by a 40 W universal laptop power supply (Maplin N59GU). To this gearbox was attached a custom fibre collecting rods.

The speed of the motor was calibrated to the voltage output by the switching power supply. This voltage was monitored by a multimeter (Duratool DT9205) and the rotation rate of the fibre collecting rod monitored via standard lab stopwatch. Fig. 10.13 shows the calibration curve used to calculate the rate of rotation of the rod.

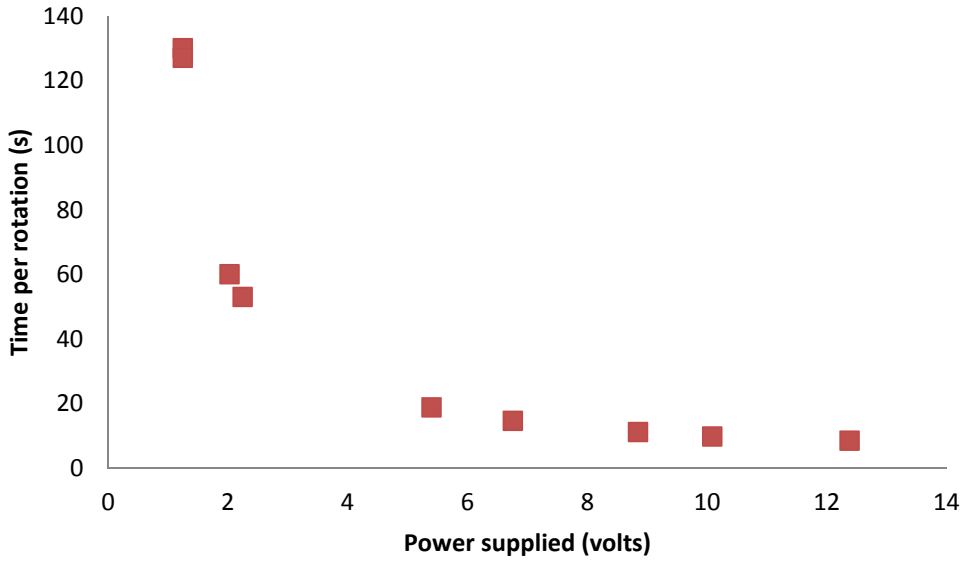


Fig. 10.13 speed of motor as a function of the voltage applied to it. This curve can be approximated by the equation $y=153.54x^{-1.2}$ with an R^2 value of 0.9941 where x is volts, y time per rotation.

The spinning rate of silk fibres was then calculated by noting the voltage indicated by the multimeter and calculating using the equation for time per rotation and the diameter of the rod.

C.f.i. Generation 2

Although the power supply used in Generation 1 was theoretically possible of supplying anything between 0 and 30 v, in practice it was difficult to obtain precise voltage outputs from the single turn rotary potentiometer, nor could the supply output voltages below 1.25 v. Therefore an extra rotary variable resistor was added to the system to allow very fine control and slow speeds to be accessible. This was integrated into a box (Fig. 10.14) that also held the controls for horizontal traversing of the collecting rod, such that each control could be ergonomically accessed.

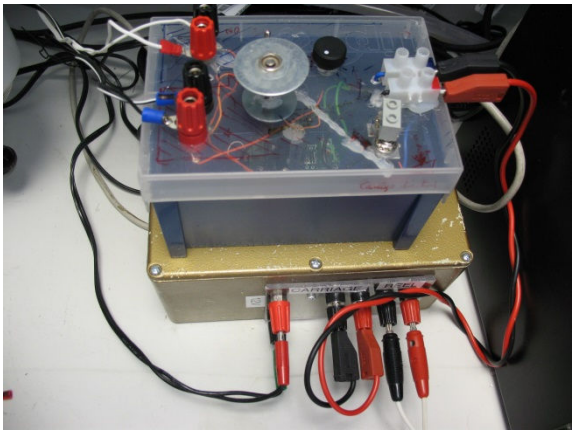


Fig. 10.14 Collecting rod speed controller box (top) and hardware interface with the computer program (bottom).

C.g. Collecting rods

The first iteration used a brass collar with a setscrew to lock to the gearbox output shaft, and another setscrew to lock to a brass rod.

Unfortunately the holes through the collar were larger than the gearbox output shaft and the brass rod. This meant that the whole assembly circumscribed a cone shape, which meant that while the motor was turning the distance between the rod and the nozzle tip was constantly varying. This variation made starting to spin from the fragile nozzle tip very difficult, and would sometimes break the tip entirely off the nozzle.

To solve the problem of off centre rotation, a custom rod was designed and built. It had an aluminium collar that was a tight concentric fit over the gearbox output shaft, and a brass rod 4 mm in diameter was pressed into another tight fitting hole the other side of the collar. A hole was drilled and tapped into the brass collar to take a set screw to secure the assembly to the gearbox output shaft.

This new assembly (Fig. 10.15, top) increased reduced the variability of the position of the tip of the collecting rod from almost one centimetre to one millimetre.

Uncoiling the tight 4 mm rings spun fibres made around the brass rod often led to kinking of fibres, which introduced weak points when tensile tested. Therefore there was a need for a rod of a larger diameter with larger rings. 10 mm diameter aluminium bar stock was chosen, both ends faced off, and a hole that fitted the gearbox output shaft tightly bored in one end. A tapered hole was made in the other end, to interface with apparatus for fibre mounting on card. A setscrew was attached in the same manner as the previous collecting rod.

Two collecting rods were made of this design (Fig. 10.15 bottom), so the rods could be alternated and spinning could be continued before mounting the fibres.

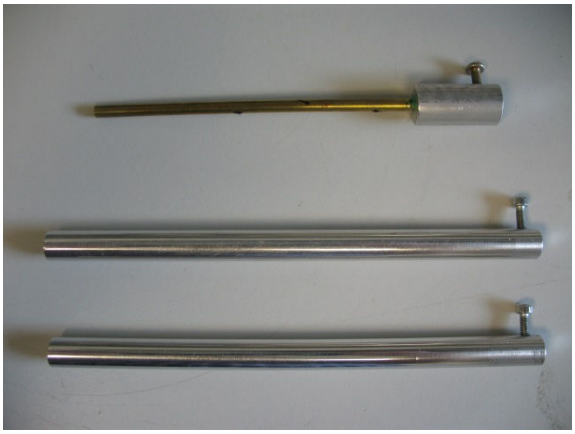


Fig. 10.15 Fibre collecting rods. Top, brass, middle and bottom, aluminium.

C.h. Horizontal movement

C.h.i. Lego with motor

Although moving the collecting rod axially by hand meant more fibre could be collected, problems were revealed when longer lengths of fibre were spun. Fibre spinning was fairly unstable, so large jerky hand movements often broke the fibre being spun, or the sudden movement increased the speed at which fibres were spun. Therefore a more controlled method of moving the fibre collecting rod was desired.

The collecting rod motor was mounted upon a carriage made from Lego ®, which ran between smooth Lego tracks on an acrylic base (Fig. 10.16 (A)). A second security camera and gearbox (RS 336-286) with its driveshaft mounted vertically was connected to two arms, connected to the Lego carriage (Fig. 10.16 (B)), which converted the rotary movement of the motor to horizontal movement of the carriage.

This second motor was driven by a standard lab power pack.

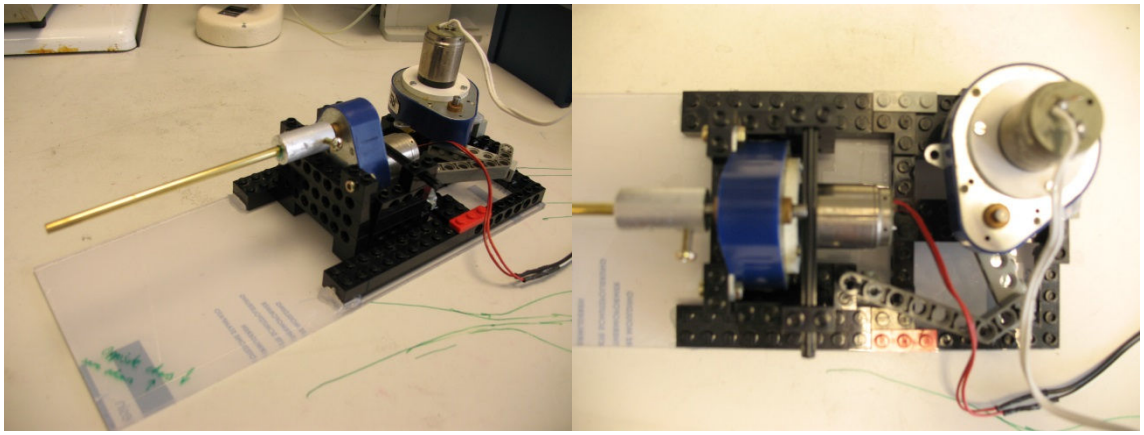


Fig. 10.16 Lego based horizontal movement setup, (A) full device view, (B) top view showing motor arm detail.

C.h.ii. Floppy disc drive frame with motor

Although the Lego carriage system allowed the motor to control the position of the carriage, the motor was too highly geared to permit continuous operation at very slow speeds without sticktion of the Lego carriage to the rails. This resulted in mostly periods of little or no movement, followed by large jumps as the sticktion in the system became released. This was better than moving by hand but still not very good for spinning regular fibres.

Therefore the rails were upgraded to have less friction. The frame and rails were dissembled from a 3.5" floppy disc drive and attached to the acrylic plate. A smaller carriage was made and attached to the traversing reader head of the floppy drive, still mounted upon the linear bearings. This was moved by the second motor, gearbox and arm as before.

This worked very much smoother than before. Now that very much more of the collecting rod could be used, there became a problem from the corner of the carriage hitting the Peltier plate that was clamped above. Therefore the motor was move from the output shaft being in a central position to the top left hand side of the carriage, as close to the spinning nozzle tip as possible (Fig. 6.15). having an arm rather than for example a pulley and cable meant the speed of the horizontal carriage changed depending on the position of the lever, but this small disadvantage was preferable to the more complicated system a pulley would require.

C.i. Software details and code

C.i.i. Background

To overcome the problem of low continuous voltage being insufficient to move the inertia of the collecting rod horizontal movement motor, instead very short pulses of higher voltage were controlled by the software. Thus the speed control part of the software is simply a timer, with adjustable parameters of output voltage, output time and time between pulses. For diagnostics the boxes at the bottom left count up the time since previous action.

The slider to the far right hand edge of the form controls the voltage sent to the Peltier controller. For indication only the box below the slider roughly displays the temperature of the controller, calibrated by a 3 point curve and a trend line drawn in Excel.

To rapidly move the collecting rod horizontal motor, a 'fast mode' setting overrides the pulses and outputs to the motor a constant voltage as specified in the 'fast speed' slider.

The software loaded the values shown in the figure as the default setting, which gave a good starting speed and temperature for spinning. The settings could be returned to their default positions with the 'Reset' button. If power to the PWM board was lost then regained, the 'Reconnect' button initiates communication again.

C.i.ii. Code

Written in Visual Basic .NET. Green text is comments.

```
Public Class Form1
  Inherits System.Windows.Forms.Form
```

```
#Region " Windows Form Designer generated code "
...
#End Region


 Declare Function InitMotoBee Lib "mtb.dll" () As Boolean
 Declare Function Digital_IO Lib "mtb.dll" (ByRef inputs As Integer, ByVal outputs As Integer)
As Boolean
 Declare Function SetMotors Lib "mtb.dll" (ByVal on1 As Integer, ByVal speed1 As Integer, ByVal
on2 As Integer, ByVal speed2 As Integer, ByVal on3 As Integer, ByVal speed3 As Integer, ByVal
on4 As Integer, ByVal speed4 As Integer, ByVal servo As Integer) As Boolean
 Dim TimeUp As Integer
 Private Sub Form1_Load(ByVal sender As System.Object, ByVal e As System.EventArgs) Handles
MyBase.Load
 InitMotoBee() ' initialise the MotorBee
 TimeUp = 0


 End Sub

 Private Sub butgo_KeyDown(ByVal sender As Object, ByVal e As System.Windows.Forms.KeyEventArgs)
Handles Butgo.KeyDown
 If e.Alt And e.KeyCode.ToString = "Q" And speed3.Value < (speed3.Maximum) Then
 Me.KeyPreview = True
 speed3.Value = speed3.Value + 1
 ElseIf e.Alt And e.KeyCode.ToString = "A" And speed3.Value > (speed3.Minimum) Then
 Me.KeyPreview = True
 speed3.Value = speed3.Value - 1

 ElseIf e.Alt And e.KeyCode.ToString = "W" And speed3.Value < (speed3.Maximum - 9) Then
 Me.KeyPreview = True
 speed3.Value = speed3.Value + 10
 ElseIf e.Alt And e.KeyCode.ToString = "S" And speed3.Value > (speed3.Minimum + 9) Then
 Me.KeyPreview = True
 speed3.Value = speed3.Value - 10

 ElseIf e.Alt And e.KeyCode.ToString = "E" And nudOn.Value < (nudOn.Maximum - 9) Then
 Me.KeyPreview = True
 nudOn.Value = nudOn.Value + 10
 ElseIf e.Alt And e.KeyCode.ToString = "D" And nudOn.Value > (nudOn.Minimum + 9) Then
 Me.KeyPreview = True
 nudOn.Value = nudOn.Value - 10

 ElseIf e.Alt And e.KeyCode.ToString = "R" And nudOff.Value < (nudOff.Maximum - 9) Then
 Me.KeyPreview = True
 nudOff.Value = nudOff.Value + 10
 ElseIf e.Alt And e.KeyCode.ToString = "F" And nudOff.Value > (nudOff.Minimum + 9) Then
 Me.KeyPreview = True
 nudOff.Value = nudOff.Value - 10

 ElseIf e.Alt And e.KeyCode.ToString = "T" And NUDFast.Value < (NUDFast.Maximum - 9) Then
 Me.KeyPreview = True
 NUDFast.Value = NUDFast.Value + 10
 ElseIf e.Alt And e.KeyCode.ToString = "G" And NUDFast.Value > (NUDFast.Minimum + 9) Then
 Me.KeyPreview = True
 NUDFast.Value = NUDFast.Value - 10

 ElseIf e.Alt And e.KeyCode.ToString = "I" And speed3.Value < (speed1.Maximum) Then
 Me.KeyPreview = True
```

```
 speed1.Value = speed1.Value + 1
 ElseIf e.Alt And e.KeyCode.ToString = "K" And speed3.Value > (speed1.Minimum) Then
 Me.KeyPreview = True
 speed1.Value = speed1.Value - 1
 End If
 End Sub

 Private Sub Button1_Click(ByVal sender As System.Object, ByVal e As System.EventArgs) Handles
Button1.Click
 InitMotoBee() ' initialise the MotorBee
 End Sub

 Private Sub Button2_Click(ByVal sender As System.Object, ByVal e As System.EventArgs) Handles
Button2.Click
 Dim s1, s2, s3, s4 As Integer
 Dim o1, o2, o3, o4 As Integer
 Dim sv As Integer
 Dim inputs As Integer
 Dim outputs As Integer

 s1 = speed1.Text
 s2 = speed2.Text
 s3 = speed3.Text
 s4 = speed4.Text
 sv = servo.Text

 If on1.Checked Then
 o1 = 1
 Else
 o1 = 0
 End If

 If on2.Checked Then
 o2 = 1
 Else
 o2 = 0
 End If

 If on3.Checked Then
 o3 = 1
 Else
 o3 = 0
 End If
 If on4.Checked Then
 o4 = 1
 Else
 o4 = 0
 End If

 SetMotors(o1, s1, o2, s2, o3, s3, o4, s4, sv)

 outputs = 0

 Digital_IO(inputs, outputs)
 End Sub

 Private Sub Timer1_Tick(ByVal sender As System.Object, ByVal e As System.EventArgs) Handles
Timeron.Tick
 Dim s1, s2, s3, s4 As Integer
```

```
 Dim o1, o2, o3, o4 As Integer
 Dim sv As Integer
 Dim inputs As Integer
 Dim outputs As Integer
 TimeUp = TimeUp + 10
 TextBox1.Text = TimeUp


 s1 = speed1.Text
 s2 = speed2.Text
 s3 = speed3.Text
 s4 = speed4.Text
 sv = servo.Text


 o3 = 1
 o1 = 1
 CheckBox1.Checked = True

 SetMotors(o1, s1, o2, s2, o3, s3, o4, s4, sv)

 If TimeUp >= nudOn.Value Then
 TimeUp = 0
 Timeron.Enabled = False
 Timeroff.Enabled = True
 o3 = 0
 o1 = 1
 CheckBox1.Checked = False

 SetMotors(o1, s1, o2, s2, o3, s3, o4, s4, sv)

 End If
 End Sub
 Private Sub TimerOff_Tick(ByVal sender As System.Object, ByVal e As System.EventArgs) Handles
Timeroff.Tick
 TimeUp = TimeUp + 10
 TextBox2.Text = TimeUp

 If TimeUp >= nudOff.Value Then
 TimeUp = 0
 Timeron.Enabled = True
 Timeroff.Enabled = False

 End If
 End Sub

 Private Sub ButGo_Click(ByVal sender As System.Object, ByVal e As System.EventArgs) Handles
Butgo.Click

 If Timeron.Enabled = False And Timeroff.Enabled = False Then
 Timeron.Enabled = True
 ButFast.Enabled = True
 Butgo.Text = "Stop"


 Else
 Timeron.Enabled = False
 Timeroff.Enabled = False
 ButFast.Enabled = False
```

```
 Butgo.Text = "Go"

 CheckBox1.Checked = False
 Dim s1, s2, s3, s4 As Integer
 Dim o1, o2, o3, o4 As Integer
 Dim sv As Integer
 Dim inputs As Integer
 Dim outputs As Integer

 s1 = speed1.Text
 s2 = speed2.Text
 s3 = speed3.Text
 s4 = speed4.Text
 sv = servo.Text

 o1 = 1


 o3 = 0


 SetMotors(o1, s1, o2, s2, o3, s3, o4, s4, sv)
 End If
 End Sub

 Private Sub ButReset_Click(ByVal sender As System.Object, ByVal e As System.EventArgs) Handles
ButReset.Click
 TimeUp = 0
 TextBox1.Text = TimeUp
 TextBox2.Text = TimeUp
 End Sub


 Private Sub TrackBar1_Scroll(ByVal sender As System.Object, ByVal e As System.EventArgs)
Handles TrackBar1.Scroll
 speed3.Value = TrackBar1.Value
 End Sub

 Private Sub speed3_valueChanged(ByVal sender As System.Object, ByVal e As System.EventArgs)
 TrackBar1.Value = speed3.Value
 End Sub

 Private Sub TBOn_Scroll(ByVal sender As System.Object, ByVal e As System.EventArgs) Handles
TBOn.Scroll
 nudOn.Value = TBOn.Value
 End Sub

 Private Sub NudOn_ValueChanged(ByVal sender As System.Object, ByVal e As System.EventArgs)
Handles nudOn.ValueChanged
 TBOn.Value = nudOn.Value
 End Sub

 Private Sub TBOff_Scroll(ByVal sender As System.Object, ByVal e As System.EventArgs) Handles
TBOff.Scroll
 nudOff.Value = TBOff.Value
 End Sub
```

```
 Private Sub NudOff_ValueChanged(ByVal sender As System.Object, ByVal e As System.EventArgs)
Handles nudOff.ValueChanged
 TBOff.Value = nudOff.Value
 End Sub



 Private Sub TBFast_Scroll(ByVal sender As System.Object, ByVal e As System.EventArgs) Handles
TBFast.Scroll
 NUDFast.Value = TBFast.Value
 End Sub

 Private Sub NumericUpDown1_ValueChanged(ByVal sender As System.Object, ByVal e As
System.EventArgs) Handles NUDFast.ValueChanged
 TBFast.Value = NUDFast.Value
 End Sub

 Private Sub Button3_Click(ByVal sender As System.Object, ByVal e As System.EventArgs) Handles
ButFast.Click
 If Timeron.Enabled = False And Timeroff.Enabled = False Then
 Timeron.Enabled = True
 ButFast.Text = "Fast mode"


 Else
 Timeron.Enabled = False
 Timeroff.Enabled = False

 CheckBox1.Checked = True
 Dim s1, s2, s3, s4 As Integer
 Dim o1, o2, o3, o4 As Integer
 Dim sv As Integer
 Dim inputs As Integer
 Dim outputs As Integer

 s1 = speed1.Text
 s2 = NUDFast.Value
 s3 = speed3.Text
 s4 = speed4.Text
 sv = servo.Text


 o3 = 1
 o1 = 1

 SetMotors(o1, s1, o2, s2, o3, s3, o4, s4, sv)
 ButFast.Text = "Normal mode"
 End If

 End Sub



 Private Sub TrackBar2_Scroll(ByVal sender As System.Object, ByVal e As System.EventArgs)
Handles TrackBar2.Scroll
 speed1.Value = TrackBar2.Value
 NUDTempEst.Value = (0.454945396340605 * speed1.Value + 0.742646070721619)
 End Sub
```

```
 Private Sub NumericUpDown1_ValueChanged_1(ByVal sender As System.Object, ByVal e As
System.EventArgs) Handles speed1.ValueChanged
 TrackBar2.Value = speed1.Value
 NUDTempEst.Value = (0.454945396340605 * speed1.Value + 0.742646070721619)
 End Sub
End Class
```

Appendix D. References

1996. Conical fittings with a 6% (Luer) taper for syringes, needles and certain other medical equipment - Lock fittings. European Committee for Standardization.

AKAI, H. 1983. The Structure and Ultrastructure of the Silk Gland. *Experientia,* 39**,** 443-449.

AKIN, J. E. 2010. *Finite Element Analysis Concepts: Via Solidworks*, World Scientific.

ALBÉROLA, N. D., MÉLÉ, P. & BAS, C. 1997. Tensile mechanical properties of PEEK films over a wide range of strain rates. II. *Journal of Applied Polymer Science,* 64**,** 1053-1059.

ALTMAN, G. H., DIAZ, F., JAKUBA, C., CALABRO, T., HORAN, R. L., CHEN, J. S., LU, H., RICHMOND, J. & KAPLAN, D. L. 2003. Silk-based biomaterials. *Biomaterials,* 24**,** 401-416.

AN, B., HINMAN, M. B., HOLLAND, G. P., YARGER, J. L. & LEWIS, R. V. 2011. Inducing beta-Sheets Formation in Synthetic Spider Silk Fibers by Aqueous Post-Spin Stretching. *Biomacromolecules,* 12**,** 2375-2381.

ARCIDIACONO, S., MELLO, C. M., BUTLER, M., WELSH, E., SOARES, J. W., ALLEN, A., ZIEGLER, D., LAUE, T. & CHASE, S. 2002. Aqueous processing and fiber spinning of recombinant spider silks. *Macromolecules,* 35**,** 1262-1266.

ASAKURA, T., UMEMURA, K., NAKAZAWA, Y., HIROSE, H., HIGHAM, J. & KNIGHT, D. 2007a. Some Observations on the Structure and Function of the Spinning Apparatus in the Silkworm Bombyx mori. *Biomacromolecules,* 8**,** 175-181.

ASAKURA, T., YAO, J., YANG, M., ZHU, Z. & HIROSE, H. 2007b. Structure of the spinning apparatus of a wild silkworm Samia cynthia ricini and molecular dynamics calculation on the structural change of the silk fibroin. *Polymer,* 48**,** 2064-2070.

ASKARIEH, G., HEDHAMMAR, M., NORDLING, K., SAENZ, A., CASALS, C., RISING, A., JOHANSSON, J. & KNIGHT, S. D. 2010. Self-assembly of spider silk proteins is controlled by a pH-sensitive relay. *Nature,* 465**,** 236-U125.

AYOUB, N. A., GARB, J. E., TINGHITELLA, R. M., COLLIN, M. A. & HAYASHI, C. Y. 2007. Blueprint for a high-performance biomaterial: full-length spider dragline silk genes. *PLoS ONE,* 2**,** e514.

BANCROFT, J. D. & GAMBLE, M. 2008. *Theory and practice of histological techniques*, Churchill Livingstone Elsevier.

BAOQI, Z., LEIGEN, L. & ZHENGYU, W. 2007. Effect on properties of regenerated silk fibroin fiber coagulated with aqueous methanol/ethanol. *Journal of Applied Polymer Science,* 106**,** 53-9.

BARTH, A. & ZSCHERP, C. 2002. What vibrations tell us about proteins. *Quarterly Reviews of Biophysics,* 35**,** 369-430.

BELL, A. L. & PEAKALL, D. B. 1969. Changes in fine structure during silk protein production in ampullate gland of spider Araneus sericatus. *Journal of Cell Biology,* 42**,** 284-295.

BEPPU, M. M., VIEIRA, R. S., AIMOLI, C. G. & SANTANA, C. C. 2007. Crosslinking of chitosan membranes using glutaraldehyde: Effect on ion permeability and water absorption. *Journal of Membrane Science,* 301**,** 126-130.

BLUDSZUWEIT, C. 1995. 3-dimensional numerical prediction of stress loading of blood particles in a centrifugal pump. *Artificial Organs,* 19**,** 590-596.

BODAS, D. & KHAN-MALEK, C. 2007. Hydrophilization and hydrophobic recovery of PDMS by oxygen plasma and chemical treatment - An SEM investigation. *Sensors and Actuators B-Chemical,* 123**,** 368-373.

BOULET-AUDET, M., BUFFETEAU, T., BOUDREAULT, S., DAUGEY, N. & PEZOLET, M. 2010. Quantitative Determination of Band Distortions in Diamond Attenuated Total Reflectance Infrared Spectra. *Journal of Physical Chemistry B,* 114**,** 8255-8261.

BOULET-AUDET, M., TERRY, A., VOLLRATH, F. & HOLLAND, C. In preparation. Silk fibrillogenesis mechanism revealed by Rheo-IR.

BOULET-AUDET, M., VOLLRATH, F. & HOLLAND, C. 2011. Rheo-attenuated total reflectance infrared spectroscopy: a new tool to study biopolymers. *Physical Chemistry Chemical Physics,* 13**,** 3979-3984.

BOULIGAND, Y. & GIRAUD-GUILLE, M. M. 1985. Spatial organization of collagen fibrils in skeletal tissues. *In:* BAIRATI, A. & GARRONE, R. (eds.) *Biology of Invertebrate and Lower Vertebrate Collagens.* New York: Plenum Press.

BRESLAUER, D. N., LEE, L. P. & MULLER, S. J. 2009. Simulation of Flow in the Silk Gland. *Biomacromolecules,* 10**,** 49-57.

BRIDGMAN, P. W. 1922. *Dimensional analysis*, Yale University Press.

BRISTOWE, W. S. 1958. *The World of Spiders,* London, Collins.

BROOKS, A. E., STRICKER, S. M., JOSHI, S. B., KAMERZELL, T. J., MIDDAUGH, C. R. & LEWIS, R. V. 2008. Properties of synthetic spider silk fibers based on *Argiope aurantia* MaSp2. *Biomacromolecules,* 9**,** 1506-1510.

CAMPBELL, F. L. 1929. The detection and estimation of insect chitin; and the irrelation of "chitinization" to hardness and pigmentation of the cuticula of the American cockroach, Periplaneta americana L. *Annals of the Entomological Society of America,* 22**,** 401-426.

CARDENAS, G., CABRERA, G., TABOADA, E. & MIRANDA, S. P. 2004. Chitin characterization by SEM, FTIR, XRD, and C-13 cross polarization/mass angle spinning NMR. *Journal of Applied Polymer Science,* 93**,** 1876-1885.

CARLSTROM, D. 1957. The crystal structure of a-chitin (poly-AT-acetyl-D-glucosamine). *J. biophys. biochem. Cytol. ,* 3**,** 669-683.

CASEM, M. L., TRAN, L. P. P. & MOORE, A. M. F. 2002. Ultrastructure of the major ampullate gland of the black widow spider, Latrodectus hesperus. *Tissue & Cell,* 34**,** 427-436.

CHEN, G. Y., CUCULO, J. A. & TUCKER, P. A. 1992. Characteristics and design procedure of hyperbolic dies. *Journal of Polymer Science Part B-Polymer Physics,* 30**,** 557-561.

CHEN, X., KNIGHT, D. P., SHAO, Z. Z. & VOLLRATH, F. 2001. Regenerated Bombyx silk solutions studied with rheometry and FTIR. *Polymer,* 42**,** 9969-9974.

CHEN, X., KNIGHT, D. P., SHAO, Z. Z. & VOLLRATH, F. 2002a. Conformation transition in silk protein films monitored by time-resolved Fourier transform infrared spectroscopy: Effect of potassium ions on Nephila spidroin films. *Biochemistry,* 41**,** 14944-14950.

CHEN, X., KNIGHT, D. P. & VOLLRATH, F. 2002b. Rheological characterization of Nephila spidroin solution. *Biomacromolecules,* 3**,** 644-648.

CHEN, X., SHAO, Z. & VOLLRATH, F. 2006. The spinning processes for spider silk. *Soft Matter,* 2**,** 448-451.

CHEN, X., ZHOU, L., SHAO, Z. Z., ZHOU, P., KNIGHT, D. P. & VOLLRATH, F. 2003. Conformation transition of silk protein membranes monitored by time-resolved FT-IR spectroscopy - Conformation transition behavior of regenerated silk fibroin membranes in alcohol solution at high concentrations. *Acta Chimica Sinica,* 61**,** 625-629.

CHO, H. J., YOO, Y. J., KIM, J. W., PARK, Y. H., BAE, D. G. & UM, I. C. 2012. Effect of molecular weight and storage time on the wet- and electro-spinning of regenerated silk fibroin. *Polymer Degradation and Stability,* 97**,** 1060-1066.

CODDINGTON, J. A. 1989. Spinneret silk spigot morphology - evidence for the monophyly of orbweaving spiders, Cyrtophorinae (Araneidae), and the group Theridiidae plus Nesticidae. *Journal of Arachnology,* 17**,** 71-95.

CODDINGTON, J. A., CHANZY, H. D., JACKSON, C. L., RATY, G. & GARDNER, K. H. 2002. The unique ribbon morphology of the major ampullate silk of spiders from the genus Loxosceles (Recluse spiders). *Biomacromolecules,* 3**,** 5-8.

CRAIG, C. L. 1997. Evolution of arthropod silks. *Annual Reviews of Entomology,* 42**,** 231-267.

CUNNIFF, P. M., FOSSEY, S. A., AUERBACH, M. A. & SONG, J. W. 1994. Mechanical-Properties of Major Ampulate Gland Silk Fibers Extracted from Nephila-Clavipes Spiders. *In:* KAPLAN,

D., ADAMS, W. W., FARMER, B. & VINEY, C. (eds.) *Silk Polymers: Materials Science and Biotechnology.* Washington: American Chemical Society.

CUNNIFF, P. M. F., STEPHEN A.; AUERBACH, MARGARET A.; SONG, JOHN W. 1994. Mechanical properties of major ampullate gland silk fibers extracted from Nephila clavipes spiders. *ACS Symposium Series; silk polymer,* 544**,** 234-251.

DABORA, J. M. & MARQUSEE, S. 1994. Equilibrium unfolding of Escherichia-coli ribonuclease-h - characterization of a partially folded state. *Protein Science,* 3**,** 1401-1408.

DAWYDOFF, C. 1949. Developpement embryonnaire des arachnides. *In:* GRASSE, P.-P. (ed.) *Traite de zoologie. Anatomie, systematique, biologie. VI. Onychophores. Tardi-grades. Arthropodes, Trilobitomorphes. Chelicerates.*

DICKO, C., KENNEY, J. M., KNIGHT, D. & VOLLRATH, F. 2004a. Transition to a beta-sheet-rich structure in spidroin in vitro: The effects of pH and cations. *Biochemistry,* 43**,** 14080-14087.

DICKO, C., PORTER, D., BOND, J., KENNEY, J. M. & VOLLRATHT, F. 2008. Structural disorder in silk proteins reveals the emergence of elastomericity. *Biomacromolecules,* 9**,** 216-221.

DICKO, C., VOLLRATH, F. & KENNEY, J. M. 2004b. Spider Silk Protein Refolding Is Controlled by Changing pH. *Biomacromolecules,* 5**,** 704-710.

EBERHARD, W. G. 2010. Possible functional significance of spigot placement on the spinnerets of spiders. *Journal of Arachnology,* 38**,** 407-414.

ELICES, M., GUINEA, G. V., PLAZA, G. R., KARATZAS, C., RIEKEL, C., AGULLO-RUEDA, F., DAZA, R. & PEREZ-RIGUEIRO, J. 2011. Bioinspired Fibers Follow the Track of Natural Spider Silk. *Macromolecules,* 44**,** 1166-1176.

ELICES, M., PLAZA, G. R., ARNEDO, M. A., PEREZ-RIGUEIRO, J., TORRES, F. G. & GUINEA, G. V. 2009. Mechanical Behavior of Silk During the Evolution of Orb-Web Spinning Spiders. *Biomacromolecules,* 10**,** 1904-1910.

FOCHER, B., NAGGI, A., TORRI, G., COSANI, A. & TERBOJEVICH, M. 1992. Chitosans from Euphausia-superba 2. Characterization of solid-state structure. *Carbohydrate Polymers,* 18**,** 43-49.

FOELIX, F. R. 1971a. Some morphological aspects of the innervation of a spiders silk gland. *Tissue & Cell,* 3**,** 423-432.

FOELIX, R. F. 1971b. Some morphological aspects of innervation of a spiders silk gland. *Tissue & Cell,* 3**,** 423-432.

FOELIX, R. F. 1982. *Biology of Spiders,* Cambridge, MA, Harvard University Press.

FOELIX, R. F. 1996. *Biology of Spiders*, Oxford University Press.

FOO, C. W. P., BINI, E., HENSMAN, J., KNIGHT, D. P., LEWIS, R. V. & KAPLAN, D. L. 2006. Role of pH and charge on silk protein assembly in insects and spiders. *Applied Physics A: Materials Science & Processing,* 82**,** 223-233.

FRANZ, H., GOODWIN, G. B. & MARIETTI, G. J. 1996. *Water repellent surface treatment for plastic and coated plastic substrates*. USA patent application US19940363804 19941227

FRESNAIS, J., CHAPEL, J. P. & PONCIN-EPAILLARD, F. 2006. Synthesis of transparent superhydrophobic polyethylene surfaces. *Surface & Coatings Technology,* 200**,** 5296-5305.

FU, C. J., SHAO, Z. Z. & FRITZ, V. 2009. Animal silks: their structures, properties and artificial production. *Chemical Communications***,** 6515-6529.

GAINES, W. A., SEHORN, M. G. & MARCOTTE, W. R. 2010. Spidroin N-terminal Domain Promotes a pH-dependent Association of Silk Proteins during Self-assembly. *Journal of Biological Chemistry,* 285.

GARRIDO, M. A., ELICES, M., VINEY, C. & PEREZ-RIGUEIRO, J. 2002a. Active control of spider silk strength: comparison of drag line spun on vertical and horizontal surfaces. *Polymer,* 43**,** 1537-1540.

GARRIDO, M. A., ELICES, M., VINEY, C. & PÉREZ-RIGUEIRO, J. 2002b. Active control of spider silk: comparison of drag line spun on vertical and horizontal surfaces. *Polymer,* 43**,** 1537-1540.

GEDAY, M. A., KAMINSKY, W., LEWIS, J. G. & GLAZER, A. M. 2000. Images of absolute retardance L.Δn, using the rotating polariser method. *Journal of Microscopy,* 198**,** 1-9.

GERTSCH, W. J. 1979. *AMERICAN SPIDERS*.

GEURTS, P., ZHAO, L., HSIA, Y., GNESA, E., TANG, S., JEFFERY, F., LA MATTINA, C., FRANZ, A., LARKIN, L. & VIERRA, C. 2010. Synthetic Spider Silk Fibers Spun from Pyriform Spidroin 2, A Glue Silk Protein Discovered in Orb-Weaving Spider Attachment Discs. *Biomacromolecules,* 11**,** 3495-3503.

GHIRADELLA, H. 2010. Insect Cuticular Surface Modifications: Scales and Other Structural Formations. *In:* CASAS, J. & SIMPSON, S. J. (eds.) *Advances in Insect Physiology: Insect Integument and Colour.*

GOSLINE, J. M., DEMONT, M. E. & DENNY, M. W. 1986. The structure and properties of spider silk. *Endeavour,* 10**,** 37-43.

GRONAU, G., QIN, Z. & BUEHLER, M. J. 2013. Effect of sodium chloride on the structure and stability of spider silk's N-terminal protein domain. *Biomaterials Science,* 1**,** 276-284.

GROOME, J. R., TOWNLEY, M. A., DETSCHASCHELL, M. & TILLINGHAST, E. K. 1991. Detection and isolation of proctolin-like immunoreactivity in arachnids - possible cardioregulatory role for proctolin in the orb-weaving spiders argiope and araneus. *Journal of Insect Physiology,* 37**,** 9-19.

GUAN, J., PORTER, D. & VOLLRATH, F. 2012. Silks cope with stress by tuning their mechanical properties under load. *Polymer,* 53**,** 2717-2726.

GUAN, J., PORTER, D. & VOLLRATH, F. 2013. Thermally Induced Changes in Dynamic Mechanical Properties of Native Silks. *Biomacromolecules,* 14**,** 930-937.

GUAN, J., VOLLRATH, F. & PORTER, D. 2011. Two Mechanisms for Supercontraction in Nephila Spider Dragline Silk. *Biomacromolecules,* 12**,** 4030-4035.

GUEHRS, K. H., SCHLOTT, B., GROSSE, F. & WEISSHART, K. 2008. Environmental conditions impinge on dragline silk protein composition. *Insect Molecular Biology,* 17**,** 553-564.

GUINEA, G. V., ELICES, M., REAL, J. I., GUTIERREZ, S. & PEREZ-RIGUEIRO, J. 2005. Reproducibility of the tensile properties of spider (Argiope trifasciata) silk obtained by forced silking. *Journal of Experimental Zoology,* 303A**,** 37-44.

GUOHONG, L., HONG, L., TIANDUO, L. & JIYANG, W. 2012. Surface modification and functionalization of silk fibroin fibers/fabric toward high performance applications. *Materials Science & Engineering: C (Materials for Biological Applications),* 32**,** 627-36.

HA, S. W., PARK, Y. H. & HUDSON, S. M. 2003. Dissolution of Bombyx mori silk fibroin in the calcium nitrate tetrahydrate-methanol system and aspects of wet spinning of fibroin solution. *Biomacromolecules,* 4**,** 488-496.

HA, S. W., TONELLI, A. E. & HUDSON, S. M. 2005. Structural studies of Bombyx mori silk fibroin during regeneration from solutions and wet fiber spinning. *Biomacromolecules,* 6**,** 1722-1731.

HABEL, R. E. 1963. Carbohydrates, phosphatases, and esterases in mucosa of ruminant forestomach during postnatal development. *American Journal of Veterinary Research,* 24**,** 199.

HAGN, F., EISOLDT, L., HARDY, J. G., VENDRELY, C., COLES, M., SCHEIBEL, T. & KESSLER, H. 2010. A conserved spider silk domain acts as a molecular switch that controls fibre assembly. *Nature,* 465**,** 239-U131.

HAGSTRUM, D. W. 1971. Carapace width as a tool for evaluating rate of development of spiders in laboratory and field. *Annals of the Entomological Society of America,* 64**,** 757.

HAJER, J., MALY, J. & REHAKOVA, D. 2013. Silk Fibers and Silk-Producing Organs of Harpactea rubicunda (C. L. Koch 1838) (Araneae, Dysderidae). *Microscopy Research and Technique,* 76**,** 28-35.

HAYASHI, C. Y., SHIPLEY, N. H. & LEWIS, R. V. 1999. Hypotheses that correlate the sequence, structure, and mechanical properties of spider silk proteins. *International Journal of Biological Macromolecules,* 24**,** 271-275.

HEPBURN, H. R. & BALL, A. 1973. Structure and mechanical properties of beetle shells. *Journal of Materials Science,* 8**,** 618-623.

HIJIRIDA, D. H., DO, K. G., MICHAL, C., WONG, S., ZAX, D. & JELINSKI, L. W. 1996. C-13 NMR of Nephila clavipes major ampullate silk gland. *Biophysical Journal,* 71**,** 3442-3447.

HILBRANT, M. 2008. *Development and Evolution of the Spider Silk Producing System.* Inaugural Dissertation, Universität zu Köln.

HINMAN, M. B., JONES, J. A. & LEWIS, R. V. 2000. Synthetic spider silk: a modular fiber. *Trends in Biotechnology,* 18**,** 374-379.

HOLL, A. & HENZE, M. Pigmentary constituents of yellow threads of Nephila webs. European Society of Arachnology: 11th european colloquium, 1988. 350.

HOLLAND, C., O'NEIL, K., VOLLRATH, F. & DICKO, C. 2012a. Distinct structural and optical regimes in natural silk spinning. *Biopolymers,* 97**,** 368-373.

HOLLAND, C., TERRY, A. E., PORTER, D. & VOLLRATH, F. 2006a. Comparing the rheology of native spider and silkworm spinning dope. *Nature Materials,* 5**,** 870-874.

HOLLAND, C., TERRY, A. E., PORTER, D. & VOLLRATH, F. 2007. Natural and unnatural Silks. *Polymer,* 48**,** 3388-3392.

HOLLAND, C., URBACH, J. S. & BLAIR, D. L. 2012b. Direct visualization of shear dependent silk fibrillogenesis. *Soft Matter,* 8**,** 2590-2594.

HOLLAND, C., VOLLRATH, F., RYAN, A. J. & MYKHAYLYK, O. O. 2012c. Silk and Synthetic Polymers: Reconciling 100 Degrees of Separation. *Advanced Materials,* 24**,** 105-109.

HOLLAND, C. A., TERRY, A. E., PORTER, D. & VOLLRATH, F. 2006b. Comparing the rheology of native spider and silkworm spinning dope. *Nature Materials,* 5**,** 870-874.

HOSSAIN, K. S., NEMOTO, N. & MAGOSHI, J. 1999. Rheological study on aqueous solutions of silk fibroin extracted from the middle division of Bombyx Mori silkworm. *Nihon Reoroji Gakkaishi,* 27**,** 129-130.

IBRAHIM, M., NADA, A. & KAMAL, D. E. 2005. Density functional theory and FTIR spectroscopic study of carboxyl group. *Indian Journal of Pure & Applied Physics,* 43**,** 911-917.

IIZUKA, E. 1966. Mechanism of fiber formation by the silkworm Bombyx Mori. *Biorheology,* 3**,** 141-152.

JACKSON, M. & MANTSCH, H. H. 1995. The Use and Misuse of FTIR Spectroscopy in the Determination of Protein-Structure. *Critical Reviews in Biochemistry and Molecular Biology,* 30**,** 95-120.

JANG, H., KIM, S., CHO, J. & CHAR, K. 2003. Spin-coated ultrathin multilayers and their micropatteming using microfluidic channels. *Korea-Australia Rheology Journal,* 15**,** 1-7.

JANG, M. K., KONG, B. G., JEONG, Y. I., LEE, C. H. & NAH, J. W. 2004. Physicochemical characterization of alpha-chitin, beta-chitin, and gamma-chitin separated from natural resources. *Journal of Polymer Science Part A-Polymer Chemistry,* 42**,** 3423-3432.

JEONG, H. J., KIM, D. K., LEE, S. B., KWON, S. H. & KADONO, K. 2001. Preparation of water-repellent glass by sol-gel process using perfluoroalkylsilane and tetraethoxysilane. *Journal of Colloid and Interface Science,* 235**,** 130-134.

JIN, H. J. & KAPLAN, D. L. 2003. Mechanism of silk processing in insects and spiders. *Nature,* 424**,** 1057-1061.

JONES, R. G., WILKS, E. S., METANOMSKI, W. V., KAHOVEC, J., HESS, M., STEPTO, R. & KITAYAMA, T. (eds.) 2009. *Compendium of Polymer Terminology and Nomenclature, IUPAC Recommendations 2008*: RSC.

KAPLAN, D. L., ADAMS, W. W., VINEY, C. & FARMER, B. L. (eds.) 1994. *Silk Polymers: Materials Science and Biotechnology.,* Washington, DC: American Chemical Society.

KASTON, B. J. 1964. The evolution of spider webs. *American Zoologist,* 4**,** 191-207.

KASTON, B. J. & KASTON, E. 1953. *How to Know the Spiders,* Dubuque, Iowa, USA, WM. C. Brown Company.

KENNEY, J. M., KNIGHT, D., WISE, M. J. & VOLLRATH, F. 2002. Amyloidogenic nature of spider silk. *European Journal of Biochemistry,* 269**,** 4159-4163.

KERKAM, K., KAPLAN, D., LOMBARDI, S. & VINEY, C. 1991. Liquid crystalline characteristics of natural silk secretions. *Mater. Res. Soc. Symp. Proc.,* 218**,** 239-44.

KESEL, A. B., PHILIPPI, U. & NACHTIGALL, W. 1998. Biomechanical aspects of the insect wing: an analysis using the finite element method. *Computers in Biology and Medicine,* 28**,** 423-437.

KEYES, J., JUNKIN, M., CAPPELLO, J., WU, X. Y. & WONG, P. K. 2008. Evaporation-induced assembly of biomimetic polypeptides. *Applied Physics Letters,* 93.

KHORASANI, M. T., MIRZADEH, H. & KERMANI, Z. 2005. Wettability of porous polydimethylsiloxane surface: morphology study. *Applied Surface Science,* 242**,** 339-345.

KHORASANI, M. T., MIRZADEH, H. & SAMMES, P. G. 1996. Laser induced surface modification of polydimethylsiloxane as a super-hydrophobic material. *Radiation physics and chemistry,* 47**,** 881-888.

KI, C. S., LEE, K. H., BAEK, D. H., HATTORI, M., URN, I. C., IHM, D. W. & PARK, Y. H. 2007. Dissolution and wet spinning of silk fibroin using phosphoric acid/formic acid mixture solvent system. *Journal of Applied Polymer Science,* 105**,** 1605-1610.

KINAHAN, M. E., FILIPPIDI, E., KOESTER, S., HU, X., EVANS, H. M., PFOHL, T., KAPLAN, D. L. & WONG, J. 2011. Tunable Silk: Using Microfluidics to Fabricate Silk Fibers with Controllable Properties. *Biomacromolecules,* 12**,** 1504-1511.

KNIGHT, D. P., KNIGHT, M. M. & VOLLRATH, F. 2000. Beta transition and stress-induced phase separation in the spinning of spider dragline silk. *International Journal of Biological Macromolecules,* 27**,** 205-210.

KNIGHT, D. P. & VOLLRATH, F. 1999. Liquid crystals and flow elongation in a spider's silk production line. *Proceedings of the Royal Society B: Biological Sciences***,** 519-523.

KNIGHT, D. P. & VOLLRATH, F. 2001. Changes in element composition along the spinning duct in a Nephila spider. *Naturwissenschaften,* 88**,** 179-182.

KNIGHT, D. P. & VOLLRATH, F. 2002a. Biological liquid crystal elastomers. *Philosophical Transactions Of The Royal Society Of London Series B-Biological Sciences,* 357**,** 155-163.

KNIGHT, D. P. & VOLLRATH, F. 2002b. Spinning an elastic ribbon of spider silk. *Philosophical Transactions of the Royal Society of London Series B-Biological Sciences,* 357**,** 219-227.

KNIGHT, D. P. & VOLLRATH, F. 2005. *Apparatus and method for forming materials*. US 10/148,101.

KO, J. S., LEE, K. H., BAE, D. G. & UM, I. C. 2010. Miscibility, Structural Characteristics, and Thermal Behavior of Wet Spun Regenerated Silk Fibroin/Nylon 6 Blend Filaments. *Fibers and Polymers,* 11**,** 14-20.

KOJIC, N., BICO, J., CLASEN, C. & MCKINLEY, G. H. 2006. Ex vivo rheology of spider silk. *Journal of Experiemental Biology,* 209**,** 4355-4362.

KOJIC, N., KOJIC, M., GUDLAVALLETI, S. & MCKINLEY, G. 2004. Solvent removal during synthetic and Nephila fiber spinning. *Biomacromolecules,* 5**,** 1698-1707.

KOVOOR, J. 1977. La soie et les glandes sericigenes des arachnides. *L'année Biologique Serie 4,* 16**,** 97-171.

KOVOOR, J. 1987. Comparative Structure and Histochemistry of silk-producing organs in Arachnids. *In:* NENTWIG, W. (ed.) *Ecophysiology of Spiders.* Berlin-Heidelberg-New York: Springer.

KOVOOR, J. 1990. The silk-gland system in some Tetragnathinae (Araneae : Araneidae). comparative anatomy and histochemistry. *Acta Zoologica Fennica,* 190**,** 215-222.

KOVOOR, J. & ZYLBERBERG, L. 1972. Morphologie et ultrastructure du canal des glandes ampullacées d'Araneus diadematus Clerck (Arachnida, Araneidae) *Zeitschrift Fur Zellforschung Und Mikroskopische Anatomie,* 128**,** 188-&.

KOVOOR, J. & ZYLBERBERG, L. 1980. Fine structural aspects of silk secretion in a spider (Araneus diadematus). I Elaboration in the pyriform glands. *Tissue & Cell,* 12**,** 547 - 556.

KOVOOR, J. & ZYLBERBERG, L. 1982. Fine-structural aspects of silk secretion in a spider .2. conduction in the pyriform glands. *Tissue & Cell,* 14**,** 519-530.

KRISHNAMOORTHY, C. S. 1994. *Finite Element Analysis: Theory & Programming*, Tata McGraw-Hill.

LAWRENCE, C. J. & ZHOU, W. 1991. Spin coating of non-Newtonian fluids. *Journal of Non-Newtonian Fluid Mechanics,* 39**,** 137-187.

LAZARIS, A., ARCIDIACONO, S., HUANG, Y., ZHOU, J.-F., DUGUAY, F., CHRETIEN, N., WELSH ELIZABETH, A., SOARES JASON, W. & KARATZAS COSTAS, N. 2002. Spider silk fibers spun from soluble recombinant silk produced in mammalian cells. *Science,* 295**,** 472-6.

LE TIEN, C., LACROIX, M., ISPAS-SZABO, P. & MATEESCU, M. A. 2003. N-acylated chitosan: hydrophobic matrices for controlled drug release. *Journal of Controlled Release,* 93**,** 1-13.

LEFÈVRE, T., BOUDREAULT, S., CLOUTIER, C. & PÉZOLET, M. 2008. Conformational and orientational transformation of silk proteins in the major ampullate gland of Nephila clavipes spiders. *Biomacromolecules,* 9**,** 2399-2407.

LEISK, G. G., LO, T. J., YUCEL, T., LU, Q. & KAPLAN, D. L. 2010. Electrogelation for Protein Adhesives. *Advanced Materials,* 22**,** 711-+.

LI, S. F. Y., MCGHIE, A. J. & TANG, S. L. 1994. New Internal Structure of Spider Dragline Silk Revealed by Atomic-Force Microscopy. *Biophysical Journal,* 66**,** 1209–1212.

LIBOWITZKY, E. & ROSSMAN, G. R. 1997. An IR absorption calibration for water in minerals. *American Mineralogist,* 82**,** 1111-1115.

LIIVAK, O., BLYE, A., SHAH, N. & JELINSKI, L. W. 1998. A Microfabricated Wet-Spinning Apparatus To Spin Fibers of Silk Proteins. Structure-Property Correlations. *Macromolecules,* 31**,** 2947-2951.

LIIVAK, O., FLORES, A., LEWIS, R. & JELINSKI, L. W. 1997. Conformation of the Polyalanine Repeats in Minor Ampullate Gland Silk of the Spider Nephila clavipes. *Macromolecules,* 30**,** 7127-7130.

LIU, W. G., SUN, S. J., ZHANG, X. & DE YAO, K. 2003. Self-aggregation behavior of alkylated chitosan and its effect on the release of a hydrophobic drug. *Journal of Biomaterials Science-Polymer Edition,* 14**,** 851-859.

LIU, Y., SHAO, Z. & VOLLRATH, F. 2005. Relationships between supercontraction and mechanical properties of spider silk. *Nature Materials,* 4**,** 901-905.

LU, Q., HUANG, Y., LI, M., ZUO, B., LU, S., WANG, J., ZHU, H. & KAPLAN, D. L. 2011. Silk fibroin electrogelation mechanisms. *Acta Biomaterialia,* 7**,** 2394-2400.

LUO, C. J., STOYANOV, S. D., STRIDE, E., PELAN, E. & EDIRISINGHE, M. 2012. Electrospinning versus fibre production methods: from specifics to technological convergence. *Chemical Society Reviews,* 41**,** 4708-4735.

MADSEN, B., SHAO, Z. Z. & VOLLRATH, F. 1999. Variability in the mechanical properties of spider silks on three levels: interspecific, intraspecific and intraindividual. *International Journal of Biological Macromolecules,* 24**,** 301-306.

MADSEN, B. & VOLLRATH, F. 2000. Mechanics and morphology of silk drawn from anesthetized spiders. *Naturwissenschaften,* 87**,** 148-153.

MAGOSHI, J., MAGOSHI, Y. & NAKAMURA, S. 1994. Mechanism of Fiber Formation of Silkworm. *In:* KAPLAN, D. L., ADAMS, W. W., VINEY, C. & FARMER, B. L. (eds.) *Silk Polymers: Materials Science and Biotechnology.* Washington, DC: American Chemical Society.

MANOUDIS, P. N., KARAPANAGIOTIS, I., TSAKALOF, A., ZUBURTIKUDIS, I. & PANAYIOTOU, C. 2008. Superhydrophobic composite films produced on various substrates. *Langmuir,* 24**,** 11225-11232.

MARSANO, E., CORSINI, P., AROSIO, C., BOSCHI, A., MORMINO, M. & FREDDI, G. 2005. Wet spinning of Bombyx mori silk fibroin dissolved in N-methyl morpholine N-oxide and properties of regenerated fibres. *International Journal of Biological Macromolecules,* 37**,** 179-188.

MATSUMOTO, K., UEJIMA, H., IWASAKI, T., SANO, Y. & SUMINO, H. 1996. Studies on regenerated protein fibers .3. Production of regenerated silk fibroin fiber by the self-dialyzing wet spinning method. *Journal of Applied Polymer Science,* 60**,** 503-511.

MAZIARSKI, S. & LOZINSKI, P. 1911. Über die Malpighischen gefäße der Myrmeleonidenlarven als Spinndrüsen. *Zoologischer Anzeiger,* 38**,** 401-417.

MOON, M.-J. 2012. Organization of the spinnerets and spigots in the orb web spider, Argiope bruennichi (Araneae: Araneidae). *Entomological Research,* 42**,** 85-93.

MOON, M. J., KIM, C. S. & KIM, W. K. 1988. Ultrastructure of the ampullate gland in the orb web spider Nephila clavata L. Koch. I. Excretory duct of the large ampullate gland. *Korean Journal of Electron Microscopy,* 18**,** 77-90.

MOON, S. & FARRIS, R. J. 2009. Electrospinning of Heated Gelatin-Sodium Alginate-Water Solutions. *Polymer Engineering and Science,* 49**,** 1616-1620.

MORIYA, M., OHGO, K., MASUBUCHI, Y. & ASAKURA, T. 2008a. Flow analysis of aqueous solution of silk fibroin in the spinneret of Bombyx mori silkworm by combination of viscosity measurement and finite element method calculation. *Polymer,* 49**,** 952-956.

MORIYA, M., OHGO, K., MASUBUCHI, Y., KNIGHT, D. P. & ASAKURA, T. 2008b. Micro-computerized tomographic observation of the spinning apparatus in Bombyx mori silkworms. *Polymer,* 49**,** 5665-5669.

MUZZARELLI, R. A. A. 1977. *Chitin,* Oxford, Pergamon Press.

NZAI, J. M. & PROCTOR, A. 1999. Soy lecithin phospholipid determination by Fourier transform infrared spectroscopy and the acid digest arseno-molybdate method: A comparative study. *Journal of the American Oil Chemists Society,* 76**,** 61-66.

OCHI, A., HOSSAIN, K. S., MAGOSHI, J. & NEMOTO, N. 2002a. Rheology and dynamic light scattering of silk fibroin solution extracted from the middle division of Bombyx mori silkworm. *Biomacromolecules,* 3**,** 1187-1196.

OCHI, A., NEMOTO, N., MAGOSHI, J., OHYAMA, E. & HOSSAIN, K. S. 2002b. Rheological behaviors of aqueous solution of silk fibroin. *Journal of the Society of Rheology Japan,* 30**,** 289-294.

OPELL, B. D. 2002. How spider anatomy and thread configuration shape the stickiness of cribellar prey capture threads. *Journal of Arachnology,* 30**,** 10-19.

ORTIZ, R., CESPEDES, W., NIEVES, L., ROBLES, I. V., PLAZAOLA, A., FILE, S. & CANDELAS, G. C. 2000. Small ampullate glands of Nephila clavipes. *Journal of Experimental Zoology,* 286**,** 114-119.

ORTLEPP, C. & GOSLINE, J. M. 2008. The scaling of safety factor in spider draglines. *Journal of Experimental Biology,* 211**,** 2832-2840.

ORTLEPP, C. S. & GOSLINE, J. M. 2004. Consequences of forced silking. *Biomacromolecules,* 5**,** 727-731.

OSAKI, S. 1996. Spider silk as mechanical lifeline. *Nature,* 384**,** 419-419.

OYAMA, F., MIZUNO, S. & SHIMURA, K. 1984. Studies on immunological properties of fibroin heavy and light chains. *J Biochem,* 96**,** 1689-94.

PARK, E. A. & MOON, M. J. 2009. Silk Spinning Apparatuses in the Cribellate Spider Nurscia albofasciata (Araneae: Titanoecidae). *Animal Cells and Systems,* 13**,** 153-160.

PARK, J. G. & MOON, M. J. 2008. Spinning apparatus for the dragline silk in the funnel-web spider Agelena limbata (Araneae : Agelenidae). *Animal Cells and Systems,* 12**,** 109-116.

PARKER, K. D. & RUDALL, K. M. 1957. Structure of the Silk of Chrysopa Egg-stalks. *Nature,* 179**,** 905-906.

PAULINO, A. T., SIMIONATO, J. I., GARCIA, J. C. & NOZAKI, J. 2006. Characterization of chitosan and chitin produced from silkworm crysalides. *Carbohydrate Polymers,* 64**,** 98-103.

PEAKALL, D. B. 1969. Synthesis of silk mechanism and location. *American Zoologist,* 9**,** 71-79.

PEREZ-RIGUEIRO, J., BIANCOTTO, L., CORSINI, P., MARSANO, E., ELICES, M., PLAZA, G. R. & GUINEA, G. V. 2009. Supramolecular organization of regenerated silkworm silk fibers. *International Journal of Biological Macromolecules,* 44**,** 195-202.

PEREZ-RIGUEIRO, J., ELICES, M., PLAZA, G. R., REAL, J. I. & GUINEA, G. V. 2006. The influence of anaesthesia on the tensile properties of spider silk. *Journal of Experimental Biology,* 209**,** 320-326.

PETERS, H. M. & KOVOOR, J. 1991. The silk-producing system of *Linyphia triangularis* (Araneae, Linyphiidae) and some comparisons with Araneidae. *Zoomorphology,* 111**,** 1-17.

PETERS, W. (ed.) 1992. *Peritrophic Membranes*: Springer.

PHILLIPS, C. E. & VANDEBERG, J. S. 1976. Mechanism for sensillum fluid-flow in trichogen and tormogen cells of *Phormia-regina* (meigen) (Diptera-Calliphoridae). *International Journal of Insect Morphology & Embryology,* 5**,** 423-431.

PHILLIPS, D. M., DRUMMY, L. F., NAIK, R. R., DE LONG, H. C., FOX, D. M., TRULOVE, P. C. & MANTZ, R. A. 2005. Regenerated silk fiber wet spinning from an ionic liquid solution. *Journal of Materials Chemistry,* 15**,** 4206-4208.

PILLAI, C. K. S., PAUL, W. & SHARMA, C. P. 2009. Chitin and chitosan polymers: Chemistry, solubility and fiber formation. *Progress in Polymer Science,* 34**,** 641-678.

PLAZA, G. R., CORSINI, P., MARSANO, E., PEREZ-RIGUEIRO, J., ELICES, M., RIEKEL, C., VENDRELY, C. & GUINEA, G. V. 2012. Correlation between processing conditions, microstructure and mechanical behavior in regenerated silkworm silk fibers. *JOURNAL OF POLYMER SCIENCE PART B-POLYMER PHYSICS,* 50**,** 455-465.

PLAZA, G. R., CORSINI, P., PEREZ-RIGUEIRO, J., MARSANO, E., GUINEA, G. V. & ELICES, M. 2008. Effect of water on Bombyx mori regenerated silk fibers and its application in modifying their mechanical properties. *Journal of Applied Polymer Science,* 109**,** 1793-1801.

PORTER, D. 1995. *Group Interaction Modelling of Polymer Properties,* New York, Marcel Dekker.

PORTER, D. & GOULD, P. J. 2009. Predictive nonlinear constitutive relations in polymers through loss history. *International Journal of Solids and Structures,* 46**,** 1981-1993.

PORTER, D., GUAN, J. & VOLLRATH, F. 2012. Spider Silk: Super Material or Thin Fibre? *Advanced Materials,* 25**,** 1275–1279.

PORTER, D., GUAN, J. & VOLLRATH, F. 2013. Spider Silk: Super Material or Thin Fibre? *Advanced Materials,* 25**,** 1275-1279.

PORTER, D. & VOLLRATH, F. 2008. The role of kinetics of water and amide bonding in protein stability. *Soft Matter,* 4**,** 328-336.

PORTER, D., VOLLRATH, F. & SHAO, Z. 2005. Predicting the mechanical properties of spider silk as a model nanostructured polymer. *The European Physical Journal E-Soft Matter,* 16**,** 199-206.

PRUDHOMME, J. C. & COUBLE, P. 1979. The adaption of the silk gland cell to the production of fibroin in *Bombyx mori*. *Biochimie,* 61**,** 215-227.

QIN, G., HU, X., CEBE, P. & KAPLAN, D. L. 2012. Mechanism of resilin elasticity. *Nature Communications,* 3.

RAMMENSEE, S., HUEMMERICH, D., HERMANSON, K. D., SCHEIBEL, T. & BAUSCH, A. R. 2006. Rheological characterization of hydrogels formed by recombinantly produced spider silk. *Applied Physics A: Materials Science & Processing,* 82**,** 261-264.

RAMMENSEE, S., SLOTTA, U., SCHEIBEL, T. & BAUSCH, A. R. 2008. Assembly mechanism of recombinant spider silk proteins (microfluidic). *Proceedings of the National Academy of Sciences of the United States of America,* 105**,** 6590-6595.

RAVI KUMAR, M. N. V. 2000. A review of chitin and chitosan applications. *Reactive and Functional Polymers,* 46**,** 1-27.

RAVINDRANATH, M. H. R. & RAVINDRANATH, M. H. 1975. A simple procedure to detect chitin in delicate structures. *Acta Histochemica,* 53**,** 203-205.

RIEKEL, C., MADSEN, B., KNIGHT, D. & VOLLRATH, F. 2000. X-ray diffraction on spider silk during controlled extrusion under a synchrotron radiation X-ray beam. *Biomacromolecules,* 1**,** 622-626.

RIEKEL, C., MÜLLER, M. & VOLLRATH, F. 1999. In Situ X-ray Diffraction during Forced Silking of Spider Silk. *Macromolecules,* 32**,** 4464-4466.

RISING, A., NIMMERVOIL, H., GRIP, S., FERNANDEZ-ARIAS, A., STORCKENFELDT, E., KNIGHT, D. P., VOLLRATH, F. & ENGSTROEM, W. 2005. Spider silk proteins - mechanical property and gene sequence. *Zoological Science,* 22**,** 273-281.

ROBERTS, M. J. 1995. *Spiders of Britain & Northern Europe*, HarperCollins.

ROUSSEAU, M. E., LEFEVRE, T. & PEZOLET, M. 2009. Conformation and Orientation of Proteins in Various Types of Silk Fibers Produced by Nephila clavipes Spiders. *Biomacromolecules,* 10**,** 2945-2953.

RUIZ-HERRERA, J. & MARTINEZ-ESPINOZA, A. D. 1999. Chitin biosynthesis and structural organization *in vivo*. *In:* JOLLÈS, P. & MUZZARELLI, R. A. A. (eds.) *Chitin and Chitinases.* Springer.

SCHARTAU, W. & LEIDESCHER, T. J. 1983. Composition of the hemolymph of the Tarantula Eurypelma-Californicum. *Journal of Comparative Physiology,* 152**,** 73-77.

SEHNAL, F. & AKAI, H. 1990. Insect silk glands: their types, development and function, and effects of environmental factors and morphogenetic hormones on them. *International Journal of Insect Morphology & Embryology,* 19**,** 79-132.

SEIDEL, A., LIIVAK, O., CALVE, S., ADASKA, J., JI, G., YANG, Z., GRUBB, D., ZAX, D. B. & JELINSKI, L. W. 2000. Regenerated Spider Silk: Processing, Properties, and Structure. *Macromolecules,* 33**,** 775-780.

SEIDEL, A., LIIVAK, O. & JELINSKI, L. W. 1998. Artificial Spinning of Spider Silk. *Macromolecules,* 31**,** 6733-6736.

SELDEN, P. A., SHEAR, W. A. & BONAMO, P. M. 1991. A spider and other arachnids from the Devonian of New-York, and reinterpretations of Devonian araneae. *Palaeontology,* 34**,** 241-281.

SEVERS, N. J. 2007. Freeze-fracture electron microscopy. *Nat. Protocols,* 2**,** 547-576.

SHAO, Z. Z. & VOLLRATH, F. 2002. Materials: Surprising strength of silkworm silk. *Nature,* 418**,** 741-741.

SHAO, Z. Z., VOLLRATH, F., YANG, Y. & THOGERSEN, H. C. 2003. Structure and behavior of regenerated spider silk. *Macromolecules,* 36**,** 1157-1161.

SHEAR, W. A., PALMER, J. M., CODDINGTON, J. A. & BONAMO, P. M. 1989. A Devonian Spinneret: Early Evidence of Spiders and Silk Use. *Science,* 246**,** 479-481.

SHULTZ, J. W. 1987. The origin of the spinning apparatus in spiders. *Biological Reviews,* 62**,** 89-113.

SNODGRASS, R. E. 1935. *Principles of insect morphology*.

SOHN, S. & GIDO, S. P. 2009. Wet-Spinning of Osmotically Stressed Silk Fibroin. *Biomacromolecules,* 10**,** 2086-2091.

SORENSEN, G. S., CRIBB, B. W., MERRITT, D., JOHNSON, M. L. & ZALUCKI, M. P. 2006. Structure and ultrastructure of the silk glands and spinneret of Helicoverpa armigera (Hubner) (Lepidoptera : Noctuidae). *Arthropod structure & development,* 35**,** 3-13.

SPONNER, A., SCHLOTT, B., VOLLRATH, F., UNGER, E., GROSSE, F. & WEISSHART, K. 2005. Characterization of the protein components of Nephila clavipes dragline silk. *Biochemistry,* 44**,** 4727-4736.

STARK, M., GRIP, S., RISING, A., HEDHAMMAR, M., ENGSTROM, W., HJALM, G. & JOHANSSON, J. 2007. Macroscopic Fibers Self-Assembled from Recombinant Miniature Spider Silk Proteins. *Biomacromolecules*.

SUTHERLAND, T., YOUNG, J. & WEISMAN, S. 2009. Insect Silk: One Name, Many Materials. *Annual review of entomology,* 55**,** 171-188.

TAMBURRO, A. M., PANARIELLO, S., SANTOPIETRO, V., BRACALELLO, A., BOCHICCHIO, B. & PEPE, A. 2010. Molecular and Supramolecular Structural Studies on Significant Repetitive Sequences of Resilin. *ChemBioChem,* 11**,** 83-93.

TANNER, S. F., CHANZY, H., VINCENDON, M., ROUX, J. C. & GAILL, F. 1990. High-resolution solid-state C-13 nuclear-magnetic-resonance study of chitin. *Macromolecules,* 23**,** 3576-3583.

TASHIRO, Y. & OTSUKI, E. 1970. Studies On Posterior Silk Gland Of Silkworm Bombyx Mori .4. Ultracentrifugal Analyses of Native Silk Proteins, Especially Fibroin Extracted from the Middle Silk Gland of the Mature Silkworm. *Journal of Cell Biology,* 46**,** 1-16.

TATHAM, A. S. & SHEWRY, P. R. 2000. Elastomeric proteins: biological roles, structures and mechanisms. *Trends in Biochemical Sciences,* 25**,** 567-571.

TERRY, A. E., KNIGHT, D. P., PORTER, D. & VOLLRATH, F. 2004. PH induced changes in the rheology of silk fibroin solution from the middle division of Bombyx mori silkworm. *Biomacromolecules,* 5**,** 768-772.

TEULE, F., FURIN, W. A., COOPER, A. R., DUNCAN, J. R. & LEWIS, R. V. 2007. Modifications of spider silk sequences in an attempt to control the mechanical properties of the synthetic fibers. *Journal of Materials Science,* 42**,** 8974-8985.

THOMSEN, M. N. 1921. Some observations on the biology and anatomy of a cocoon-making Chalcid larva, *Euplectrus bicolor*. *Swed. Naturhist Med Dansk For,* 384**,** 73-89.

TILLINGHAST, E. K., CHASE, S. F. & TOWNLEY, M. A. 1984. Water extraction by the major ampullate duct during silk formation in the spider, Argiope aurantia Lucas. *Journal of Insect Physiology,* 30**,** 591-596.

TILLINGHAST, E. K. & TOWNLEY, M. 1987. Chemistry, physical properties and synthesis of Araneidae orb webs. *In:* NENTWIG, W. (ed.) *Ecophysiology of Spiders.* Heidelberg: Springer.

TILLINGHAST, E. K. & TOWNLEY, M. A. 1986. The Independent Regulation Of Protein-Synthesis In The Major Ampullate Glands Of Araneus-Cavaticus (Keyserling). *Journal of Insect Physiology,* 32**,** 117-123.

TILLINGHAST, E. K., TOWNLEY, M. A., BERNSTEIN, D. T. & GALLAGHER, K. S. 1991. Comparative study of orb web hygroscopicity and adhesive spiral composition in three araneid spiders. *Journal of Experimental Zoology,* 259**,** 154-165.

TOMA, C., PITTENGER, M. F., CAHILL, K. S., BYRNE, B. J. & KESSLER, P. D. 2002. Human mesenchymal stem cells differentiate to a cardiomyocyte phenotype in the adult murine heart. *Circulation,* 105**,** 93-98.

TOWNLEY, M. A., HORNER, N. V., CHERIM, N. A., TUGMON, C. R. & TILLINGHAST, E. K. 1991a. Selected Aspects of Spinning Apparatus Development in Araneus- Cavaticus (Araneae, Araneidae). *Journal of Morphology,* 208**,** 175-&.

TOWNLEY, M. A., HORNER, N. V., CHERIM, N. A., TUGMON, C. R. & TILLINGHAST, E. K. 1991b. Selected aspects of spinning apparatus development in Araneus-cavaticus (Araneae, Araneidae). *Journal of Morphology,* 208**,** 175-191.

TOWNLEY, M. A. & TILLINGHAST, E. K. 2009. Developmental changes in spider spinning fields: a comparison between Mimetus and Araneus (Araneae: Mimetidae, Araneidae). *Biological Journal of the Linnean Society,* 98**,** 343-383.

TOWNLEY, M. A., TILLINGHAST, E. K. & CHERIM, N. A. 1993a. Molt-Related Changes in Ampullate Silk Gland Morphology and Usage in the Araneid Spider Araneus-Cavaticus. *Philosophical Transactions of the Royal Society of London Series B-Biological Sciences,* 340**,** 25-38.

TOWNLEY, M. A., TILLINGHAST, E. K. & CHERIM, N. A. 1993b. Moult-related changes in ampullate silk gland morphology and usage in the araneid spider araneus-cavaticus. *Philosophical Transactions of the Royal Society of London Series B-Biological Sciences,* 340**,** 25-38.

TRABBIC, K. A. & YAGER, P. 1998. Comparative structural characterization of naturally- and synthetically-spun fibers of Bombyx mori fibroin. *Macromolecules,* 31**,** 462-471.

VICTORIANO, E. & GREGORIO, E. A. 2002. Ultrastructure of the excretory duct in the silk gland of the sugarcane borer Diatraea saccharalis (Lepidoptera : Pyralidae). *Arthropod structure & development,* 31**,** 15-21.

VINCENT, J. F. V. 2012. Structural Biomaterials. 3rd ed. Princeton, New Jersey, and Woodstock, UK: Princeton University Press.

VINCENT, J. F. V. & WEGST, U. G. K. 2004. Design and mechanical properties of insect cuticle. *Arthropod structure & development,* 33**,** 187-199.

VOLLRATH, F. 1992. Spider webs and silks. *Scientific American,* 266**,** 70-76.

VOLLRATH, F. & KNIGHT, D. P. 1999. Structure and function of the silk production pathway in the spider Nephila edulis. *International Journal of Biological Macromolecules,* 24**,** 243-249.

VOLLRATH, F. & KNIGHT, D. P. 2001. Liquid crystalline spinning of spider silk. *Nature,* 410**,** 541-548.

VOLLRATH, F., KNIGHT, D. P. & HU, X. W. 1998. Silk production in a spider involves acid bath treatment. *Proceedings of the Royal Society of London Series B-Biological Sciences,* 265**,** 817-820.

VOLLRATH, F., MADSEN, B. & SHAO, Z. 2001. The effect of spinning conditions on the mechanics of a spider's dragline silk. *Proceedings of the Royal Society of London Series B-Biological Sciences,* 268**,** 2339-2346.

VOLLRATH, F. & PORTER, D. 2006. Spider silk as a model biomaterial. *Applied Physics a-Materials Science & Processing,* 82**,** 205-212.

VOLLRATH, F., PORTER, D. & HOLLAND, C. 2011. There are many more lessons still to be learned from spider silks. *Soft Matter,* 7**,** 9595-9600.

WAINWRIGHT, S. A., BIGGS, W. D., CURREY, J. D. & GOSLINE, J. M. 1976a. *Mechanical design in organisms*.

WAINWRIGHT, S. A., BIGGS, W. D., CURREY, J. D. & GOSLINE, J. M. 1976b. *Mechanical Design in Organisms,* New York, John Wiley and Sons.

WASHBURN, E. W. 1921. The Dynamics of Capillary Flow. *Physical Review,* 17**,** 273.

WEI, W., ZHANG, Y., SHAO, H. & HU, X. 2011a. Posttreatment of the dry-spun fibers obtained from regenerated silk fibroin aqueous solution in ethanol aqueous solution. *Journal of Materials Research,* 26**,** 1100-1106.

WEI, W., ZHANG, Y., ZHAO, Y., LUO, J., SHAO, H. & HU, X. 2011b. Bio-inspired capillary dry spinning of regenerated silk fibroin aqueous solution. *Materials Science and Engineering: C,* 31**,** 1602-1608.

WEI, W., ZHANG, Y., ZHAO, Y., SHAO, H. & HU, X. 2012. Studies on the post-treatment of the dry-spun fibers from regenerated silk fibroin solution: Post-treatment agent and method. *Materials & Design,* 36**,** 816-822.

WEIGUO, Q., CAPPELLO, J. & XIAOYI, W. 2011. Autoclaving as a chemical-free process to stabilize recombinant silk-elastinlike protein polymer nanofibers. *Applied Physics Letters,* 98**,** 263702 (3 pp.)-263702 (3 pp.).

WEIS-FOGH, T. 1960. A Rubber-Like Protein in Insect Cuticle. *Journal of Experimental Biology,* 37**,** 889-907.

WEISMAN, S., HARITOS, V. S., CHURCH, J. S., HUSON, M. G., MUDIE, S. T., RODGERS, A. J. W., DUMSDAY, G. J. & SUTHERLAND, T. D. 2010. Honeybee silk: recombinant protein production, assembly and fiber spinning. *Biomaterials,* 31**,** 2695-700.

WENZEL, R. N. 1936. Resistance of solid surfaces to wetting by water. *Industrial & engineering chemistry,* 28**,** 988-994.

WILLCOX, P. J., GIDO, S. P., MULLER, W. & KAPLAN, D. L. 1996. Evidence of a cholesteric liquid crystalline phase in natural silk spinning processes. *Macromolecules,* 29**,** 5106-5110.

WILSON, R. S. 1962a. The Control of Dragline Spinning in the Garden Spider. *Quarterly Journal of Microscopical Science,* 103**,** 557-571.

WILSON, R. S. 1962b. The Structure of the Dragline Control Valves in the Garden Spider. *Quarterly Journal of Microscopical Science,* 103**,** 549-555.

WILSON, R. S. 1969. Control of Drag-Line Spinning in Certain Spiders. *American Zoologist,* 9**,** 103-111.

WORK, R. W. 1977. Mechanisms of major ampullate silk fiber formation by orb-web-spinning spiders. *Trans. Amer. Micros. Soc.,* 96**,** 170-189.

WORK, R. W. & EMERSON, P. D. 1982. An Apparatus and Technique for the Forcible Silking of Spiders. *Journal of Arachnology,* 10**,** 1-10.

WYNNE, A. 1997. *Textiles,* Oxford, UK, Macmillan Education.

XIA, Q. Y., ZHOU, Z. Y., LU, C., CHENG, D. J., DAI, F. Y., LI, B., ZHAO, P., ZHA, X. F., CHENG, T. C., CHAI, C. L., PAN, G. Q., XU, J. S., LIU, C., LIN, Y., QIAN, J. F., HOU, Y., WU, Z. L., LI, G. R., PAN, M. H., LI, C. F., SHEN, Y. H., LAN, X. Q., YUAN, L. W., LI, T., XU, H. F., YANG, G. W., WAN, Y. J., ZHU, Y., YU, M. D., SHEN, W. D., WU, D. Y., XIANG, Z. H., YU, J., WANG, J., LI, R. Q., SHI, J. P., LI, H., LI, G. Y., SU, J. N., WANG, X. L., LI, G. Q., ZHANG, Z. J., WU, Q. F., LI, J., ZHANG, Q. P., WEI, N., XU, J. Z., SUN, H. B., DONG, L., LIU, D. Y., ZHAO, S. L., ZHAO, X. L., MENG, Q. S., LAN, F. D., HUANG, X. G., LI, Y. Z., FANG, L., LI, D. W., SUN, Y. Q., ZHANG, Z. P., YANG, Z., HUANG, Y. Q., XI, Y., QI, Q. H., HE, D. D., HUANG, H. Y., ZHANG, X. W., WANG, Z. Q., LI, W. J., CAO, Y. Z., YU, Y. P., YU, H., LI, J. H., YE, J. H., CHEN, H., ZHOU, Y., LIU, B., YE, J., JI, H., LI, S. T., NI, P. X., ZHANG, J. G., ZHANG, Y., ZHENG, H. K., MAO, B. Y., WANG, W., YE, C., LI, S. G., WONG, G. K. S. & YANG, H. M. 2004. A draft sequence for the genome of the domesticated silkworm (Bombyx mori). *Science,* 306**,** 1937-1940.

XIA, X.-X., QIAN, Z.-G., KI, C. S., PARK, Y. H., KAPLAN, D. L. & LEE, S. Y. 2010a. Native-sized recombinant spider silk protein produced in metabolically engineered Escherichia coli results in a strong fiber. *Proceedings of the National Academy of Sciences*.

XIA, X. X., QIAN, Z. G., KI, C. S., PARK, Y. H., KAPLAN, D. L. & LEE, S. Y. 2010b. Native-sized recombinant spider silk protein produced in metabolically engineered Escherichia coli results in a strong fiber. *Proceedings of the National Academy of Sciences of the United States of America,* 107**,** 14059-14063.

YAMADA, H., NAKAO, H., TAKASU, Y. & TSUBOUCHI, K. 2001. Preparation of undegraded native molecular fibroin solution from silkworm cocoons. *Mat Sci Eng C-Bio S,* 14**,** 41-46.

YAN, J. P., ZHOU, G. Q., KNIGHT, D. P., SHAO, Z. Z. & CHEN, X. 2010. Wet-Spinning of Regenerated Silk Fiber from Aqueous Silk Fibroin Solution: Discussion of Spinning Parameters. *Biomacromolecules,* 11**,** 1-5.

YAO, J. M., MASUDA, H., ZHAO, C. H. & ASAKURA, T. 2002. Artificial spinning and characterization of silk fiber from Bombyx mori silk fibroin in hexafluoroacetone hydrate. *Macromolecules,* 35**,** 6-9.

YIN, J. W., CHEN, E. Q., PORTER, D. & SHAO, Z. Z. 2010. Enhancing the Toughness of Regenerated Silk Fibroin Film through Uniaxial Extension. *Biomacromolecules,* 11**,** 2890-2895.

YONEMURA, N. & SEHNAL, F. E. 2006. The Design of Silk Fiber Composition in Moths Has Been Conserved for More Than 150 Million Years. *Journal of Molecular Evolution,* 63**,** 42-43.

YOUNG, J. H. & MERRITT, D. J. 2003. The ultrastructure and function of the silk-producing basitarsus in the Hilarini (Diptera : Ernpididae). *Arthropod structure & development,* 32**,** 157-165.

YUAN, Q. Q., YAO, J. R., HUANG, L., CHEN, X. & SHAO, Z. Z. 2010. Correlation between structural and dynamic mechanical transitions of regenerated silk fibroin. *Polymer,* 51**,** 6278-6283.

YUCEL, T., KOJIC, N., LEISK, G. G., LO, T. J. & KAPLAN, D. L. 2010. Non-equilibrium silk fibroin adhesives. *Journal of Structural Biology,* 170**,** 406-412.

ZHAO, C., YAO, J., MASUDA, H., KISHORE, R. & ASAKURA, T. 2003. Structural characterization and artificial fiber formation of bombyx mori silk fibroin in hexafluoro-Iso-Propanol solvent system. *Biopolymers,* 69**,** 253-259.

ZHENGHUA, Z., IMADA, T. & ASAKURA, T. 2009. Preparation and characterization of regenerated fiber from the aqueous solution of Bombyx mori cocoon silk fibroin. *Materials Chemistry and Physics,* 117**,** 430-3.

ZHENGHUA, Z., OHGO, K., WATANABE, R., TAKEZAWA, T. & ASAKURA, T. 2008. Preparation and characterization of regenerated Bombyx mori silk fibroin fiber containing recombinant cell-adhesive proteins; nonwoven fiber and monofilament. *Journal of Applied Polymer Science,* 109**,** 2956-63.

ZHOU, G. Q., SHAO, Z. Z., KNIGHT, D. P., YAN, J. P. & CHEN, X. 2009. Silk Fibers Extruded Artificially from Aqueous Solutions of Regenerated Bombyx mori Silk Fibroin are Tougher than their Natural Counterparts. *Advanced Materials,* 21**,** 366-370.

ZHOU, J., ELLIS, A. V. & VOELCKER, N. H. 2010. Recent developments in PDMS surface modification for microfluidic devices. *Electrophoresis,* 31**,** 2-16.

ZHU, Z., KIKUCHI, Y., KOJIMA, K., TAMURA, T., KUWABARA, N., NAKAMURA, T. & ASAKURA, T. 2010. Mechanical Properties of Regenerated Bombyx mori Silk Fibers and Recombinant Silk Fibers Produced by Transgenic Silkworms. *Journal of Biomaterials Science-Polymer Edition,* 21**,** 395-412.

ZHU, Z. H., OHGO, K. & ASAKURA, T. 2008. Preparation and characterization of regenerated Bombyx mori silk fibroin fiber with high strength. *Express Polymer Letters,* 2**,** 885-889.